Identification and characterization of genes involved with iron-dependent root growth under limiting phosphorus

Dissertation

zur Erlangung des

Doktorgrades der Naturwissenschaften (Dr. rer. nat.)

der

Naturwissenschaftlischen Fakultät I

-Biowissenschaftlen-

der Martin-Luther-Universität Halle-Wittenberg

vorgelegt von

Herrn Maniero, Rodolfo Augusto

Reviewers:

I. **Prof. Dr. Nicolaus von Wirén**

Leibniz Institute of Plant Genetics and Crop Plant Research (IPK)

Gatersleben, Germany

II. **Prof. Dr. Klaus Humbeck**

Institute of Biology/Plant Physiology, Martin-Luther-University Halle-Wittenberg

Halle (Saale), Germany

III. **Prof. Dr. Ute Krämer**

Faculty of Biology and Biotechnology, Ruhr University Bochum

Bochum, Germany

Chair of thesis defense:

Prof. Dr. Steffen Abel

Leibniz Institute of Plant Biochemistry, Martin-Luther-University Halle-Wittenberg

Halle (Saale), Germany

Date of thesis defense: 21.01.2025

Datum der Verteidigung der Dissertation: 21.01.2025

Halle (Saale)

Parts of this thesis are published in:

Maniero, R. A., Picco, C., Hartmann, A., Engelberger, F., Gradogna, A., Scholz-Starke, J., Melzer, M., Künze, G., Carpaneto, A., von Wirén, N., Giehl, R. F. H. (2024). Ferric reduction by a CYBDOM protein counteracts increased iron availability in root meristems induced by phosphorus deficiency. *Nature Communications*, 15, 422.

Table of contents

1 Summary

Phosphorus (P)[1] is essential for plant growth and development. In most soils, P availability is often limited due to its strong sorption onto aluminum (Al) and iron (Fe) oxides. To mobilize P from the soil, many plant species secrete malate, which forms complexes with Fe(III) and Al(III), thus releasing the sorbed/precipitated phosphate for root uptake. Besides increasing P availability, the release of malate can induce an overaccumulation of Fe in the apoplast of root tips leading to primary root growth inhibition. However, it remains elusive how cells in this root zone cope with the increased Fe availability under low P conditions. In the present thesis, two molecular players involved in Fe-dependent root growth under low P availability were identified and characterized. From a transcriptome analysis of *Arabidopsis thaliana* roots, one uncharacterized gene from the cytochrome *b*561 associated with dopamine β-monooxygenase N-terminal (DOMON) family was identified to be induced in response to P deficiency. A knockout insertional mutant for the gene exhibited impaired meristematic integrity and cell elongation specifically under low-P conditions. Therefore, the gene was named *HYPERSENSITIVE TO LOW P1* (*HYP1*). It was found that HYP1 is a plasma membrane protein, which in P-deficient roots is mainly present in the root cap cells and adjacent cells above the quiescent center in the root apical meristem. Disruption of *HYP1* results in Fe overaccumulation and callose deposition in the root meristem, while *HYP1* overexpression decreases the concentration of apoplastic Fe and improves the tolerance of roots to low P. HYP1 is a CYBDOM protein possessing a DOMON domain fused to a cytochrome *b*561 domain, thus sharing structural similarities with ferric reductases of animal cells. By expressing *HYP1* in the ferric-reductase-deficient mutant *fro2* it was possible to demonstrate HYP1-mediated ferric reduction activity. It was further found that HYP1 can mediate the reduction of cupric substrates, suggesting that HYP1 is a metalloreductase. In root meristems, it was possible to demonstrate that HYP1-mediated ferric reduction counteracts the increased Fe availability induced by malate release, allowing the excess pools of apoplastic Fe to dissipate. Furthermore, it was possible to rescue the short-root phenotype of *hyp1* plants with ferrous Fe, highlighting the importance of ferric reduction for the maintenance of root growth under low P. Since *HYP1* belongs to a multigene family, transcriptional reporters were generated to investigate the tissue-specific expression of all 11 DOMON-coding genes of *A. thaliana*. Transcriptional activity for four of them was detected in the primary root tip, in similar cell-types were *HYP1* is expressed, while all were expressed in leaves and six in flowers and siliques. Thus, the overlapping tissue-specific expression domains of several DOMON-encoding genes may suggest partial redundant functions in different plant tissues. The second gene identified

[1] In the present thesis, the abbreviation “P” is preferentially used throughout the text as it refers to all pools of the essential mineral element phosphorus, while the abbreviation “Pi” is only used when specifically refering to inorganic phosphate.

in this study was *MONODEHYDROASCORBATE REDUCTASE 3* (*MDHAR3*), which encodes a putative ascorbate regenerating enzyme and was among the P deficiency-induced genes in roots. Ascorbate was demonstrated to be an efficient electron donor for HYP1 and, thus, it was hypothesized that MDHAR3 could maintain cytosolic pools of reduced ascorbate for HYP1-mediated reduction of apoplastic substrates. The analysis of generated transcriptional and translational fusion reporters revealed that MDHAR3 is present in several cell layers of the root apical meristem and located in the cytosol, thus partially co-localizing with HYP1. Although the disruption in *MDHAR3* did not cause a significant decrease in primary root growth as in *hyp1* mutants, it was found that MDHAR3 is required when HYP1 is functional. Taken together, the present thesis uncovered a novel mechanism involving ferric reduction by an ascorbate-dependent metalloreductase and the putative recycling of cytosolic ascorbate pools to maintain root meristem integrity under low P conditions.

2 Introduction

Phosphorus (P) is an important macronutrient for plant growth and development, as it is involved in nearly all processes that are crucial to cell functionality. This element is an essential key component in several biomolecules, such as adenosine triphosphate (ATP), nicotinamide adenine dinucleotide phosphate (NADPH), nucleic acids (DNA and RNA), phospholipids, and sugar phosphates. It is also required in several metabolic processes, such as glycolysis, photosynthesis, nucleic acid synthesis, membrane synthesis, enzyme activation/inactivation, signaling, carbohydrate metabolism, and nitrogen fixation (Bieleski and Ferguson, 1983; Schachtman et al., 1998; Raghothama, 1999; Vance et al., 2003). In most plant species, the P concentration considered as optimal for growth is in the order of 60 µmol g^{-1} of dry matter, which corresponds to approximately 0.2% of the total plant dry weight (Epstein and Bloom, 2004). The cytosolic concentration of P ranges from 5 to 17 µM, whereas the apoplastic concentration is generally less than 2 µM (Mimura et al., 1996; Mimura, 1999). Because the concentration of Pi in the soil solution is often low, ranging from 2 to 10 mM (Raghothama, 1999) and, consequently, the supply of Pi to the root surface by diffusion is slow (Fitter and Hay, 2012), a highly efficient transporter system is required in order to meet the whole plant demands for P. Otherwise, P deficiency can have detrimental effects, including reduced leaf expansion, decreased leaf number, suppressed tillering, altered shoot-to-root biomass ratios, premature senescence, and reduced size and number of flowers and grains (Hammond and White, 2008).

In most soils, the total amounts of P are considerably low, or the P that is present is only poorly available to plants, making P one of the most limiting nutrients for plant growth and development. Low P availability originates because the negatively charged $H_2PO_4^-$ and HPO_4^{2-} anions, which are the main forms of P taken up by plant roots, are often precipitated with calcium (Ca) or strongly adsorbed onto iron (Fe) and aluminum (Al) (hydro)oxides (Shen et al., 2011). To cope with limiting P availability in soils, plants have evolved a series of mechanisms to mobilize and efficiently acquire this nutrient from the rhizosphere (Lambers et al., 2022). One of these mechanisms is the exudation of carboxylates, which is responsible for the release of the sorbed phosphate (Ryan et al., 2001). Interestingly, the increased release of malate by P-deficient roots does not only increase the availability of P but also of Fe (Lopez-Hernandez et al., 1979). The impact of this interaction has been characterized in more detail in the model plant *Arabidopsis thaliana* (hereafter Arabidopsis). In this species, root inhibition under low P can be attenuated by removing Fe from the growth medium or by disrupting P deficiency-induced malate release (Svistoonoff et al., 2007; Ward et al., 2008; Müller et al., 2015; Balzergue et al., 2017; Mora-Macías et al., 2017). Furthermore, it has been shown that overaccumulation of labile Fe – the intracellular nonprotein-bound Fe that can generate oxygen

radicals via Fenton reaction and play critical roles in diverse biological processes in living cells – in the apoplast triggers ectopic deposition of callose in the root apical meristem and increases cell wall stiffening in the elongation zone (Müller et al., 2015; Balzergue et al., 2017; Gutiérrez-Alanís et al., 2018). Fe-dependent primary root inhibition stimulates the development of a shallow and highly branched root system (Pérez-Torres et al., 2008; Gruber et al., 2013), an architectural change thought to improve P foraging from the topsoil (Lynch and Brown, 2001). However, if not counteracted, excess Fe may ultimately disrupt stem cell niche identity and root apical meristem integrity (Müller et al., 2015).

In most plant cells and organelles, Fe uptake is driven by Fe(III) reduction via chemical reductants and membrane-bound metalloreductases of the ferric reductase oxidase (FRO) family (Jain et al., 2014). In Arabidopsis roots, Fe reduction relies on plasma membrane-bound FRO2 and the release of redox-active coumarins (Robinson et al., 1999; Rajniak et al., 2018; Paffrath et al., 2024). Interestingly, *FRO2* is not expressed in the root apical zone and is repressed in response to P deficiency elsewhere (Connolly et al., 2003; Li and Lan, 2015), whereas *FRO3* expression in the root apical meristem is only detected in Fe-deficient roots (Mukherjee et al., 2006). Furthermore, since the promoters of genes encoding the main coumarin biosynthesis enzymes are only active in the root hair zone (Schmidt et al., 2014; Rajniak et al., 2018), it remains elusive how Fe homeostasis is maintained in root tips of P-deficient plants. The following sections provide an overview of P availability in soils and highlight the role of molecular players involved in the acquisition, sensing, and signaling of this nutrient in plants. A particular focus is placed on the crosstalk between P and Fe, a dynamic interaction that leads to profound changes in root system architecture.

2.1 P in the soil: forms and availability

In most soils, P exists as inorganic and organic forms, with their concentrations varying depending on the soil type (Hansen et al., 2004; Turner et al., 2007). However, in general, the inorganic fraction is the most prominent, with concentrations ranging from 35% to 70% in soils (Harrison, 1987). Inorganic phosphate (Pi) in soils originates from primary minerals, such as apatite [$Ca_5(PO_4)_3(F,Cl,OH)$], strengite ($FePO_4.2H_2O$), and variscite ($AlPO_4.2H_2O$). The Pi present in these minerals is extremely stable, and it can only be released into the soil through slow weathering processes. Such processes are gradual and, alone, insufficient to meet the high P demand of crops. Therefore, in agriculture, fertilizers derived from Pi-rich rocks are widely employed to replenish pools of available P to sustain optimal crop growth and yield.

Due to its high reactivity, Pi is rarely found in soils in its free form. Instead, Pi is strongly sorbed onto secondary minerals containing elements like calcium (Ca), and Al and Fe oxides.

All the Pi that is trapped on the surface of the secondary minerals can only be slowly released through weathering process in a similar fashion to the Pi sorbed onto the primary minerals. However, the dissolution rate is much slower and depends on specific conditions, such as soil pH and particle size (Pierzynski et al., 2005; Oelkers and Valsami-Jones, 2008). For example, as the soil pH increases, the solubility of complexes of Fe- and Al-Pi increases, while the solubility of Ca-Pi complexes decreases (Hinsinger, 2001).

Reactions of sorption and desorption, the latter defined as the process of releasing Pi from Al/Fe oxides and clay particles, coexist in soils around the world. Under acidic conditions, which represent 30% of the topsoil and 75% of the subsoil across Earth's ice-free land area (Food and Agriculture Organization, 2016), Pi is predominantly immobilized by Al and Fe (hydro)oxides (Liao et al., 2001). These minerals include gibbsite, hematite, and goethite (Parfitt, 1989). At the surface of clay minerals of Al/Fe oxides, Pi is sorbed forming non-protonated and protonated bidentate surface complexes at pH 4.5, whereas non-protonated bidentate inner-sphere surface complexes are formed at soil pH > 7.5 (Luengo et al., 2006; Arai and Sparks, 2007). Clay minerals and Al/Fe oxides have a larger surface area, allowing for a higher sorption capacity, which becomes even greater with an increase in the ionic strength of the charges on the surface of these minerals. For these reasons, Pi is typically trapped within the nanopores of these minerals, making it inaccessible to plants for acquisition (Arai and Sparks, 2007).

In neutral and alkaline soils, P fixation primarily occurs through precipitation reactions with Ca (Larsen, 1967; Liao et al., 2001). These reactions result in the formation of dicalcium phosphate, which is available to plants. However, alkaline conditions favor the conversion of dicalcium phosphate into hydroxyapatite, which, in turn, is not readily available to plants (Arai and Sparks, 2007). Hydroxyapatite is often found in calcareous soils and can undergo dissolution processes with soil acidification (Wang and Nancollas, 2008).

Organic P (Po) is also an important fraction of P, representing approximately 30-65% of the total P depending on the soil and the management system (Harrison, 1987; Hansen et al., 2004). Po pools are primarily constituted of inositol phosphates and phosphonates, which are relatively stable. In addition to these forms, Po can also be present in active forms, such as orthophosphate diesters, labile orthophosphate monoesters, and organic polyphosphates. Po can be released through mineralization processes, influenced by various factors, including moisture, temperature, pH, and the presence of microorganisms. Compared to inositol phosphates, the release of inorganic P from phosphate diesters (*e.g.*, nucleic acids and phospholipids) occurs quicker in the soil, offering a valuable source of nutrition for organisms (Bowman and Cole, 1978; Harrison, 1982; Turner, 2007). Therefore, changes in the chemical

composition of Po during ecosystem development significantly affect P bioavailability in the soil.

To address the issue of low P bioavailability in agricultural soils and to sustain food production, P is extensively extracted from phosphate-rich rock reserves around the world, converted into P fertilizers, and widely applied in the fields by farmers (Herrera-Estrella and López-Arredondo, 2016). The complication is that such P reserves are finite and unevenly distributed, with the largest phosphate-rock reserves located in Morocco and Western Sahara (70%), followed by China (5%), Egypt (4%), Algeria (3%), and Syria (3%) (Jasinski, 2024). Annually, around 20 million metric tons of P are extracted from the Earth's crust to meet the demands of crop production (Cordell et al., 2011). According to the International Fertilizer Association (IFA), between the years 2019 and 2021, the global demand for P increased by 7%, reaching nearly 50 million tons, with South Asia and Latin America being the driving forces behind this growing P use. With the ever-growing demand for food production, it is estimated that by the next 50 years, the consumption of P fertilizers will increase by 40-50% (Grizzetti et al., 2020). With such increase in the demand for P fertilizers, it is possible to predict various problems associated with P overuse, including socioeconomic and environmental issues. According to a report from The World Bank, in 2022 the price of Pi rock was $321.7 per metric ton (https://www.worldbank.org/en/research/commodity-markets). Thus, it is expected that this price will increase in the next few decades and that both European and developing countries will be directly affected, due to their high dependency on P fertilization. As the demand for P continues to grow, various studies have estimated that natural P reserves will be largely depleted within the next 40-100 years, jeopardizing food security worldwide (Van Kauwenbergh, 2010; Gilbert, 2014; Sattari et al., 2016; Ockenden et al., 2017).

The application of P fertilizers and P-containing manure in agricultural soils can also result in environmental issues. To reduce the problem of P fixation in agricultural soils, lime and large amounts of P fertilizers are regularly applied to especially increase the availability of Pi (Cheng et al., 2020). However, the surplus of P can be easily lost due to leaching, erosion, and runoff, exacerbating the problems of P bioavailability in agroecosystems. Estimates indicate that about 25-75% of all the P that is applied to crop fields is lost to the environment (Grizzetti et al., 2020). As a result, P use efficiency is relatively low for most crops and cultivation systems. Soil erosion is also a significant contributor to P losses (Carpenter and Bennett, 2011; Alewell et al., 2020). Due to climate change and poor land management, it is estimated that occurrences of erosion will increase from 30% up to 66% by 2070 (Borrelli et al., 2020). The P that ends up in waterways leads to anthropogenic eutrophication, in which high quantities of P promote the overgrowth of algae, depleting all the oxygen in the water, negatively affecting aquatic and marine ecosystems and harming both animal and human

health (Bajželj et al., 2014). Therefore, the comprehensive understanding of P form and availability in soils, coupled with the development of sustainable utilization strategies, is essential to secure environmental protection and conserve natural P reserves, while at the same time sustaining optimal crop yield.

2.2 P acquisition and transport in plants

The intracellular concentration of P in most plant species is in the range of 5-10 mM (Hinsinger, 2001). A recent cell type-specific elemental analysis of non-stressed *A. thaliana* roots detected 10-20 mM P in protoplasts from the epidermis and up to 40 mM in protoplasts from the endodermis (Giehl et al., 2023). In soils, total P concentrations range from 10^1 to 10^3 g P kg^{-1}, depending on the soil type and soil horizon (Kruse et al., 2015). However, P concentration in the soil solution is much lower, typically ranging from 1 to 10 µM (Hinsinger, 2001). Thus, plants depend on an efficient P transport system for maintaining internal P homeostasis. Plants take up Pi in the form of orthophosphates ($H_2PO_4^-$ or HPO_4^{2-}) via specialized membrane-bound Pi transporters (Młodzińska and Zboińska, 2016). Similar to other membrane transporter proteins, Pi transporters are classified into high-affinity transporters (HATs) and low-affinity transporters (LATs), depending on their transport affinity at a specific nutrient concentration (Teng et al., 2017).

Transporters from different families are responsible for Pi uptake and transport across different tissues, cells, and organelles (Srivastava et al., 2018). Members of the Phosphate Transporter (PHT) family have different structures, affinities, and tissue-specific localizations. PHTs are grouped into five main families (PHT1-PHT5) (Wan et al., 2020), with PHT1-type transporters transporting Pi at high affinity while members of the PHT2 to PHT5 transport at low affinity (Teng et al., 2017). The *A. thaliana* genome harbors a total of 19 *PHTs*, nine of which belonging to PHT1 family (*AtPHT1;1-AtPHT1;9*) (Gho and Jung, 2019). PHT1 transporters are located in the plasma membrane and belong to the Pi/H^+ symporter family of the MAJOR FACILITATOR SUPERFAMILY (MFS) (Ai et al., 2009). As a result, the transport of Pi through PHT1 occurs via a proton gradient across the plasma membrane generated by H^+-ATPase, thus consuming energy. In Arabidopsis, the primary transporters involved in the root uptake of Pi from the soil are PHT1;1, PHT1;4, and PHT1;2 (Shin et al., 2004), with PHT1;1 and PHT1;4 contributing up to 75% of the total Pi uptake capacity of roots (Misson et al., 2005; Catarecha et al., 2007; LeBlanc et al., 2013). PHT1;8 and PHT1;9 are engaged in relocating Pi from the root to the aerial part (Remy et al., 2012), while PHT1;5 facilitates the movement of Pi from the aerial part to the root (Liu et al., 2012). The proper targeting of PHT1 transporters from the endoplasmic reticulum to the plasma membrane requires PHOSPHATE

TRANSPORTER TRAFFIC FACILITATOR 1 (PHF1) (Gonzalez et al., 2005), and their protein abundance is controlled mainly by a PHO2-mediated degradation pathway according to the cellular P status (Huang et al., 2013).

It has been well-established that plants predominantly take up Pi through their root epidermis, as most of the *PHT1* genes have been shown to be present and active within this cellular layer (Karthikeyan et al., 2002; Mudge et al., 2002; Misson et al., 2004; Nussaume et al., 2011). The presence of Pi transporters in root hairs increases Pi uptake capacity, as root hairs increase the surface area of the root in contact with the soil (Péret et al., 2011). Tissue-specific transcriptomic studies of Arabidopsis roots (Birnbaum et al., 2003) and *PHT1* tissue-specific expression analysis have revealed that PHTs are also in the root tip, and their abundance increases under P deficiency (Karthikeyan et al., 2002; Mudge et al., 2002; Misson et al., 2004). By analyzing reporter lines expressing transcriptional and translational fusions for the high affinity transporters expressed in the root (*PHT1;1* and *PHT1;4*) and for *PHF1*, it was shown that these molecular components are localized in the root cap, the protective structure encasing the root tip (Kanno et al., 2016). Additionally, by using a high-resolution real-time radioisotope imaging technique with ^{33}P, it was possible to demonstrate that up to 20% of root Pi uptake occurs at the root cap (Kanno et al., 2016), highlighting the importance of this small root structure in nutrient acquisition.

PHT2 transporters are proteins homologous to the Na^+-dependent Pi transporters from non-plant species, such as PHO89 of *Saccharomyces cerevisiae* (Martinez and Persson, 1998) and Ram-1 and GLVR1 from animals (Kavanaugh et al., 1994). In Arabidopsis, PHT2;2 is located in chloroplasts and represents the sole member of the PHT2 family. Its primary function involves transporting Pi in the aerial part, playing a crucial role in Pi allocation in plant tissues (Daram et al., 1999; Versaw and Harrison, 2002). The PHT3 family comprises transporters situated in the inner mitochondrial membrane (Zhu et al., 2012), possibly catalyzing either Pi/H^+ symport or Pi/OH^- antiport (Poirier and Bucher, 2002). The Arabidopsis genome encodes three *PHT3* genes, which have high homology to the *MITOCHONDRIAL Pi TRANSLOCATOR1* (*MPT1*) of birch tree (*Betula pendula*) (Kiiskinen et al., 1997), and up to six PHT4 members, capable of low-affinity Pi transport between the cytosol and plastids (Guo et al., 2008). The PHT5 family consists of transporters mainly located in the tonoplast and is crucial for storing Pi in the vacuole to maintain cellular P homeostasis (Liu et al., 2016).

PHOSPHATE 1 (PHO1) represents another class of plant Pi transporters. Through map-based cloning of a mutant with significantly decreased shoot Pi concentration, *PHO1* was identified as responsible for long-distance signaling from the root to the shoot during P deficiency (Hamburger et al., 2002). *PHO1* is mainly expressed in stelar cells and the lower

part of the hypocotyl, suggesting a role in transporting P from stelar cells into the xylem (Hamburger et al., 2002). A later study confirmed this function by using ^{31}P-nuclear magnetic resonance *in vivo* in leaves of Arabidopsis overexpressing *PHO1*, revealing that PHO1 is responsible for the efflux of Pi (Stefanovic et al., 2011). Of the 11 Arabidopsis PHO1 and PHO1 homologues (*e.g.*, PHO1;H1 to PHO1;H10) (Wang et al., 2004), only two (*e.g.*, PHO1 and PHO1;H1) have been shown to be involved in root-to-shoot Pi transport (Secco et al., 2010). PHO1 features six membrane-spanning domains at the C-terminal and shows no homology with any other previously characterized Pi transporters (Hamburger et al., 2002). The N-terminal of PHO1 faces the cytosolic side and contains the SPX domain, providing a binding site for signaling molecules such as inositol polyphosphates (Austin and Mayer, 2020). This suggests that PHO1 may play an important role in sensing and signaling of P deficiency.

2.3 Plant responses to P deficiency

As P limitation is one of the major challenges for plant growth in various natural soils, plants have evolved several strategies aiming to increase contact with soil P and its uptake. One common strategy in many plant species is the establishment of symbiotic associations with mycorrhizal fungi, which improve P acquisition (Krüger et al., 2015). Plants can also rearrange their root system architecture to increase their P foraging capacity. One dramatic example is the formation of “root clusters”, characterized as dense clusters of roots, rootlets, and/or root hairs, and produced only by some plant species, such as from the Proteaceae family (Lambers et al., 2015). The main advantage of these specialized root structures is the maximization of P acquisition from soils of low fertility, especially when P is strongly sorbed onto soil particles or present in insoluble sources. Another common response of plants to P deficiency that involves altering root morphology is the development of a shallower spatial distribution of roots. Since P concentrations are typically higher in the topsoil (Jobbagy and Jackson, 2001), a shallower root system has been proposed to be more suitable for P foraging (Lynch and Brown, 2001). Interestingly, in many plant species, root contact with a low-P medium inhibits primary root growth and favors the development and elongation of lateral roots and the formation of root hairs (Lynch and Brown, 2001; Gruber et al., 2013). The combination of decreased primary root growth and increased formation of lateral roots and root hairs is, therefore, thought to represent a strategy to forage P and other nutrients in the topsoil.

Besides altering root system architecture and morphology, P-deficient plants can also produce and secrete a suite of enzymes, such as phosphohydrolases and nucleases, aimed at retrieving P from P-containing biomolecules (Chen et al., 2000). Furthermore, P-deficient roots can synthesize and release low-molecular-weight carboxylates into the rhizosphere, such

as the organic acids malate and citrate (Meyer et al., 2010). This is a widely employed strategy by plants to mobilize scarcely available Pi from the rhizosphere (Vance et al., 2003; Ticconi and Abel, 2004; Fang et al., 2009; Richardson et al., 2009). By forming chelates with Al and Fe, citrate and malate solubilize Pi, which then becomes available for root uptake (Lambers et al., 2006).

2.3.1 Systemic control of P starvation-induced responses

Plant morphological, physiological, and biochemical responses to P deficiency are regulated by two main regulatory systems, one acting locally and one at the whole-plant (*i.e.*, systemic) level (Thibaud et al., 2010). The systemic mechanism entails a complex network of molecular components that regulate uptake and transport according to dynamic changes in internal P demands. Studies with split-roots have demonstrated that plants respond to P deficiency after cytosolic P levels fall below optimal levels (Martín et al., 2000; Franco-Zorrilla et al., 2005). In turn, disruption of Pi uptake leading to a decrease in the internal P status drives continuous upregulation of P starvation-induced genes, even when plants are maintained under Pi-rich conditions (Gonzalez et al., 2005). In a screening of Arabidopsis EMS mutants, a mutant displaying high P concentration in the shoots was identified (Delhaize and Randall, 1995; Dong et al., 1998). This mutant, named as *pho2*, was characterized by a point mutation in the *PHOSPHATE 2* (*PHO2/UBC24*) gene, which encodes a ubiquitin E2 conjugase (Aung et al., 2006; Bari et al., 2006). Subsequent studies have demonstrated that PHO2 controls the abundance of a subset of P deficiency-induced proteins, including PHT1;8 and PHT1;9 (Figure 1; Bari et al., 2006). Moreover, it has been shown that PHO2 colocalizes with PHO1 and modulates its degradation in endomembranes to maintain P homeostasis in plants during P starvation (Figure 1; Liu et al., 2012). Therefore, if this mechanism is disrupted, high levels of Pi accumulate in the shoots (Lin et al., 2008).

Additional components regulating long-distance communication between roots and shoots have also been identified. For instance, *miR399* (*microRNA399*), a signaling molecule that moves from shoots to roots, prevents the translation of PHO2 in roots (Figure 1; Pant et al., 2008). Other non-coding RNAs, such as *At4* and *IPS1*, are activated during Pi shortage to negatively regulate *miR399* (Franco-Zorrilla et al., 2007). Thus, the combined action of *At4*, *IPS1*, and *miR399* helps fine-tuning whole-plant P homeostasis.

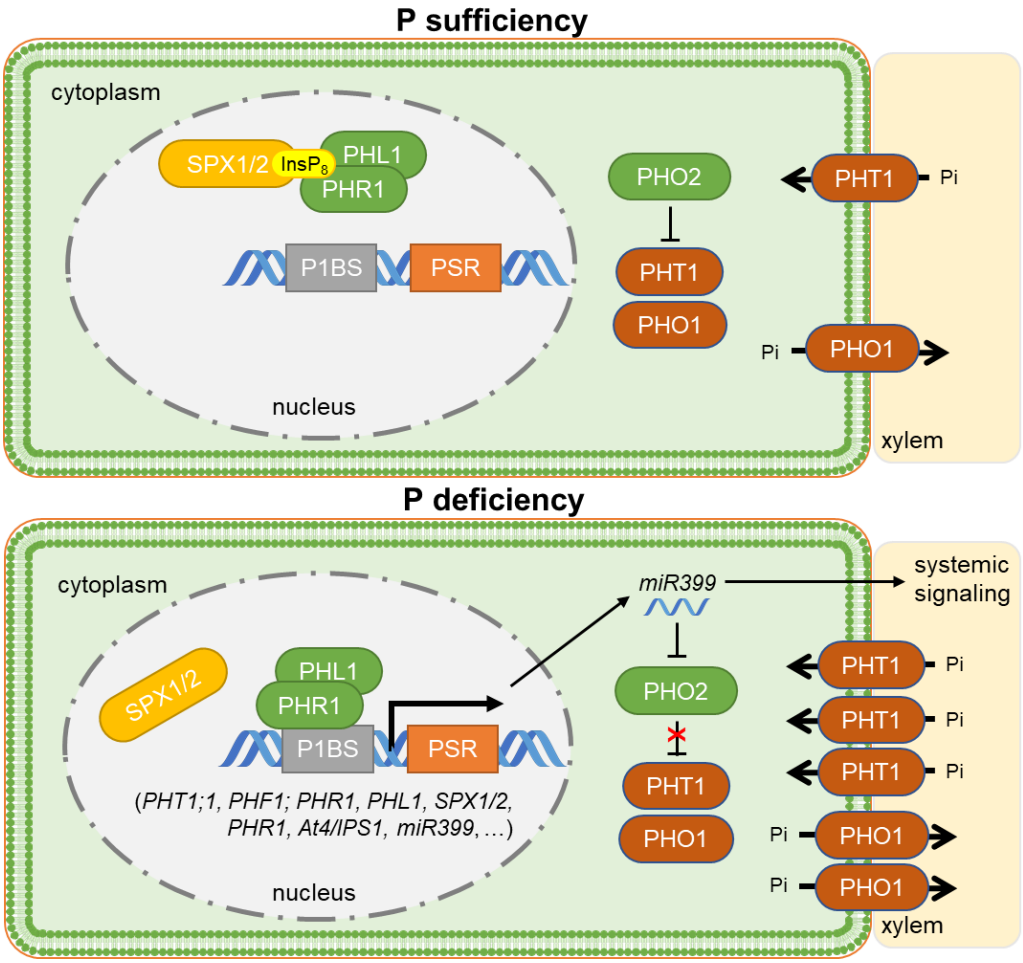

Figure 1. Simplified model showing the main molecular components of the systemic P starvation responses in Arabidopsis.

The black lines represent the mode of action at the levels of transcription and post transcription. Arrows indicate positive effects, whereas lines ending with a short bar represent negative effects. Full gene names are indicated in the text.

The MYB transcription factors PHOSPHATE STARVATION RESPONSE 1 (PHR1) (Rubio et al., 2001) and its close homologue PHR1-like (PHL1) are master regulators of transcriptional responses induced by P deficiency (Figure 1; Rubio et al., 2001; Bustos et al., 2010; Jiang et al., 2019). PHR1 itself is controlled by the interaction with stand-alone SPX proteins such as SPX1 and SPX2, which prevents PHR1 from binding to the P1BS sequence (GNATATNC) in the promoters of P deficiency-induced genes (Rubio et al., 2001; Duan et al., 2008; Puga et al., 2014). This physical interaction depends primarily on the intracellular P status and is even stronger under sufficient P. Studies focusing on the structure and function of various SPX domain-containing proteins have revealed that inositol pyrophosphates, even at micromolar ranges, are able to bind to the SPX domain (Wild et al., 2016; Gerasimaite et al., 2017; Qi et al., 2017). The synthesis and back-conversion of the inositol pyrophosphates

5-$InsP_7$ and 1,5-$InsP_8$ from phytic acid ($InsP_6$) rely on two bifunctional enzymes, respectively, 1,3,4-TRISPHOSPHATE 5-/6-KINASE 1 (ITPK1) and DIPHOSPHOINOSITOL PENTAKISPHOSPHATE KINASE 1/2 (VIH1/2) (Laha et al., 2019; Zhu et al., 2019; Whitfield et al., 2020; Riemer et al., 2021). Interestingly, both cellular P and ATP levels regulate the activity of ITPK1 and VIH1/2 and, consequently, 1,5-$InsP_8$ synthesis (Zhu et al., 2019; Riemer et al., 2021). Thus, under sufficient P, $InsP_8$ is produced and binds to SPX1, stimulating its interaction with PHR1 (Ried et al., 2021). When P is insufficient, $InsP_8$ levels decrease, leading to the dissociation of the SPX1-PHR1 complex, enabling PHR1 binding to the P1BS element of its target genes (Figure 1).

2.3.2 Local responses to P

Several studies have previously reported that plants can adjust their root growth and development in response to changes in external P levels (Drew, 1975; Linkohr et al., 2002; Gruber et al., 2013). As a consequence, plant roots elicit responses or signals that assist in adapting the root system for better P uptake from the rhizosphere. Unlike the systemic responses, which are triggered by the plant's P nutritional status and cause direct changes in the plant metabolic processes, the local responses are mainly triggered by external P availability and result in morphological changes of different root traits (Abel, 2011; Péret et al., 2014), including the size of root cells (Reymond et al., 2006), the length and density of root hairs (Bates and Lynch, 1996), the meristematic activity in root tips (Ticconi and Abel, 2004; Svistoonoff et al., 2007; Arnaud et al., 2010), and lateral root development (Linkohr et al., 2002; López-Bucio et al., 2002; Reymond et al., 2006). The following section provides a more detailed overview of the main components involved in the local response of roots to low P, with emphasis on primary roots.

2.4 Low P-induced primary root inhibition

Root tip contact to external Pi concentration is sufficient to induce alterations in root system architecture (Reymond et al., 2006; Svistoonoff et al., 2007). The root apical meristem mainly contains undifferentiated cells that are not connected to other tissues through the vasculature. Therefore, it might respond locally to changes in external P availability. The primary root growth inhibition in response to P deficiency involves a network of interactions within the root apical meristem itself (Figure 2). Several studies have highlighted *LOW PHOSPHATE ROOT1* (*LPR1*) and its homolog *LPR2* as critical in inhibiting the primary root in response to low external Pi levels (Svistoonoff et al., 2007; Ticconi et al., 2009). LPR1/2 are

two cell-wall localized multicopper ferroxidases playing a key role in the control of root apical meristem activity under low P (Müller et al., 2015). Additionally, PHOSPHATE DEFICIENCY RESPONSE2 (PDR2), a P_5-type ATPase protein located in the endoplasmic reticulum, was also identified as significant in reducing the primary root under P deficiency, due to its genetic interaction with LPR1 (Ticconi et al., 2009; Müller et al., 2015). ALUMINUM SENSITIVE 3 (ALS3) and SENSITIVE TO ALUMINUM RHIZOTOXICITY1 (STAR1) were also shown to play a role on primary root growth inhibition under low P, although they were first known for their role in plant tolerance to Al toxicity (Larsen et al., 2005; Huang et al., 2010; Dong et al., 2017). Both ALS3 and STAR1 physically interact in the tonoplast and are transcriptionally regulated in response to P availability. Together, PDR2 and ALS3/STAR1 interact to control LPR1/2-dependent Fe oxidation in the root apoplast to elicit a series of events that result in the formation of callose deposition around meristematic cells and blockage of the symplastic communication within the stem cell niche (Figure 2; Müller et al., 2015).

LPR1 is located in the cell wall and is capable of oxidizing apoplastic ferrous Fe [Fe(II)] into ferric Fe [Fe(III)] in the root apical meristem (Müller et al., 2015; Naumann et al., 2022). Additionally, studies indicated that a probable accumulation of Fe(III), dependent on malate, is also crucial in controlling root growth and cellular reprogramming during P deficiency (Balzergue et al., 2017; Mora-Macías et al., 2017). In response to P deficiency, low pH, Fe excess and Al toxicity, the transcription factor *SENSITIVE TO PROTON RHIZOTOXICITY 1* (*STOP1*) is induced (Ojeda-Rivera et al., 2020), activating the expression of the membrane-bound efflux channel *ALUMINUM ACTIVATED MALATE TRANSPORTER1* (*ALMT1*) (Balzergue et al., 2017). ALMT1 is primarily involved in organic acid exudation into the apoplast, such as malate, which is thought to chelate Fe(III) thereby releasing sorbed Pi from insoluble Fe(III)-Pi complexes (Lambers et al., 2006). Excess Fe(III) accumulation in the root apoplast results in reactive oxygen species (ROS) formation (Balzergue et al., 2017; Mora-Macías et al., 2017), followed by callose deposition in the stem cell niche. This process leads to the blockage of cell-to-cell communication via plasmodesmata, preventing the movement of SHORT ROOT (SHR) to adjacent cells of the quiescent center, which leads to premature cell differentiation and reduced cell division (Müller et al., 2015; Hoehenwarter et al., 2016; Balzergue et al., 2017; Mora-Macías et al., 2017). Consecutively, in the elongation zone, Fe stimulates the activity of class III peroxidases, which increase cell wall stiffness thereby restricting cell elongation (Balzergue et al., 2017).

The SHR/SCARECROW (SHR/SCR) pathway is further regulated under low-P conditions by the CLAVATA3/ENDOSPERM SURROUNDING REGION 14 (CLE14) peptide, which functions downstream of LPR1-PDR2 and matches its gene expression pattern with the Fe distribution in the meristem of P-deficient roots (Gutiérrez-Alanís et al., 2017). Upon

perception by the CLAVATA 2 (CLV2) and PEP1 RECEPTOR2 (PEPR2) receptors located at the plasma membrane, CLE14 downregulates the transcription of *SHR/SCR* and *PIN-FORMED* (*PIN*)-auxin pathways via activation of two phosphatases, POLTERGEIST (POL) and POL-LIKE1 (PLL1) (Gutiérrez-Alanís et al., 2017). Consequently, CLE14 is responsible for driving root apical meristem exhaustion, but without involving the formation of callose in the stem cell niche. Together, all these mechanisms highlight the existence of a strong interaction between Pi and Fe in the apoplast, which modulates root growth and meristem integrity under low-P conditions.

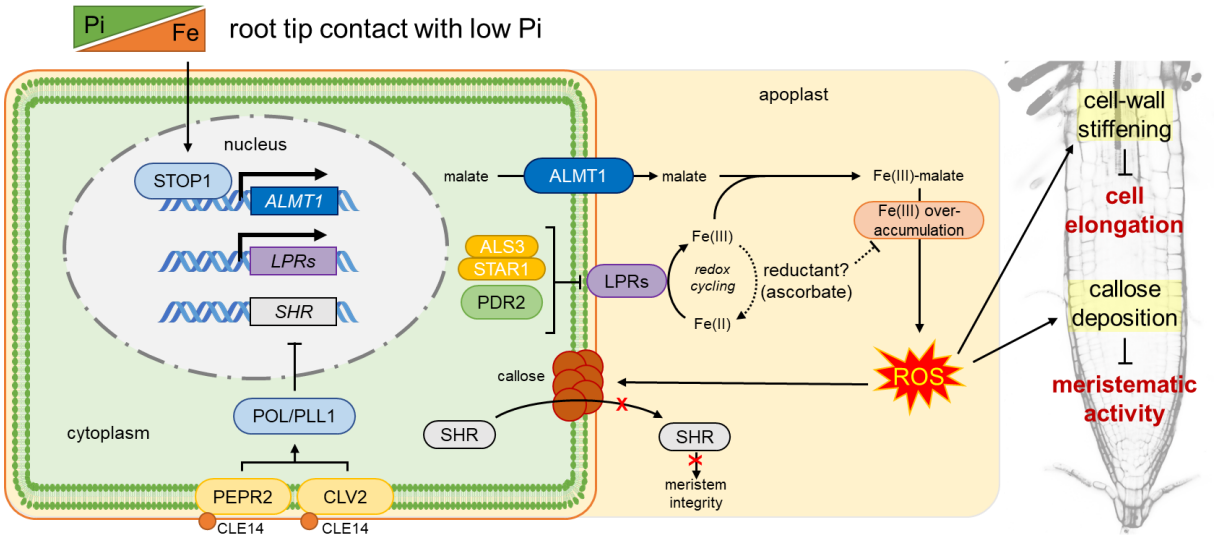

Figure 2. Model depicting the main components involved in local responses induced by the contact of the root tip of an Arabidopsis plant with a low-P medium.

The black lines represent the mode of action at the levels of transcription and post transcription. Dashed lines indicate research gap. Arrows indicate positive effects, whereas lines ending with a short bar represent negative effects. Full gene names are indicated in the text.

2.5 The role of Fe in root growth adjustment to low P

While the contact of the root tip with low P media is sufficient to inhibit the elongation of the primary root of Arabidopsis plants (Svistoonoff et al., 2007), removal of Fe from the P-deprived medium can largely rescue root elongation (Svistoonoff et al., 2007; Ward et al., 2008). Through screenings of Arabidopsis EMS mutants and T-DNA insertion lines, mutants with insensitive root inhibition under low P have been identified (Sánchez-Calderón et al., 2006; Svistoonoff et al., 2007; Müller et al., 2015). Two of the genes underlying low P-insensitive root growth are *LPR1* and *LPR2*, which encode two cell-wall bound multicopper oxidases capable of catalyzing the oxidation of ferrous iron [Fe(II)] to ferric iron [Fe(III)] via the consumption of O_2 and the generation of water, using copper (Cu) as cofactor (Svistoonoff et al., 2007; Müller et al., 2015; Naumann et al., 2022). Thus, together, these findings have

demonstrated that the presence of Fe and the redox state of this transition metal affect root growth under low-P conditions.

The same physico-chemical properties that make Fe essential for life also make it a potential trigger of oxidative stress. That is because un-ligated or loosely coordinated Fe ions in their reduced or oxidized forms can react with different ROS. The key mechanism for Fe-induced ROS formation is the reaction of Fe(II) with hydrogen peroxide (H_2O_2) to form hydroxyl radicals ($OH^{\bullet}$), a highly reactive and damaging type of ROS (Richards et al., 2015). In addition, the reaction may also initiate redox cycling as Fe(III) generated in the Fenton reaction can react with superoxide radicals ($O_2^{\bullet -}$) to form Fe(II), which, in turn, can drive another round of Fenton chemistry to re-initiate the cycle. The central role of Fe(II) in driving the generation of $OH^{\bullet}$ means that in any cellular compartment Fe can tip the balance between the function of ROS in signaling or oxidative damage.

In P-supplied plants, phosphate and Fe co-localize in the walls of the stem cell niche in the root apical meristem (Müller et al., 2015). Under these conditions, poorly soluble ferric hydroxyl phosphates are formed and, therefore, are thought to be unable to trigger oxidative reactions. On the other hand, under low P, LPR1/2-dependent redox reactions of Fe in the root tips were shown to be responsible for root growth inhibition, as the ROS generated by this reaction promotes peroxidase-dependent cell-wall stiffening in the transition zone (Müller et al., 2015). Furthermore, the activity of LPRs enhance callose deposition in plasmodesmata, thereby blocking cell-to-cell communication vital for undisturbed root development (Müller et al., 2015; Balzergue et al., 2017). In particular, H_2O_2 accumulation was detected not only in the differentiation zone, but also in the transition zone of primary roots (Balzergue et al., 2017). This pattern of ROS accumulation correlates with the deposition of Fe and callose in the cell walls of the root apical meristem under low P (Müller et al., 2015). Although the impact of Fe-dependent ROS accumulation on root system architecture has already been studied (Reyt et al., 2015), the mechanism that regulates Fe accumulation and its relocation in the apoplast of the root apical meristem in P-deprived roots remains poorly understood.

In Arabidopsis, Fe uptake in most cells and organelles requires Fe(III) reduction. In Fe-deficient roots, ferric-chelate reduction is largely dependent on the activity of the membrane-bound NADPH-dependent ferric reductase FRO2 and root-borne coumarins with Fe(III)-reducing capacity (Robinson et al., 1999; Rajniak et al., 2018; Paffrath et al., 2024). Interestingly, *FRO2* is not expressed in the root apex and is repressed by P deficiency elsewhere (Connolly et al., 2003; Li and Lan, 2015), whereas clear *FRO3* expression in the root apical meristem is only detected in Fe-deficient roots (Mukherjee et al., 2006). Furthermore, it has also been shown that enzymes involved with coumarin synthesis are not

expressed in root apices (Schmidt et al., 2014; Rajniak et al., 2018; Paffrath et al., 2024). Thus, a FRO- or coumarin-mediated Fe(III) reduction in root tips under low P appears unlikely. Meanwhile, it has been speculated that apoplastic ascorbate (vitamin C) could reduce the Fe(III) produced by LPR1/LPR2 to initiate Fe redox cycles (Grillet and Schmidt, 2017; Mora-Macías et al., 2017). In fact, P deficiency induces the expression of the ascorbate biosynthesis gene *VITAMINC4* (*VTC4*) in the root apex (Mora-Macías et al., 2017). However, so far ascorbate-dependent Fe(III) reduction mechanisms have only been observed in seeds (Grillet et al., 2014) or restricted to the vacuole (Hoang et al., 2021). Nonetheless, the putative involvement of ascorbate is intriguing, as this molecule can function either as an antioxidant or a pro-oxidant. Indeed, while ascorbate can directly react with and scavenge major ROS types, including $OH^{\bullet}$ (Zhang and Zhang, 2013), it can theoretically also act as a strong reducing agent for Fe(III) and Cu(II) in the apoplast (Makavitskaya et al., 2018). However, whether ascorbate is directly or indirectly involved in the control of root meristem activity by adjusting apoplastic Fe redox cycling and ROS formation under low P has remained unclear (Figure 2).

3 Aim of the study

In many plant species, root growth is inhibited under limited P availability. Under these conditions, carboxylates released to increase Pi solubility inevitably also increase Fe availability, triggering a series of reactions that can culminate with the inhibition of root growth. As the main components of the strategy-I Fe acquisition machinery are not present in the root apical meristem zone and are repressed in response to P deficiency elsewhere, the mechanisms that govern Fe homeostasis in the root tip of P-deprived roots still remain poorly understood. Therefore, the main aim of this study was to identify novel molecular components involved in Fe homeostasis that control primary root growth under low P in *A. thaliana*. To achieve this goal, transcriptomics, reverse genetics, genetic complementation approaches, site-directed mutagenesis, histochemical staining, and root phenotyping methods were combined to shed light on the function of previously poorly characterized genes and gene families.

The first part of the present thesis focused on the characterization of a member of the CYBDOM family. The gene, annotated to possess a “ferric reductase domain”, was identified among a set of genes upregulated in response to low P in roots. Disruption of the gene caused severe loss of meristematic integrity and more significantly inhibited cell elongation specifically under low P conditions. The gene was thus named *HYPERSENSITIVE TO LOW P1* (*HYP1*). A series of experiments, including complementation studies *in planta* further supported by electrophysiological assays in *Xenopus laevis* oocytes and protein structure modeling, revealed that HYP1 can mediate trans-plasma membrane electron transport and act as a metalloreductase. Concomitantly, protein localization studies and experiments involving tissue-specific expression and histological approaches for detection of Fe were conducted in order to provide information about the localization of HYP1 and its involvement with Fe distribution in primary roots exposed to different P concentrations. Furthermore, the tissue-specific expression pattern of other 10 members of the CYBDOM family was investigated to provide initial insights into potential redundancies and specificities of these trans-plasma membrane electron transporters. In the second part, a second gene identified from the transcriptome study was characterized. The gene *MONODEHYDROASCORBATE REDUCTASE 3* (*MDHAR3*) encodes an enzyme putatively involved in regenerating ascorbate from partially oxidized pools. By determining the tissue-specific and subcellular localization of MDHAR3 and its genetic interaction with HYP1, it was investigated whether MDHAR3 acts in concert with HYP1 to maintain root growth under low P. Finally, this thesis concludes with a discussion on the significance and role of ascorbate and the two identified proteins in preventing aberrant Fe accumulation and maintaining meristematic integrity in roots exposed to low P.

4 Materials and methods

4.1 Plant material

If not noted otherwise, the *A. thaliana* accession Columbia-0 (Col-0) was used as wild-type in all experiments performed in this study. The *A. thaliana* accession Columbia *glabra1* (Col-*gl1*) was used as wild-type for the *fro2* mutant. The following T-DNA insertion lines and reporter lines were used in this study: SALK_115548 (*hyp1*), SALK_009629 (*almt1*), SALK_016297 and SALK_091930 (*lpr1 lpr2*), SALK_202530 (*crr*), SALK_013527 (*At4g12980*), SALK_006551 (*At3g59070*), SALK_092983 (*At4g17280*), SALK_204800 (*At5g47530*), SALK_110375 (*At3g07570*), SALK_111270 (*At3g61750*), SALK_089061 (*At5g54830*), SALK_205490 (*air12*), SALK_012348 (*At2g04850*), SAIL_444_A03 (*mdhar3*), *proSHR::SHR:GFP* (Nakajima *et al.*, 2001), *proCYCB1;1::GUS* (Ferreira et al., 1994), and *proWOX5::GFP* (Blilou et al., 2005). All *A. thaliana* T-DNA insertion lines were obtained from the Nottingham Arabidopsis Stock Centre, except the *lpr1 lrp2* double mutant which was kindly provided by Prof. Dr. Steffen Abel (IPB, Halle). The lines *almt1 hyp1*, *hyp1 crr*, *hyp1 mdhar3*, and *lpr1 lpr2 hyp1* were generated by crossing the single *almt1*, *crr*, and *mdhar3* or double *lpr1 lrp2* mutants with *hyp1*. Homozygous double or triple mutant plants were identified by PCR using the primers listed in Table 1.

Table 1. Primers used for genotyping single, double, and triple mutants by PCR.

T-DNA line	Primer sequence
SALK_115548 (*hyp1*)	For: ACAATGAACCAAGTGAGTGGC
	Rev: TTACTAAATCATTTGGAACCCAC
SALK_202530 (*crr*)	For: GCCAAAAGCCTTTACGGTTAC
	Rev: CTTGTGATCTTTCTTAGGCCG
SALK_009629 (*almt1*)	For: GAAATTATTTGGGGAAGCTGC
	Rev: TCTTTACCCATGGGAAAAACC
SALK_016297 (*lpr1*)	For: CTCATCGCCAGTAGGTAGCTG
	Rev: ACTCATGGGTGTGAACCAAAG
SALK_091930 (*lpr2*)	For: CATAGCCTGGCTCTTGAGTTG
	Rev: GTCATAGCTCAGTCGAATCGC
SALK_205490 (*air12*)	For: CTCATCGCCAGTAGGTAGCTG
	Rev: ACTCATGGGTGTGAACCAAAG
SAIL_444_A03 (*mdhar3*)	For: CATAGCCTGGCTCTTGAGTTG
	Rev: GTCATAGCTCAGTCGAATCGC

4.2 Plant growth conditions

Seeds of *A. thaliana* were surface sterilized by 70% ethanol with 0.05% (v/v) Triton X-100, and pre-cultured on half-strength Murashige and Skoog salt mixture (½ MS) (Duchefa Biochemie, Haarlem, Netherlands; batch number M0221) solid medium containing 0.5% (w/v) sucrose, 1 mM MES (pH 5.5), and 1% (w/v) Difco agar (Becton, Dickinson and Company, New Jersey, United States; batch number 1131496). Seeds were then stratified for 2 days in the

dark at 4 °C. Afterwards, Petri dishes were transferred to a growth chamber vertically positioned under a 22 °C/18 °C and 10-h/14-h (light/dark) regime at light intensity of 120 µmol photons m^{-2} s^{-1}. For the transcriptome profiling shown in Figure 4, plants were cultivated exactly as described previously (Gruber et al., 2013). The P treatments were 625 µM KH_2PO_4 (+P) and 100 µM KH_2PO_4 (-P) with Fe supplied as 75 µM Fe(III)-EDTA. The same growth conditions were also used in the initial phenotyping experiment shown in Figure 5.

In all other experiments, roots were shielded from direct light exposure using the setup depicted in Figure 3. In these experiments, 10-day-old seedlings instead of seven-day-old were transferred from the pre-culture to square Petri dishes (12 x 12 cm) containing modified ½ MS medium without P and Fe (Duchefa Biochemie, Haarlem, Netherlands; customized order), with 0.5% (w/v) sucrose, 2.5 mM MES (pH 5.5), 1% (w/v) Difco agar, 625 µM KH_2PO_4 (+P) or 5 µM KH_2PO_4 + 620 µM KCl (-P). The medium was supplemented with or without 150 µM $FeCl_3$ as the sole Fe source (+Fe or -Fe, respectively), which was supplied after the autoclaved agar had cooled down.

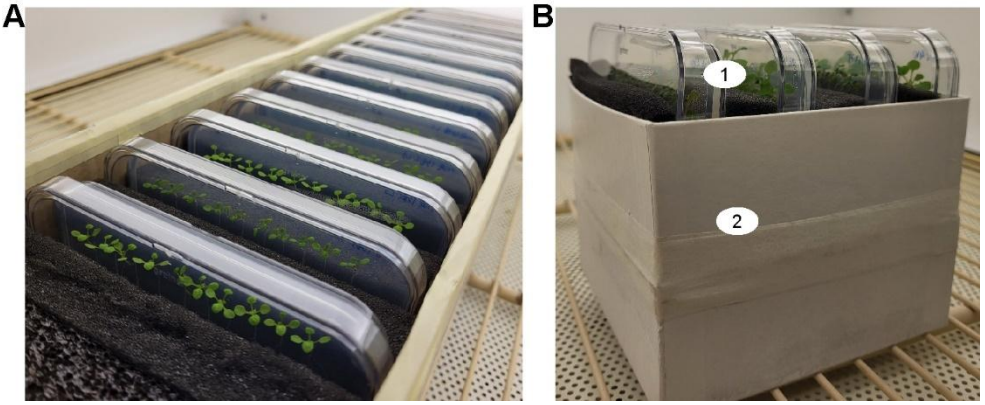

Figure 3. Modified system used in the present study to cultivate *A. thaliana* plants with roots shielded from direct light exposure.

(**A**) Overview of the system. Translucent Petri dishes were placed within a box with dishes separated by a 3-cm thick black foam extending from the bottom of the box until the height where shoots were located. (**B**) At shoot level (position marked with 1), 130 ± 15 µmol m^{-2} s^{-1} of light reached the plants while at root level (position marked with 2) 8 ± 5 µmol m^{-2} s^{-1} were detected.

In experiments with complemented *fro2* plants, different Fe conditions were obtained by transferring 10-day-old seedlings to a modified ½ MS medium without Fe (Duchefa Biochemie, Haarlem, Netherlands; customized order), with 0.5% (w/v) sucrose, 1 mM MES (pH 5.5), 1% (w/v) Difco agar, 75 µM Fe(III)-EDTA (+Fe, control), 20 µM Fe(III)-EDTA (low Fe), no added Fe (-Fe), as indicated in the legends of the corresponding figures. To phenotype plants under Cu excess, 10-day-old plants cultivated as indicated above were transferred to a fresh solid ½ MS medium containing 0.05 µM (control) or 50 µM $CuSO_4$. Phenotyping under

low Fe was performed with plants completely exposed to light condition, whereas the phenotyping under high Cu was performed using the root-shaded setup described above and in Figure 3.

In experiments testing the involvement of HYP1 on primary root growth response to high concentrations of ammonium, 10-day-old seedlings were transferred to a fresh ½ MS medium without nitrogen (Duchefa Biochemie, Haarlem, Netherlands; customized order), with 0.5% (w/v) sucrose, 1 mM MES (pH 5.5), 1% (w/v) Difco agar, supplemented with either 1 mM KNO_3, 1 mM NH_4Cl, or 10 mM NH_4Cl, and analyzed after 6 d of treatment. Phenotyping under different ammonium concentrations was performed with plants completely exposed to light condition.

4.3 RNA extraction and quantitative real-time PCR

Total RNA was extracted from homogenized root samples using the NucleoSpin RNA Mini Kit (Machery-Nagel), followed by on-column DNase treatment (QIAGEN), according to the manufacturers' protocols. cDNA was synthesized from 0.5-1 µg RNA by reverse transcription using the RevertAid First Strand cDNA synthesis Kit (Thermo Fisher Scientific) and oligo(dT) primer. A ten- or twenty-times diluted cDNA sample was then used for quantitative real-time (RT) PCR analysis with the CFX384 Touch Real-Time PCR Detection System (Bio-Rad Laboratories) and the iQ SYBR Green Supermix (Bio-Rad Laboratories), using the primers listed in Table 2. Amplification cycles were as follow: 2 min at 95 °C; 40 cycles of 6 s at 95 °C and 30 s at 60 °C. Melting curves were verified at the end of 40 cycles for confirmation of primer specificities. All reactions were repeated in two technical and three biological replicates. Average Cq values were normalized by ΔΔCt formula against *UBIQUITIN2* (At2g36170) or *ACTIN2* (At3g18780) expression, as indicated in the legend of the corresponding figures.

4.4 Analysis of a microarray dataset for candidate gene identification

For the identification of novel P deficiency-induced genes, a microarray study was previously performed in the laboratory (Bhosale et al., 2018). Plants were grown in solid medium as described under +P (625 µM KH_2PO_4) or -P (100 µM KH_2PO_4 + 525 µM KCl) as described previously (Gruber et al., 2013), with Fe supplied as 75 µM Fe(III)-EDTA and roots not shielded from direct light exposure. Whole roots were harvested 1, 2, 4 and 6 days after transfer to treatments. Roots of 50 plants were pooled together to constitute one biological replicate. In brief, RNA was extracted from whole roots using a RNeasy plant mini kit (Qiagen)

Table 2. Primers used for real-time quantitative PCR.

Fragment	Primer sequence
qPCR At2g36170 (UBIQUITIN2)	For: AGACGAACGCAAAGATGCAG
	Rev: CCGGCGAAGATCAACCTCTG
qPCR At3g18780 (ACTIN2)	For: GACCAGCTCTTCCATCGAGAA
	Rev: CAAACGAGGGCTGGAACAAG
qPCR At2g04850	For: TGATGGGCGTGGTGAATGTG
	Rev: ACCAGCGTCGACAGACATAG
qPCR At3g07390 (AIR12)	For: CTCCCACCGTGTGTTGAGTT
	Rev: GTTCCTCGTCAATGACCCCG
qPCR At3g07570	For: CCCCACTTGGTTCTATGCCC
	Rev: ATTATTGGCCTTGAGCCGGT
qPCR At3g61750	For: CGAATGGCGGATAATGGAGGA
	Rev: AGATGGTGAGCCGATAGTGC
qPCR At3g25290 (CRR)	For: ACCATGGAGTCGGTTATGCG
	Rev: AGAGCAAAGCAATGCCTCCA
qPCR At4g12980	For: ACCACCACGGAGTTGGATAC
	Rev: CGTGATGCCTCCTAAGGTCC
qPCR At5g35735 (HYP1)	For: CGAGCCACTCACTTGGTTCA
	Rev: CTAGGCGTCCTGGTGATGTG
qPCR At3g59070	For: ATCGGAGAGACGGAAAAGGC
	Rev: AGAAGCGGCGGAGAAGTATG
qPCR At4g17280	For: GAGTCCCAAGAAGCAGTGGA
	Rev: TAGATGCTCCATGCTGAGCC
qPCR At5g47530	For: GAGAAACGCTTACACCGCCA
	Rev: ACCATCGTTGCCTACTCGTT
qPCR At5g54830	For: ACGTGGACGGGCTTAACTTG
	Rev: TCCACATTCCCCAAAACCCAA
qPCR At5g48750	For: TGCACGCCATGAGTGGAAAT
	Rev: TCCCCCAACACACTGCATTC
qPCR At3g52880 (MDHAR1)	For: AACGCTTTCACACGATCGGA
	Rev: TTAAGATGCTGGCAGAGACG
qPCR At5g03630 (MDHAR2)	For: AATCCGCTGAACAAGCCGTA
	Rev: CGAATTTCGGCTTTGGCGAT
qPCR At3g09940 (MDHAR3)	For: CCTCGAAGTCAATCCGACCC
	Rev: TGCCCACAATTAGATCAATCCCT
qPCR At3g27820 (MDHAR4)	For: GAAGGACTCGGGTTTGCTCA
	Rev: CATACCAAAACGCGAACGCA

with on-column DNase treatment according to the manufacturer's instructions. cDNA was prepared using random hexamer primers and SuperScript II reverse transcriptase (Life Technologies) according to the manufacturer's protocol. RNA amplification, labeling and hybridization to Agilent microarrays (Arabidopsis V4, 021169, Gene Expression Microarray) were conducted following the manufacturer's protocol (Agilent Technologies). The expression of selected root hair-related genes from this microarray dataset was already reported previously (Bhosale et al., 2018). In the present thesis, a more detailed analysis of the dataset was performed to identify novel Fe-related genes responsive to P deficiency. For that purpose, one additional time-point (6 days after transfer) from the same experiment was also evaluated. Analysis of microarray data was performed with the R package limma (Ritchie et al., 2015).

Raw feature intensities were background corrected using “normexp,” and the “quantile” normalization method was used to normalize between arrays. Differential expression was calculated by fitting a linear model to $\log_2$-transformed data by an empirical Bayes method (Smyth, 2004). To extract genes with significant expression differences, a cutoff for $|\log_2 FC| \geq 1$ and the Benjamini–Hochberg false discovery rate (FDR) was applied. Significant differential expressed genes (DEGs) over four time points between -P and +P samples were visualized in a heat map ($|\log_2 FC| \geq 1$, FDR < 0.05) generated with the hierarchical clustering (HCL) algorithm by using Pearson distance and average linkage clustering. The full dataset was deposited in the NCBI Gene Expression Omnibus under accession ID GSE217790.

4.5 RNA-seq and GO term enrichment analysis

For RNA-seq analysis, wild-type, *hyp1* and *35S::HYP1* plants were exposed to different P conditions with root protected from direct light exposure for 3 days. The solid medium of the treatment plates was as described above and contained +P (625 µM KH_2PO_4) or -P (5 µM KH_2PO_4 + 620 µM KCl) with 150 µM $FeCl_3$ as the sole Fe source. A total of 30 roots was pooled as one biological replicate. Total RNA was extracted from whole roots using a RNeasy plant mini kit (Qiagen) with on-column DNase treatment according to the manufacturer’s instructions. Library construction and sequencing were performed at Novogene (UK) Company Limited. RNA integrity and quantitation were determined with the Agilent 2100 Bioanalyzer. Total mRNA was enriched with oligo(dT) beads and randomly fragmented with a fragmentation buffer. A stranded specific library was then prepared for each sample and sequenced with a NovaSeq 6000 PE150 platform, yielding about 44 million high-quality reads per sample. After removal of adapters, reads containing ploy-N and low-quality reads, the clean reads were aligned to the Arabidopsis genome (TAIR10) using HISAT2 (Kim et al., 2019) with the default parameters. The reads mapped on exons were counted using featureCounts (Liao et al., 2014). Significant differentially expressed genes (DEGs) were identified with $|\log_2 FC| \geq 1$ and FDR < 0.05 using DESeq2 (Love *et al.*, 2014). To visualize intersections of DEGs in the three different genotypes in upset plots the R package Complex Upset (Lex et al., 2014) was applied. Heat maps were drawn using the R package Complex Heatmap (Gu, 2022) by using Euclidean distance and centroid linkage clustering. Gene ontology (GO) enrichment analyses were performed with clusterProfiler (Wu et al., 2021). Statistical significance of GO terms was declared when the *p*-value of Benjamini–Hochberg false discovery rate (FDR) multiple testing correction was < 0.05. To reduce redundant GO terms and keep one representative term, the method *simplify* was applied with a similarity cutoff > 0.7. Dot plot representations of significant GO terms were obtained using the R package enrichPlot (Yu, 2021). The raw RNA sequencing

data have been deposited and available in the European Nucleotide Archive (ENA) under project ID PRJEB65916.

4.6 *In silico* analysis

For phylogenetic analysis, DOMON-containing protein sequences of *A. thaliana* were retrieved from TAIR (https://www.arabidopsis.org/) and aligned using MAFFT 7 (Katoh and Standley, 2013). The alignment was imported into MEGA11 (Tamura et al., 2021), followed by phylogenetic tree construction using the neighbor-joining (NJ) method with default parameter settings and bootstrap analysis with 1,000 replicates. DOMON and Cyt*b*561 conserved domains were identified using the Conserved Domain Database (CDD; https://www.ncbi.nlm.nih.gov/Structure/cdd/cdd.shtml). Prediction of intracellular localization of DOMON-containing proteins and of MONODEHYDROASCORBATE REDUCTASE (MDHAR) proteins was conducted with Cell eFP viewer in the ePlant server (https://bar.utoronto.ca/eplant/). Transmembrane prediction of HYP1 was obtained using DeepTMHMM (https://dtu.biolib.com/DeepTMHMM). Signal peptide of HYP1 was predicted using SignalP (https://services.healthtech.dtu.dk/services/SignalP-5.0/).

4.7 Plasmid construction and generation of transgenic lines

All constructs for plant expression were generated by GreenGate modular cloning (Lampropoulos et al., 2013). The 2151-bp *HYP1* promoter sequence and the 2019-bp of *HYP1* open reading frame (without stop codon) were amplified from genomic DNA of Col-0 (CS60000) and the 1212-bp long *HYP1* coding sequence (without stop codon) amplified from complementary DNA (cDNA). To drive *HYP1* expression in specific cell types, the 2008-bp promoter fragment of *BRN1* (At1g33280), 2086-bp of *SGN1* (At1g61590), 2309-bp of *LPR1* (At1g23010), and 1941-bp of *FRO2* (At1g01580) were amplified from genomic DNA of Col-0 (CS60000). To study the involvement of DOMON domain in HYP1 function, 819-bp of AIR12 open reading frame (without stop codon) were amplified from genomic DNA of Col-0 (CS60000), the 507-bp long of HYP1's DOMON domain and 186-bp long of AIR12's glycosylphosphatidylinositol (GPI) domain sequence amplified from complementary DNA (cDNA). The 1249-bp *MDHAR3* promoter sequence and the 2600-bp of *MDHAR3* open reading frame (without stop codon) were amplified from genomic DNA of Col-0 (CS60000). To generate transcriptional GUS reporter lines of all CYBDOMs, approx. 2000-bp promoter fragments of all CYBDOM members were amplified from genomic DNA of Col-0 (CS60000).

Amplification was performed using the Phusion High-Fidelity DNA Polymerase (New England Biolabs) using primers listed in Table 3. Promoters, open reading frame and coding sequences were cloned into the GreenGate entry modules pGGA000 and pGGC000 or pGGD000, respectively. Correct integration of the fragments into entry modules was verified by restriction digestion reactions and the cloned sequences verified by sequencing. To generate transcriptional reporters and translational GFP and BFP fusions, individual entry modules were assembled either into the GreenGate binary vector pGGZ001, including a phosphinothricin or hygromycin resistance cassette for antibiotic selection in plants, or into pFASTR A-G for selection of transgenic plants based on the presence of red fluorescence in seeds. Mutated HYP1^{M90L}, HYP1^{H174L} and HYP1$^{H211L/H278L}$ variants were generated by site-directed mutagenesis using the double-primer method (Zheng et al., 2004) and the primers listed in Table 3. The final binary vectors were transformed into the *Agrobacterium tumefaciens* strain GV3101 (containing the helper plasmid pSOUP if transformed with pGGZ001) and finally transferred to *A. thaliana* (Col-0; CS60000) plants via the flower dip method (Clough and Bent, 1998). Representative transgenic lines for each construct were selected from 6-8 independent transformants and used for analysis. If not noted otherwise, the transgenic line overexpressing *HYP1* in Col-0 used in the experiments was the homozygous line *35S::HYP1* 5d. In order to express native or mutated *HYP1* variants in oocytes, the corresponding cDNA fragments were amplified with primers containing *Xma*I (forward) or *Xba*I (reverse) restriction sites and cloned into pGEMHE (Picco et al., 2015). The generated plasmids were then sent to the laboratory of Prof. Dr. Armando Carpaneto (NRC/University of Genoa, Italy) for electrophysiological characterization in oocytes.

Table 3. Primers used for cloning.

Fragment	Sequence length	Primer sequence
HYP1 promoter for pENTR	2151 bp	For: CACCTGGTGAAGCGTTGACTCTC
		Rev: GTCTTCGTGTTCTGTTTTGAAAG
*Bsa*I mutation in *HYP1* promoter	-	For: GGTGGGACTCAAACTCTCAATGG
		Rev: GTTTGAGTCCCACCCAAAAAAAGC
HYP1 promoter for pGGA000	2151 bp	For: AACAGGTCTCAACCTTGGTGAAGCGTTGACTCTC
		Rev: AACAGGTCTCATGTTGTCTTCGTGTTCTGTTTTGAAAG
HYP1 ORF for pGGC000	2019 bp	For: AACAGGTCTCAGGCTAAATGGACCGAACACAATCTC
		Rev: AACAGGTCTCACTGAGGCGTCCTGGTGATGTGG
FRO2 promoter for pENTR	1941 bp	For: CACCGCGTTTTCTTGTTACCAATCG
		Rev: CCTCTCTTTCCTCTCAGGATTTC
*Bsa*I mutation in *FRO2* promoter	-	For: GGAGGACTCATATCTTCTTCAACCC
		Rev: ATATGAGTCCTCCCAAATTGGAT
FRO2 promoter for pGGA000	1941 bp	For: AACAGGTCTCAACCTGCGTTTTCTTGTTACCAATCG
		Rev: AACAGGTCTCATGTTCCTCTCTTTCCTCTCAGGATTTC
HYP1^{M90L} mutation	-	For: TCAGCTGGTTGGGACGCAAG
		Rev: CAACCAGCTGAGTACTACTTGGG
HYP1^{H174L} mutation	-	For: CGAGTCTTCAAACCTCAGGAGATAATATG
		Rev: GTTTGAAGACTCGCAGGAACACC

Table 3. Primers used for cloning (continued).

Fragment	Sequence length	Primer sequence
HYP1^{H211L} mutation	-	For: AGACGCTTGGAGTACTAAATGC
		Rev: CTCCAAGCGTCTGTTTTCATAAAG
HYP1^{H278L} mutation	-	For: AACCCTTCGTAACCTTGGAATAG
		Rev: TACGAAGGGTTGAGTAAGATG
HYP1 cDNA in pGemHE	1212 bp	For: TAAGCACCCGGGATGGACCGAACACAATCTC
		Rev: TGCTTATCTAGACTAGGCGTCCTGGTGATGTGG
BRN1 promoter for pGGA000	2008 bp	For: AACAGGTCTCAACCTGGTCAATTCTGGTTTCCGTTA
		Rev: ACCAGGTCTCATGTTTCGGTTATTAAATGATCAATGTTT
SGN1 promoter for pGGA000	2086 bp	For: AACAGGTCTCAACCTATGAGGACCCTGTGCATTG
		Rev: AACAGGTCTCATGTTTTTTTGTGTTGTAAGATTTTAGGAG
LPR1 promoter for pGGA000	2309 bp	For: AACAGGTCTCAACCTCCTAGAATGTTATTGATGTTTCTTG
		Rev: AACAGGTCTCATGTTTTCTGACAAGTCAATTCAGTTTTGA
At3g25290 (*CRR*) promoter for pGGA000	2054 bp	For: AACAGGTCTCAACCTATGCTCTGGATGCCTCTTGG
		Rev: AACAGGTCTCATGTTTGTTGGATGGCTTGTAGTAACC
At3g59070 promoter for pGGA000	2269 bp	For: AACAGGTCTCAACCTCCGGCGACAATTAAGCTTTG
		Rev: AACAGGTCTCATGTTGATAATAATTATGATTGTGGCTTTTCTC
At4g12980 promoter for pGGA000	2100 bp	For: AACAGGTCTCAACCTACCGCGAGTTAAATTCTACTTTGT
		Rev: AACAGGTCTCATGTTGATGAATGATGATGATGCAAAGAATTGTAG
At5g48750 promoter for pGGA000	1856 bp	For: AACAGGTCTCAACCTTCAGGGATATGCTCGAAGCG
		Rev: AACAGGTCTCATGTTGATGATGGATTTTCCGAGAGAAC
At5g54830 promoter for pGGA000	2066 bp	For: AACAGGTCTCAACCTTGCCCTAATTTGGAGACGCT
		Rev: AACAGGTCTCATGTTGGTGTTGGGTGAGAGATTTACTC
At2g04850 promoter for pGGA000	2095 bp	For: AACAGGTCTCAACCTAGGACTCAACTTTGAATTGAAACAA
		Rev: AACAGGTCTCATGTTTGTTTGATCATCTCTGTTTTTTTTG
At3g07390 (*AIR12*) promoter for pGGA000	2097 bp	For: AACAGGTCTCAACCTAAGAACAAAAGCGTGTGCAA
		Rev: AACAGGTCTCATGTTGTGATGTTTATATAGAAGGGCAATG
At3g07570 promoter for pGGA000	2063 bp	For: AACAGGTCTCAACCTTGTGTTTGTGCATAGTTGGTAAC
		Rev: AACAGGTCTCATGTTGTTTTGTTCTCTTTCTCTCTCTCTGGATC
At3g61750 promoter for pGGA000	2343 bp	For: AACAGGTCTCAACCTATGGCACGTAAGTCATCCGC
		Rev: AACAGGTCTCATGTTGGTTGGAATCGAAACAGAGACG
At4g17280 promoter for pGGA000	1943 bp	For: AACAGGTCTCAACCTCCACCCAAATGGAATGTGGC
		Rev: AACAGGTCTCATGTTGAATCAGAAGGTTAGAAAGAAAAAGACTC
At5g47530 promoter for pGGA000	1930 bp	For: AACAGGTCTCAACCTCTCGGGAAGTGCAGAGGAAA
		Rev: AACAGGTCTCATGTTGGAAACAGAATCTCGAGTAATGATTA
AIR12 for pGGC000	819 bp	For: AACAGGTCTCAGGCTAAATGTCCCTGTGTCTTAAAATACCTC
		Rev: AACAGGTCTCACTGAGAAAATAAAAATAGAACCCAACAAAA
HYP1$_{DOMON}$ for pGGC000	507 bp	For: AACAGGTCTCAGGCTAAATGGACCGAACACAATCTCC
		Rev: AACAGGTCTCACTGAACCGTTGACAACAGGTCCC
AIR12$_{GPI}$ for pGGD000	186 bp	For: AACAGGTCTCATCAGAAACAGAAGATGCAGCACCGG
		Rev: AACAGGTCTCAGCAGTCAGAAAATAAAAATAGAACCCAACA
MDHAR3 promoter for pGGA000	1249 bp	For: AACAGGTCTCAACCTTTTCATCTCCTTCATTTATCTTGTTT
		Rev: AACAGGTCTCATGTTAATTAATAAATAAAACTTCTTTCTCAG
MDHAR3 ORF for pGGC000	2600 bp	For: AACAGGTCTCAGGCTAAATGGCGGAAGAGAAAAGCTA
		Rev: AACAGGTCTCACTGAAAGAGAGGTGCTATAGAACTTGGTG

4.8 Measurement of primary root, meristem and mature cell lengths

To determine primary root lengths, if necessary, roots were first spread and separated from one another on the agar plate and then scanned using an Epson Expression 12000XL scanner (Seiko Epson) with a resolution of 300 dots per inch. Primary root length was quantified with ImageJ software. Measurements of meristem cell length and mature cortical

cell length were performed with ZEN 3.4 Blue Edition imaging software (Carl Zeiss Microscopy).

4.9 GUS histochemical assay

GUS activity of plants expressing *proHYP1::GUS* and all other lines expressing GUS reporter gene driven by the promoters of 10 additional genes from the DOMON family were assessed by incubating root, leaf, inflorescence, and silique samples in a solution containing 20 mg mL^{-1} 5-bromo-4 chloro-3-indolyl-β-day-glucuronic acid (X-gluc) in 100 mM sodium phosphate, 0.5 mM $K_3Fe(CN)_6$, 0.5 mM $K_4Fe(CN)_6$ and 0.1% (v/v) Triton X-100 at 37 °C in darkness. For plants expressing *proCYCB1;1::GUS* and *proMDHAR3::GUS*, only root samples were incubated in the staining solution. For *proHYP1::GUS* and *proMDHAR3::GUS*, samples were incubated up to 30 min. For *proCYCB1;1::GUS* and for tissue specific expression localization of all CYBDOMs, samples were incubated overnight. Samples were then mounted on a clearing solution (chloral hydrate : water : glycerol = 8:3:1) and imaged using a Axio Imager 2 light microscope (Carl-Zeiss).

4.10 Callose staining

Callose deposition was assessed by staining roots with aniline blue as described previously (Müller et al., 2015). In brief, roots were incubated for 1.5 h in a solution containing 0.1% (w/v) aniline blue (AppliChem) in 100 mM Na-phosphate buffer (pH 7.2). Stained roots were mounted on water and directly visualized with a laser-scanning confocal microscope.

4.11 Fe staining

The staining of Fe by Perls/DAB was based on a procedure described previously (Roschzttardtz et al., 2009), with modifications. In the assays performed in the present thesis, roots were rinsed one time with ultrapure water for 1 min, and then incubated for 5 min in a freshly prepared Perls staining solution [0.5% (v/v) HCl and 0.5% (w/v) K-ferrocyanide]. Roots were shortly rinsed in water to remove agar adhering to roots, while the more diluted Perls staining solution compared to the original protocol was necessary to prevent meristem disintegration by otherwise high HCl concentration. Subsequently, roots were incubated in a methanol solution containing 10 mM NaN_3 and 0.3% (v/v) H_2O_2 for 1 h in the dark at room temperature. After washing three times with 100 mM phosphate buffer (pH 7.4) for 1 min each, roots were finally incubated for 5 min in an intensification solution containing

0.025% (w/v) DAB and 0.005% (v/v) H_2O_2 in 100 mM phosphate buffer (pH 7.4). Samples were then mounted on a clearing solution (chloral hydrate : water : glycerol = 8:3:1) and immediately imaged using a Axio Imager 2 light microscope (Carl Zeiss Microscopy, Germany). To quantify the intensity of Perls/DAB staining, ImageJ software was used. First, images were converted to 8-bit grayscale format. Subsequently, the image colors were inverted to enhance contrast. A region of interest (ROI) was defined in the area directly above the quiescent center within the root meristem, and the mean pixel intensity of this region was measured to assess staining levels.

For Fe localization in root sections, roots stained with Perls/DAB as described above were subjected to a combined conventional and microwave-assisted root tissue preparation in a PELCO BioWave®34700-230 microwave system (Ted Pella, Inc., Redding CA, USA). The procedure included a series of aldehyde fixation, dehydration, and resin embedding as detailed in Table 4. Semi-thin sections of 2.5 µm thickness were cut using a Leica UCT microtome (Leica Microsystems, Germany), and mounted on slides in rapid mounting medium Entelan (Sigma-Aldrich, Germany). Sections were recorded with a 40X objective at fixed exposure time using a Zeiss Axio Imager M2 (Carl Zeiss Microscopy, Germany).

For detection of Fe(II) in the apical meristem, root tips were excised and incubated for 10 min in a freshly prepared buffer solution (2 mM $CaSO_4$ and 500 mM MES pH 5.5 adjusted with KOH) containing 2.5 µM RhoNox-1 fluorescent dye (Hirayama et al., 2013). Roots were rinsed and mounted with the same buffer solution without the probe and immediately visualized with a confocal laser-scanning microscope.

Table 4. Protocol for fixation, dehydration and embedding of root tissue.

Process	Reagent	Power [W]	Time [s]	Vacuum [mm Hg]
1. Fixation	2.0% (v/v) glutaraldehyde and 2.0% (v/v) paraformaldehyde in 0.05 M cacodylate buffer (pH 7.2)	150 0 150 0 150	60 60 60 60 60	0 0 0 0 0
	After step samples were kept for additional overnight on a shaker at 4 °C			
2. Wash	1x 0.05 M cacodylate buffer (pH 7.2) and 3x distilled water	150	60	0
5. Dehydration	Ethanol series: 30%, 40%, 50%, 60%, 70%, 80%, 90%, 2x 100%, and 100% acetone	150	60	0
	After each step samples were kept for additional 5 min on a shaker at RT			
6. Resin infiltration	25% Spurr resin in acetone 50% Spurr resin in acetone 75% Spurr resin in acetone 100% Spurr resin in acetone	2 h on shaker at RT 2 h on shaker at RT 2 h on shaker at RT overnight on shaker at RT		
5. Polymerization	24 h at 100 °C in prepolymerized flat embedding molds with disc in a heating cabinet at 70 °C			

4.12 Confocal microscopy analyses

For protein localization studies, roots of transgenic lines expressing GFP and/or BFP were excised, stained with propidium iodide (10 µg mL^{-1}) for 10 min, and mounted in water. GFP- and/or BFP- and propidium iodide-dependent fluorescence were acquired with a confocal laser-scanning microscope (LSM 780; Zeiss, Germany) equipped with a 20x/0.8 M27 objective. GFP was excited with a 488 nm Argon laser and the emitted light was detected at 505-535 nm, BFP was excited at 405 nm and detected at 410-529 nm, and propidium iodide was excited at 561 nm and detected at 600-700 nm. For co-localization of GFP with plasma membrane, root segments were stained with 4 µM FM4-64 (Invitrogen) in 50 mM Na-phosphate buffer (pH 7.2) for 15 min at 4 °C, and mounted in 50 mM Na-phosphate buffer (pH 7.2). FM4-64 was excited at 488 nm and detected at 640 nm. Aniline blue-stained callose was excited at 405 nm and emission detected at 415-480 nm. Fe(II)-RhoNox-1 complex was excited at 514 nm and emission detected at 531-703 nm. GFP-, BFP-, and RhoNox-1-derived fluorescence intensity signal was measured using ZEN 3.4 Blue Edition imaging software, by defining a ROI directly as indicated.

Confocal microscopy analyses of *X. laevis* oocytes expressing *HYP1:GFP,* *HYP1*$^{H211L/H278L}$*:GFP*, and *HYP1*^{M90L}*:GFP* were performed in the laboratory of Prof. Dr. Armando Carpaneto (NRC/University of Genoa, Italy) using a Leica SP2 microscope equipped with a 40x oil-immersion objective. FM4-64, diluted at a final concentration of 15 µM, was used to stain the plasma membrane. Both GFP and FM4-64 were excited at 488 nm, and emissions were monitored at 505-512 nm and 645-655 nm, respectively. Confocal images were obtained by an axial laser scan line (*z* scan) along a 10-µm section (0.5-µm steps) at the bottom of the oocyte.

4.13 Oocyte expression and two-electrode voltage clamp recordings

The following procedures were performed in collaboration with the research group of Prof. Dr. Armando Carpaneto (NRC/University of Genoa, Italy). Oocytes were surgically removed from adult female *Xenopus laevis* frogs treated with collagenase (1 mg mL^{-1}) for 30 min at room temperature under constant shaking, and washed twice with standard bath solution composed of 96 mM NaCl, 2 mM KCl, 1 mM $CaCl_2$, 1 mM $MgCl_2$, and 5 mM HEPES (pH 7.5). Isolated oocytes were injected with *HYP1* cRNA at 40 ng per oocyte (or with an equivalent volume of nuclease-free water) using a Drummond Nanoject microinjector. Oocytes were incubated at 18 °C in standard solution (supplemented with 0.1 mg mL^{-1} gentamicin) for at least 24 h before voltage-clamp experiments.

Whole-cell membrane currents were measured at room temperature using a home-made two-electrode voltage-clamp amplifier and 0.2–0.4 MΩ glass electrodes with a tip diameter of a few micrometers, filled with 3 M KCl. By convention, negative currents are inward currents mediated by the efflux of anions/electrons (or influx of cations). Membrane currents elicited by exposure to extracellular electron acceptors were generally recorded at a holding potential of -20 mV. In some assays, as indicated in the text and figure legends, the standard bath solution was modified by setting the pH to 5.5. This was achieved by substituting 10 mM HEPES with an equimolar concentration of MES, or by replacing NaCl, KCl, $CaCl_2$ and $MgCl_2$ with 200 mM MES and 20 mM BTP at pH 5.5 (BTP-MES solution). In experiments with a negative holding voltage of -120 mV, 1 mM lanthanum chloride was supplied to the bath solution, in order to inhibit endogenous background currents activated at these negative voltages. A gravity-driven perfusion system was used for continuous superfusion of oocytes during voltage-clamp recordings and for switching between different bath solutions. Ferric compounds were prepared as stock solutions and diluted appropriately in the bath solution.

For ascorbate injection experiments, ascorbate stock solutions (100 mM) were prepared freshly and adjusted to pH 7.0 with KOH. To raise the cytosolic ascorbate (Asc_{cyt}) concentration to 10 mM, oocytes were removed from the voltage-clamp setup after the initial recording series and injected with ascorbate stock solution using the Drummond Nanoject microinjector. A first injection of 50 nL stock solution and a second injection of 100 nL resulted in an increase of the initial Asc_{cyt} of 10 and 30 mM, respectively, considering a volume of about 500 nL for a mean oocyte diameter of 1 mm. After the injection, the oocyte volume transiently increased, but recovered to its original size within min. Injected oocytes were allowed to recover for 30 min at room temperature before voltage-clamp measurements were resumed.

4.14 Ferric-chelate and cupric reductase assays

To determine the ferric-chelate reductase activity of roots, roots of intact plants were placed in a reaction solution containing 0.2 mM $CaSO_4$, 5 mM MES pH 5.5 (adjusted with KOH) and 0.2 mM 3-(2-pyridyl)-5,6-diphenyl-1,2,4-triazine-4′,4″-disulfonic acid (FerroZine). The ferric substrates in these assays were either 0.1 mM Fe(III)-EDTA, when HYP1 complementation of *fro2* was tested, or freshly prepared 0.1 mM $FeCl_3$: L-(−)-malic acid complexes (1 : 2), when ferric-chelate reductase was assayed in response to P deficiency.

Cupric reductase activity was assessed as described previously (Bernal et al., 2012). The reaction solution was composed of 0.2 mM $CuSO_4$, 0.6 mM Na_3citrate, and 0.4 mM bathocuproine disulfonic acid (BCDS) (Sigma-Aldrich) in ultrapure water. The absorbance of formed Fe(II)-FerroZine or Cu(I)-BCDS complexes was determined at 562 nm

or 483 nm, respectively, using a NanoDrop 2000 (NanoDrop). Extinction coefficients were 28.6 mM^{-1} cm^{-1} for the Fe(II)-FerroZine complex and 12.25 mM^{-1} cm^{-1} for the Cu(I)-BCDS complex.

4.15 Shoot chlorophyll analysis

To extract chlorophyll, samples consisting of whole shoots were weighed and incubated for 1-2 days at 4 °C in N,N'-dimethylformamide (Roth). The absorbance of the extracts was measured at 647 nm and 664 nm using a NanoDrop 2000 (NanoDrop) and the chlorophyll *a*+*b* concentration was determined as described previously (Porra et al., 1989).

4.16 Elemental analysis

Whole root or shoot samples were dried at 65 °C and weighed into polytetrafluoroethylene tubes. Plant material was digested with concentrated HNO_3 (67-69%; Bernd Kraft) and pressurized in a high-performance microwave reactor (UltraCLAVE IV, MLS GmbH). Digested samples were diluted with deionized water (Milli-Q Reference A+, Merck Millipore). Element analysis was carried out by high resolution inductively coupled plasma mass spectrometry (HR-ICP-MS) (ELEMENT 2, Thermo Fisher Scientific, Germany).

4.17 Root tip extract preparation and ascorbate quantification

For the quantification of total, reduced, and oxidized pools of ascorbate in root tips of *A. thaliana*, extracts were prepared from wild-type (Col-0) and *HYP1*-overexpressing plants grown for 6 days on P-sufficient (+P; 625 µM KH_2PO_4) or P-limited (-P; 5 µM KH_2PO_4 and 620 µM KCl) solid media, with 150 µM $FeCl_3$ as the sole Fe source. To prepare the root extracts, 0.5 mm root tip segments were manually excised using a sterile micro surgical scalpel blade under a stereomicroscope and placed in a 1.5-mL microcentrifuge tube containing 25 µL of zirconium silicate (Zr-58wt%Si) grinding beads (diameter, 1-1.2 mm; RIMAX ZS-R, Mühlmeier GmbH). The samples were then flash-frozen in liquid nitrogen. Each biological replicate consisted of approx. 1 mg FW (fresh weight) of root tips. The frozen material was homogenized using a tissue homogenizer (Retsch MM 400, Haan, Germany) for 2 cycles of 1 min at 30 Hz at -80 °C, followed by the addition of 75 µL of 0.1% (v/v) formic acid. After adding formic acid, the samples were homogenized for 2 cycles of 1 min at 30 Hz at 4 °C, followed by a 3-min ultrasonic bath. Subsequently, the samples were centrifuged at 13,200 rpm for 15 min at 4 °C. Following centrifugation, an aliquot of 50 µL of the supernatant

was transferred to a glass vial equipped with a 100-µL high recovery conical glass insert for HPLC injection.

Chromatographic separation was performed on a Vanquish™ UHPLC system (Thermo Fischer Scientific, Germering, Germany). The baseline separation for compounds of interest [dehydroascorbic acid (DHA) and ascorbic acid (ASC)] was achieved on a reversed phase Acquity UPLC® HSS T3 column (100 Å, 2.1 × 150 mm, 1.8 µm, Waters) using a two steps gradient elution of A [0.1% (v/v) formic acid (FA) in water] and B [0.1% (v/v) formic acid (FA) in methanol] as follows: 0-2 min, 0.1% B; 2-3 min, 0.1% to 10% B; 3-5 min 10% B; 5-6 min, 10% to 85% B. Additional time for column wash and re-equilibration to a total run time of 10 min was included. To preserve the integrity of the column a guard column (130 Å, 2.1 × 5 mm, 1.8 µm, Waters) was used. The column temperature was set at 30 °C and the flow rate at 0.3 mL min^{-1}. The injection volume was 5 µL. The UHPLC system was coupled to a Q Exactive Plus Mass Spectrometer (Thermo Fischer Scientific, Bremen, Germany) equipped with a Heated Elestrospray Ionization (HESI) source operating in negative ion mode. Source values were set as follow: spray voltage 2.5 kV; capillary temperature 255 °C; S-lens RF level 40; Aux gas heater temp 410 °C; sheath gas flow rate 47; Aux gas flow rate 11. For spectra acquisition, a Full MS/dd-MS^2 experiment was performed. Resolution in Full Scan was set to 70000. For MS/MS experiments, resolution was set to 17,500 and a Normalized Collision Energy (NCE) of 30 V was used. MS data were acquired and processed by Trace Finder Software (v. 4.1, Thermo Scientific, San Jose, USA). Two stock solutions of 10,000 and 1,000 ng mL^{-1} DHA/ASC in water containing 1% (v/v) FA were prepared. Twelve calibration solutions in the range of 5 to 8,000 ng mL^{-1} were prepared from the two stock solutions. To generate a calibration curve, the peak area on the extracted ion chromatogram (XIC) of the molecular ion $[M-H]^-$ was measured. A least-square linear regression weighting by the reciprocal of the concentration was used to best fit the linearity curve. The identification of compounds found in root tip extracts was based on comparison of its retention time, exact mass and MS2 spectrum (when available) with the standards.

4.18 Modeling of HYP1 structure and ascorbate docking

The modeling and docking studies were performed by the group of Dr. Georg Künze (Leipzig University, Germany) using AlphaFold (Jumper et al., 2021). In addition, a homology model of HYP1 was developed before the release of AlphaFold, using the comparative modeling protocol available in the Rosetta software (Leman et al., 2020). The following template structures were considered in comparative modeling: the cytochrome domain of cellobiose dehydrogenase enzymes from *Phanerodontia chrysosporium* (PDB: 1D7C),

Myriococcum thermophilum (PDB: 4QI3) and *Neurospora crassa* (PDB: 4QI7), and the cytochrome domain of pyranose dehydrogenase from *Coprinopsis cinerea* (PDB: 6JT6) as templates for the DOMON domain of HYP1, as well as the *A. thaliana* cytochrome *b*561 (PDB: 4O6Y, 4O79, 4O7G) and human duodenal cytochrome *b* structures (PDB: 5ZLE, 5ZLG) as templates for the cytochrome *b* domain of HYP1. The AlphaFold- and Rosetta-predicted HYP1 structure models were in close agreement with each other (Cα atom RMSDs of 1.5 Å and 2.3 Å over the cytochrome *b* and DOMON domains, respectively). For modeling the interactions with *b*-heme and soluble ligands, the AlphaFold-generated model of HYP1 was used because of its estimated higher accuracy.

Three *b*-heme molecules were placed in the HYP1 structure model at positions inferred from the template structures listed above. The positions of the *b*-heme molecules were refined using the FastRelax protocol in the Rosetta software. Distance restraints between the Fe atom in the *b*-heme molecule and the coordinating His residues were applied in this step: restraints were set up between H245+H314 and one *b*-heme in the cytochrome *b*561 domain, between H211+H278 and the other *b*-heme in the cytochrome *b*561 domain, and between H174 and the *b*-heme in the DOMON domain. The final step was an unrestrained minimization of the whole structure in the Amber14:EHT force field using the MOE software (v. 2022.02 Chemical Computing Group ULC, Montreal, Canada).

The molecular binding modes of ascorbate (PubChemID: 54679076), Fe(III)-EDTA (PubChemID: 28283), Fe(III)-malate (PubChemID: 10176445), and Fe(III)-nitrilotriacetate (PubChemID: 92043310) were modeled using ligand docking calculations with the Rosetta software. Ascorbate was docked into HYP1's cytoplasmic facing pocket, which was identified by structural comparison with the ascorbate-bound structure of cytochrome *b*561 (PDB ID: 4O79). The structure analysis indicated that residues K77, K81, and R150 in cytochrome *b*561 coordinate ascorbate through hydrogen bonds. The equivalent residues in HYP1 are K234, R307 and R299. The centroid of these three residues was used as the starting point to place the ascorbate molecule in the HYP1 pocket prior to the docking calculations.

4.19 Statistical analysis

To analyze the significant differences among multiple groups, one-way ANOVA followed by post hoc Tukey's test at $P < 0.05$ was applied. Significant differences between two groups were assessed by two- or one-tailed Student's *t*-test, as indicated in the legend of the figures. Statistical tests were performed using SigmaPlot 11.0 software and plots prepared with GraphPad Prism software v.9.3.1 (https://www.graphpad.com/).

5 Results

5.1 Analysis of a transcriptome study to identify putative Fe- and ascorbate-related genes induced in response to P deficiency

To identify novel genes required for P-dependent root growth responses, a time-course root transcriptome of *A. thaliana* (Col-0 accession) plants grown on sufficient (625 µM) or low (100 µM) P concentrations was performed and analyzed in depth. Part of the dataset was previously used to specifically assess the expression of genes involved in P deficiency-induced root hair development (Bhosale et al., 2018). In the present thesis, all data derived from the microarray experiment were integrated, including one additional time point from the same experiment (*i.e.*, 6 days after transfer) that was not considered in the previously published study of Bhosale *et al.* (2018). Using $\log_2$-fold change ($\log_2$FC) ≥ |1.0| and FDR < 0.05 as cut-off parameters, 2,327 genes that responded significantly to low P in at least one time point were identified (Figure 4A). Following a hierarchical analysis, the genes were distributed into four major clusters. Among the cluster containing genes downregulated in response to P deficiency (cluster 1,901 genes), the gene ontology (GO) terms composed by the cluster “iron metal homeostasis” were strongly enriched (Figure 4B). The expression of major genes involved in root Fe uptake, including *FRO2* and *IRT1*, was indeed downregulated, as reported earlier (Misson et al., 2005; Thibaud et al., 2010; Li and Lan, 2015; Hoehenwarter et al., 2016). To gain insights about Fe reduction in P-deficient roots, the expression of genes related with ferric Fe reduction, including genes encoding the membrane-bound FROs and the enzymes involved with the synthesis of coumarins or ascorbate, was inspected in more detail. Among *FRO*s, only *FRO8* was consistently upregulated during the time-course of P deficiency (Figure 4C). However, FRO8 has been predicted to reside in mitochondrial membranes, a localization partially supported by the analysis of *A. thaliana* mitochondrial proteome (Heazlewood et al., 2004). Thus, these results indicated that ferric reduction by plasma membrane-bound FRO-type metalloreductases and coumarins is decreased in P-deficient roots. The expression of *S8H* and *CYP82C4*, critical for the synthesis of coumarins with ferric reduction capacity (Rajniak et al., 2018; Paffrath et al., 2024), was strongly downregulated under low P (Figure 4C). Regarding ascorbate, the ascorbate biosynthesis gene *VITAMINC2* (*VTC2*) and, especially, *VTC4* were progressively upregulated as the time of exposure to the low-P medium was extended (Figure 2C). This result is in line with a previous study (Mora-Macías et al., 2017), suggesting a potential role for ascorbate in P-deficient roots.

In order to identify novel genes related to Fe acquisition or homeostasis among the low P-induced genes, the dataset was screened for the presence of relevant protein domains, including “ferric reductase” or “Fe/Cu oxidase”. One gene significantly upregulated in response

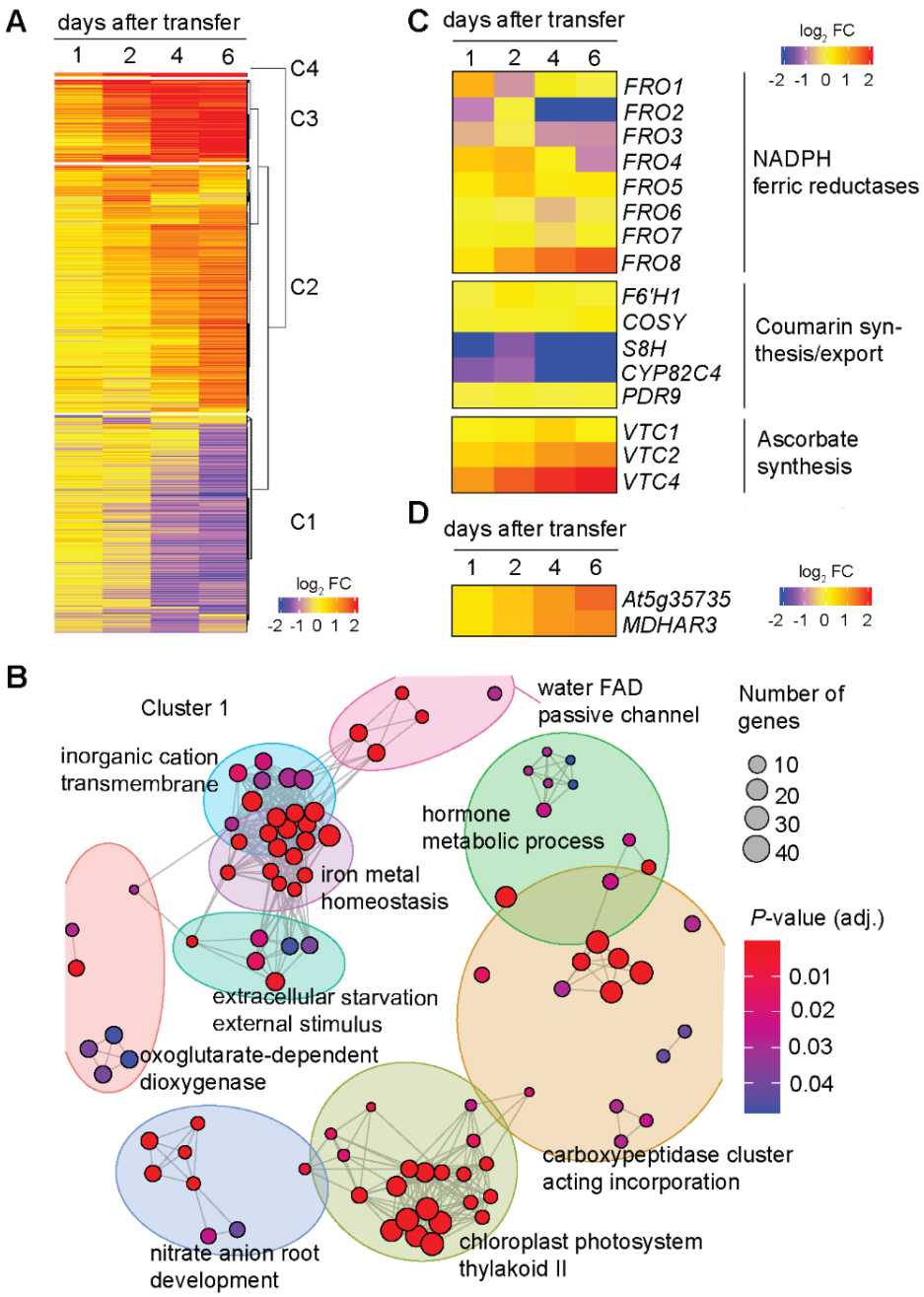

Figure 4. Overview of time-dependent transcriptional responses induced in roots exposed to low-P conditions.

(**A**) Heat map for hierarchically clustered genes significantly regulated in response to P deficiency in *A. thaliana* roots at four time-points after transfer to P-sufficient (625 µM KH_2PO_4) or P-limiting (100 µM KH_2PO_4 + 525 µM KCl) conditions containing 100 µM Fe(III)-EDTA as Fe source. The heatmap shows $|\log_2 FC| \geq 1$ of -P *versus* +P (FDR < 0.05). Each treatment consisted of three independent biological replicates. The gene set was split into four gene expression clusters (C1 to C4). (**B**) GO term enrichment network depicting all significantly enriched GO terms detected in cluster 1 (adjusted Benjamini-Hochberg *p*-values, FDR < 0.05). Each GO term is represented as a node, and functionally related GO terms are clustered (k-means clustering). The size of the node reflects the number of genes enriched in the GO term, and the colors indicate the FDR. Edges between nodes represent the similarity between GO terms (Jaccard similarity coefficient method). The stronger the similarity, the shorter and thicker the edges. Heatmap showing differential expression ($|\log_2 FC| \geq 1$, -P *versus* +P, FDR < 0.05) of genes encoding known membrane-bound ferric-chelate reductases or enzymes involved with the synthesis of coumarins or ascorbate during the time course of P treatments (**C**) and the two novel genes that are induced in roots of Arabidopsis in response to low P (**D**).

to low P (Figure 4D) and predicted to encode a protein with a “Cytochrome b561/ferric reductase transmembrane” domain according to InterPro (www.ebi.ac.uk/interpro/) was identified. The gene *At5g35735*, was present in cluster 2 and had not been previously characterized. An earlier phylogenetic analysis has identified At5g35735 as a CYBDOM-type protein (Preger et al., 2009). These proteins possess a cytochrome *b*561 fused to a DOMON domain, which was initially identified in dopamine β-hydroxylase, the enzyme that generates norepinephrine from dopamine in humans (Levin et al., 1960; Aravind, 2001). Interestingly, cytochrome *b*561 proteins were shown to mediate electron transport across membranes, using cytosolic ascorbate as the electron donor (Picco et al., 2015; Gradogna et al., 2023). Further analysis of the transcriptome dataset revealed that a gene encoding *MONODEHYDROASCORBATE REDUCTASE 3* (*MDHAR3*; *At3g09940*) was also significantly upregulated in response to low P supply (Figure 4D). Considering the P-responsiveness and the potential involvement of At5g35735 and At3g09940 with ferric reduction and ascorbate regeneration, respectively, they were selected for in-depth functional characterization in the present thesis.

5.2 Identification of a CYBDOM mutant with hypersensitive root growth inhibition under low P

To characterize a putative role of the P deficiency-induced CYBDOM gene *At5g35735*, one available SALK insertion line (SALK_115548), carrying a transfer DNA (T-DNA) insertion in the sole intron, was obtained. The T-DNA almost completely abolished the expression of the gene in the insertion line (Figure 5A). When the insertion line and the corresponding wild-type (Col-0) were grown in a solid agar medium with sufficient or limiting P supply, plants of the insertion line exhibited more severe primary root inhibition than the corresponding wild-type (Col-0) (Figure 5B and C). The phenotype was specifically observed under low P. Thus, based on this conditional phenotype, the mutant was named *hypersensitive to low P1* (*hyp1*).

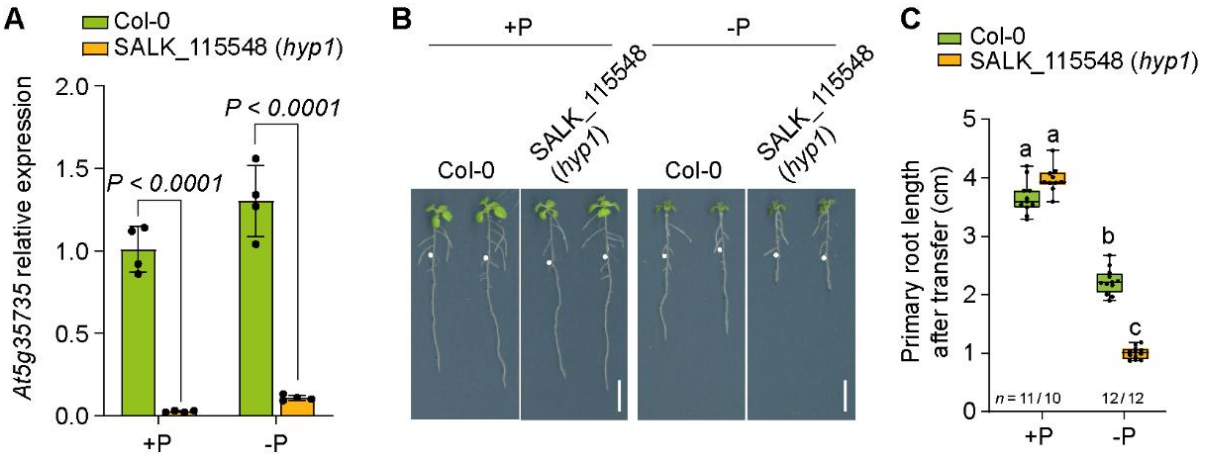

Figure 5. Identification of an *A. thaliana* mutant with hypersensitive primary root inhibition under low P supply.

(**A**) Expression of *At5g35735* in roots of wild-type plants (Col-0) and the insertion mutant SALK_115548 (*hyp1*). Seven-day-old seedlings were transferred to a fresh medium containing 625 µM P (+) or 5 µM P (-P) with 150 µM $FeCl_3$ and whole roots collected for RNA extraction after 4 d. Expression levels were normalized to *UBQ2*. Bars represent means ± s.d. ($n = 4$ independent biological replicates per condition). Visual appearance of plants (**B**) and primary root elongation (**C**) of wild-type (Col-0) and SALK_115548 (*hyp1*) mutant plants. Seven-day-old seedlings were transferred to a fresh medium containing 625 µM P (+P) or 5 µM P (-P) with 100 µM Fe(III)-EDTA and not shielded from direct light exposure. Plants were photographed and analyzed after 6 days. White dots indicate the position of the primary roots at the day of transfer. Data are presented as boxplots with each dot representing the datapoint of one biological replicate. For the boxplots, central horizontal lines, median; edges of boxes, 25th (bottom) and 75th (top) percentiles; whiskers, minimum and maximum. The letters indicate significant differences (one-way ANOVA followed by post-hoc Tukey's test, $P < 0.05$, n = 10-12 independent plants). Scale bars, 1 cm.

Since Fe(III) complexed with malate is prone to blue light-induced photoreduction, which increases the risk of Fe(II)-driven hydroxyl radical formation in the apoplast (Zheng et al., 2019), the phenotypic analysis was repeated by shielding the roots from direct light exposure. As shown in Figure 3, this was achieved by placing the petri dishes inside a box with a dark foam separating each petri dish. With this system, only little light reached the roots and light-induced Fe(III) reduction directly in the agar medium was almost completely prevented, as revealed by Fe(II) staining of agar with FerroZine (Figure 3A). Furthermore, Fe-EDTA was replaced by the non-chelated Fe form $FeCl_3$. This modification was made in order to more directly investigate root responses induced by Fe complexation and solubilization driven by root-exuded malate. As expected, although the amount of Fe supplied as $FeCl_3$ was higher than that provided as Fe(III)-EDTA, only a small fraction was soluble in the absence of a chelator (Annex Table 1). When plants were grown under this modified cultivation setup, the severe primary root inhibition of *hyp1* plants under low P supply still persisted (Figure 6B and C). Considering that this cultivation setup (*i.e.*, light-shielded roots and non-chelated Fe source) simulates better soil-relevant conditions, it was used in all further experiments investigating responses to P-limiting conditions.

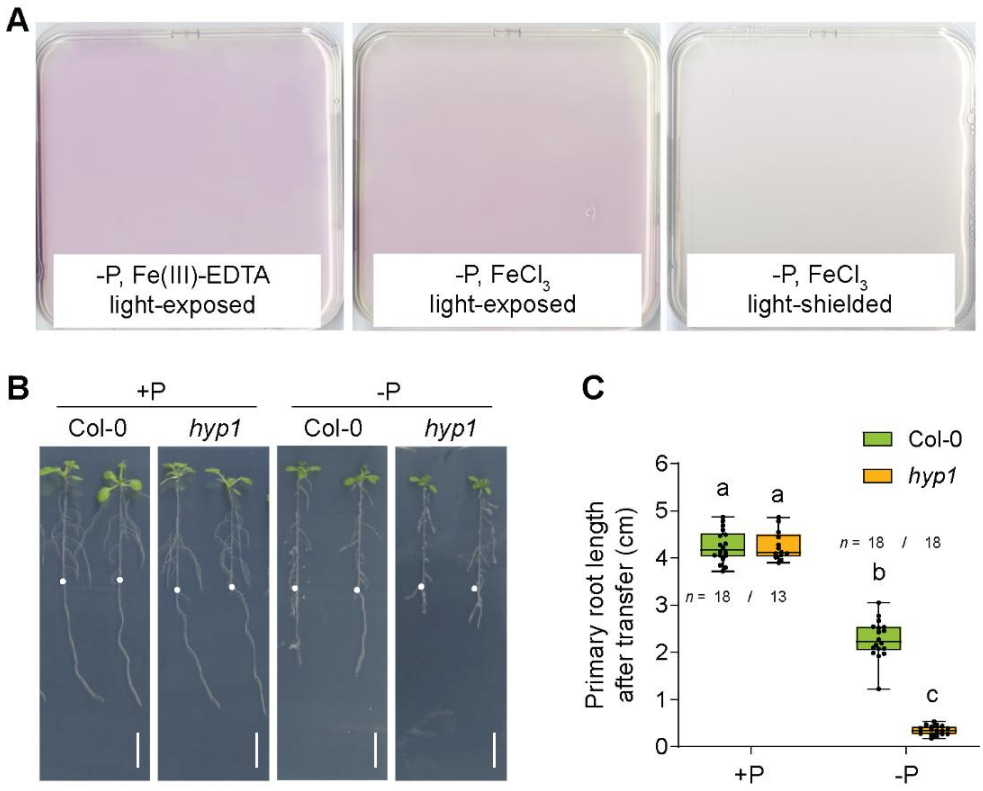

Figure 6. Primary root length of *hyp1* plants is also more severely inhibited under low P when roots are shielded from light and Fe supplied as $FeCl_3$.

(**A**) Staining of Fe(II) in the solid agar medium supplied with Fe(III)-EDTA or $FeCl_3$. Translucent Petri dishes placed or not in the light-protected boxes were stained with 50 µM FerroZine after 3 days inside the growth cabinets The appearance of a magenta stain indicates the formation of Fe(II) by photoreduction. Appearance of plants (***B***) and quantification of primary root length (***C***) of wild-type (Col-0) and *hyp1* mutant plants grown for 6 days on sufficient and low P conditions (+P and -P, respectively). Ten-day-old seedlings were transferred to a fresh medium containing 625 µM P (+P) or 5 µM P (-P) with 150 µM $FeCl_3$ and analyzed after 6 days. White dots indicate the position of the primary roots at the day of transfer. Data are presented as boxplots with each dot representing the datapoint of one biological replicate. For the boxplots, central horizontal lines, median; edges of boxes, 25th (bottom) and 75th (top) percentiles; whiskers, minimum and maximum. The letters indicate significant differences (one-way ANOVA followed by post-hoc Tukey's test, $P < 0.05$, $n = 16$ independent plants). Scale bars, 1 cm.

Since a second independent T-DNA insertion line for *HYP1* could not be obtained, the full genomic coding sequence of *HYP1* including a 2.1-kb-long promoter region was expressed in *hyp1*. Re-introduction of *HYP1* was able to fully rescue the severe root inhibition of *hyp1* (Figure 7A). The intron between the two exons of *HYP1* is a putative rolling-circle (*Helitron*) transposon element (Figure 7B). To rule out a possible involvement of a predicted transposon element with the short-root phenotype of *hyp1* plants, complementation was also attempted with *HYP1* complementary DNA (cDNA) under the control of the *HYP1* promoter. As shown in Figure 7D and E, *HYP1* cDNA also complemented the hypersensitive primary root inhibition of *hyp1* under low P (Figure 7C and D). Thus, these results demonstrated that disruption of *HYP1* is causal for the P deficiency-induced hypersensitive root phenotype of the isolated T-DNA line.

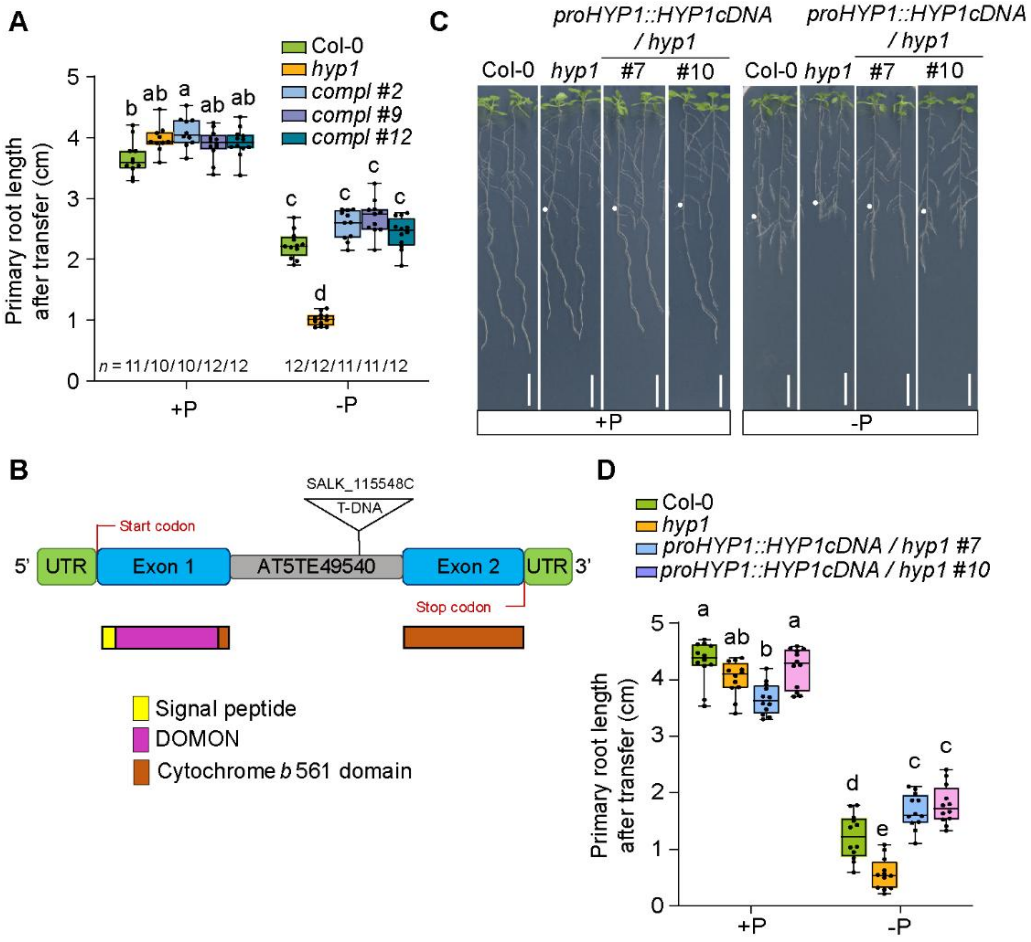

Figure 7. A predicted transposon element in *HYP1* locus is not responsible for the short-root phenotype of the *hyp1* T-DNA mutant.

(**A**) Quantification of primary root length of wild-type (Col-0), *hyp1* mutant, and three transgenic lines of *hyp1* complemented with *HYP1* full genomic DNA grown for 6 days on sufficient and low P conditions (+P and -P, respectively). (**B**) Exon-intron structure of *HYP1*, showing the T-DNA insertion in the intron region, which is predicted to encode an *Helitron* transposon element in the forward strand. The approximate position of features of the translated protein relative to genomic DNA is shown. Visual appearance (**C**) and primary root length (**D**) of wild-type (Col-0), *hyp1* mutant, and two independent lines expressing *proHYP1::HYP1cDNA* in the *hyp1* mutant grown on sufficient and low P (+P and -P, respectively). Ten-day-old seedlings were transferred to a fresh medium containing 625 µM P (+P) or 5 µM P (-P) with 150 µM $FeCl_3$ and analyzed after 6 days. White dots indicate the primary root length at the moment seedlings were transferred to treatment media. Data are presented as boxplots with each dot representing the datapoint of one biological replicate. For the boxplots, central horizontal lines, median; edges of boxes, 25th (bottom) and 75th (top) percentiles; whiskers, minimum and maximum. Different letters indicate significant differences (one-way ANOVA followed by post-hoc Tukey's test, $P < 0.05$; n = 10-12 (**C**), n = 12-13 (**D**) independent plants). Scale bars, 1 cm.

In order to determine whether *HYP1* overexpression can improve root growth under low-P conditions, transgenic lines expressing *35S::HYP1* in wild-type plants were generated. Ectopic expression of *HYP1* was able to completely prevent the inhibition of primary root elongation of plants grown in low-P medium (Figure 8A and B). Altogether, these results demonstrate that HYP1 is required to maintain primary root elongation when external P availability is low.

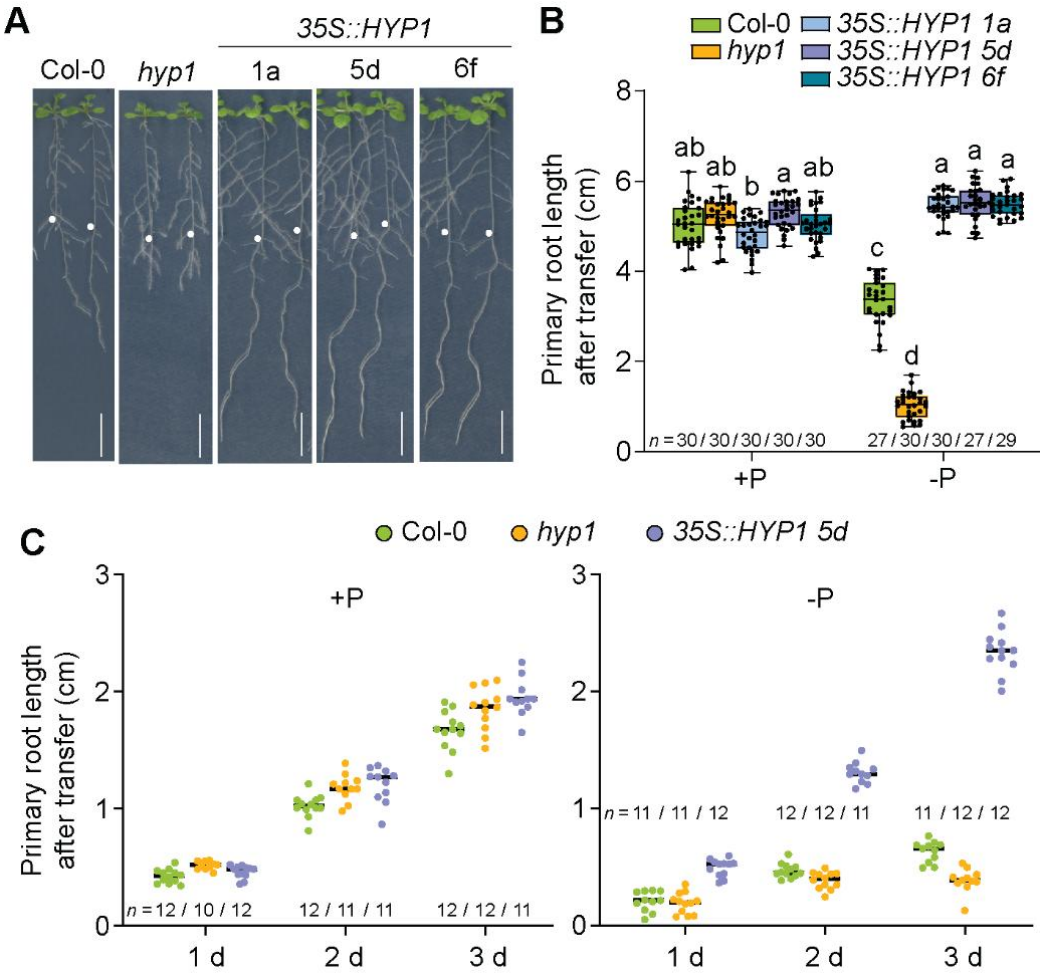

Figure 8. Overexpression of *HYP1* improves root growth under low P.

Appearance of plants (**A**) and primary root length (**B**) of wild-type (Col-0), *hyp1* mutant, and three independent transgenic lines expressing *35S::HYP1* in Col-0 grown for 6 days on sufficient or low P (+P or -P, respectively). Ten-day-old seedlings were transferred to a fresh medium containing 625 µM P (+P) or 5 µM P (-P) with 150 µM $FeCl_3$ and analyzed after 6 days. Only pictures of plants grown on low P are shown in **A**, where white dots indicate the position of the primary roots at the day of transfer. Data are presented as boxplots with each dot representing the datapoint of one biological replicate. For the boxplots, central horizontal lines, median; edges of boxes, 25th (bottom) and 75th (top) percentiles; whiskers, minimum and maximum. Letters indicate significant differences (one-way ANOVA followed by post-hoc Tukey's test, $P < 0.05$; n = 27-30 independent plants). (**C**) Time-dependent changes in primary root length after transfer to +P or -P (left or right panel, respectively). Ten-day-old seedlings were transferred to a fresh medium containing 625 µM P (+P) or 5 µM P (-P) with 150 µM $FeCl_3$ and analyzed after 1, 2, and 3 days. All individual data points are plotted and dark horizontal lines represent means (n = 10-12 independent plants). Scale bars, 1 cm.

5.3 Investigation of the involvement of other DOMON-containing proteins with root growth under low P

In *A. thaliana*, 11 genes encode for DOMON-containing proteins (Preger et al., 2009). From these, 10 are predicted to be CYBDOMs while one, *AUXIN-INDUCED IN ROOT CULTURES 12* (*AIR12*), encodes for a protein constituted by a single DOMON associated to a glycosylphosphatidylinositol (GPI) membrane anchor (Figure 9). *HYP1* was the only member

of the DOMON family that was differentially regulated in response to P deficiency (Figure 10A and B). Nonetheless, the primary root length of T-DNA insertion mutants available for 9 DOMON-expressing genes was assessed. Besides *hyp1*, only T-DNA insertion lines for At3g07390 (*AIR12*) and especially At3g25290 showed significantly shorter primary root length compared to wild-type, while most lines showed no or only small differences compared to wild-type plants (Figure 10C and D).

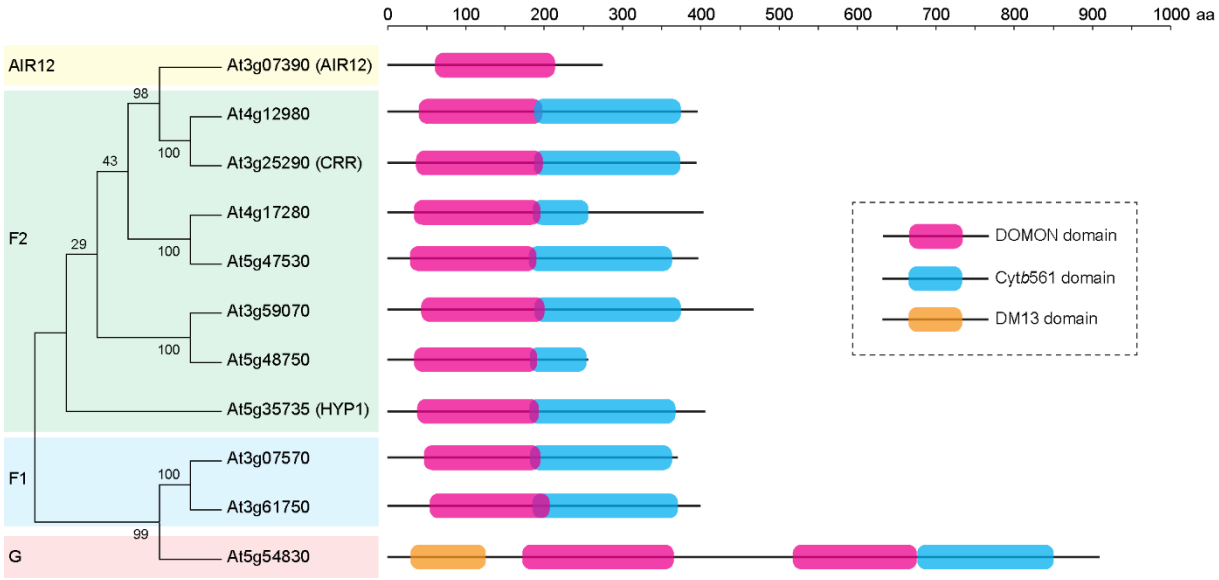

Figure 9. Phylogenetic and protein structure analysis of DOMON-containing sequences found in *A. thaliana*.

Amino acid sequences of DOMON-containing proteins were aligned with MAFFT 7 (Katoh and Standley, 2013) and a phylogenetic tree was constructed with MEGA 11 (Tamura et al., 2021) using the neighbor-joining (NJ) method with default parameter settings. Each node is represented by a number that indicates the bootstrap value for 1000 replicates. Sequences are clustered into AIR12, F1, F2, and G groups according to a previous phylogenetic classification (Preger et al., 2009).

Independently of the present study, Clúa et al. (2024) have recently reported the characterization of At3g25290, which has been named *CYBDOM ROOT REDUCTION* (*CRR*). Because the T-DNA insertion mutant line for *CRR* also displayed significantly shorter primary root length compared to wild-type, a double *hyp1 crr* mutant was generated. The simultaneous disruption of *HYP1* and *CRR* further exacerbated the primary root inhibition under low P (Figure 11A and B), suggesting that these two CYBDOM proteins may act in an additive way to sustain root growth under low-P conditions.

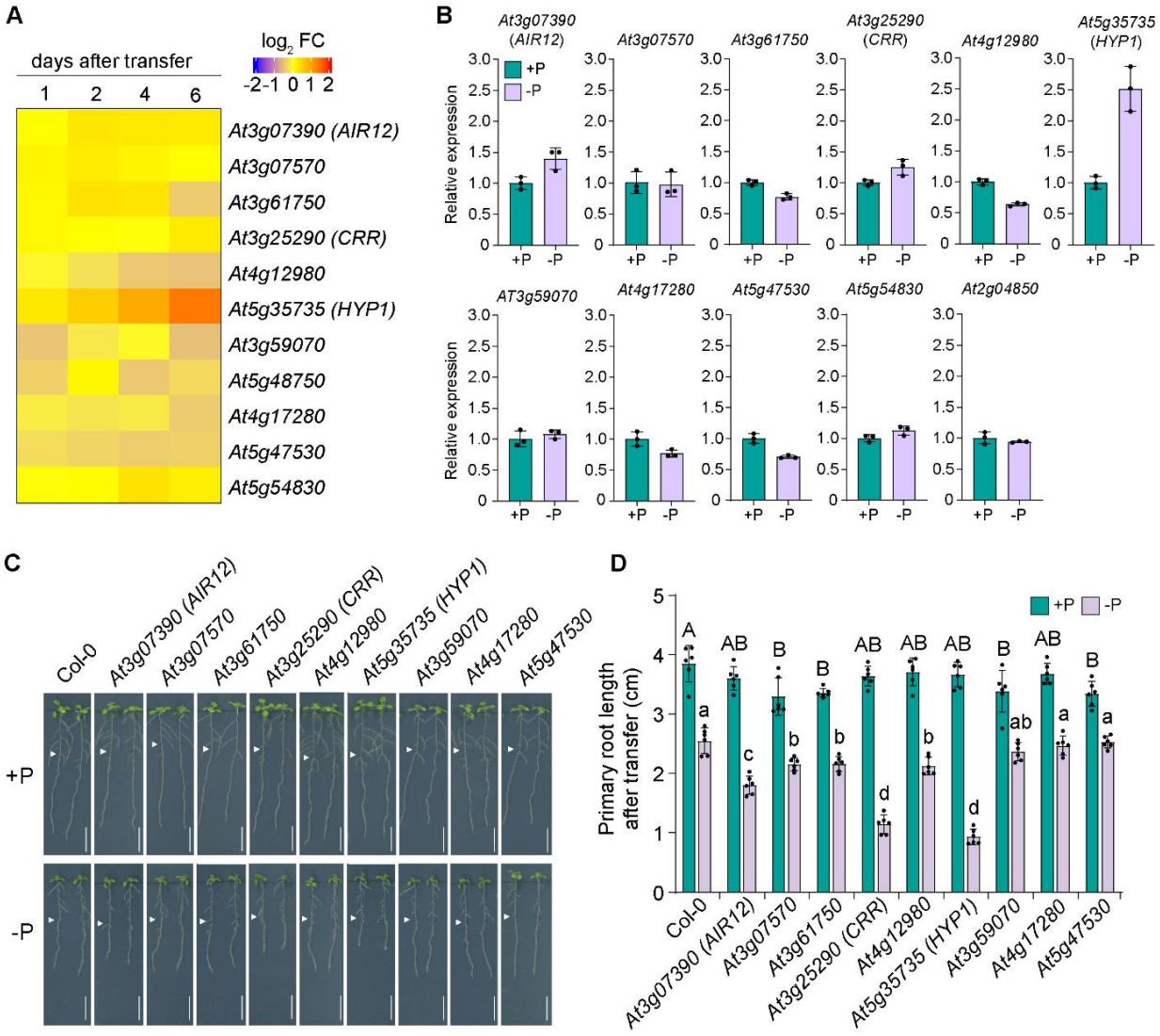

Figure 10. Gene expression analysis and phenotypes of mutants of the DOMON family.

(**A**) Heatmap showing the differential expression ($|\log_2 FC| \geq 1$ -P *versus* +P, FDR < 0.05) of genes encoding DOMON-containing proteins in *A. thaliana* during a time course of P treatments according to microarray analysis (*n* = 3 independent biological replicates per condition). (**B**) qPCR validation of the expression of the indicated genes of the DOMON family in response to P deficiency. Expression levels were normalized to *UBQ2*. Seven-day-old seedlings were transferred to a fresh medium containing 625 µM P (+P) or 5 µM P (-P) with 150 µM $FeCl_3$ and analyzed after 6 days. Values represent means ± s.d. (*n* = 3 replicates containing 12 roots each). Visual appearance (**C**) and primary root length (**D**) of available T-DNA insertion mutant plants for CYBDOM genes. Seven-day-old seedlings were transferred to a fresh medium containing 625 µM P (+P) or 5 µM P (-P) with 150 µM $FeCl_3$ and analyzed after 6 d. White arrows indicate the position of the primary roots at the day of transfer. Values represent means ± s.d. (*n* = 6 independent plants). All individual data points are plotted. Different letters indicate significant differences among +P or -P plants (one-way ANOVA followed by post-hoc Tukey's test, *P* < 0.05, *n* = 6 independent plants). Scale bars, 1 cm.

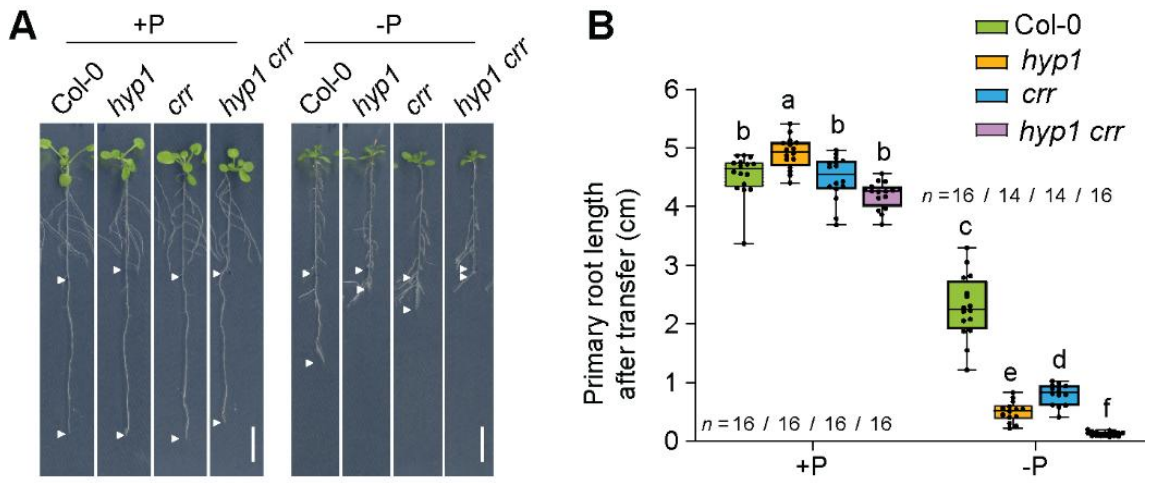

Figure 11. Phenotypic characterization of a *hyp1 crr* double mutant.

Visual appearance of plants (**A**) and primary root length (**B**) of wild-type (Col-0), *hyp1*, *crr* and *hyp1 crr* plants. Ten-day-old seedlings were transferred to a fresh medium containing 625 µM P (+P) or 5 µM P (-P) with 150 µM $FeCl_3$ and analyzed after 6 days. Upper white arrows indicate the position of the primary roots at the day of transfer, while the bottom arrows indicate the position of the primary root after 6 days of transfer. Data are presented as boxplots with each dot representing the datapoint of one biological replicate. For the boxplots, central horizontal lines, median; edges of boxes, 25th (bottom) and 75th (top) percentiles; whiskers, minimum and maximum. Different letters indicate significant differences (one-way ANOVA followed by post-hoc Tukey's test, $P < 0.05$; n = 14-16 independent plants). Scale bars, 1 cm.

5.4 Role of HYP1 in meristem integrity maintenance and cell elongation under low P

HYP1 expression is gradually induced in roots in response to P deficiency (Figure 10A). By tracking primary root length in a time-course experiment, it was possible to determine that *35S::HYP1* plants maintained higher primary root length specifically at low-P conditions, whereas significant differences of primary root growth were observed between wild-type and *hyp1* mutant plants at the third day after transfer to this treatment (Figure 12A). A closer inspection of primary root tips revealed that primary root meristem size and meristem cell number were significantly decreased in *hyp1* plants 3 days after transfer to low P (Figure 12B and C). A significant decrease in mature cell length was even observed after 2 days (Figure 12D). Probably as a result of the smaller meristems and shorter cells, and potentially of an accelerated cell differentiation, root hairs were detected much closer to the primary root apex of *hyp1* than in wild-type plants under low P (Figure 12A). Within the assessed 3 days, exposure of roots to low-P medium did not significantly decrease meristem size, cell number and mature cell length of *35S::HYP1* plants (Figure 12).

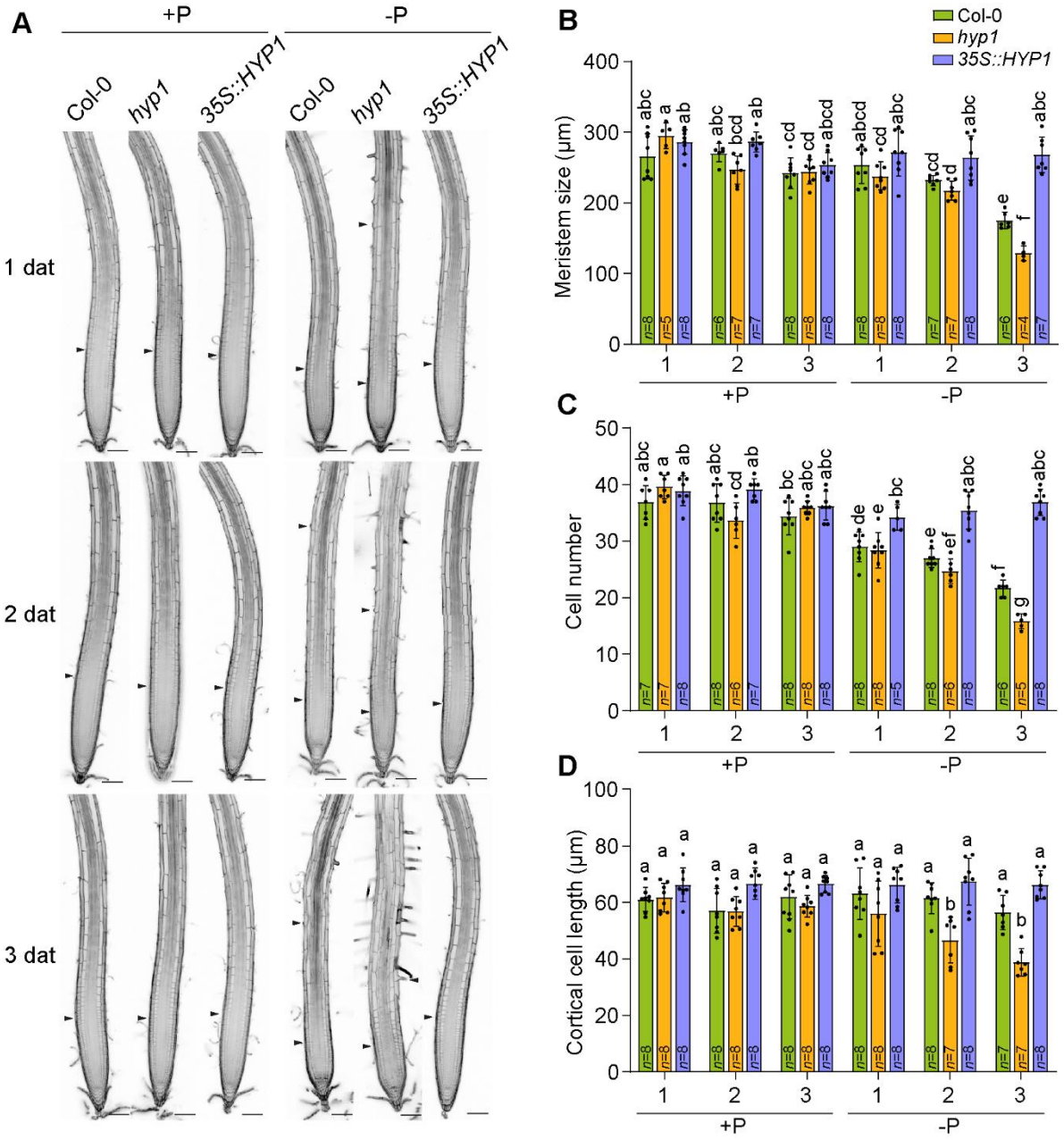

Figure 12. HYP1 prevents inhibition of cell elongation and loss of meristematic integrity under low-P conditions.

(**A**) Confocal images of propidium iodide-stained root tips of wild-type (Col-0), *hyp1* mutant plants, and one independent transgenic line expressing *35S::HYP1* in Col-0. Ten-day-old seedlings were transferred to a fresh medium containing 625 µM P (+P) or 5 µM P (-P) with 150 µM $FeCl_3$ and evaluated 1, 2, and 3 days after transferring plants to the indicated conditions. Arrowheads indicate the boundary between meristem and transition zone. Quantification of meristem cell length (**B**), meristem cell number (**C**), and mature cortical cell length (**D**). Values represent means ± s.d. (n = 4-8 independent plants). All individual data points are plotted. The letters indicate statistical significance (one-way ANOVA followed by post-hoc Tukey's test, $P < 0.05$). Scale bars, 100 µm.

To assess stem cell niche integrity, the localization of *WUSCHEL-RELATED HOMEOBOX 5* (*WOX5*) in the root apical meristem was checked with a transcriptional reporter. Under low-P conditions, *proWOX5::GFP*-derived fluorescence was not anymore confined to

quiescent center cells but detected in several meristematic cells (Figure 13A), indicating disintegration of the stem cell niche. Furthermore, analysis of mitotic activity with the *proCYCB1;1::GUS* reporter line revealed that loss of HYP1 activity decreased the number of cells undergoing division in the root apical meristem in response to low P (Figure 13B). Taken together, these results showed that the hypersensitive primary root phenotype of *hyp1* plants under low P is due to loss of root apical meristem integrity and inhibition of cell elongation in the elongation zone.

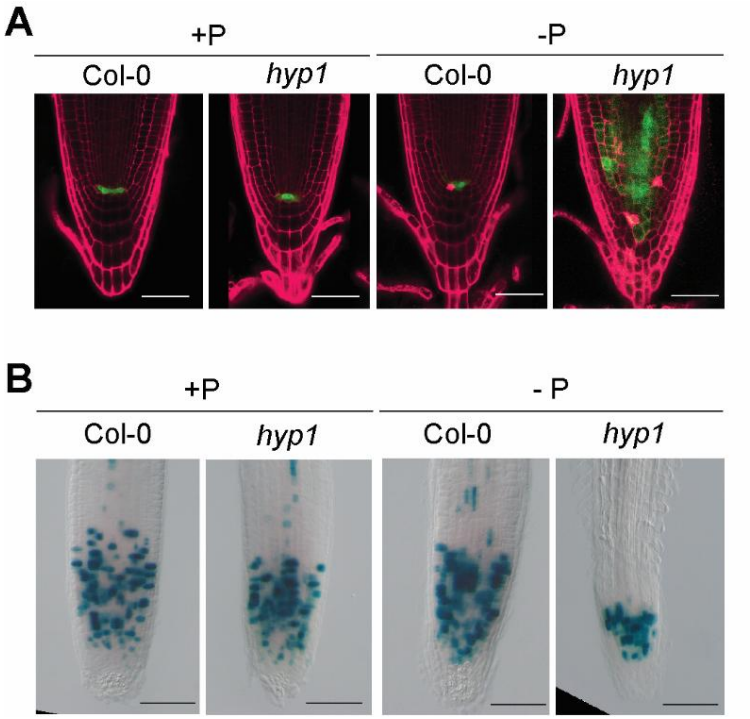

Figure 13. Disruption of *HYP1* decreases the number of cells undergoing division in the root apical meristem under low P.

Expression of the quiescent center marker *proWOX5::GFP* (**A**) and of the mitotic activity reporter *proCYCB1;1::GUS* (**B**) in root tips of wild-type (Col-0) and *hyp1* plants. Seven-day-old seedlings were transferred to a fresh medium containing 625 µM P (+P) or 5 µM P (-P) with 150 µM $FeCl_3$ and analyzed 3 days after transfer. Scale bars, 50 µm.

5.5 Tissue-specific and subcellular localization of HYP1

To get insights into the tissue-specific expression of *HYP1*, *proHYP1::GUS* lines were generated. In young seedlings, *proHYP1*-driven GUS activity was mainly detected in the two cotyledons and throughout most parts of primary and lateral roots, including the apical zone (Figure 14A). In line with the transcriptome and qPCR results (Figure 10A and B), the intensity of GUS staining increased when plants were cultivated on low P, reinforcing that *HYP1* is induced in response to P deficiency. An in-depth analysis of root tips revealed that *HYP1* promoter activity was prominent in root cap cells and, under low P, strongly increased in cells surrounding the stem cell niche (Figure 14B).

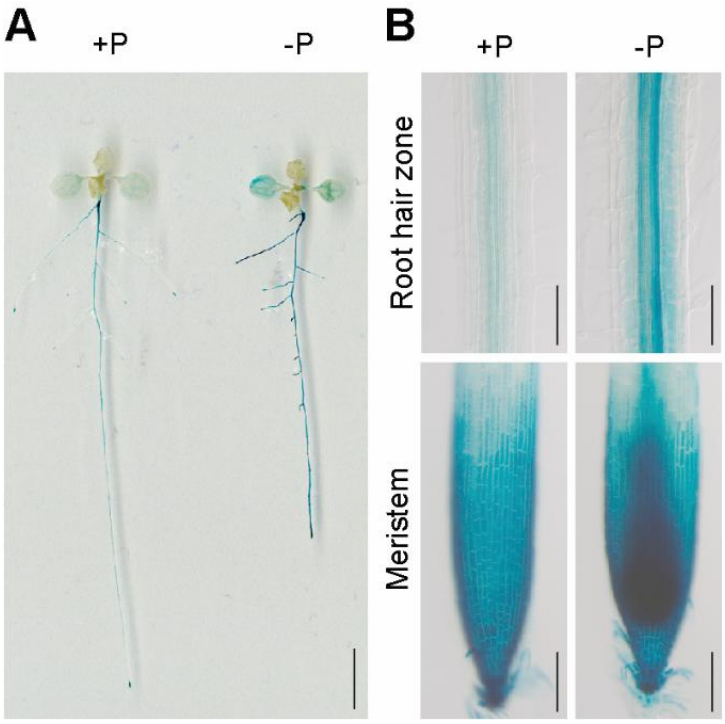

Figure 14. Localization of *HYP1* promoter activity in different plant tissues and in response to P supply.

P-dependent changes in HYP1 promoter activity in whole seedlings (**A**) and in the indicated zones of the primary root (**B**). Seven-day-old seedlings were transferred to a fresh medium containing 625 µM P (+P) or 5 µM P (-P) with 150 µM $FeCl_3$ and analyzed 3 days after transfer. Scale bars, 1 cm (**A**), 50 µm (**B**).

Next, to assess in more detail where the HYP1 protein is located, a translational fusion line carrying GFP in the C-terminal part of HYP1 and driven by the *HYP1* promoter was generated. Under sufficient P, HYP1:GFP was detected in the vasculature along the mature root hair zone, whereas in the root apex it was confined to the root cap and mature columella cells (Figure 15A). Low P availability increased the abundance of HYP1:GFP and, in the root apical meristem, induced its appearance in several cell files above the stem cell niche, as well as in vascular tissues (endodermis) of the root hair zone, while having no effect on HYP1:GFP-derived fluorescence in root cap cells (Figure 15B).

To obtain information about the subcellular localization of HYP1 and other DOMON-containing proteins, an *in silico* analysis was performed. By searching the gene ID in the browser ePlant (https://bar.utoronto.ca/eplant/) and selecting the Cell eFP viewer, the highest score predicted for HYP1 was plasma membrane (Figure 16A). In comparison, the predicted subcellular localization of other DOMON-containing proteins indicated that AIR12, At3g07570, CRR, At4g12980, and At4g17280 are also highly likely to localize in the plasma membrane, whereas At3g61750, At3g59070, At5g48750, At5g47530, and At5g54830 are predicted to localize either in the endoplasmic reticulum, Golgi, or outside of the cytoplasm (Figure 16B).

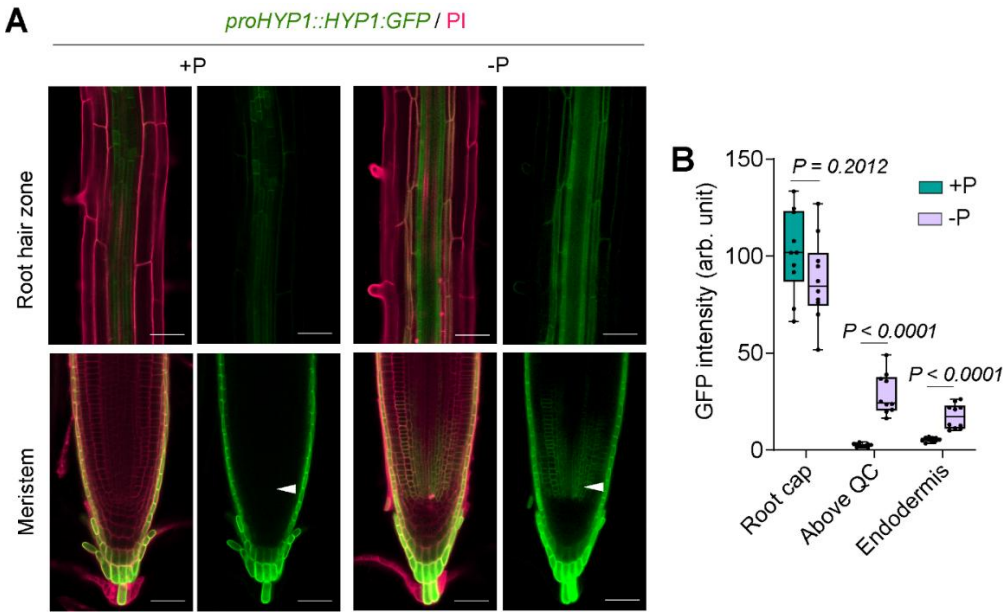

Figure 15. Cell type-specific localization of HYP1 in different root zones.

(**A**) HYP1:GFP localization in the meristem and root hair zone of roots counterstained with the cell wall stain propidium iodide (PI) 3 days after transfer to indicated treatments. Seven-day-old seedlings were transferred to a fresh medium containing 625 µM P (+P) or 5 µM P (-P) with 150 µM $FeCl_3$. The arrowheads indicate the increased abundance of HYP1:GFP in the cells above the stem cell niche. (**B**) Quantification of GFP fluorescence in different meristem regions and in the vascular tissues of the root hair zone 3 days after transfer to indicated treatments. Data are presented as boxplots with each dot representing the datapoint of one biological replicate. For the boxplots, central horizontal lines, median; edges of boxes, 25th (bottom) and 75th (top) percentiles; whiskers, minimum and maximum. The letters indicate significant differences (one-way ANOVA followed by post-hoc Tukey's test, $P < 0.05$; $n = 10$ independent plants). Scale bars, 20 µm.

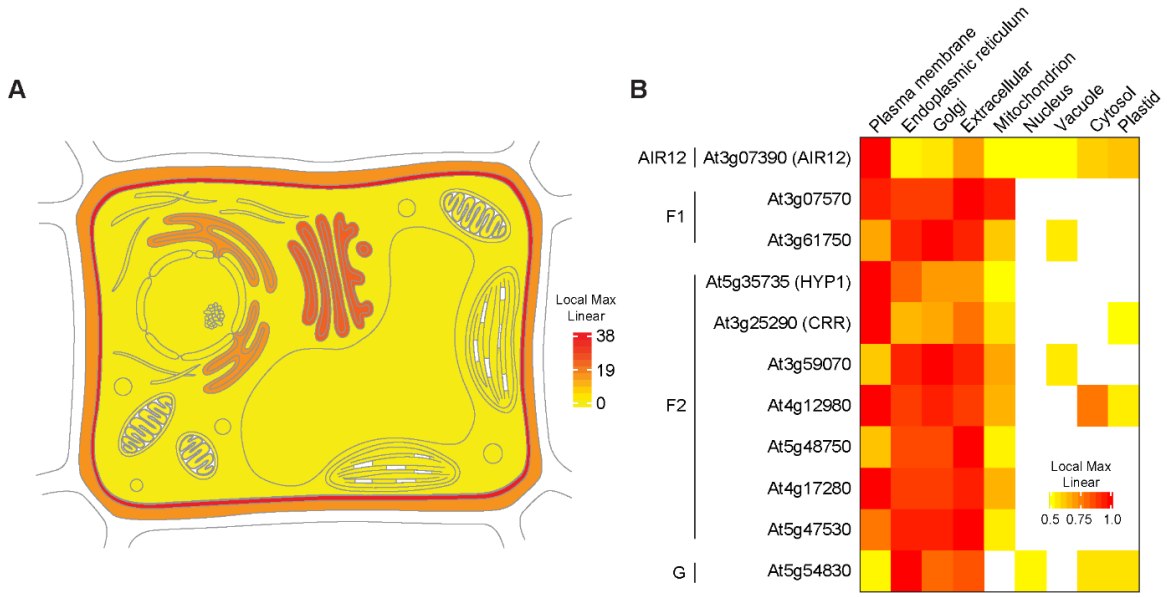

Figure 16. Prediction of subcellular localization of DOMON-containing proteins in Arabidopsis.

(**A-B**) Predicted subcellular localization of HYP1 (**A**) and other members of the DOMON family (**B**). Predictions were retrieved from the Cell eFP viewer in the ePlant browser (www.bar.utoronto.ca/eplant/). In A, localization scores: plasma membrane = 38, Golgi complex = 24, extracellular = 16, endoplasmic reticulum = 16, mitochondrion = 2. Blank spaces indicate no available data. Proteins are grouped according to phylogenetic classification (Preger et al., 2009).

To experimentally validate the subcellular localization of HYP1 in *planta*, GFP-derived fluorescence of the translational fusion reporter HYP1:GFP was visualized with a confocal microscope. In plasmolyzed root cells, strong HYP1:GFP-derived fluorescence was detected in the plasma membrane and in Hechtian strands (Figure 17A). In non-plasmolyzed root cap cells HYP1:GFP signals did not coincide with the fluorescence derived from the cell wall stain propidium iodide (PI) (Figure 17B and C). Finally, the styryl dye FM4-64, which intercalates into membranes, was used. As shown in Figure 17D and E, HYP1:GFP-derived fluorescence colocalized with this dye. Altogether, these results demonstrated that HYP1 is a plasma membrane protein present in distinct domains of the root, including the root apical meristem.

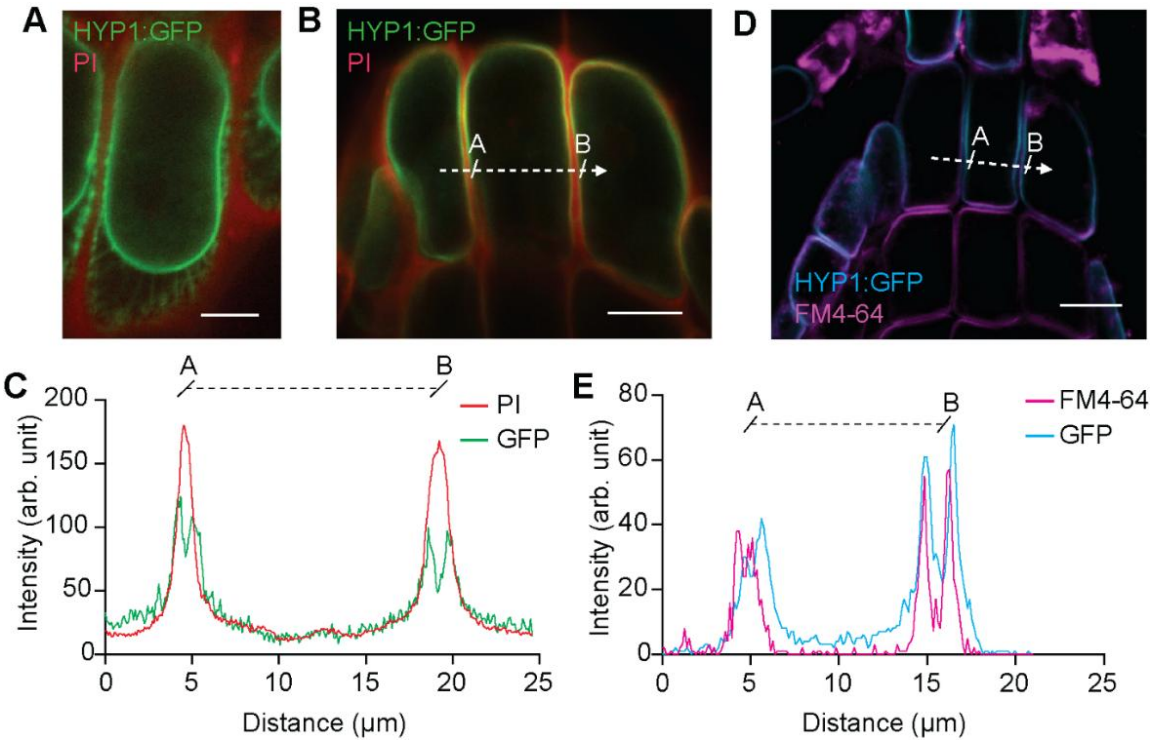

Figure 17. HYP1 localizes at the plasma membrane.

(**A**) Localization of HYP1:GFP in plasmolyzed cells counterstained with propidium iodide (PI). Ten-day-old seedlings were transferred to a fresh medium containing 5 µM P (-P) with 150 µM $FeCl_3$ and HYP1:GFP localization was assessed after 3 days. Quantification of fluorescence intensity of GFP and the cell-wall propidium iodide (PI) (**B** and **C**) or the membrane stain FM4-64 (**D** and **E**) in the sections marked with the dashed lines. Scale bars, 5 µm (**A**) 10 µm (**B** and **D**).

5.6 Tissue-specific expression analysis of genes from the DOMON family

In order to compare the tissue-specific expression patterns of *HYP1* with other members of the same family, GUS reporter lines for other 10 CYBDOM genes and for the DOMON-containing *AIR12* were generated. In young seedlings grown under adequate nutrient supply, all promoters were active in roots with varying degree of intensity while little to no

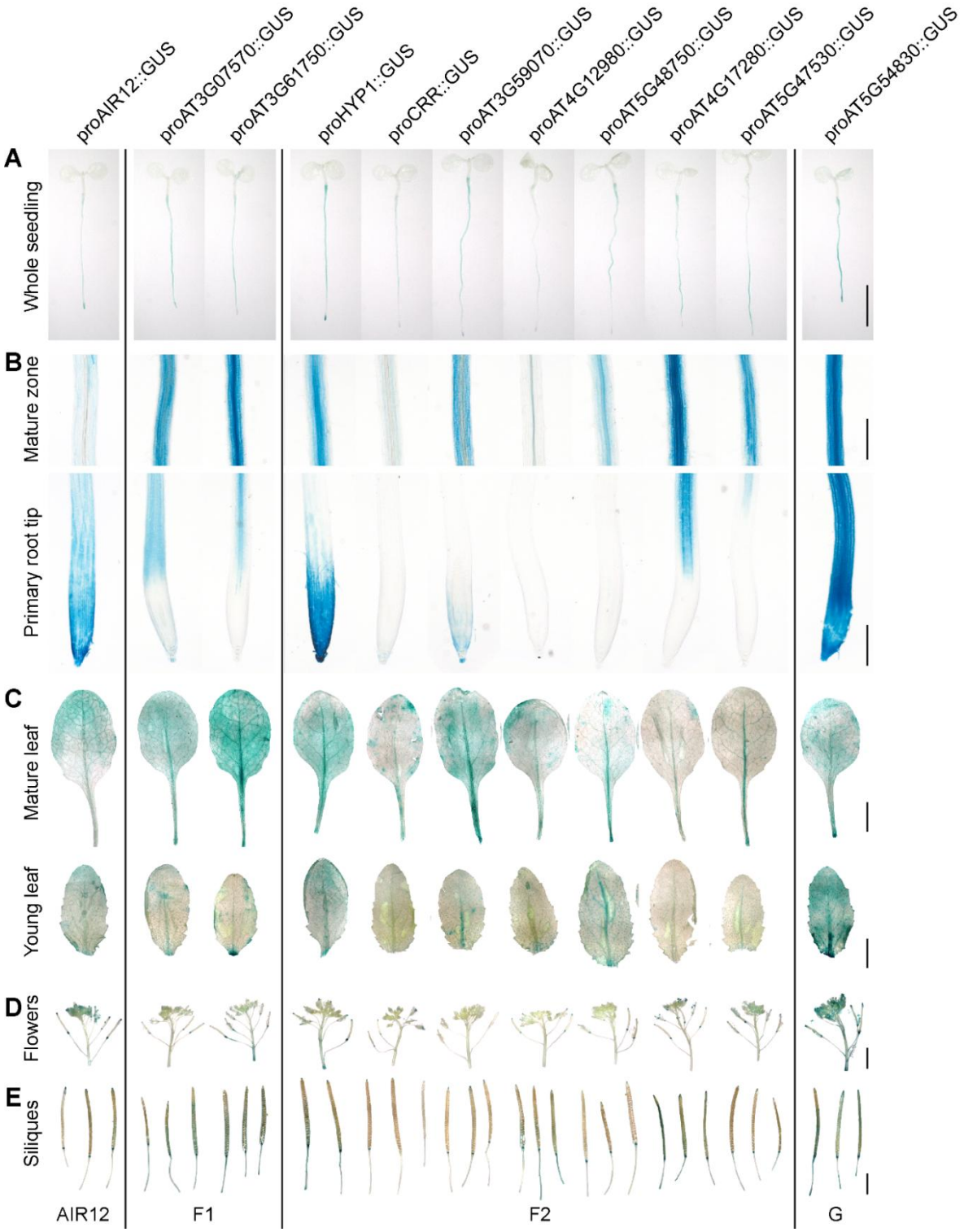

Figure 18. Tissue-specific expression analysis of genes from the DOMON family.

Promoter activity in whole seedlings (**A**), in the indicated zones of the primary root (**B**), in the indicated leaves (**C**), in inflorescence (**D**), and in siliques (**E**). (**A, B**) The indicated promoter-GUS lines were grown on ½ MS solid media for 6 days. (**C, D, E**) Six-day-old seedlings previously grown on ½ MS solid medium were transferred to substrate and kept under light regime of 22 °C/18 °C, 16/8 h light/dark, and 120 µmol photons m^{-2} s^{-1}. Mature and young leaves were harvested from 28-day-old plants; inflorescences and siliques were harvested from 30-day-old plants. Transgenic lines are grouped according to phylogenetic classification (Preger et al., 2009). Scale bars, 1 cm (**A, C, D, E**), 100 µm (**B**).

visible GUS activity was detected in the cotyledons (Figure 18A). Only the promoters of *AIR12*, *At3g59070*, and *At5g54830* were active in root cap cells, similar to *HYP1* (Figure 18B). *proAt5g54830*-driven GUS activity was detected throughout the whole root, while the promoter activity of *At3g07570*, *At3g61750*, and *At4g17280* was absent in the root apical meristem but clearly detectable in the elongation zone (Figure 18B). In the mature root, GUS activity was detected mainly in the cells surrounding the vascular tissues, except for *AIR12* and *CRR*, whose promoter activity resulted in diffuse GUS signals across the outermost root cell layers (Figure 18B). Examining the GUS activity in leaves revealed that all genes were expressed in mature and young leaves, with varying intensities (Figure 18C). For the promoters of *At3g61750*, *HYP1*, *At3g59070*, *At5g48750* and *At5g47530*, the GUS activity was more pronounced in the main or secondary vasculature of mature leaves, whereas the promoters of *At3g07570*, *CRR*, *At4g12980*, *At4g17280*, *At5g54830*, and the DOMON-only *AIR12*, drove relatively diffuse GUS expression across the leaf blade (Figure 18C). By inspecting the inflorescences, it was possible to observe GUS activity for all promoters, except for *At4g12980*, with *AIR12* and *At5g54830* showing the strongest promoter activities in these organs (Figure 18D). In siliques, strong GUS activity was detected for the promoters of *AIR12,* of genes from groups F1 and G, and *HYP1* and *At4g17280* from group F2 (Figure 18E). Taken together, these results indicate that many members of the CYBDOM family do not share the same tissue-specific expression domain and, therefore, might play partially redundant functions in different plant tissues.

5.7 Electrophysiological studies in *Xenopus laevis* oocytes

Prior to this study, cytochrome *b*561-containing proteins have been shown to mediate electron transport between a cytosolic electron donor and acceptors located on the non-cytoplasmic side (Asard et al., 2013; Picco et al., 2015). To explore the transport properties of HYP1, its corresponding cDNA fragment was cloned in an oocyte expression vector, and a series of functional assays in *Xenopus laevis* oocytes was performed in collaboration with the research group of Prof. Dr. Armando Carpaneto (NRC/University of Genoa, Italy). By employing two-electrode voltage clamp, our collaborators detected inward currents in oocytes injected with *HYP1* cRNA when ferricyanide was provided as an electron acceptor in the bathing solution (Figure 19A and B), and the currents strongly increased after raising the cytosolic concentrations of ascorbate in the oocytes (Figure 19C). The results could be fitted by a Michaelis-Menten equation revealing an apparent affinity constant of 4 mM (Annex Figure 2A), which is in line with the approx. 20 mM ascorbate detected in the cytosol of plant cells (Zechmann, 2018).

Similar to other cytochrome *b*561-containing proteins characterized up to date, it was also found that ascorbate is a specific cytosolic electron donor for HYP1 whereas reduced glutathione was not able to boost HYP1-mediated currents (Figure 19D and Annex Figure 2B). Current amplitudes were also stimulated by increasing the concentration of the electron acceptor in the bathing solution again following patterns resembling Michaelis-Menten kinetics (Figure 19E and Annex Figure 2C and D). To rule out the possibility that the detected currents were associated with ion fluxes, our collaborators manipulated the pH and ionic composition of the bathing solutions. Replacing the standard bathing solution with a solution containing only the membrane-impermeable ions 1,3-bis[tris(hydroxymethyl)methylamino]propane (BTP) and 2-(N-morpholino)ethanesulfonic acid (MES) or raising the external pH to 7.5, did not

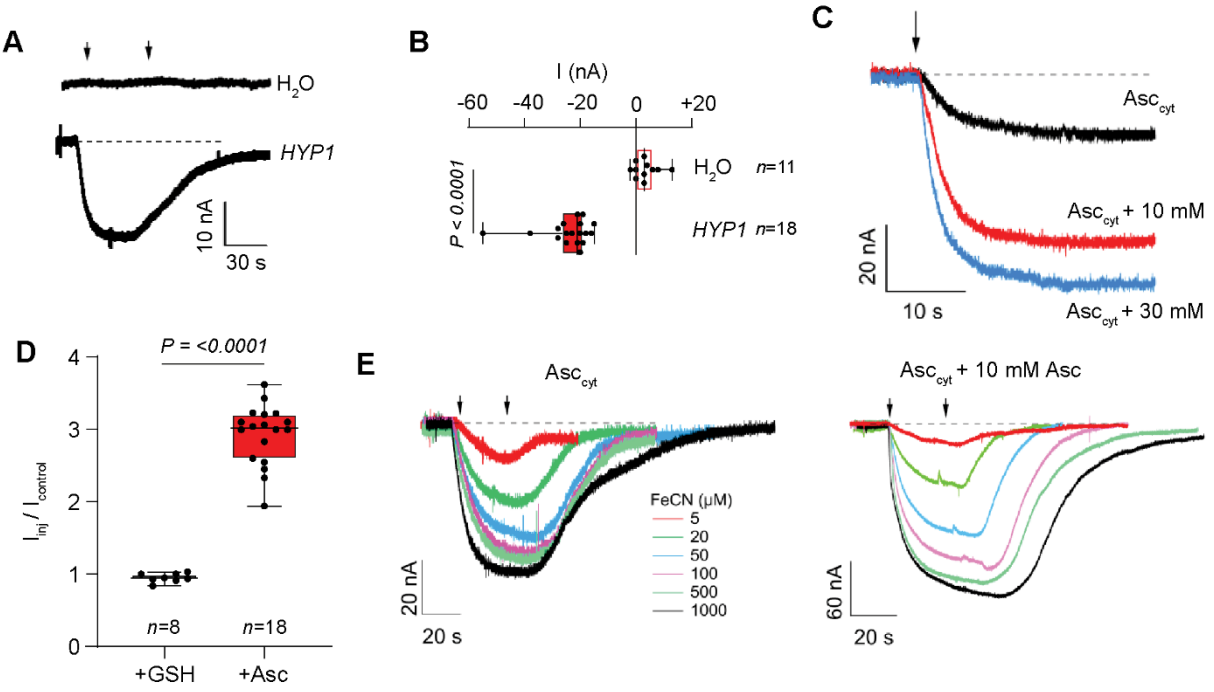

Figure 19. HYP1 mediates trans-PM electron transport in *X. laevis* oocytes and its current is dependent on cytosolic ascorbate and the external concentrations of an electron acceptor.

Trans-PM current recordings (**A**) and calculated mean currents (**B**) *X. laevis* oocytes injected with water (H_2O) or *HYP1* cRNA and exposed to 1 mM of the water-soluble electron acceptor $[Fe(CN)_6]^{3-}$ (ferricyanide) in standard bath solution (pH 5.5) at a holding potential of -20 mV. (**C**) Membrane currents elicited by 1 mM $[Fe(CN)_6]^{3-}$ (ferricyanide) in oocytes injected with *HYP1* cRNA before ascorbate injection (Asc_{cyt}, black trace), after a first ascorbate injection corresponding to Asc_{cyt} + 10 mM (red trace) and after a second ascorbate injection corresponding to Asc_{cyt} + 30 mM (blue trace). Holding potential at -20 mV. (**D**) Ratio of currents before ($I_{control}$) and after oocyte injection (I_{inj}), respectively, with glutathione (+GSH) or ascorbate (+Asc), calculated from results obtained in experiments as shown in Annex Figure 2B. (**E**) Membrane currents elicited by increasing external $[Fe(CN)_6]^{3-}$ (ferricyanide, indicated by the arrows) concentrations in oocytes injected with *HYP1* cRNA before and after ascorbate injection (+ 10 mM Asc). Holding potential set at -20 mV. In **A** and **E**, the left and right arrows indicate the addition and removal of ferricyanide, respectively. Data are presented as boxplots with each dot representing the datapoint of one biological replicate. For the boxplots in **B** and **D**, central horizontal lines, median; edges of boxes, 25th (bottom) and 75th (top) percentiles; whiskers, minimum and maximum. (*n* = independently oocytes, as indicated). *P* value according to two-tailed Student's *t*-test. Experiments were performed and data obtained in collaboration with the research group of Prof. Dr. Armando Carpaneto (NRC/University of Genoa, Italy).

significantly alter the current amplitude detected in *HYP1*-injected oocytes (Annex Figure 2E and F). Thus, these results demonstrated that HYP1 mediates trans-plasma membrane electron transport, an activity that is influenced by the concentration of cytosolic ascorbate and extra-cytoplasmic electron acceptors.

5.8 Analysis of the structural features of HYP1 *in silico* and *in vivo*

While the crystal structure of two cytochrome *b*561 proteins – CYBASC1 (AtCyt*b*561) of *A. thaliana* and the human duodenal cytochrome *b* (Dcyt*b*) – have been determined (Lu et al., 2014; Ganasen et al., 2018), no structural information was available for CYBDOM proteins. Thus, first the topology of HYP1 protein was investigated using the DeepTMHMM tool (https://dtu.biolib.com/DeepTMHMM). The analysis identified five hydrophobic regions of approximately 20 to 30 amino acid length and likely corresponding to transmembrane domains (Figure 20C). A further search of conserved domains with CD Search (Figure 20D), predicted that HYP1 harbors a signal peptide in the N terminus (from amino acids 1 to 24), and two protein domains as follows: a dopamine β-monooxygenase N-terminal (DOMON) domain (amino acids 40 to 191, cd09629) and a cytochrome *b*561 (Cyt*b*561) domain (amino acids 188 to 361, cd08760).

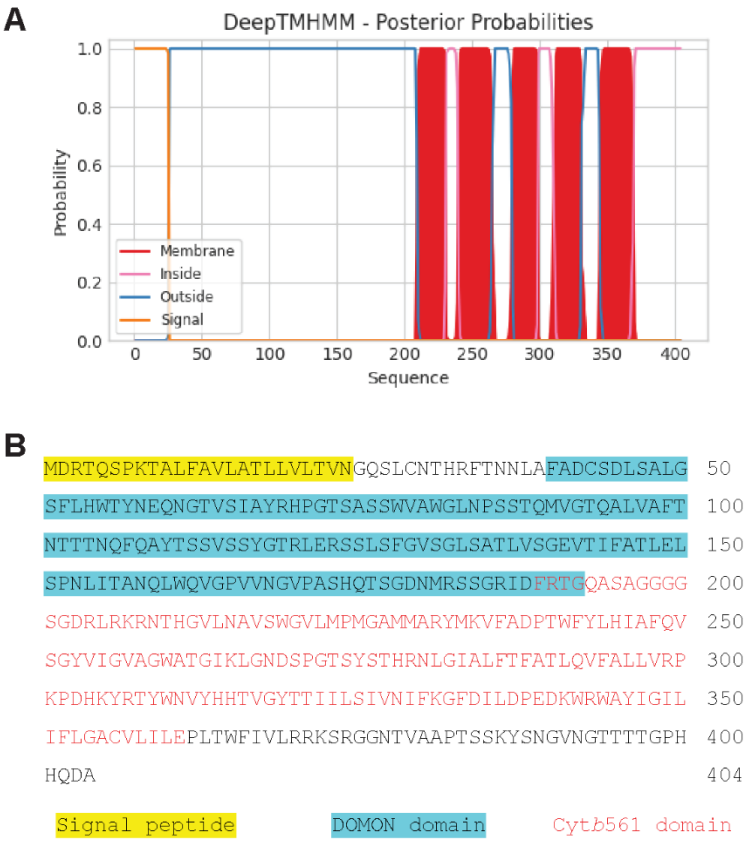

Figure 20. *In silico* analysis of HYP1.

(**A**) Transmembrane prediction of HYP1 obtained using DeepTMHMM (https://dtu.biolib.com/DeepTMHMM). HYP1 contains five highly probable transmembrane regions, from amino acids 210-230, 240-264, 280-298, 310-330, and 345-369. (**B**) Amino acid sequence of HYP1 depicting the signal peptide and the conserved domains predicted using SignalP (https://services.healthtech.dtu.dk/services/SignalP-5.0/) and CD search (https://www.ncbi.nlm.nih.gov/Structure/cdd/wrpsb.cgi), respectively. The signal peptide is predicted to encompass the amino acids 1-24. Two conserved domains were found with high confidence located at the positions 40-191 and 188-361, which correspond to the dopamine β-monooxygenase N-terminal (DOMON) domain (accession *cd09629*) and the cytochrome *b*561 (Cyt*b*561) domain (accession *cd08760*), respectively.

To gain structural insights, HYP1 structure was predicted with AlphaFold (Jumper et al., 2021) in collaboration with Dr. Georg Künze (Leipzig University, Germany). The resulting predicted model revealed that the cytochrome *b*561 domain is formed by five α-helical transmembrane segments while the DOMON resembles a sandwiched β-sheet structure (Figure 21A). Moreover, the presence of a secretory signal peptide in the N-terminal part and HYP1 localization in the plasma membrane suggested that HYP1's DOMON is apoplastic (Figure 21A). Next, the putative binding site for ascorbate was modeled on the cytosol-facing side using Rosetta ligand docking calculations. For guiding the modeling calculations, the structure of ascorbate-bound cytochrome *b*561 was used (PDB ID: 4O79). The predicted binding model for ascorbate indicated that hydrogen bond interactions with the side chains of residues arginine 307 (R307) and asparagine 311 (N311) and possibly with the backbone of proline 302 (P302) help to stabilize the binding of ascorbate to the heme propionate groups (Figure 21B). Furthermore, the structural model revealed that two conserved histidine pairs H245–H314 and H211–H278 represent putative coordination sites to two *b*-heme groups, one at the cytoplasmic side and another at the apical side of the cytochrome *b*561 domain, respectively (Figure 21B).

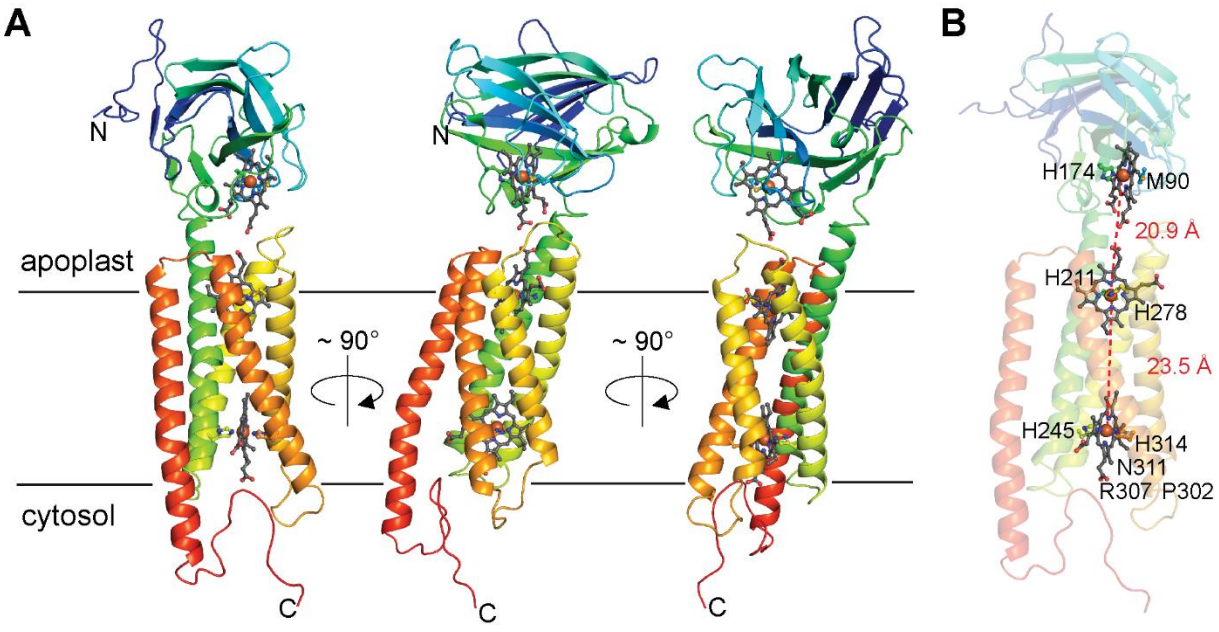

Figure 21. Structural model of HYP1 as predicted by AlphaFold.

Structural organization of the cytochrome *b*561 and DOMON domains of HYP1 (**A**) and residues critical for electron transfer (**B**) were predicted with AlphaFold (Jumper et al., 2021), in collaboration with Dr. Georg Künze (Leipzig University, Germany). Red spheres indicate the atom Fe at the center of a *b*-heme. Dashed lines in red depict the distances between two *b*-heme coordination sites.

According to the predicted model of HYP1, the Fe-to-Fe distance between the two *b*-heme groups is approx. 23.5 Ångstrom (Å) (Figure 21B), which is comparable to the distances reported for the crystal structures of the cytochrome *b*561 proteins CYBASC1 (AtCyt*b*561) and Dcyt*b* (Lu et al., 2014; Ganasen et al., 2018). It was possible to confirm the critical function of the H211–H278 pair for HYP1 function by replacing these positively charged, imidazole-containing histidine residues with non-polar leucine. The concomitant H211L and H278L substitutions completely abolished HYP1-mediated electron transport in oocytes without affecting its plasma membrane localization (Annex Figure 4 and Annex Figure 5A-D). To test the critical role of the two residues *in planta*, a mutated HYP1$^{H211L/H278L}$:GFP variant was generated and introduced into *hyp1*. As shown in Figure 22A and B, the mutated variant lost the ability to complement the short-root phenotype of *hyp1* in contrast to native HYP1:GFP. Importantly, HYP1$^{H211L/H278L}$:GFP was still localized at the plasma membrane (Figure 22C).

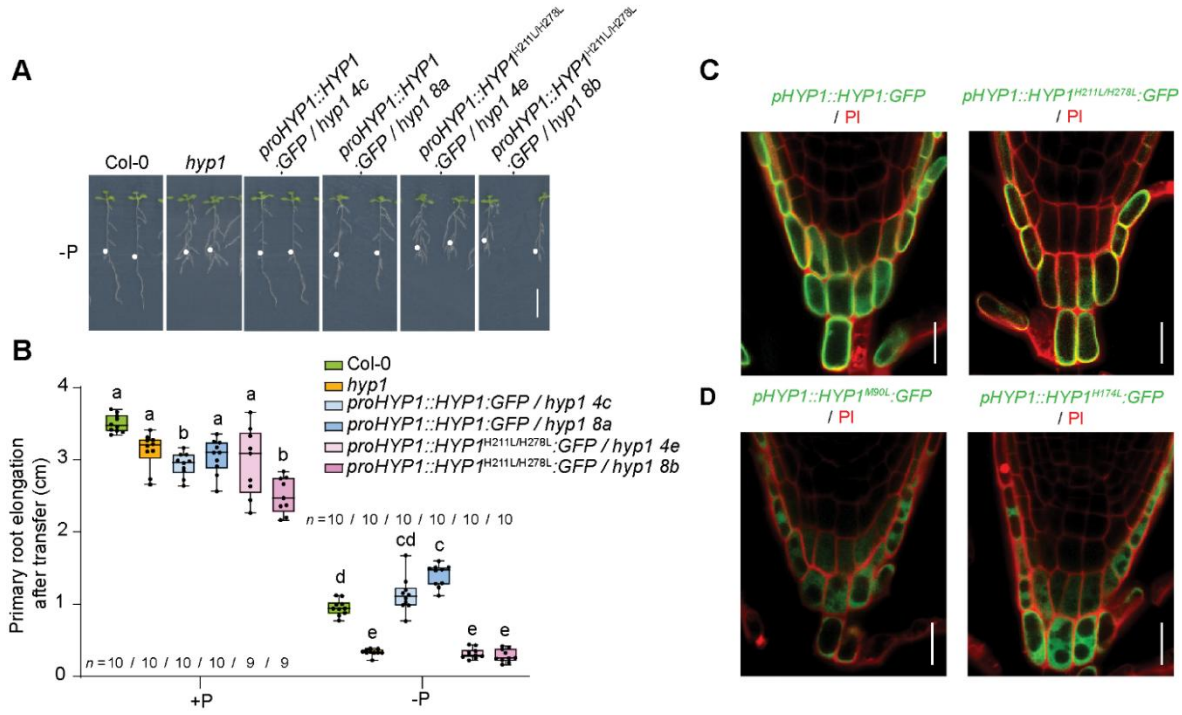

Figure 22. Apoplast-facing *b*-heme coordination site is critical for HYP1's biochemical function.

Appearance of plants (**A**) and primary root length (**B**) of wild-type (Col-0), *hyp1* mutant, and two independent transgenic lines of *hyp1* expressing HYP1:GFP or HYP1$^{H211L/H278L}$:GFP grown for 6 days on sufficient or low P (+P or -P, respectively). Ten-day-old seedlings were transferred to a fresh medium containing 625 µM P (+P) or 5 µM P (-P) with 150 µM $FeCl_3$ and analyzed after 6 days. White dots indicate the position of the primary roots at the day of transfer. Data are presented as boxplots with each dot representing the datapoint of one biological replicate. For the boxplots, central horizontal lines, median; edges of boxes, 25th (bottom) and 75th (top) percentiles; whiskers, minimum and maximum. The letters indicate significant differences (one-way ANOVA followed by post-hoc Tukey's test, $P < 0.05$; n = 9-10 independent plants). (**C** and **D**)**,** Localization of wild-type HYP1:GFP and one variant carrying mutations in amino acid residues putatively involved with *b*-heme coordination in the apical part of the cytochrome *b*561 domain (HYP1$^{H211L/H278L}$:GFP) (**C**), and variants carrying mutations in amino acid residues putatively involved with *b*-heme coordination in the DOMON domain (HYP1^{M90L}:GFP and HYP1^{H174L}:GFP) (**D**). The construct was expressed in the *hyp1* background. Localization was assessed in roots counterstained with the cell wall stain propidium iodide (PI) of plants grown under low P for 3 days. Scale bar, 1 cm (**A**), and 20 µm (**C** and **D**).

Previous studies suggested that DOMON domains can bind *b*-heme or sugars (Iyer et al., 2007; Preger et al., 2009). Taking cellobiose dehydrogenase (PDBs 4QI3B, 1PL3, 4QI7), which contains a heme-binding site in a DOMON-like structure, as template, the *de novo* structural model of HYP1 identified methionine 90 (M90) and histidine 174 (H174) as candidates for *b*-heme coordination. Other H residues in the DOMON domain, including the conserved histidine at position 54, are unlikely to participate in *b*-heme coordination as they are too distant from M90 or H174. According to the AlphaFold model, one edge of the *b*-heme putatively coordinated by the M90–H174 pair in the DOMON domain is solvent-accessible (Annex Figure 3B). The distance between two Fe centers of the apical heme of the cytochrome *b*561 domain and the heme in the DOMON is approx. 20.9 Å (Figure 21B). Unfortunately, M90L or H174L substitutions resulted in impaired plasma membrane localization of HYP1 both in oocytes (Annex Figure 5E and F) and plant cells (Figure 22D) and the complementation ability of these mutated variants could not be assessed.

As an alternative to investigate the involvement of the DOMON domain in maintenance of primary root growth under low P-conditions, it was attempted to complement *hyp1* mutant plants with AIR12 or with a chimeric construct containing the DOMON domain of HYP1 fused with the GPI anchor from AIR12. In both cases, the expression was driven by the *HYP1* promoter. Under P-sufficient conditions, all transgenic lines exhibited similar primary root growth compared to wild-type and *hyp1* plants (Figure 23A and B). However, when exposed to P-limiting conditions, plants expressing either construct had significantly shorter roots compared to wild-type plants and, except for one of the lines expressing *proHYP1::AIR12*, showed no significant differences compared to *hyp1* (Figure 23A and B). These results suggest that a DOMON domain alone is not sufficient to prevent the hypersensitive root inhibition of *hyp1* plants under low P.

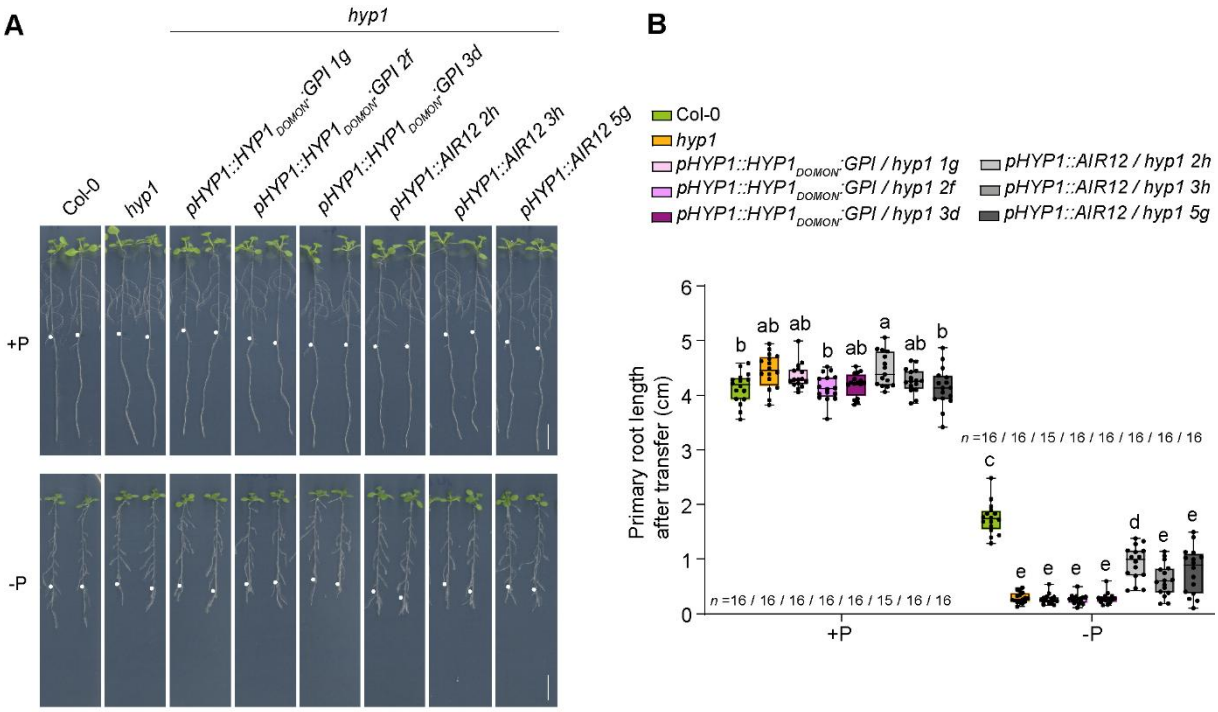

Figure 23. DOMON domains alone cannot rescue the short-root phenotype of the *hyp1* mutant under low P.

Appearance of plants (**A**) and primary root length (**B**) of wild-type (Col-0), *hyp1* mutant, and independent transgenic lines expressing the DOMON domain from *HYP1* fused with GPI anchor ($HYP1_{DOMON}$:GPI), or *AIR12* driven by the *HYP1* promoter in *hyp1* mutant background grown for 6 day on sufficient or low P (+P or -P, respectively). Ten-day-old seedlings were transferred to a fresh medium containing 625 µM P (+P) or 5 µM P (-P) with 150 µM $FeCl_3$ and analyzed after 6 days. White dots indicate the position of the primary roots at the day of transfer. Data are presented as boxplots with each dot representing the datapoint of one biological replicate. For the boxplots, central horizontal lines, median; edges of boxes, 25th (bottom) and 75th (top) percentiles; whiskers, minimum and maximum. The letters indicate significant differences (one-way ANOVA followed by post-hoc Tukey's test, $P < 0.05$; n = 16 independent plants). Scale bars, 1 cm.

5.9 Assessing the involvement of HYP1 in ferric reduction

Considering the electron transport activity of HYP1, it was then explored whether HYP1 is able to reduce ferric-chelates. In oocytes, HYP1-mediated currents were detected when different Fe(III) chelates were supplied in the bathing solution (Figure 24A and B, and Annex Figure 6A and B). In order to assess the putative role of HYP1 as a ferric reductase *in planta*, *HYP1:GFP* under the control of *FRO2* or CaMV *35S* promoters was introduced in the *fro2* mutant plant. Expression of either construct in *fro2* plants significantly increased the root ferric-chelate reductase activity by approximately 1.6 times, allowing these plants to reach up to 60% of the activity detected in wild-type plants (Figure 24C). Constitutive or Fe deficiency-induced *HYP1* expression was also able to alleviate the Fe deficiency symptoms of *fro2* plants by significantly increasing shoot chlorophyll concentration and shoot Fe contents (Figure 24D-F).

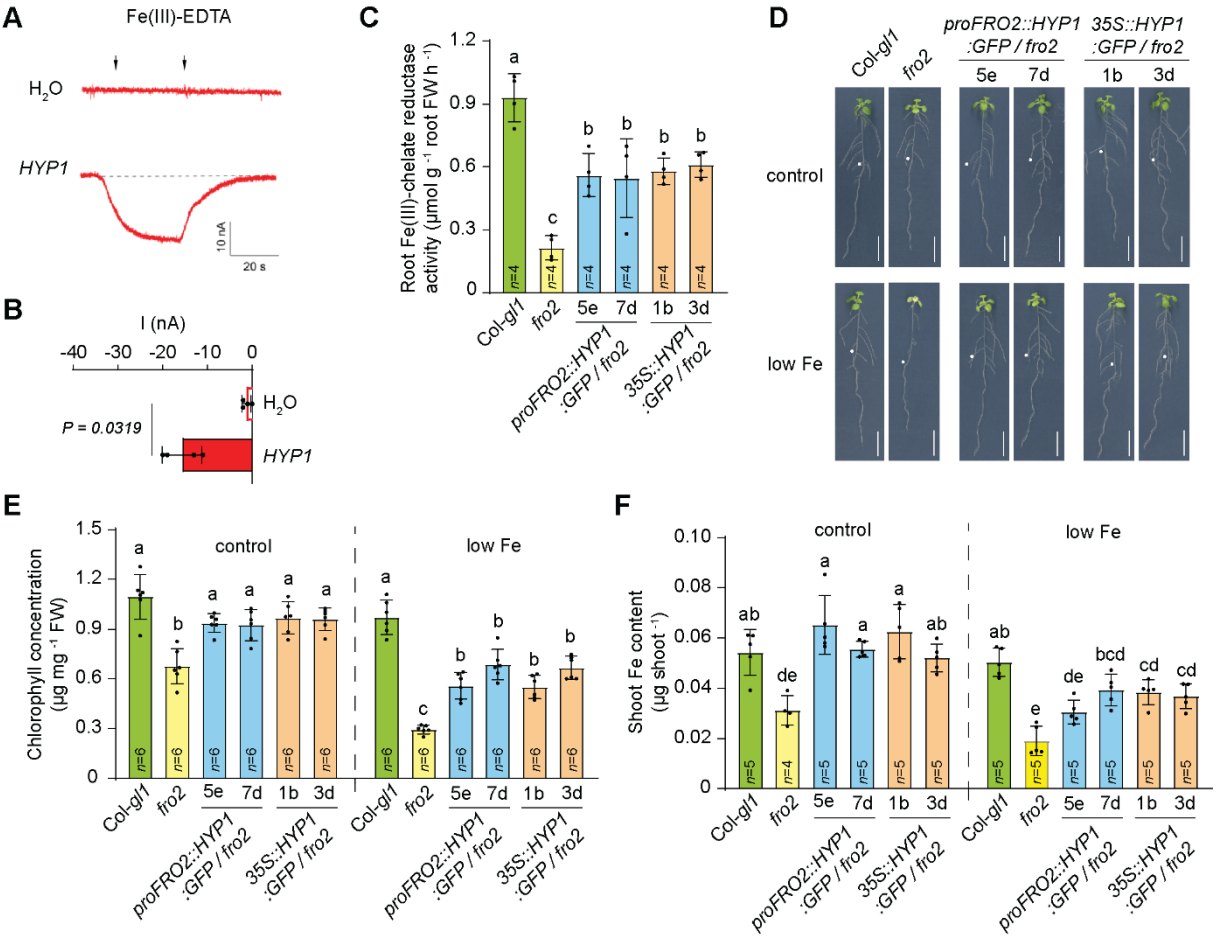

Figure 24. HYP1 mediates ferric-chelate reductase activity *in planta*.

Trans-plasma membrane currents (**A**) and mean amplitudes (**B**) elicited by 1 mM Fe(III)-EDTA in *X. laevis* oocytes injected with water (H_2O) or *HYP1* cRNA (*HYP1*). Oocytes were pre-injected with 10 mM ascorbate and traces recorded at a holding potential of -120 mV. The left and right arrows indicate the addition and removal of Fe(III)-EDTA, respectively. Bars represent means ± s.d. (H_2O-injected, n = 6 and HYP1-injected, n = 6 independent oocytes). P value according to two-tailed Student's t-test. Experiments were performed and data obtained in collaboration with the research group of Prof. Dr. Armando Carpaneto (NRC/University of Genoa, Italy). (**C**) Ferric-chelate reductase activity of wild-type (Col-*gl1*), *fro2*, and *fro2* plants expressing *HYP1:GFP* under the control of the *FRO2* or CaMV *35S* promoter. Ten-day-old seedlings were transferred to a fresh medium without added Fe and assayed after 3 days with Fe(III)-EDTA as substrate to estimate the ferric-chelate reductase activity. Bars represent means ± s.d. (n = 4 replicates containing 6 plants each). (**D**) Appearance wild-type (Col-*gl1*), *fro2*, and *fro2* plants expressing *HYP1:GFP* under the control of the *FRO2* or CaMV *35S* promoter and grown for 6 days on 75 µM (control) or 25 µM Fe(III)-EDTA (low Fe). White dots indicate the position of the primary roots at the day of transfer. (**E**) Chlorophyll concentration of plants grown for 6 days on the indicated treatments. Values represent means ± s.d. (n = 6 replicates containing 6 plants each). (**F**) Shoot Fe contents of plants grown for 6 days on the indicated treatments. Bars represent means ± s.d. (n = 4-5 replicates containing 6 plants each, as indicated in the figure). In **C**, **E** and **F**, different letters indicate significant differences (one-way ANOVA followed by post-hoc Tukey's test, $P < 0.05$). Scale bars, 1 cm.

5.10 Assessing the involvement of HYP1 in cupric reduction

An elemental analysis revealed that *35S::HYP1* plants accumulated higher Cu concentrations in shoots when grown under low P (Figure 25A and Annex Figure 7). Since

some members of the FRO family can reduce cupric ions (Cu^{2+}) (Yi and Guerinot, 1996; Bernal et al., 2012), it was then assessed whether HYP1 can mediate cupric reduction. In oocytes, *HYP1* was able to induce trans-plasma membrane currents when the Cu(II) salts $CuSO_4$ and $CuCl_2$ were supplied in the bathing solution (Figure 25B and C) Then, the root Cu(II) reductase activity of wild-type, *hyp1*, *35S::HYP1* and the double CYBDOM mutant *hyp1 crr* plants was assessed. While disruption of *HYP1* alone did not significantly change the Cu(II) reduction capacity of roots, a small but significant decrease was detected in the *hyp1 crr* double mutant (Figure 25D). In contrast, *HYP1* overexpression increased the root Cu(II) reduction activity by two-fold.

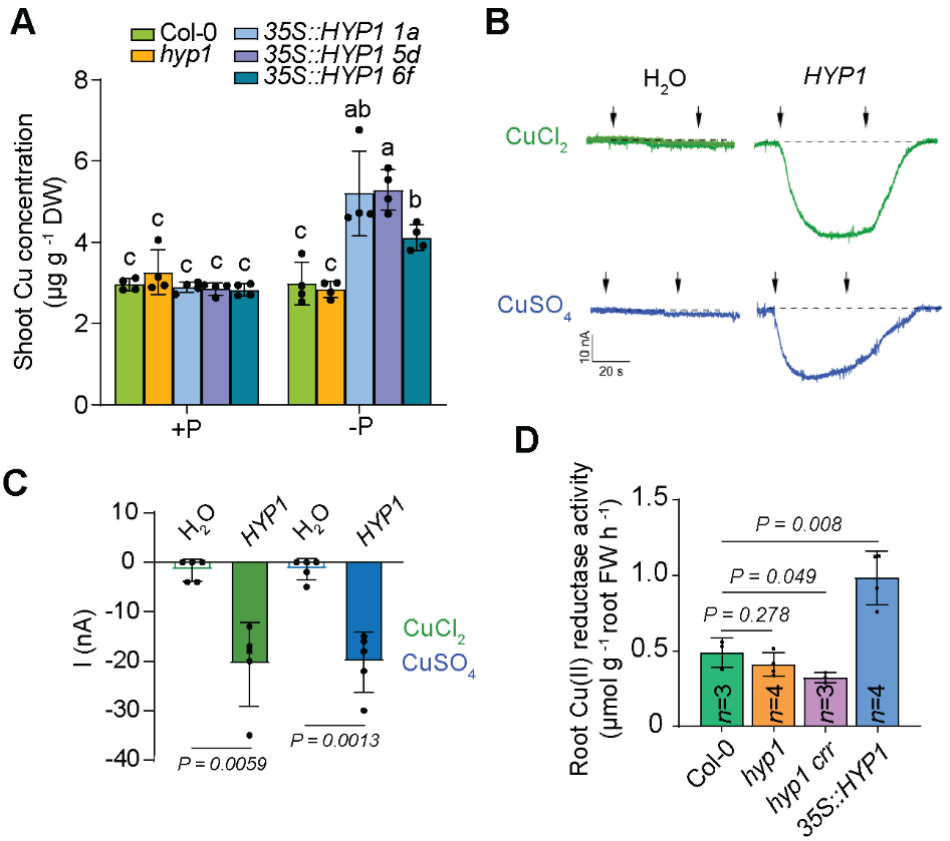

Figure 25. Characterization of cupric reduction activity by HYP1.

(**A**) Shoot Cu concentration of wild-type (Col-0), *hyp1* mutant plant, and three independent transgenic lines expressing *35S::HYP1* in Col-0 after long-term growth on low-P conditions. Ten-day-old seedlings were transferred to a fresh medium containing 625 µM P (+P) or 5 µM P (-P) and analyzed after 20 day. Bars represent means ± s.d. ($n = 4$ replicates containing 4 plants each). Different letters indicate significant differences (one-way ANOVA followed by post-hoc Tukey's test, $P < 0.05$). DW, dry weight. Trans-plasma membrane current recordings (**B**) and calculated mean currents (**C**) in *X. laevis* oocytes injected with water or cRNA of *HYP1* in response to two sources of Cu(II) ($CuSO_4$ and $CuCl_2$) in standard bathing solution (pH 5.5), at a holding potential of -20 mV. The left and right arrows indicate the addition and removal of the Cu substrates, respectively. Bars represent means ± s.d. (H_2O-injected, $n = 5$ and HYP1-injected, $n = 5$ oocytes). *P* value according to two-tailed Student's *t*-test. Experiments were performed and data obtained in collaboration with the research group of Prof. Dr. Armando Carpaneto (NRC/University of Genoa, Italy). (**D**) Cu(II) reductase activity of wild-type (Col-0), *hyp1*, *hyp1 crr* and one transgenic line overexpressing *HYP1*. Ten-day-old seedlings grown on standard half-strength MS medium were used for the assay. Bars represent means ± s.d. ($n = 4$ replicates containing 6 plants each). *P* values (two-tailed, Student's *t*-test). FW, fresh weight.

Since Cu uptake relies on a reductive mechanism and excess Cu can inhibit root elongation (Lequeux et al., 2010; Bernal et al., 2012), the role of HYP1 on tolerance of elevated external Cu(II) concentrations was assessed. While the primary root of *hyp1* plants was slightly longer than wild-type plants under high Cu, root growth of plants overexpressing *HYP1* was strongly inhibited (Figure 26A and B). A closer inspection of roots showed that overexpression of *HYP1* decreased the length and number of cells in the meristem and the length of mature cells when plants were exposed to high Cu (Figure 26C and D). In *hyp1*, meristem size and cell length were less affected by high Cu and remained higher than in wild-type plants (Figure 26D). Taken together, these results demonstrate that HYP1 can mediate Cu(II) reduction, affecting the accumulation and tolerance of plants to Cu.

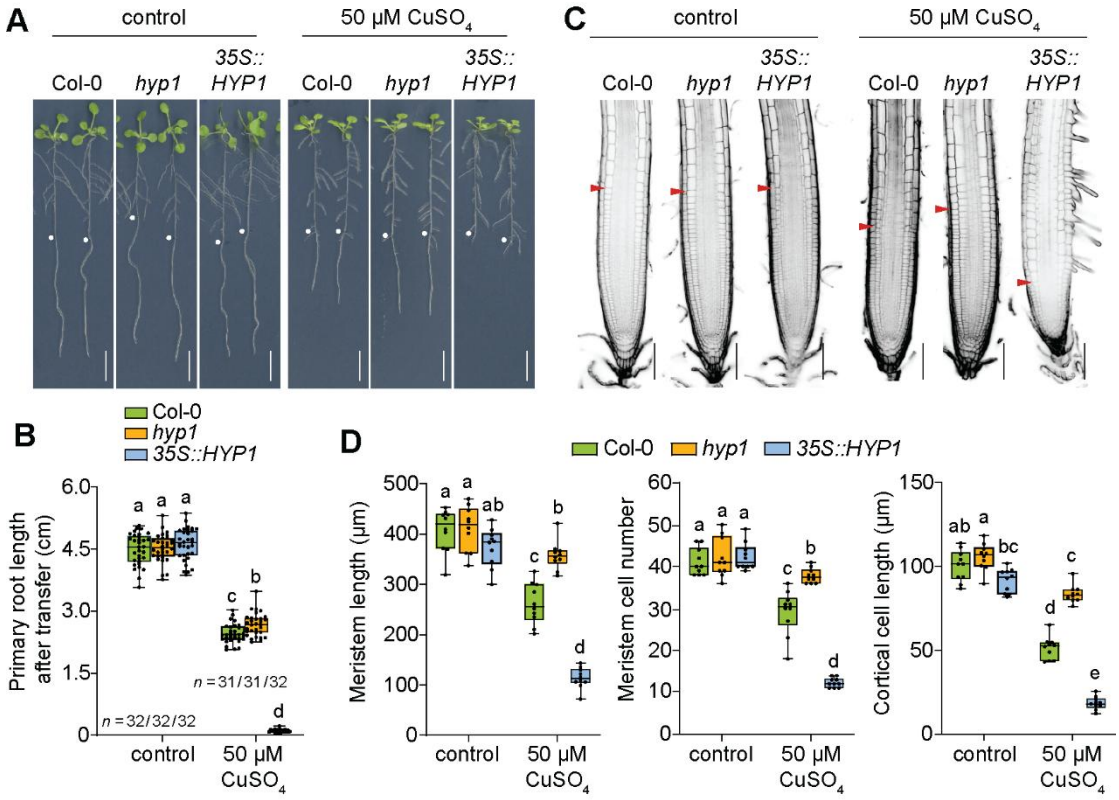

Figure 26. *HYP1* overexpression increases the sensitivity of primary roots to high Cu concentrations.

Appearance of plants (**A**) and primary root length (**B**) of wild-type (Col-0), *hyp1* mutant, and one independent transgenic line expressing *35S::HYP1* in Col-0 6 days after growth on fresh medium containing 0.05 µM (control) or 50 µM $CuSO_4$. White dots indicate the position of the primary roots at the day of transfer. (**C**) Root tip morphology of wild-type (Col-0), *hyp1* mutant, and one independent transgenic line expressing *35S::HYP1* in Col-0 6 days after growth on fresh medium containing 0.05 µM (control) or 50 µM $CuSO_4$. Arrowheads indicate the boundary between meristem and transition zone. (**D**) Changes in meristem cell length, meristem cell number, and mature cortical cell length in primary roots of wild-type (Col-0), *hyp1* mutant and one *HYP1*-overexpressing line in response to high Cu concentrations. For the boxplots, horizontal line, median; edges of boxes, 25th (bottom) and 75th (top) percentiles; whiskers, minimum and maximum; and dots, individual biological replicates. Different letters indicate significant differences (one-way ANOVA followed by post-hoc Tukey's test, $P = 0.05$; n = 31-32 (**B**), n = 10 (**D**) independent roots). Scale bars, 1 cm (**A**), 100 µm (**B**).

5.11 Role of HYP1 in apoplastic Fe accumulation in root meristems under low P or high ammonium

In order to reconcile the ferric-chelate reduction capacity of HYP1 and the conditional root phenotype of *hyp1*, the role of Fe in HYP1-mediated root growth in response to P deficiency was investigated. When Fe was omitted from the growth medium, the primary root growth of *hyp1* plants was fully rescued (Figure 27A and B), suggesting that the hypersensitive primary root inhibition of *hyp1* plants under low P is Fe-dependent. Using a split-agar experiment in which root tips were exposed to a low-P medium supplied or not with Fe, it was possible to demonstrate that the more severe primary root inhibition of *hyp1* plants was only triggered when the root tip was in direct contact with Fe (Figure 27C and D).

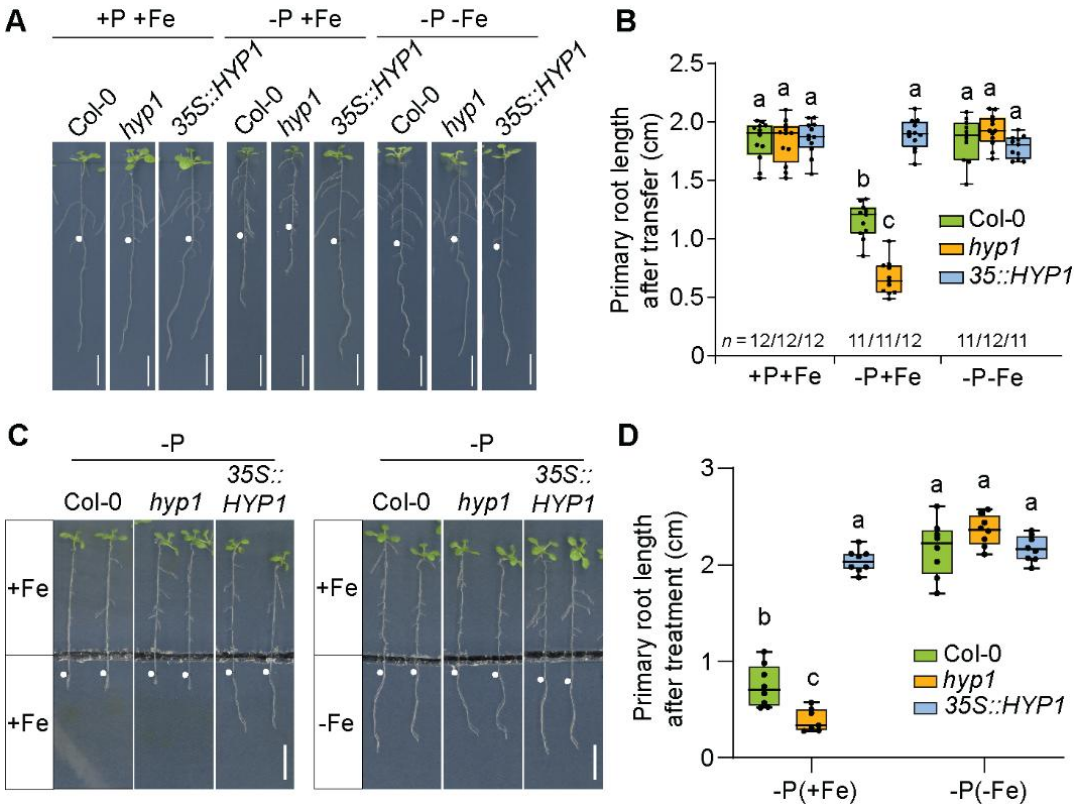

Figure 27. Direct contact of the root tip with Fe is required to inhibit primary root elongation of *hyp1* plants.

(**A**) Appearance and (**B**) quantification of primary root length of wild-type (Col-0), *hyp1* mutant plants and one *HYP1*-overexpressing line. Ten-day-old seedlings were transferred to a fresh medium containing 625 µM P (+P) or 5 µM P (-P) with 150 µM $FeCl_3$ (+Fe) or without added Fe (-Fe) and analyzed after 6 days. Appearance of plants (**C**) and primary root length (**D**) of wild type (Col-0), *hyp1* mutant, and a transgenic line expressing *35S::HYP1* in Col-0 grown for 3 days on low P solid media (-P) with Fe in the upper section and with or without Fe in the bottom section of the agar plate. Ten-day-old seedlings were transferred to fresh medium containing 5 µM P (-P) with or without 150 µM $FeCl_3$ in the bottom section of the agar plate and analyzed after 3 days. Data are presented as boxplots with each dot representing the datapoint of one biological replicate. For the boxplots, central horizontal lines, median; edges of boxes, 25th (bottom) and 75th (top) percentiles; whiskers, minimum and maximum. The letters indicate significant differences (one-way ANOVA followed by post-hoc Tukey's test, $P < 0.05$; n = 11-12 (**B**), n = 7-8 independent plants (**D**)). Scale bars, 1 cm.

Next, the Fe distribution in the apical zone of primary roots was monitored with Perls/DAB. Under sufficient P, Fe was enriched in the meristematic zone and especially near the stem cell niche, with Perls/DAB-dependent staining being comparable in wild-type and *hyp1* roots (Figure 28A and B). As shown previously (Müller et al., 2015), this pool of stainable Fe likely reflects Fe precipitated as Fe-phosphate in the apoplast. Under low P, Fe accumulation remained more concentrated around and within the stem cell niche but was strongly intensified in *hyp1* roots (Figure 28A and B). Interestingly, Perls/DAB-stainable apoplastic Fe was decreased when *HYP1* was overexpressed, almost completely disappearing under low P. To better determine where Fe was accumulating in the root meristems of low-P plants, longitudinal cross-sections of Perls/DAB-stained meristems were prepared and imaged. In root tips of wild-type plants, Fe was mainly deposited around stem cells, cortical cells and in some cells of the columella and root cap, while in meristems of *35S::HYP1* plants stainable Fe was strongly diminished with only little deposits being detected around the QC (Figure 28C). In *hyp1* meristems, Perls/DAB staining was more intense and was additionally detected around endodermal cells and in the stele (Figure 28C).

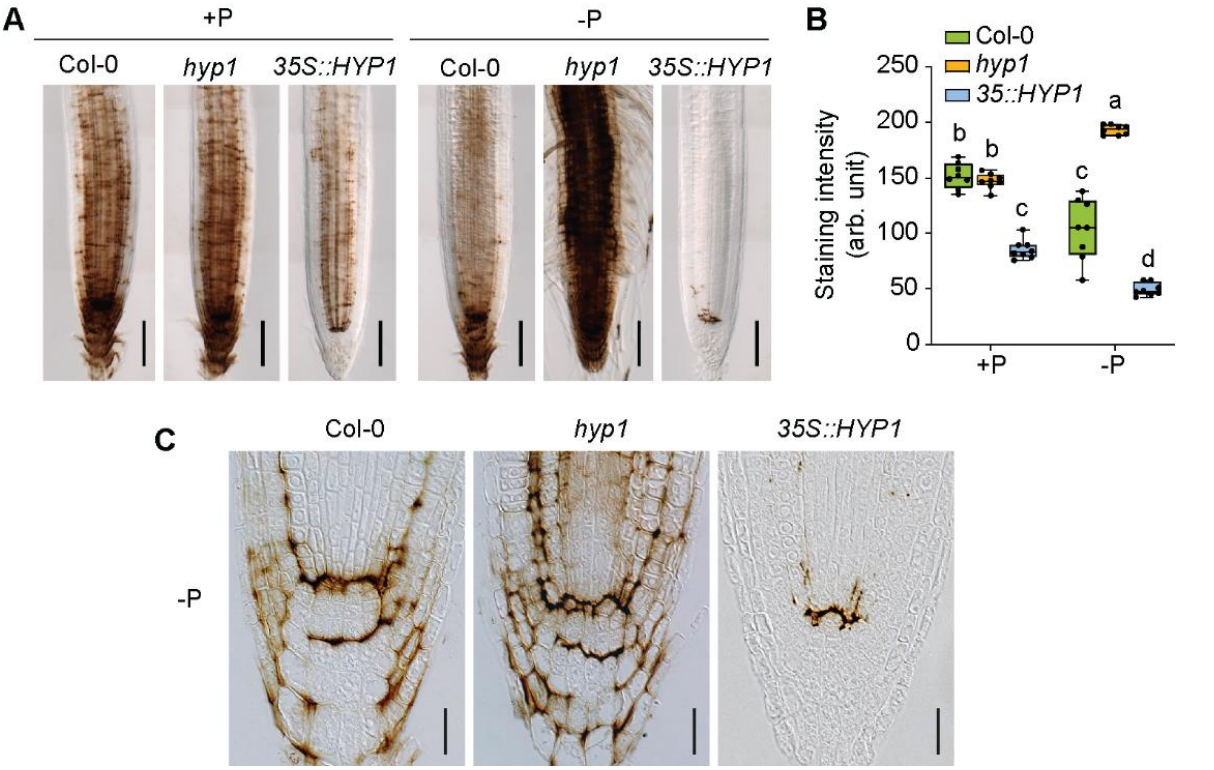

Figure 28. HYP1 activity affects Fe accumulation in the root apical meristem under low P.

Fe accumulation and distribution (**A**) and quantification of Perls/DAB-stained Fe (**B**) in the apical region of primary roots of wild-type (Col-0), *hyp1* mutant plants and one *HYP1*-overexpressing line. Ten-day-old seedlings were transferred to a fresh medium containing 625 µM P (+P) or 5 µM P (-P) with 150 µM $FeCl_3$ and roots were stained after 3 days. For the boxplots, horizontal line, median; edges of boxes, 25th (bottom) and 75th (top) percentiles; whiskers, minimum and maximum; and dots, individual biological replicates. Different letters indicate significant differences (one-way ANOVA followed by post-hoc Tukey's test, $P < 0.05$, $n = 8$ independent roots). (**C**) Longitudinal sections of Perls/DAB-stained root tips of the indicated genotypes 2 days after transfer from +P to -P medium. Roots were Perls/DAB stained after 2 days on the indicated treatment. Scale bars, 100 µm (**A**), 20 µm (**C**).

The stained Fe pools appeared mainly apoplastic, as the staining was strongly concentrated around cell boundaries and was highly reminiscent of apoplastic Fe localization reported previously (Müller et al., 2015). These results suggested that HYP1 prevents aberrant Fe accumulation in the meristem of roots exposed to low-P medium.

Previous research has demonstrated that ammonium (NH_4^+) can induce Fe deposition in root tips, resulting in primary root inhibition (Liu et al., 2022a; Liu et al., 2022b). Given that HYP1 activity is crucial for preventing Fe-dependent root inhibition under low P conditions, and its domain of expression encompass the root cap, stem cell niche, and vascular tissues of mature root zones (Figure 15), it was then assessed whether HYP1 also helps to maintain primary root growth under toxic NH_4^+ conditions. At 1 mM external NH_4^+ concentration, the primary root was only slightly inhibited when compared to 1 mM nitrate (NO_3^-), and no differences were observed among the tested genotypes (Figure 29A and B). When NH_4^+ concentrations were increased to 10 mM, all lines exhibited NH_4^+ toxicity displayed as more severe primary root inhibition (Figure 29A and B). Interestingly, while loss of *HYP1* did not significantly increase the sensitivity of the primary root to high NH_4^+-induced inhibition, *HYP1* overexpression slightly but significantly improved root growth (Figure 29A and B).

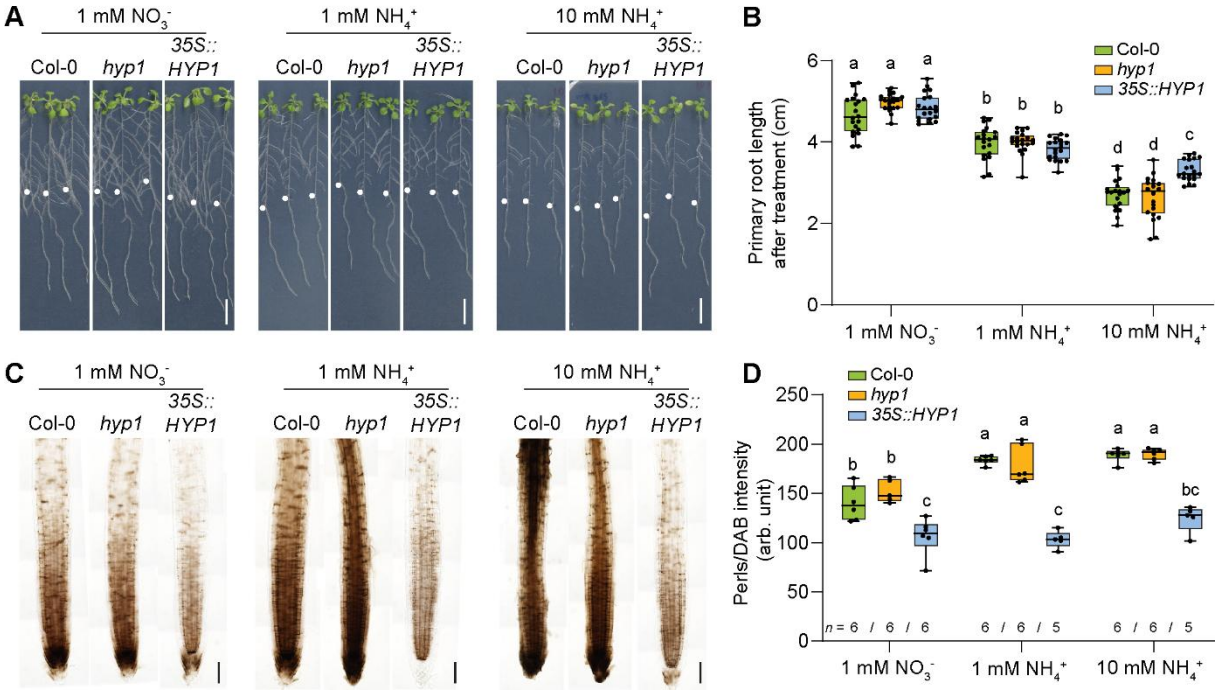

Figure 29. *HYP1* overexpression prevents overaccumulation of Fe in root tips under NH_4^+ toxicity.

Appearance of plants (**A**), quantification of primary root length (**B**), Fe accumulation and distribution (**C**), and quantification of Perls/DAB-stained Fe in root tips (**D**) of wild-type (Col-0), *hyp1* mutant and one *HYP1*-overexpressing line. Ten-day-old seedlings were transferred to a fresh medium containing 1 mM KNO_3, 1 mM NH_4Cl, or 10 mM NH_4Cl, and analyzed after 6 d. For the boxplots, horizontal line, median; edges of boxes, 25th (bottom) and 75th (top) percentiles; whiskers, minimum and maximum; and dots, individual biological replicates. Different letters indicate significant differences (one-way ANOVA followed by post-hoc Tukey's test, $P < 0.05$; n = 20 (**B**), n = 5-6 independent roots (**C**)). Scale bars, 1 cm (**A**), 100 µm (**C**).

Perls/DAB staining revealed that ammonium-exposed roots of wild-type and *hyp1* plants exhibited significantly higher Fe accumulation compared to exposure to NO_3^-. Similar to low-P conditions, overexpression of *HYP1* significantly decreased stainable Fe accumulation even under the highest NH_4^+ concentration (Figure 29C and D). These results demonstrate that *HYP1* overexpression largely prevents excess NH_4^+-induced Fe accumulation in the roots but has only a limited capacity to restore primary root growth under high NH_4^+.

It has been previously shown that enhanced callose formation under low P depends on Fe availability, which ultimately interferes with symplastic communication in the stem cell niche (Müller et al., 2015). Staining of callose with aniline blue revealed that the increased Fe accumulation in *hyp1* meristems was accompanied by increased callose deposition, especially in the stem cell niche and around cortical and endodermal cells in the meristem (Figure 30A and B). To determine whether this was also the case in the root apical meristem of *hyp1* plants, the mobility of the transcription factor SHORT ROOT (SHR) was assessed.

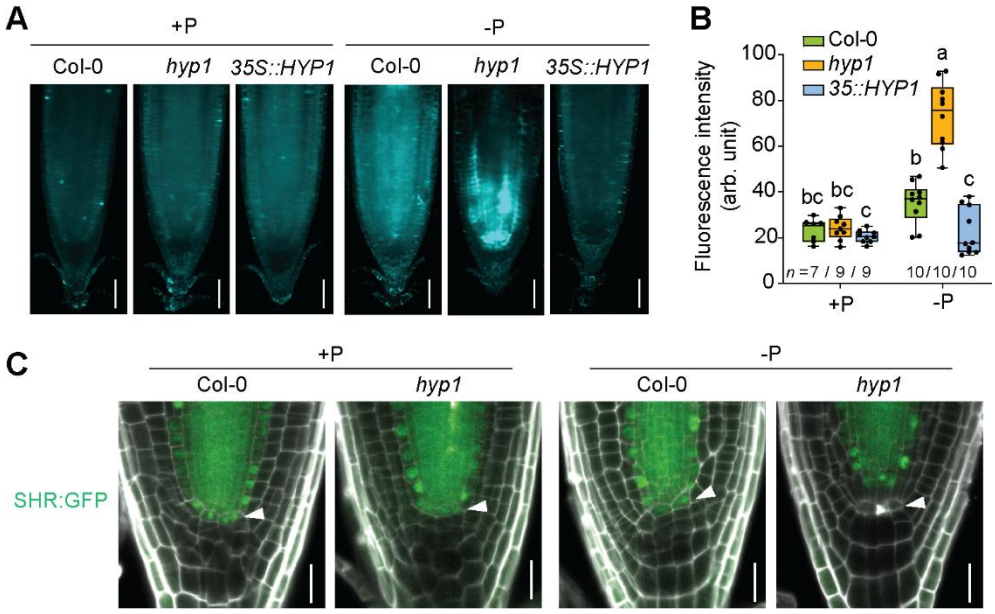

Figure 30. Loss of *HYP1* intensifies callose deposition and impairs the movement of SHR in root meristems under low P.

Callose deposition (**A**), and quantification of aniline blue-stained callose (**B**) in the apical region of primary roots of wild-type (Col-0), *hyp1* mutant and one *HYP1*-overexpressing line. Ten-day-old seedlings were transferred to a fresh medium containing 625 µM P (+P) or 5 µM P (-P) with 150 µM $FeCl_3$ and roots were stained after 3 days. For the boxplots, horizontal line, median; edges of boxes, 25th (bottom) and 75th (top) percentiles; whiskers, minimum and maximum; and dots, individual biological replicates. Different letters indicate significant differences (one-way ANOVA followed by post-hoc Tukey's test, $P < 0.05$, n = 7-10 independent roots). (**C**) Confocal images of root tips of wild-type (Col-0) and *hyp1* plants expressing *proSHR::SHR:GFP*. Seven-day-old seedlings were transferred to a fresh medium containing 625 µM P (+P) or 5 µM P (-P). SHR:GFP protein localization (green fluorescence) in the root apical meristem after 3 days on the indicated treatments. Experiment was conducted before the light-shielded root system was developed, therefore roots in this experiment were exposed to light. Cell walls were stained with propidium iodide (shown as white fluorescence) to reveal the cell borders. Arrowheads indicate the position of the quiescent center. Scale bars, 100 µm (**A**), 20 µm (**C**).

As shown in Figure 30, the movement of SHR:GFP from the stele into quiescent center cells was more severely impaired in *hyp1* than in the wild-type, suggesting disturbed symplastic cell-to-cell communication in the root apical meristem of *hyp1* roots (Figure 30C).

5.12 Assessing HYP1-dependent transcriptional responses in roots by RNA-seq

To gain more insights into the putative role of HYP1 in Fe homeostasis and global transcriptional responses under low P, root tips of plants grown for 3 days on +P (625 µM P) or -P (5 µM P) in the presence of 150 µM $FeCl_3$ were subjected to a whole transcriptome sequencing (RNA-seq) analysis. Genes exhibiting $|\log_2 FC| \geq 1.0$ (-P versus +P) at FDR < 0.05 were considered as differentially expressed. Clear differences were detected when comparing the expression pattern of genes differentially expressed in wild-type, *hyp1* and *35S::HYP1* (Figure 31A). In wild-type root tips, 1,113 genes were differentially expressed in response to low P (Figure 31B). This number was even larger in *hyp1* (*i.e.*, 1627) with 829 genes being differentially expressed exclusively in *hyp1* roots (322 upregulated and 507 downregulated).

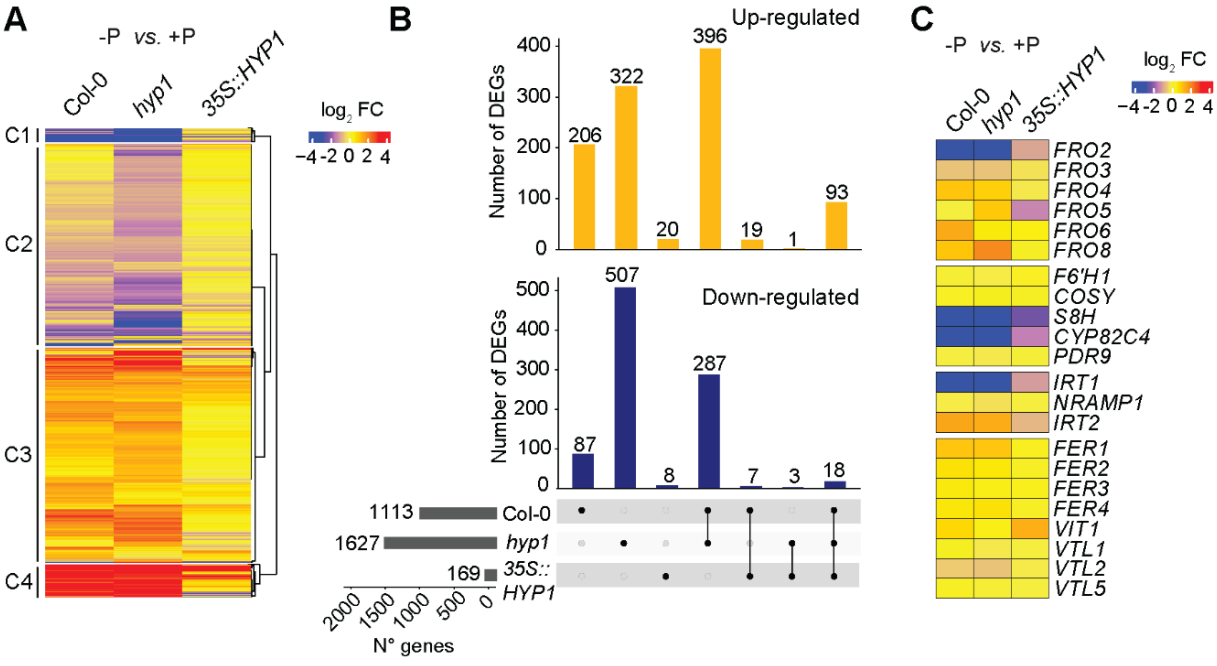

Figure 31. Overview of transcriptional changes induced by low P in root tips of wild type (Col-0), *hyp1* and one *HYP1*-overexpressing line.

(**A**) Heat map for hierarchically clustered genes significantly regulated in response to P deficiency in *Arabidopsis* root tips (0.5 cm long) after transfer to P-sufficient or P-deficient conditions for 3 days ($|\log_2 FC| \geq 1$ -P *versus* +P, FDR < 0.05). Each treatment consisted of three independent biological replicates containing up to 30 individual plants each. The gene set was split into four gene expression clusters (C1 to C4). (**B**) UpSet plots showing the number of genes up- or downregulated in a single genotype or shared between the indicated genotypes. (**C**) Heatmap showing differential expression ($|\log_2 FC| \geq 1$ -P *versus* +P, FDR < 0.05) of genes related to Fe reduction, uptake or storage.

In contrast, a comparatively small number of genes (169 in total) was significantly altered in root tips of low P-grown *35S::HYP1* plants, most of them being upregulated. The majority of differentially expressed genes (DEGs) in *35S::HYP1* roots overlapped with genes significantly responding to low P also in roots of wild-type and *hyp1* plants (Figure 31B). According to Gene Ontology (GO) analysis, this subset of DEGs was significantly enriched with functional groups related to phosphate starvation responses, phosphate transport and phosphate homeostasis (Figure 31B and Figure 32A), suggesting that primary P starvation responses were not significantly disturbed by HYP1. This result also indicated that *HYP1* overexpression restricted the transcriptional responses mainly to P starvation and less to secondary effects typically derived from the interaction with Fe. In fact, the expression of many Fe-related genes, including *IRT1*, *FRO2*, *FRO8*, *S8H*, *CYP82C4* and *FER1*, which were strongly responsive to low P in wild-type and *hyp1* roots, were only mildly or not differentially regulated in *35S::HYP1* (Figure 31C).

Among genes that failed to respond to low P in *hyp1* roots (*i.e.*, upregulated in wild-type but not in *hyp1*) GO terms related to cell wall composition or organization were detected, while genes related to heme binding, Fe-S cluster binding and cell-cell junction organization were specifically downregulated in roots of *hyp1* in response to low P (Figure 32B and C). Together, these results highlighted the impact of Fe on transcriptional responses induced in P-deficient roots, indicated that loss of HYP1 significantly affects P deficiency-induced processes in the apoplast, and reinforced a putative involvement of HYP1 in maintaining Fe homeostasis under low P.

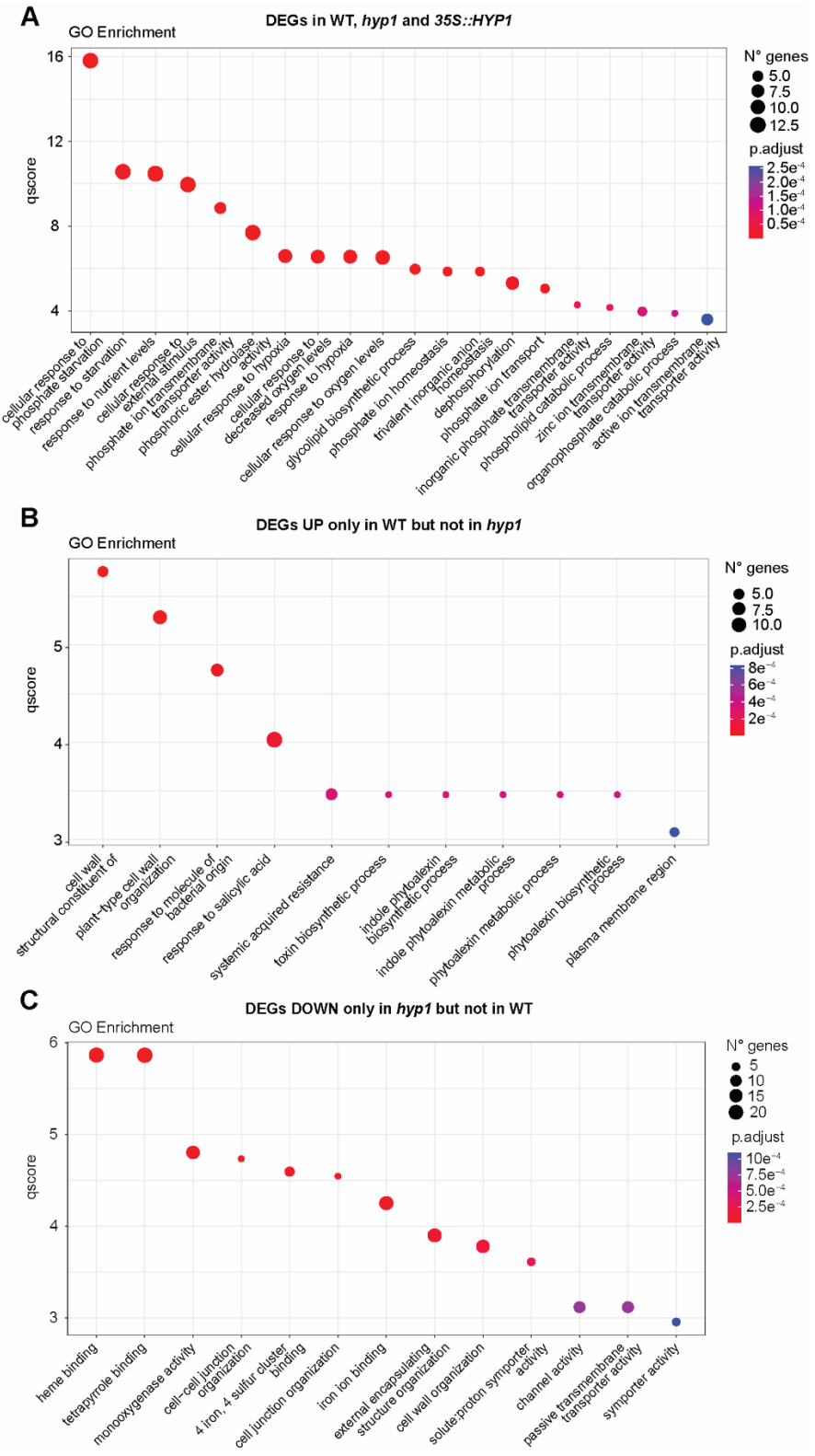

Figure 32. GO enrichment analysis of overrepresented categories of genes significantly altered by P supply in lines with modulated *HYP1* expression.

(**A**, **B**, and **C**) Most significant GO terms among differentially expressed genes in response to low P in root tips (|log2 FC| ≥ 1 -P *versus* +P, *FDR* < 0.05) of wild-type (Col-0), *hyp1* and *35S::HYP1* plants, only significantly upregulated in roots of Col-0 but not in *hyp1*, or only significantly downregulated in roots of *hyp1* but not in Col-0, respectively. The size of the circles represents the number of DEGs. The color gradient indicates the adjusted *P* value assigned to the GO term, calculated according to Benjamin-Hochberg FDR.

5.13 Investigating the link between P deficiency-induced malate secretion and HYP1 activity in Fe accumulation under low P

Considering the Fe-dependent root phenotype of the *hyp1* mutant, the HYP1-dependent ferric reductase activity in roots and the weak Perls/DAB staining in root tips of *35S::HYP1* plants (Figure 24 and Figure 28), it was hypothesized that HYP1 function is required to counteract the increased Fe solubility resulting from P deficiency-induced malate release. To test this possibility, a *hyp1 almt1* double mutant was generated. In the absence of ALMT1, disruption of *HYP1* did not anymore increase primary root sensitivity to low P (Figure 33A and B). Furthermore, the strong accumulation of Perls/DAB-stainable Fe pools in root tips of *hyp1* plants, was prevented in the *almt1* background (Figure 33C and D).

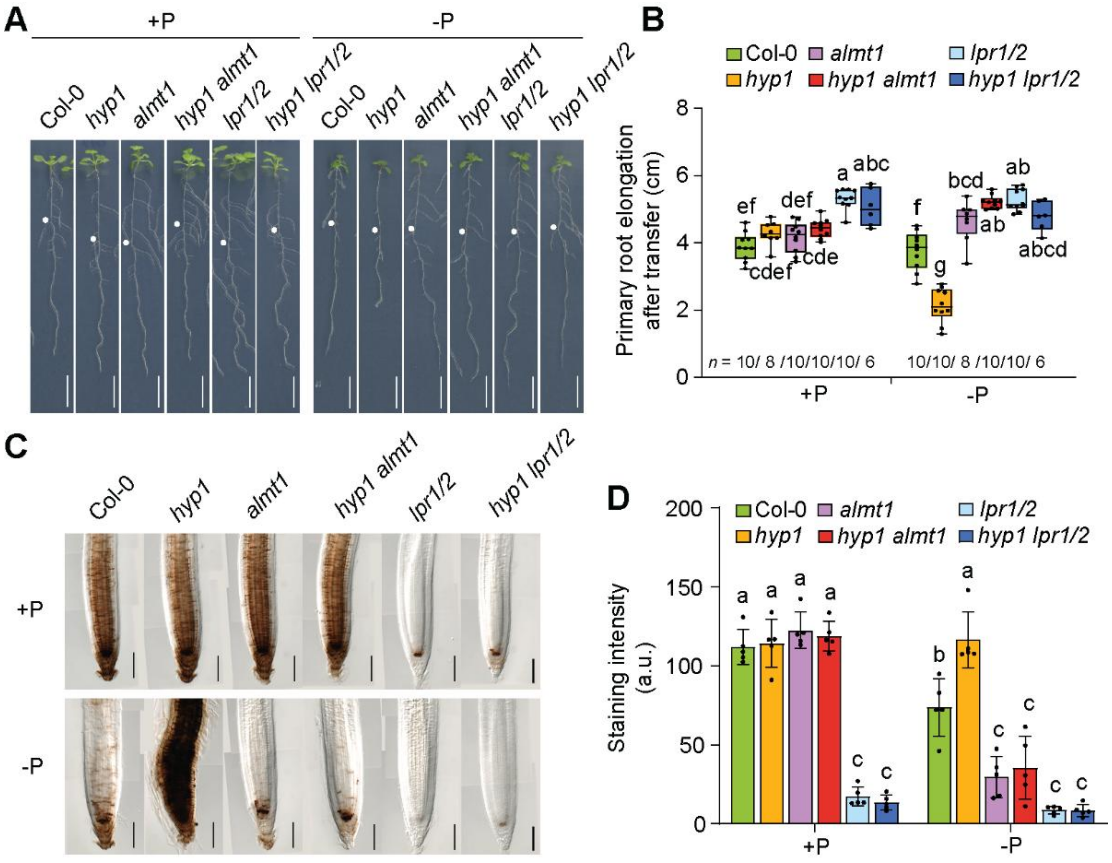

Figure 33. HYP1 function under low P is critical only when ALMT1, LPR1 and LPR2 are functional.

Appearance of plants (**A**) and quantification of primary root length (**B**) after 6 days in the indicated treatments. Ten-day-old seedlings were transferred to a fresh medium containing 625 µM P (+P) or 5 µM P (-P) with 150 µM $FeCl_3$. Data are presented as boxplots with each dot representing the datapoint of one biological replicate. For the boxplots, horizontal line, median; edges of boxes, 25th (bottom) and 75th (top) percentiles; whiskers, minimum and maximum. Letters indicate significant differences (one-way ANOVA followed by post-hoc Tukey's test, $P < 0.05$, n = 6-10 independent roots). White dots indicate the position of the primary roots at the day of transfer. Perls/DAB staining of Fe (**C**) and quantification of Perls/DAB staining (**D**) of plants after 3 days in the indicated treatments. Ten-day-old seedlings were transferred to a fresh medium containing 625 µM P (+P) or 5 µM P (-P) with 150 µM $FeCl_3$. Bars represent means ± s.d. (n = 5 independent roots). Different letters indicate significant differences (one-way ANOVA followed by post-hoc Tukey's test, $P < 0.05$). Scale bars, 1 cm (**A**), 100 µm (**C**).

Then, to test the interplay of HYP1 with LPRs, *hyp1 lpr1 lpr2* triple mutant was generated. Disrupting *HYP1* in the *lpr1 lpr2* double mutant background, in which LPR-dependent ferroxidase activity is largely diminished (Müller et al., 2015), did not significantly alter primary root growth nor Perls/DAB-stainable Fe as compared to *lpr1 lpr2* double mutant plants (Figure 33A and D). Thus, these results suggested that HYP1 activity becomes critical only when ALMT1-mediated malate exudation and LPR-dependent apoplastic Fe(II) oxidation are active.

As malate becomes a predominant Fe(III)-chelator in P-starved roots (Balzergue et al., 2017; Mora-Macías et al., 2017), it was next assessed whether HYP1 can reduce Fe(III) when bound to malate. In oocytes injected with *HYP1* cRNA, small but significant currents were detected when Fe(III)-malate was supplied in the bathing solution (Figure 34A and B). Next, HYP1-dependent ferric reduction of freshly prepared Fe(III)-malate complexes was assessed *in planta*. The capacity of roots of P-deficient wild-type plants to reduce Fe(III) decreased by approx. 50% (Figure 34C), which probably reflected the strong downregulation of *FRO2* (Figure 4C). An even stronger decrease was detected for the CYBDOM double mutant *hyp1 crr*, while overexpression of *HYP1* maintained root ferric-chelate reductase activity at the same level as under sufficient P. Together, these results demonstrated that overexpression of *HYP1* can overcome ALMT1-induced Fe solubilization by restoring, together with CRR, ferric reduction capacity in P-deficient roots.

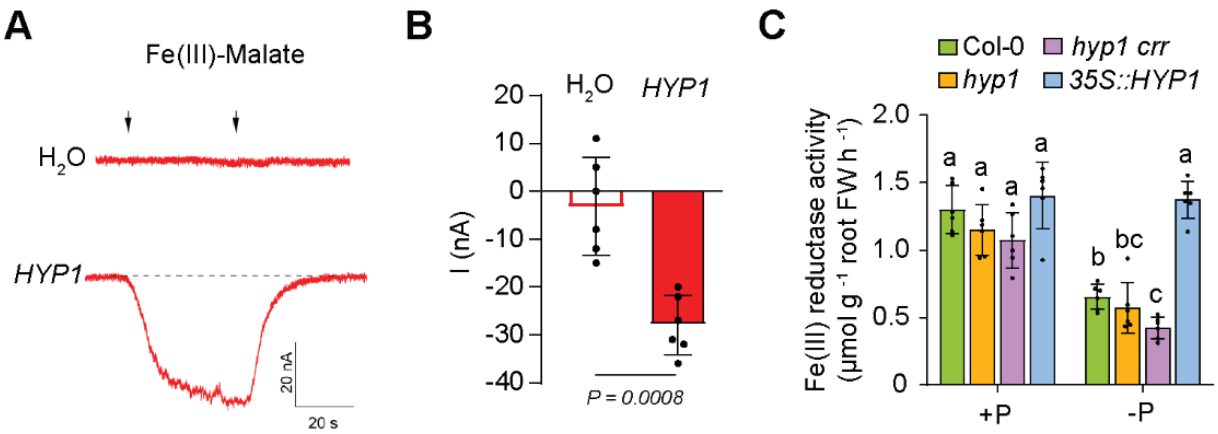

Figure 34. Fe(III)-malate reduction by HYP1.

Trans-plasma membrane currents (**A**) and mean amplitudes (**B**) elicited by 1 mM Fe(III)-malate in *X. laevis* oocytes injected with water (H_2O) or cRNA of HYP1 (*HYP1*). Oocytes were pre-injected with 10 mM ascorbate and traces recorded at a holding potential of -120 mV. The left and right arrows indicate the addition and removal of Fe(III)-malate. Bars represent means ± s.d. (H_2O-injected, n = 6 and *HYP1*-injected, n = 6 independent oocytes). P value according to two-tailed Student's t-test. Experiments were performed and data obtained in collaboration with the research group of Prof. Dr. Armando Carpaneto (University of Genoa, Italy). (**C**) Ten-day-old seedlings were transferred to a fresh medium containing 625 µM P (+P) or 5 µM P (-P) with 150 µM $FeCl_3$. After 3 days, root ferric reduction capacity was assayed by using freshly prepared Fe(III)-malate complexes as substrate. Bars represent means ± s.d. (n = 6 replicates containing 6 plants each). Letters indicate significant differences (one-way ANOVA followed by post-hoc Tukey's test, $P < 0.05$).

5.14 Cell type-specific complementation of the *hyp1* mutant under low P

Since *HYP1* is not only expressed in the root apical meristem, it was investigated which expression domain is most critical for HYP1-mediated tolerance to low P by expressing *HYP1:GFP* under the control of different promoters in *hyp1*. The function of the GFP-tagged protein was confirmed by the full complementation of primary root elongation, mature cell length and meristem size and integrity with *HYP1:GFP* under the control of a 2151-bp long

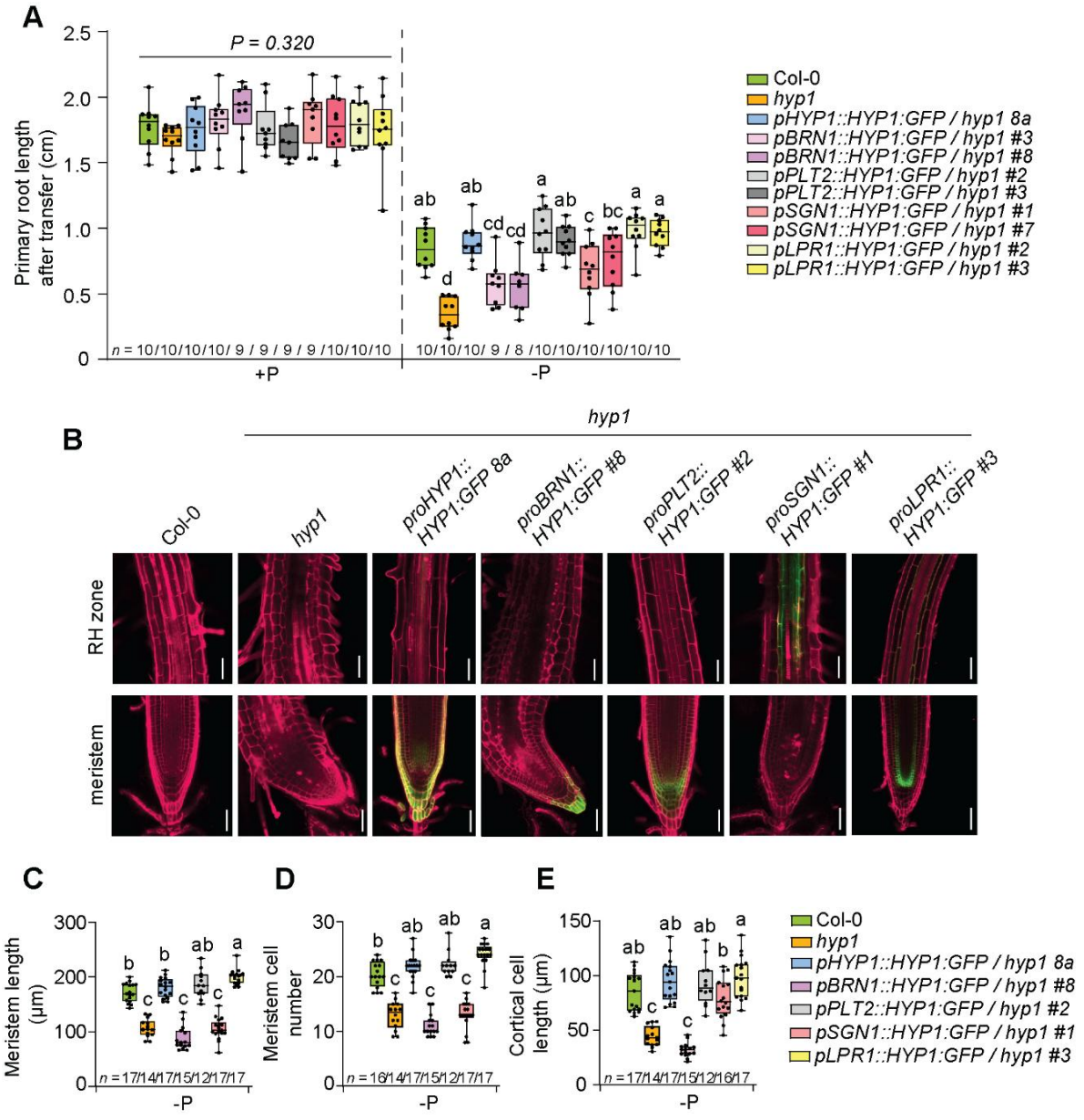

Figure 35. Cell type-specific complementation of *hyp1* with GFP-tagged HYP1.

Primary root length (**A**), confocal images of propidium iodide-stained mature root zones and root apical meristems (**B**), and quantification of meristem cell length (**C**), meristem cell number (**D**), and mature cortical cell length (**E**), respectively, of plants grown on the indicated treatments. Ten-day-old seedlings were transferred to a fresh medium containing 625 µM P (+P) or 5 µM P (-P) with 150 µM $FeCl_3$ and analyzed after 3 days. For the boxplots, horizontal line, median; edges of boxes, 25th (bottom) and 75th (top) percentiles; whiskers, minimum and maximum. Different letters indicate significant differences (one-way ANOVA followed by post-hoc Tukey's test, $P < 0.05$, n = 8-10 (**A**), n = 12-17 (**C-E**) independent roots). Scale bars, 50 µm.

segment of *HYP1*'s native promoter (Figure 35A-E). Using the promoter of *BEARSKIN1* (*BRN1*) to confine *HYP1* expression in root cap cells did neither significantly improve root growth nor prevent loss of root apical meristem integrity (Figure 35A). Similarly, expression of *HYP1* in root cap cells did also not significantly change the root apical meristem size and the length of mature cells (Figure 35C-E). In turn, expression of *HYP1* in mature endodermal cells with the promoter of *SCHENGEN1* (*SGN1*) was able to significantly increase the elongation of mature cells and partially restore primary root length but had limited effect in restoring root apical meristem integrity and size (Figure 35A-E). However, full recovery of primary root growth, mature cell length, and root apical meristem size and integrity was achieved when using the promoter of *LPR1* to drive *HYP1* expression in the stem cell niche and in proximal endodermal and cortical cells in the root apical meristem, and in endodermal cells in differentiated root zones (Figure 35A-E). Altogether, these results suggested that HYP1 activity in a confined zone in the proximal zone of the root apical meristem is required to prevent root apical meristem disintegration, while primary root elongation further relies on *HYP1* expression in mature endodermal cells.

5.15 Assessing the involvement of HYP1 activity in apoplastic Fe accumulation under low P conditions

The impact of HYP1 on the fate of apoplastic Fe pools in the root apical meristem was assessed by transferring plants from a Fe-containing to a Fe-depleted medium. As shown in Figure 36A and B, when Pi was present in the Fe-depleted medium, Fe pools were not significantly altered within 1 day after transfer and were comparable in wild-type and *hyp1* plants. Under low P, Perls/DAB-stainable Fe pools were significantly depleted in the root apical meristem of wild-type plants while remaining largely unchanged in *hyp1* plants. It was then hypothesized that the HYP1-dependent depletion of stainable Fe pools could be associated with HYP1-driven reduction of soluble Fe(III)-malate complexes formed under P-deficient conditions. An Fe(III) reduction assay of excised root tips (approximately 3 mm-long) revealed that P-deficient *hyp1* root tips had significantly lower capacity to reduce Fe(III)-malate compared to wild-type and a *HYP1*-overexpressor (Figure 36C). It was then attempted to visualize Fe(II) in the primary root with the turn-on fluorescent probe RhoNox-1 (Hirayama et al., 2013; Platre et al., 2022). In order to compare RhoNox-1 signals in similar root apical meristem areas, the staining was performed 1 day after transfer, when the size and integrity of *hyp1* root apical meristems were not yet significantly altered (Figure 12A-D). In line with the ferric-chelate reductase activity detected in excised root tips, RhoNox-1-derived fluorescence decreased in response to low P and was significantly lower in the root apical meristem of *hyp1*

and much higher in the root apical meristem of *35S::HYP1* compared to wild-type plants (Figure 36D-F). Together, these results suggested that, under low P, HYP1 promotes the depletion of apoplastic Fe pools by reducing Fe(III) previously solubilized by malate.

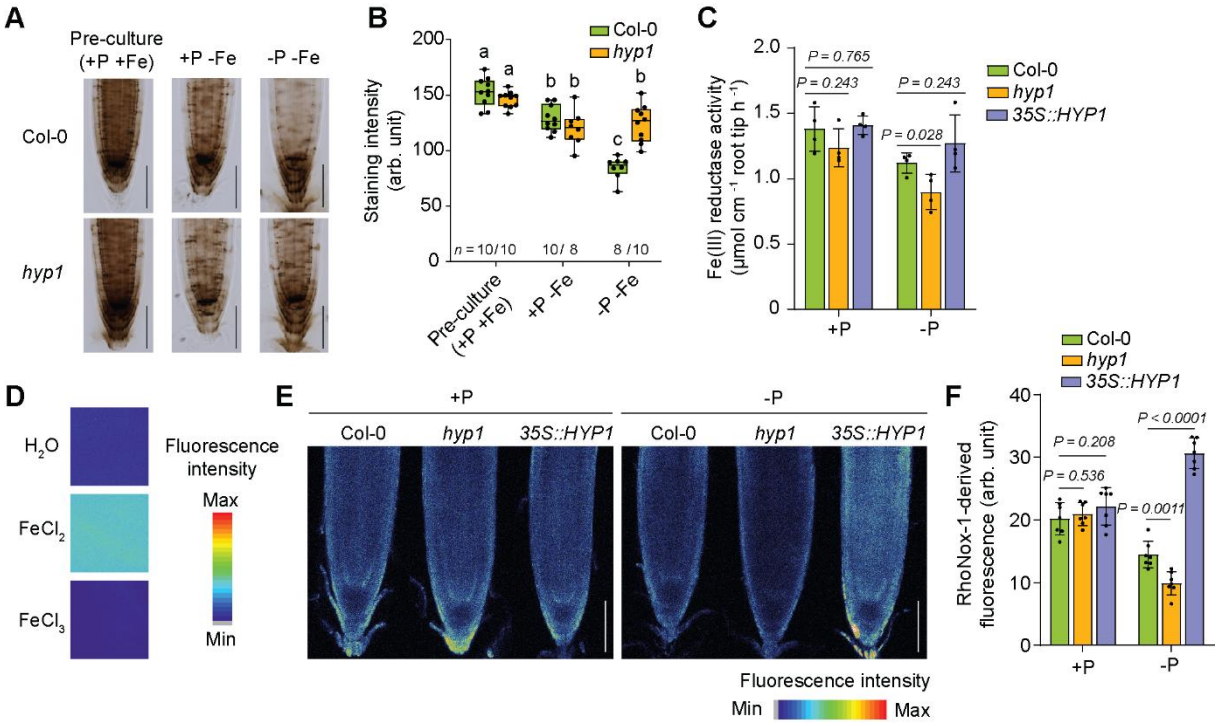

Figure 36. *HYP1* expression in the meristem depletes apoplastic Fe pools under low P.

Perls/DAB staining of Fe (**A**) and quantification of staining intensity (**B**) in the root apical meristem of the indicated plants after preculture on Fe(III)-EDTA with 625 µM P and 150 µM $FeCl_3$ (+P+Fe) and after 1 days of growth on Fe-depleted medium containing 625µM P (+P-Fe) or 5 µM P (-P-Fe). Data are presented as boxplots with each dot representing the datapoint of one biological replicate. For the boxplots, horizontal line, median; edges of boxes, 25th (bottom) and 75th (top) percentiles; whiskers, minimum and maximum. Letters indicate significant differences (one-way ANOVA followed by post-hoc Tukey's test, $P < 0.05$, n = 8-10 independent roots). (**C**) Ferric-chelate reductase activity of detached root tips (approximately 3 mm) of wild-type (Col-0), *hyp1* and *35S::HYP1* plants. Ten-day-old seedlings were transferred to a fresh medium containing 625 µM P (+P) or 5 µM P (-P) with 150 µM $FeCl_3$ and assayed after 1 day using Fe(III)-malate as substrate. Bars represent means ± s.d. ($n = 4$ replicates consisting of 6 root tips each). P values (two-tailed, Student's t-test). (**D**) HYP1-dependent ferric reduction in root tips of P-deficient plants. Reaction of the Fe(II)-sensitive fluorescent dye RhoNox-1 to solutions containing $FeCl_2$ and $FeCl_3$. Representative images (**E**) and quantification of RhoNox-1-derived signals (**F**) in root tips of wild-type (Col-0), *hyp1* and *35S::HYP1* plants. Ten-day-old seedlings were transferred to a fresh medium containing 625 µM P (+) or 5 µM P (-P) and stained with RhoNox-1 after 1 day. Bars represent means ± s.d. ($n = 7$ independent roots). Scale bars, 100 µm (**A** and **E**).

To further establish the role of Fe(III) reduction, it was next tested whether the direct supply of Fe(II) in the form of non-chelated $FeCl_2$ to the P-deprived medium can rescue the short-root phenotype of *hyp1* plants. As shown in Figure 37A and B, when $FeCl_2$ was supplied to the low-P medium instead of $FeCl_3$, the primary root length of the *hyp1* mutant was comparable to wild-type and a *HYP1*-overexpressing line (Figure 37A and B). In order to show that the Fe(II)-supplied media contained Fe(II) and not Fe(III), the agar medium was stained

with FerroZine at the date of harvest, with a Fe(III)-supplied medium serving as control. Stronger magenta color, was detected on agar plates containing low-P medium supplied with $FeCl_2$ than with $FeCl_3$ (Figure 37C), indicating that Fe(II) concentrations were higher and that most Fe(II) was not oxidized to Fe(III) during the cultivation period. Next, roots of plants cultivated on solid medium with low P and $FeCl_2$ as the sole Fe source were stained with Perls/DAB. As shown in Figure 37D, roots of all three genotypes showed a relatively weak staining of Fe. Interestingly, in many cells, stained Fe appeared as punctuated structures. These stained dot-like structures could be more clearly visualized in longitudinal cross-sections of Perls/DAB-stained meristems from wild-type and *hyp1* roots exposed to low P in the presence of $FeCl_2$ (Figure 37E). The presence of these stained dot-like structures within the cell space delimited by cell boundaries indicated that they were likely intracellular (Figure 37E).

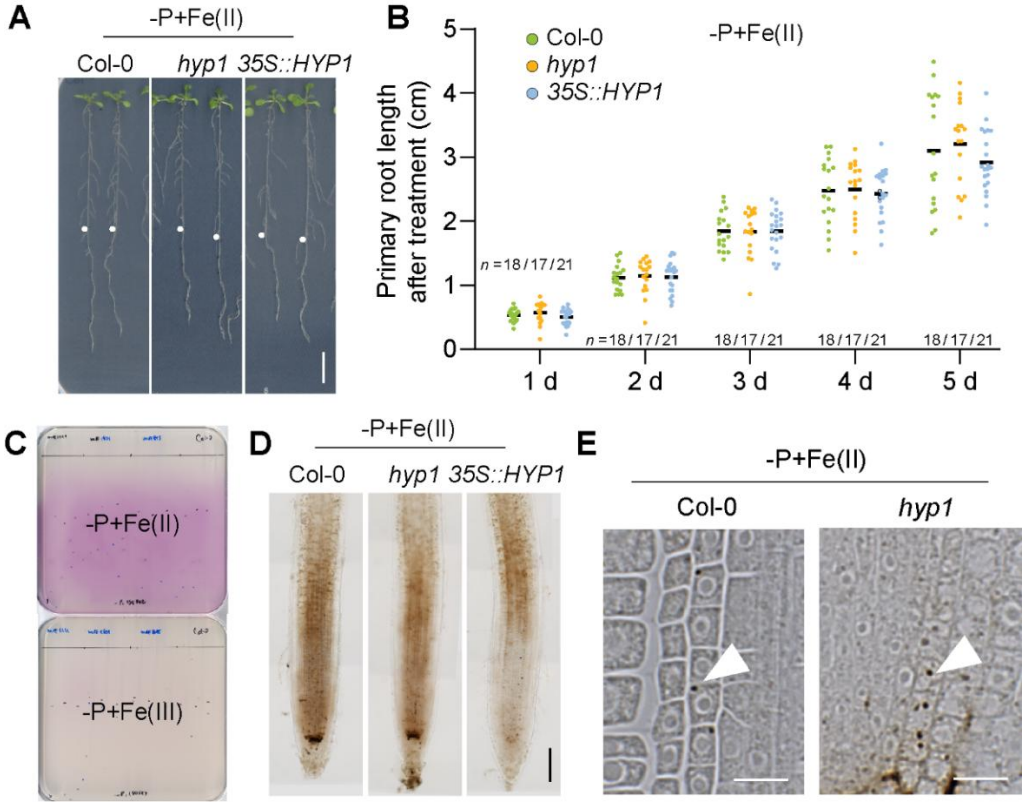

Figure 37. Supply of Fe(II) to the low-P medium prevents the severe inhibition of the primary root of *hyp1* plants.

Appearance of plants (**A**) and time-dependent changes primary root length (**B**) of wild-type (Col-0), *hyp1* mutant, and an independent transgenic line expressing *35S::HYP1* in Col-0 grown for 5 days (**A**) or up to 5 day (**B**) on low P (-P) containing Fe(II) as sole source of Fe. Ten-day-old seedlings were transferred to a fresh medium containing 5 µM P (-P) with 150 µM $FeCl_2$ and analyzed daily until 5 days after transfer. White dots indicate the position of the primary roots at the day of transfer. All individual data points are plotted and dark horizontal lines represent means ($n = 24$ independent roots). (**C**) FerroZine-stained agar plates containing low P (-P) medium and 150 µM of $FeCl_2$ [Fe(II)] or $FeCl_3$ [Fe(III)] as sole Fe source. After cultivating plants for 5 days, plants were removed from medium, 50 µM of FerroZine was applied to agar medium, and pictures were taken after 30 min of reaction. Magenta coloration indicates presence of Fe(II)-FerroZine complex. (**D**) Perls/DAB staining of Fe of plants after 3 days in the indicated treatment. (**E**) 2.5-µm thick cross-sections of Perls/DAB root tips of wild-type (Col-0) and *hyp1* mutant. Ten-day-old seedlings were transferred to a fresh medium containing 5 µM P (-P) with 150 µM $FeCl_2$ and stained after 2 days. White arrowheads point to stained dot-like structures. Scale bars, 1 cm (**A**), 100 µm (**D**), 10 µm (**E**).

Similar globular structures were previously demonstrated to represent Fe associated with ferritins (Reyt et al., 2015). Unfortunately, during the present thesis it was not possible to confirm the identity of the dot-like structures detected in $FeCl_2$-exposed roots nor whether ferritins play a role in meristem maintenance under low-P conditions.

5.16 Identification of MDHAR3 and its potential role in cytosolic ascorbate recycling

As shown in Figure 19, cytosolic ascorbate serves as an electron donor for HYP1-mediated trans-plasma membrane electron transfer. As a consequence of the reduction of the cytochrome *b*561 by ascorbate, the partially oxidized molecule monodehydroascorbate (MDHA) is produced, which can be reduced back to ascorbate by NADH-monodehydroascorbate reductases (MDHAR) or ferredoxin (Hossain and Asada, 1985; Park et al., 2016; Foyer et al., 2020). According to the transcriptome analysis presented in section 5.1, one MDHAR-encoding gene was among the genes upregulated in response to low P in the time-course transcriptome (Figure 4D). The genome of *A. thaliana* contains five *MDHARs*, namely *MDHAR1*, *2*, *3*, *4*, and *6*. According to the transcriptome, *MDHAR3* was significantly upregulated in roots 4 days after transfer to -P, with $\log_2$ FC greater than 0.75 (Figure 38A). According to ePlant browser (https://bar.utoronto.ca/eplant/), MDHAR2 and MDHAR3 are predicted to be cytosolic, whereas MDHAR1 is predicted to be present in the cytosol and peroxisomes and MDHAR4 in the cytosol, peroxisomes and plastids. MDHAR6, in turn, is predicted to be localized in plastids and with low confidence also in mitochondria (Figure 38B). The transcript levels of *MDHAR* genes encoding for the predicted cytosolic enzymes was assessed with qPCR. As shown in Figure 38C, only *MDHAR3* was significantly upregulated by low P in roots.

To determine the tissue-specific expression pattern of *MDHAR3*, a transcriptional *proMDHAR3::GUS* reporter line was generated and assessed under sufficient- and low-P conditions. In young seedlings, *proMDHAR3*-driven GUS activity was detected in roots and was virtually absent in cotyledons and in the first pair of true leaves (Figure 39A). A closer inspection of the root tips revealed that *MDHAR3* promoter activity was present in most cell layers of the root apical meristem (Figure 39B). In accordance with the transcriptome data and the qPCR validation (Figure 4D and Figure 38A, respectively), the intensity of *proMDHAR3*-driven GUS staining was increased in roots exposed to low P supply (Figure 39B). Next, to evaluate the exact localization of MDHAR3, a BFP-translational fusion reporter line with MDHAR3 protein was generated. In root tips, strongest MDHAR3:BFP-derived fluorescence was detected in root cap cells, while in the mature root it was detected in the cells surrounding

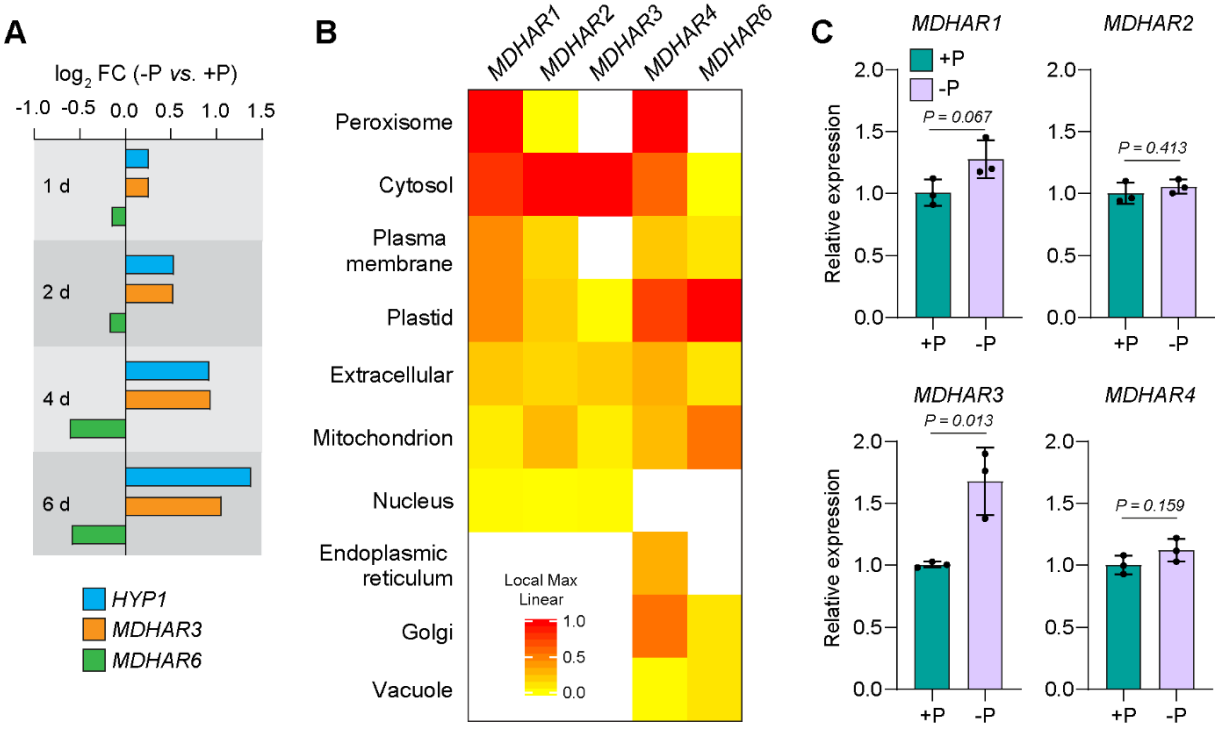

Figure 38. *MDHAR3* is upregulated in response to low P availability in roots and encodes a monodehydroascorbate reductase predicted to localize in the cytosol.

(**A**) Log_2 fold-change (FC) value (FDR < 0.05) of Arabidopsis genes encoding *HYP1* and *MDHAR* proteins during the time course of P treatments according to microarray analysis (*n* = 3 independent biological replicates per condition). (**B**) Subcellular localization of the *MDHAR* genes obtained from the Cell eFP viewer in the ePlant browser (www.bar.utoronto.ca/eplant/). Localization scores were normalized at the maximal value for each gene. Blank spaces indicate no available data to be shown. (**C**) qPCR validation of the expression of the indicated genes of the cytosolic-localized *MDHAR* family in response to P deficiency. Expression levels were normalized to *UBQ2*. Seven-day-old seedlings were transferred to a fresh medium containing 625 µM P (+P) or 5 µM P (-P) with 150 µM $FeCl_3$ and analyzed after 6 days. Bars represent means ± s.d. (*n* = 3 independent replicates containing 12 roots each). *P* values (two-tailed, Student's *t*-test).

the vascular tissues (Figure 39C and D). In both root zones, MDHAR3:BFP intensity increased when plants were exposed to low P. At the subcellular level, MDHAR3:BFP-derived fluorescence was detected in the cytosol and did not colocalize with the plasma membrane dye FM4-64 or cell wall dye propidium iodide (Figure 39E and F). In order to determine whether MDHAR3 co-localizes with HYP1, a transgenic line expressing *proHYP1::HYP1:GFP* was transformed with *proMDHAR3::MDHAR3:BFP*. By analyzing roots from plants grown for 3 days on low P, colocalization of BFP and GFP signals were detected in root cap cells (Figure 39G). However, only very faint MDHAR3:BFP-derived fluorescence was detected in the zone above the quiescent center, where HYP1:GFP accumulates in response to low P. Taken together, these results indicated that MDHAR3 is likely cytosolic and, in the root apical meristem, co-localizes with HYP1 mainly in root cap cells.

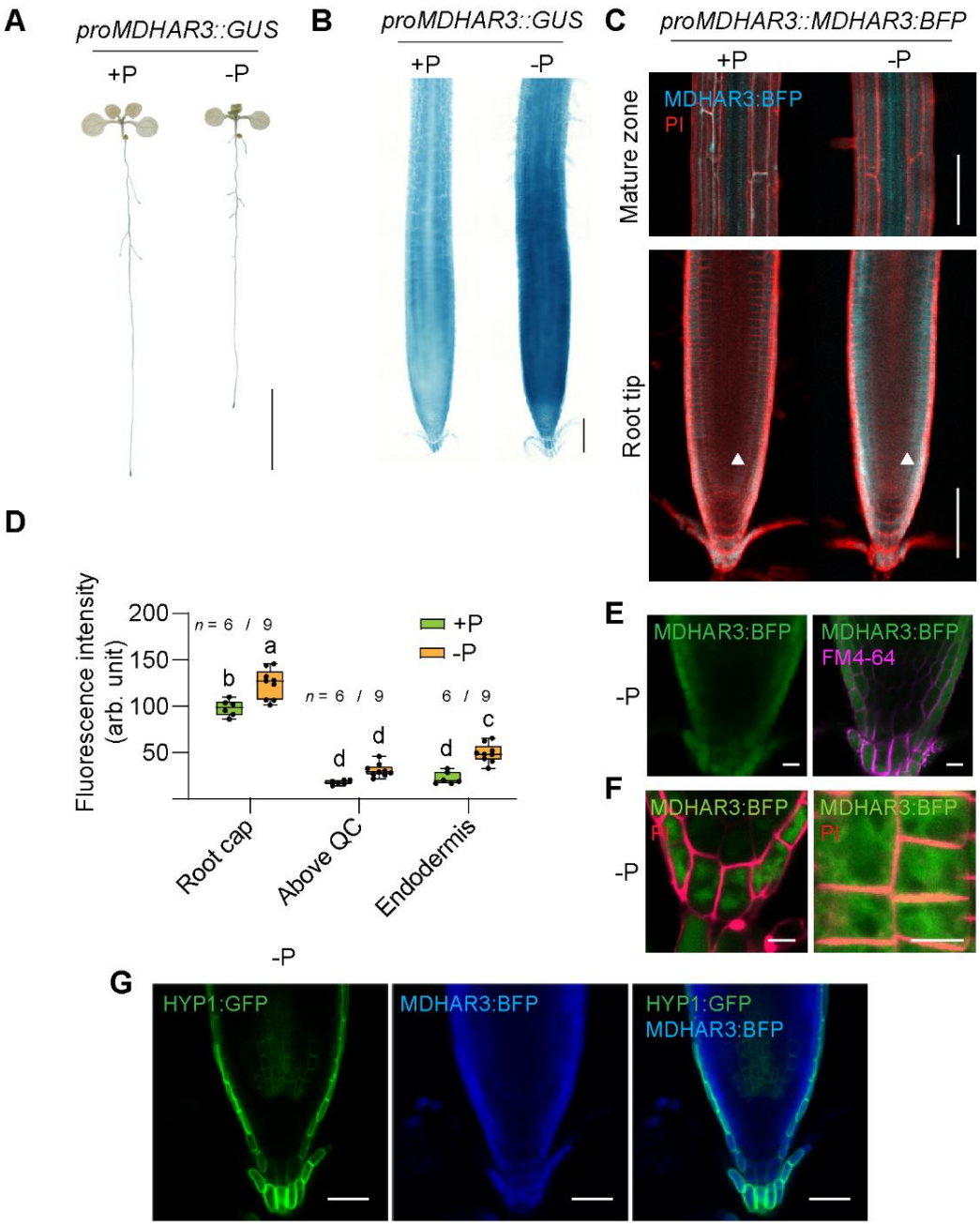

Figure 39. MDHAR3 is localized in the cytosol, induced in response to P deficiency and partially co-localized with HYP1 in the root apical meristem.

P-dependent changes in *HYP1* promoter activity in whole seedlings (**A**) and in primary root tips (**B**). Seven-day-old seedlings were transferred to fresh medium containing 625 µM P (+P) or 5 µM P (-P) with 150 µM $FeCl_3$ and stained 3 days after transfer. (**C-D**) MDHAR3:BFP (blue fluorescence) localization (**C**) and quantification (**D**) in the indicated root zones or cell types. Ten-day-old seedlings were transferred to fresh medium containing 625 µM P (+P) or 5 µM P (-P) with 150 µM $FeCl_3$ and imaged after 3 days. Roots were counterstained with the cell wall stain propidium iodide (PI, red fluorescence) Data are presented as boxplots with each dot representing the datapoint of one biological replicate. For the boxplots, horizontal line, median; edges of boxes, 25th (bottom) and 75th (top) percentiles; whiskers, minimum and maximum. Letters indicate significant differences (one-way ANOVA followed by post-hoc Tukey's test, $P < 0.05$, n = 6-9 independent roots). MDHAR3:BFP (shown here as green fluorescence for better contrast) localization in root tips grown for 3 days on the indicated treatment, counterstained with the plasma membrane probe FM4-64 (in magenta) (**E**) or the cell wall stain propidium iodide (PI, in red) (**F**). (**G**) Co-localization of MDHAR3:BFP (blue fluorescence) and HYP1:GFP (green fluorescence) in root tips grown for 3 days under low P (-P). White arrows indicate region above the quiescent center. Scale bars, 1 cm (**A**), 100 µm (**B** and **C**), 5 µm (**E** and **F**), 20 µm (**G**).

The cytosolic localization of MDHAR3 may suggest that the protein participates in the recycling of ascorbate pools in the cytosol. To investigate whether this putative function is critical for root growth under low P, one available T-DNA insertion line for *MDHAR3* was isolated and phenotyped. The primary root of the *mdhar3* single mutant was only slightly shorter compared than the wild type under low P (Figure 40A and B). To investigate the genetic interplay of *HYP1* and *MDHAR3*, a *hyp1 mdhar3* double mutant was generated. Under sufficient P, the primary root length of the double mutant was comparable to wild-type plants (Figure 40A and B). However, at low P, the primary root of *hyp1 mdhar3* double mutant plants was shorter than the wild type and *mdhar3* single mutant but comparable to *hyp1*.

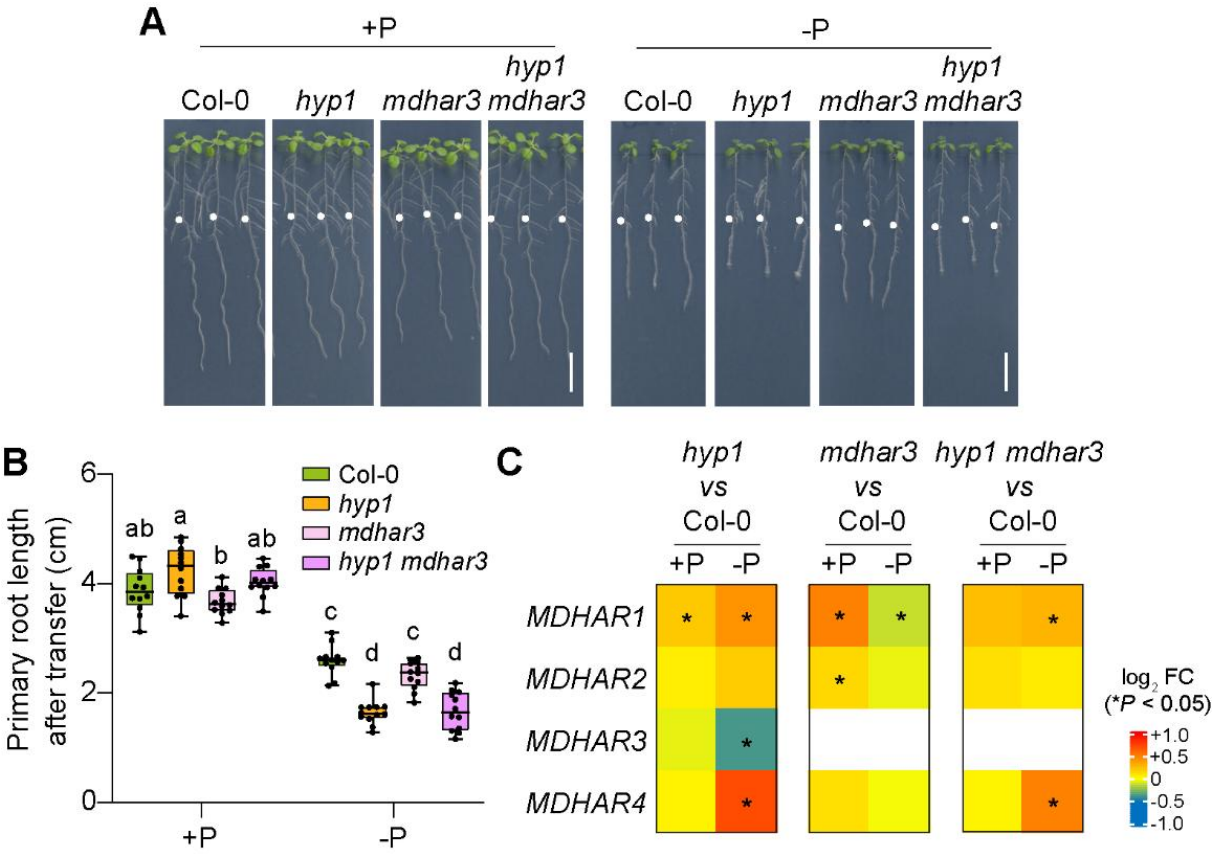

Figure 40. Phenotyping of *hyp1* and *mdhar* single and double mutants.

Appearance (**A**) and primary root length (**B**) of wild-type (Col-0), *hyp1* and *mdhar3* single mutants, and *hyp1 mdhar3* double mutant grown for 6 days on sufficient or low P (+P or -P, respectively). Seven-day-old seedlings were transferred to fresh medium containing 625 µM P (+P) or 5 µM P (-P) with 75 µM Fe-EDTA and analyzed after 6 days. This experiment was conducted before the light-shielded root system was developed and, therefore, roots in this experiment were exposed to light. White dots indicate the position of the primary roots at the day of transfer. Data are presented as boxplots with each dot representing the datapoint of one biological replicate. For the boxplots, central horizontal lines, median; edges of boxes, 25th (bottom) and 75th (top) percentiles; whiskers, minimum and maximum. The letters indicate significant differences (one-way ANOVA followed by post-hoc Tukey's test, $P < 0.05$; $n = 12$ independent roots). Scale bars, 1 cm. (**C**) Heatmap showing relative expression in $\log_2$ fold-change (FC) of the cytosolic *MDHAR* genes analysed by qPCR from *hyp1*, *mdhar3*, and *hyp1 mdhar3* double mutant *versus* Col-0 grown on sufficient- and low-P conditions for 6 d. Asterisks indicate $P < 0.05$ according to two-tailed Student's *t*-test ($n = 3$ independent replicates containing 12 roots each). Blank spaces indicate no gene expression was detected.

In order to assess whether any of the other predicted cytosolic MDHARs is transcritionally induced when *HYP1* and/or *MDHAR3* are disrupted, a qPCR analysis of roots of single and double mutants of *hyp1* and *mdhar3* grown on sufficient- and low-P supply was performed. Relative to Col-0, the expression of *MDHAR1* was significantly induced under both P conditions in *hyp1* roots (Figure 40C, left panel). Interestingly, when *hyp1* was grown under low P, the expression of *MDHAR3* was significantly repressed, whereas *MDHAR4* was induced (Figure 40C, left panel). The disruption of *MDHAR3*, in turn, upregulated the expression of *MDHAR2* and especially *MDHAR1* under +P while under -P *MDHAR1* was slightly downregulated (Figure 40C, center panel). Finally, only *MDHAR1* and *MDHAR4* were significantly upregulated in roots under low P when both *HYP1* and *MDAHR3* were absent (Figure 40C, right panel). Taken together, these results indicate that disruption of *HYP1* or *MDHAR3* changes the transcriptional profile of cytosolic *MDHAR*s. Moreover, the similar phenotype between *hyp1 mdhar3* and *hyp1* mutant plants indicates that both proteins act in the same pathway.

To investigate the effect of MDHAR3 in the tolerance of primary roots to low P, the *35S::MDHAR3* construct was introduced into the Col-0 background. Overexpression of *MDHAR3* did not improve tolerance to low P, as the primary root length of two independent *MDHAR3*-overexpressing lines was comparable or even significantly shorter than in wild-type plants irrespective of the P supply (Figure 41A and B). To further investigate the interplay between MDHAR3 and HYP1, transgenic lines ectopically expressing *MDHAR3* in the *hyp1* background were generated. As shown in Figure 41C and D, *MDHAR3* overexpression did not rescue the short-root phenotype of *hyp1* under low P. Overall, these results indicate that MDHAR3 and HYP1 work in the same pathway and that the activity of MDHAR3 in the wild-type plant is not limiting for HYP1.

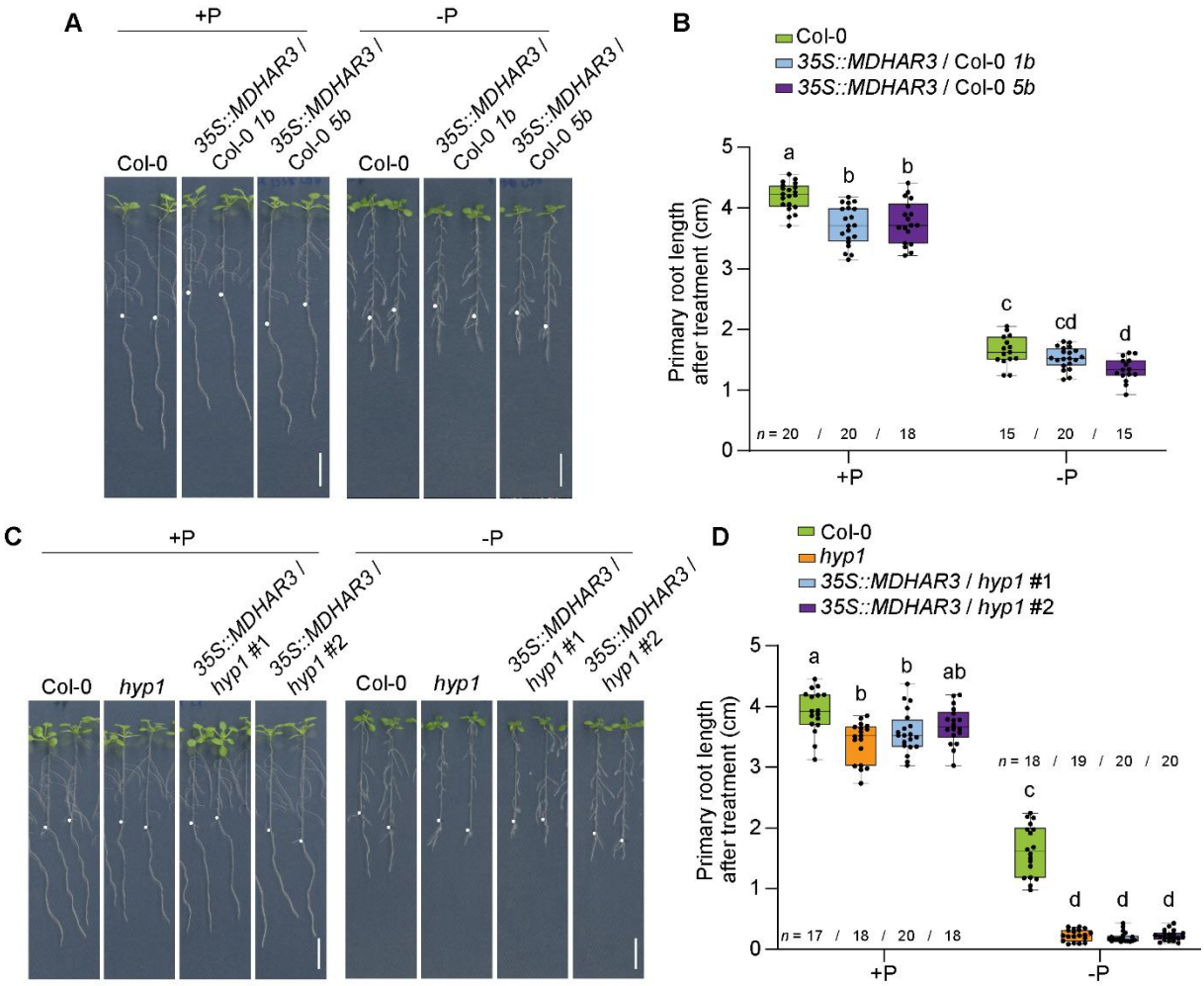

Figure 41. Phenotypic analysis of plants overexpressing *MDHAR3*.

Appearance of plants (**A** and **C**) and primary root length (**B** and **D**) of wild-type (Col-0), *hyp1* mutant, and two independent transgenic lines expressing *35S::MDHAR3* in Col-0 or *hyp1* mutant grown for 6 day on sufficient or low P (+P or -P, respectively). Ten-day-old seedlings were transferred to a fresh medium containing 625 µM P (+P) or 5 µM P (-P) with 150 µM $FeCl_3$ and analyzed after 6 days. White dots indicate the position of the primary roots at the day of transfer. Data are presented as boxplots with each dot representing the datapoint of one biological replicate. For the boxplots, central horizontal lines, median; edges of boxes, 25th (bottom) and 75th (top) percentiles; whiskers, minimum and maximum. The letters indicate significant differences (one-way ANOVA followed by post-hoc Tukey's test, $P < 0.05$; n = 15-20 (**B**), n = 20 (**D**) independent plants). Scale bars, 1 cm (**A** and **C**).

In whole roots, P deficiency significantly upregulates the expression of genes involved with ascorbate biosynthesis (Mora-Macías et al., 2017; Figure 4C) and increases total ascorbate concentrations (Tyburski et al., 2012). To determine whether ascorbate concentration and redox state are altered specifically in root tips, where HYP1 function is more critical to sustain root growth under low P (Figure 35), 0.5-mm long segments of the root apex were collected and subjected to UHPLC-MS-based determination of ASC (reduced form of ascorbate) and DHA (oxidized form of ascorbate). The total ascorbate (*i.e.*, ASC + DHA) concentration did not significantly change in response to P supply (Figure 42A). However,

when discriminating ASC and DHA pools, it was found that whereas the reduced ascorbate concentration did not change, DHA levels were 2-fold higher under -P compared to +P (Figure 42B). This suggested that P deficiency shifted the ascorbate pools towards the oxidized form. Interestingly, in root tips of *HYP1*-overexpressing plants, the concentration of the oxidized form was significantly higher than the reduced form (Figure 42C).

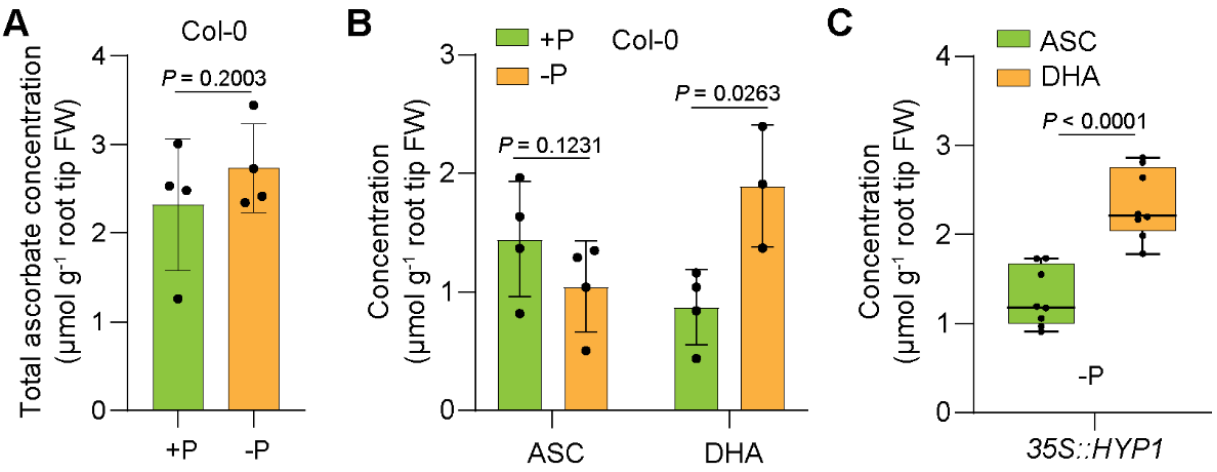

Figure 42. Quantification of ascorbate pools in root tips.

Concentrations of total ascorbate (**A**) or reduced and oxidized ascorbate (ASC and DHA, respectively) (**B**) in root tips of Arabidopsis Col-0 plants after transfer to low or sufficient P (-P or +P, respectively) for 6 days. Bars represent means ± s.d. (n = 3-4 independent replicates). P values were calculated according to one-sided Student's t-test. (**C**) Concentration of reduced and oxidized ascorbate pools (ASC and DHA, respectively) in root tips of plants overexpressing *HYP1* after transfer to low P conditions (-P) for 6 days. Data are presented as boxplots with each dot representing the data point of one biological replicate. For the boxplots, the horizontal line represents the median; edges of boxes indicate the 25th (bottom) and 75th (top) percentiles; whiskers represent the minimum and maximum values. Letters indicate significant differences (one-way ANOVA followed by post-hoc Tukey's test, $P < 0.05$, n = 8 independent replicates). FW, fresh weight.

6 Discussion

To mobilize sparingly available Pi from the soil, many plant species secrete malate to release Pi sorbed onto Al and Fe (hydro)oxides (Shen et al., 2011). In the presence of Fe, the release of malate and the combined ferroxidase activity of LPRs can provoke Fe overaccumulation in the root apoplast, triggering a series of Fe-dependent redox reactions that inhibit root growth (Müller et al., 2015). Since disruption of LPR1 and LPR2 was previously shown to alleviate low P-dependent primary root growth inhibition (Svistoonoff et al., 2007; Müller et al., 2015), it was hypothesized that a putative mechanism of Fe(III) reduction could be critical for balancing the redox state of Fe in the root apoplast and sustaining root growth on P-scarce conditions. Therefore, the present study aimed at identifying new molecular players involved in Fe homeostasis and root growth maintenance in response to low Pi availability. By combining transcriptomics, reverse genetics and Fe-staining methods, the present thesis identified and characterized two novel players underlying the local response of roots to low P. While MDHAR3 is likely involved in the regeneration of cytosolic pools of ascorbate, HYP1 mediates ascorbate-dependent trans-plasma membrane electron transport to reduce ferric and cupric substrates located in the apoplast. Together, the results from this thesis allowed to propose a working model depicting how ascorbate-driven ferric reduction by HYP1 counteracts malate-induced Fe(III) solubilization in the apoplast to prevent meristem disintegration (Figure 43).

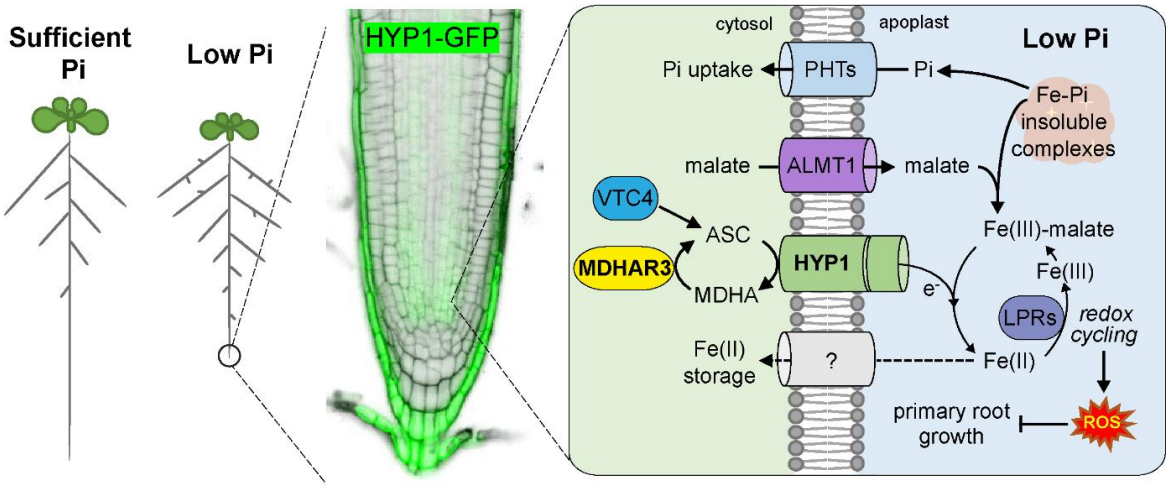

Figure 43. Hypothetical model for MDHAR3- and HYP1-mediated electron transfer for ascorbate-dependent apoplastic redox regulation in root adaptation to low-P conditions.

Increased ALMT1-mediated release of malate in response to P deficiency mobilizes Pi from Fe-Pi insoluble complexes while increasing the apoplastic concentration of Fe(III)-malate complexes. Ascorbate-driven ferric reduction by HYP1 allows that the excess Fe is taken up by a yet unknown root tip-expressed Fe(II) transporter. Depletion of soluble Fe can prevent its participation in redox cycling reactions in the apoplast that trigger aberrant callose deposition in the root apical meristem. Increased transcription and activity of ascorbate biosynthesis and cytosolic ascorbate recycling enzymes (VTC4 and MDHAR3, respectively) in P-deprived roots suggest the role of ascorbate on root tip maintenance against high availability of Fe(III). ROS, reactive oxygen species; PHTs, phosphate transporters; ASC, ascorbate; MDHA, monodehydroascorbate; e^-, electron.

6.1 CYBDOMs as novel metalloreductase in plants

In all living organisms, Fe(III) reduction is key to several processes that maintain Fe homeostasis, including Fe uptake, allocation and storage. In plant roots, ferric ions can be reduced chemically via redox molecules, such as coumarins or ascorbate (section 6.2), or enzymatically via the activity of membrane-bound enzymes, such as flavo-cytochromes of the ferric-chelate reductase oxidase (FRO) family (Yi and Guerinot, 1996; Waters et al., 2002; Li et al., 2004; Wu et al., 2005; Wang et al., 2013). While genes involved in coumarin biosynthesis are upregulated under Fe deficiency (Schmidt et al., 2014), they are downregulated under P deficiency (Figure 4C and Figure 31C), possibly due to the increased availability of Fe in the rhizosphere. Indeed, it was previously shown that P deficiency inhibits root coumarin secretion in *A. thaliana* (Ziegler et al., 2016). Because the expression of genes involved in coumarin biosynthesis is downregulated in P-deficient roots, these phenolic-derived compounds probably do not play a critical role in Fe(III) reduction in this scenario.

FRO-type metalloreductases are exclusively located in cellular membranes and are responsible for the transfer of electrons from an intracellular donor, such as NAD(P)H, to the extracellular acceptors Fe(III), Cu(II) or molecular oxygen (Robinson et al., 1999). The genome of *A. thaliana* harbors in total eight *FRO* genes, which are expressed across different tissues and cell compartments, playing specific roles depending on their localization. *FRO2*, *FRO3* and *FRO5* are expressed in the roots (Connolly et al., 2003), *FRO6*, *FRO7*, and *FRO8* are mainly localized in the shoots, whereas *FRO1* and *FRO4* are localized both in roots and shoots (Wu et al., 2005; Mukherjee et al., 2006; Jeong and Guerinot, 2009; Hindt and Guerinot, 2012; Jain et al., 2014). FRO2 was the first ferric-chelate reductase identified in Arabidopsis (Robinson et al., 1999). Together with IRON REGULATED TRANSPORTER1 (IRT1) and Fe deficiency-induced H^+-ATPases (AHA2), FRO2 represents one of the main constituents of the strategy-I Fe uptake machinery in non-gramineous plants (Chaney et al., 1972; Römheld, 1987). Except for FRO8, which is predicted to localize mitochondrial endomembranes (Heazlewood et al., 2004), all *FRO* genes are upregulated in response to Fe deficiency (Colangelo and Guerinot, 2004; Jakoby et al., 2004; Yuan et al., 2005), but repressed or non-responsive to P deficiency (Figure 4C). For instance, despite *FRO3* being present in the root apical meristem, its gene expression is only detected in Fe-deficient roots (Mukherjee et al., 2006). Therefore, it appeared unlike that any member of the FRO family mediates ferric reduction and/or Fe redox cycling in P-deficient roots.

Apart from FRO proteins, plants also encode for proteins containing a cytochrome *b*561 domain, which is common in several Fe(III) reductases active in animal cells, such as the human duodenal cytochrome *b* (Dcyt*b*) involved with dietary non-heme Fe uptake (McKie et

al., 2001; Ganasen et al., 2018). However, the plant counterparts of these putative Fe(III) reductases have not yet been functionally characterized. In plants, the cytochrome *b*561 domain can occur as a single unit, as in di-heme *b*-containing cytochrome *b*561 proteins called CYBASCs (Asard et al., 2013; Figure 9). In both animals and plants, numerous CYBASC paralogs have been identified (Tsubaki et al., 2005). The cytochrome *b*561 domain can also occur associated with one or more DOMON domains, like in CYBDOM proteins (Asard et al., 2013; Figure 9). Eukaryotic CYBDOMs have been classified into two main groups: group F (further subdivided into F1 and F2) and group G. Members of the F group contain a single DOMON-encoding domain, while CYBDOMs from the G group harbor four DOMONs (*Caenorhabditis elegans*), one DOMON plus a reelin domain (animals), or two DOMON domains plus a DM13 domain (plants) (Asard et al., 2013). Plants contain a larger number of CYBDOM genes than other organisms (Tsubaki et al., 2005; Preger et al., 2009), suggesting that the association of DOMONs with the redox-active cytochrome *b*561 plays an important role in these organisms. In *A. thaliana*, 10 CYBDOMs and one DOMON-only protein (AIR12) are present (Figure 9). The promoter activity of the genes revealed diverse to specific expression patterns under non-stress conditions (Figure 18). Only *HYP1* was significantly regulated in response to P deficiency in roots, being progressively up-regulated as exposure to a low-P medium was prolonged (Figure 10). Disruption of *HYP1* resulted in an even more severe primary root inhibition under low P (Figure 5 and Figure 6), suggesting that the up-regulation of *HYP1* in response to P deficiency is critical to sustain root growth under this stress condition. Although CYBASCs have been implicated in ascorbate recycling (Flatmark and Terland, 1971; Njus and Radda, 1978; Njus, 1983) and Fe uptake (McKie et al., 2001; Zhang et al., 2006; Bérczi et al., 2007; Ludwiczek et al., 2008; Oakhill et al., 2008), the physiological role of a CYBDOM in plants has not yet been demonstrated. Thus, the clear conditional phenotype of the *hyp1* mutant offered, for the first time, the chance to directly investigate the biological role of a plant CYBDOM protein.

The AlphaFold-supported modeling of HYP1 indicated that, unlike CYBASC proteins, which feature six membrane-spanning α-helices connected by short hydrophilic loops (Okuyama et al., 1998; Asard et al., 2000; Ponting, 2001; Bashtovyy et al., 2003; Tsubaki et al., 2005), the cytochrome *b*561 domain of HYP1 is comprised of five hydrophobic regions (Figure 21). As HYP1-GFP was detected in the plasma membrane (Figure 17), the cytochrome *b*561 domain of HYP1 likely spans the plasma membrane. The alignment with CYBASC proteins indicated that HYP1 also possesses four highly conserved His residues, able to coordinate two heme-*b* centers (Figure 21). Such a feature is also observed in FRO2, which presents four highly conserved His residues that coordinate two heme groups situated within the membrane, crucial for the electron transfer process (Robinson et al., 1999; Schagerlöf et

al., 2006). Indeed, electrophysiological assays with *X. laevis* oocytes demonstrated that HYP1 can mediate trans-plasma membrane electron transfer when different ferric substrates (*i.e.*, Fe(III)-CN, Fe(III)-EDTA, Fe(III)-NTA, and Fe(III)-malate) were provided as external electron acceptors, with currents increasing when ascorbate was injected into the oocytes (Figure 19A and B, Figure 24 A and B, Annex Figure 6 A and B, Figure 34 A and B). It is important to note that any variations in electron currents should not be attributed to differences in the redox potential of the Fe compounds, as the reduced electron acceptors that were generated through the interaction with HYP1 were eliminated by the perfusion system. Furthermore, Fe(III) reductase activity of HYP1 was validated *in planta*. By expressing *HYP1* in the *fro2* mutant, it was possible to detect significant HYP1-mediated Fe(III)-chelate reduction activity, which largely prevented the development of severe Fe-deficiency symptoms in *fro2* plants (Figure 24). By the time this work was conducted, CYBDOM ROOT REDUCTION (CRR), another member of the CYBDOM family was also identified and shown to be important for root growth maintenance under low P (Clúa et al., 2024). Expression of *CRR* in the Fe(III) reductase-deficient yeast mutant Δ*fre1* Δ*fre2* cultivated in the presence of a precursor for ascorbate biosynthesis resulted in significantly increased Fe(III) reductase activity with Fe(III)-CN and Fe(III)-malate (Clúa et al., 2024). Together, the characterization of HYP1 and CRR demonstrated the function of CYBDOMs as novel ferric reductases in plants.

Besides the Fe(III) reductase activity, it was further possible to demonstrate that HYP1 can mediate the reduction of cupric substrates. In plants, Cu is involved in redox reactions and plays a role as cofactor for several key enzymes that participate in various important biological processes (Burkhead et al., 2009; Broadley et al., 2012; Ravet and Pilon, 2013). Since Cu is a redox-active transition metal, it is therefore expected that an efficient mechanism of Cu homeostasis and regulation is necessary in plants in order to maintain appropriate cellular levels of this element (Krämer, 2024). In Arabidopsis, Cu is mainly taken up by membrane-bound proteins of the COPPER TRANSPORTER (CTR/COPT) family, composed of six members (Burkhead et al., 2009). COPT1, COPT2 and COPT6 are located at the plasma membrane and responsible for Cu uptake from the soil, while COPT3 and COPT5, which reside in endo-membranes, are involved in internal Cu homeostasis (Sancenón et al., 2003; Sancenón et al., 2004; Jung et al., 2012). In turn, a yeast mutant complementation assay did not find evidence of Cu transport by COPT4 (Sancenón et al., 2003). In the soil solution, Cu is mainly present in its oxidized form [Cu(II)] while the reduced form [Cu(I)] is the substrate of COPTs (Kampfenkel et al., 1995; Lee et al., 2002; Sancenón et al., 2003). Previous studies have pointed out that some FRO-type reductases can mediate cupric reduction for root Cu uptake (Wu et al., 2005; Mukherjee et al., 2006; Bernal et al., 2012). Interestingly, under Cu limitation, while *FRO6* transcription is repressed in shoots, *FRO4* and *FRO5* transcript

abundance was shown to be increased in roots, with both being important for Cu(II) reduction under Cu-deficient conditions (Mukherjee et al., 2006; Bernal et al., 2012). In the present work it was demonstrated that HYP1 can also mediate trans-plasma membrane electron transfer to cupric substrates in oocytes and that root cupric reductase activity is affected when *HYP1* expression is modulated (Figure 25A-C). Other plant CYBDOMs may likely also mediate cupric reduction, as a clear significant decrease in Cu(II) reduction activity was only detected in roots of the *hyp1 crr* double mutant (Figure 25D). Whereas HYP1-mediated Fe(III) reduction was found to be critical for Fe accumulation in roots under low P (section 6.3), it remains to be investigated whether Cu(II) reduction by HYP1 and CRR contributes to Cu uptake or homeostasis. The results obtained so far suggest that HYP1 activity may negatively impact plant tolerance to Cu toxicity, since primary roots were more strongly inhibited by high external Cu concentrations when *HYP1* was overexpressed (Figure 26A and B). Interestingly, higher concentrations of Cu were detected in shoots and roots of *HYP1*-overexpressing lines compared to wild type under low P condition (Annex Figure 7), suggesting that HYP1-mediated Cu(II) reduction affects Cu homeostasis and accumulation in plants.

Another important feature of HYP1 is the presence of the DOMON domain attached to the cytochrome *b*561 domain (Figure 21). The DOMON domain is often associated with domains involved in redox reactions, such as the cytochrome *b*561 in CYBDOMs (Aravind, 2001). Various DOMON domains present in bacteria and fungi have been shown to harbor a *b*-heme coordination site (Hallberg et al., 2000; Kloer et al., 2006). The AIR12 proteins from soybean (*Glycine max*) and Arabidopsis are composed of a single DOMON domain associated to the plasma-membrane via a GPI anchor (Preger et al., 2009). Electron paramagnetic resonance analysis suggested that the DOMON of AIR12 has a *b*-heme coordination site, which can be fully reduced by ascorbate. However, unlike CYBASC proteins, AIR12 can be also reduced by superoxide (O_2^-) and oxidized by either MDHA or oxygen (Preger et al., 2009; Costa et al., 2015). The reduced AIR12 slowly reacts with oxygen, reducing it to O_2^- (Costa et al., 2015). Therefore, AIR12 has been proposed to act as either an antioxidant in its oxidized state or a pro-oxidant in its reduced state depending on the redox status of the plasma membrane and the apoplast (Biniek et al., 2017). Although the precise function of AIR12 is not fully understood, its expression has been associated with superoxide generation at the plasma membrane, regulation of root development, cold tolerance, and resistance to *Botrytis cinerea* (Costa et al., 2015; Gibson and Todd, 2015; Biniek et al., 2017; Wang et al., 2021). The structural modeling presented herein predicts that the DOMON domain of HYP1 can also coordinate one *b*-heme group via an unusual His-Met pair (Figure 21 and Figure 22B). Therefore, it is proposed that HYP1 possess three *b*-hemes, which likely form an electron conduit connecting cytosolic ascorbate with electron acceptors located in the apoplast.

Unfortunately, disruption of the predicted *b*-heme coordination site in the DOMON impaired HYP1 integration in the plasma membrane (Figure 22), preventing the direct investigation of its requirement for trans-plasma membrane electron transport in oocytes and for HYP1 function *in planta*.

6.2 A putative ascorbate-dependent electron transfer mechanism reduces electron acceptors located in the root apoplast

Inhibition of root growth in contact with low external P involves the induction of a redox cycling mechanism. However, while Fe(III) generation was assigned to the activity of cell wall-localized LPR1 and LPR2, it remained elusive how ferric pools generated by LPRs were reduced in P-deficient roots. It has been speculated that apoplastic ascorbate (vitamin C) could reduce the Fe(III) produced by LPR1/LPR2 to initiate Fe redox cycles (Figure 2). In fact, the expression of genes for ascorbate biosynthesis are upregulated in roots in response to P deficiency (Mora-Macías et al., 2017, Figure 4C), with *VTC4* being even a direct target of PHR1 (Rubio et al., 2001; Bustos et al., 2010; Chacón-López et al., 2011; Mora-Macías et al., 2017). To date, the role of ascorbate in Fe homeostasis has only been demonstrated in pea (*Pisum sativum*) embryos (Grillet et al., 2014). Nonetheless, the putative involvement of ascorbate is intriguing, as this molecule can function either as an antioxidant or a pro-oxidant. Ascorbate can directly react with and scavenge major ROS types (Zhang and Zhang, 2013). On the other hand, ascorbate is theoretically also a strong reducing agent for Fe(III) and Cu(II) in the apoplast (Makavitskaya et al., 2018). Thus, apoplastic ascorbate could potentially control the redox state of transition metals as well as transition metals can affect the redox state of ascorbate. A previous study has shown that that the external application of ascorbate to low-P medium was able to prevent low P-induced primary root inhibition of Arabidopsis plants (Tyburski et al., 2012), highlighting the importance of this molecule for plant responses to low P. Moreover, together with differences in the length of the primary root observed at low and high P, changes in root tip ascorbate content and redox status were also observed (Tyburski et al., 2012). Despite these observations, the direct or indirect involvement of ascorbate on primary root growth maintenance and/or Fe homeostasis in the root apoplast in response to low P remained poorly understood.

It was previously reported that a cytochrome *b*561-containing protein possesses putative binding motifs for ascorbate facing the cytosolic side of the membrane (Ganasen et al., 2018). A previous study with one Arabidopsis CYBASC showed that only ascorbate but not vitamin E, glutathione, NADH or NADPH, serves as electron donor for the protein (Lu et al., 2014). In the same study, a high-resolution crystal structure revealed that ascorbate is docked

in a positively charged pocket present in the proximity of the heme-*b* coordination site located in the cytosol-facing part of the protein (Lu et al., 2014). Based on ligand docking predictions, it was possible to identify a putative ascorbate docking site supported by hydrogen bond interactions with the residues R307, N311, and P302 at the cytosol-oriented surface of HYP1's cytochrome *b*561 domain (Figure 21B). In line with the AlphaFold modeling of HYP1 structure, electrophysiological studies in *X. laevis* oocytes injected with HYP1 cRNA indicated that ascorbate but not glutathione serves as the electron donor for HYP1 (Figure 19D and Annex Figure 2B). Thus, both the structure and the electron donor of HYP1 differ in comparison with FROs. Indeed, FRO2 contains a large water-soluble domain, housing NADPH, flavin adenine dinucleotide (FAD), and oxidoreductase sequence motifs, all located in the cytosol-facing side of the protein (Robinson et al., 1999; Schagerlöf et al., 2006).

The upregulation of ascorbate biosynthesis genes in response to P deficiency (Mora-Macías et al., 2017; Figure 4C) suggests that substrate production for CYBDOM-mediated trans-plasma membrane electron transport is increased in P-deficient root cells. In this scenario, ascorbate may indirectly drive Fe(III)-chelate reduction at the plasma membrane besides functioning as a chemical reductant of apoplastic Fe(III) pools as proposed previously (Mora-Macías et al., 2017). However, determining whether the levels and redox state of apoplastic ascorbate in root tips are altered depending on P availability or HYP1 activity still remains a challenge. Therefore, determination of cytosolic ascorbate and its redox state by assessing root tip extracts was conducted instead. Even though P deficiency did not significantly change total cytosolic ascorbate concentrations, cytosolic DHA (the oxidized form of ascorbate) concentrations were significantly higher than ASC (the reduced form of ascorbate) in P-starved roots (Figure 42). Previous research has shown rather opposite results, most likely because the conditions of plant cultivation and the methods utilized for assessing ascorbate were different (Tyburski et al., 2012). Nevertheless, the results presented here suggest that cytosolic ascorbate is oxidized (Figure 19C-E, Figure 21B, and Annex Figure 2A and B), a process that may involve the activity of HYP1.

In plant cells, ascorbate undergoes various levels of chemical conversions (Figure 44). For instance, as the cytosolic ascorbate binds to the cytosol-facing side of HYP1 (Figure 21B), the fully reduced form of the ionized ascorbate (ASC) can donate a hydrogen atom (one electron and one proton), leading to the formation of the relatively unstable radical, monodehydroascorbate (MDHA). If not quickly recycled by the activity of NADH-dependent MONODEHYDROASCORBATE REDUCTASEs (MDHARs) or NADH-dependent cytochrome b_5 reductases (Cytb_5s), MDHA is then oxidized or reacts with itself to produce ASC and dehydroascorbate (DHA). Likewise, if DHA is not recycled and converted back to MDHA by the GSH-dependent DEHYDROASCORBATE REDUCTASE (DHAR), it can be degraded. To

prevent that cytosolic ascorbate pools are decreased, MDHARs and DHARs act to convert oxidized forms of ascorbate to its reduced form in several cellular compartments, including the cytosol (Figure 44).

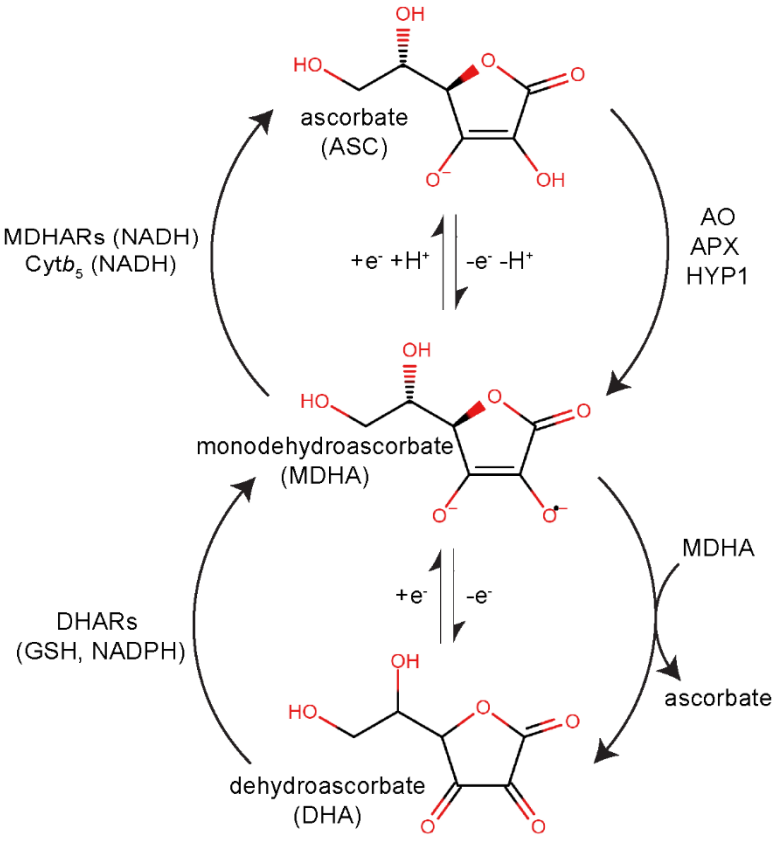

Figure 44. Major pathways of ascorbate recycling in plants.

At pH 7.0 in the cytosol, ascorbate is mostly present in its ionized form (ASC). Its reaction with O_2, H_2O_2, and transition metals [Fe(III) or Cu(II)], via the activity of ascorbate oxidases (AO), ascorbate peroxidases (APX), and cyt*b*561 containing proteins (*e.g.*, HYP1), respectively, forms the chemically unstable radical monodehydroascorbate (MDHA). Further oxidation of MDHA leads to the production of the fully-oxidized molecule dehydroascorbate (DHA). DHA can react with MDHA to form ascorbate, as well as interact with GSH- and NADPH-dependent dehydroascorbate reductases (DHARs) to produce MDHA. In turn, MDHA can be recycled back to ASC via NADH-dependent monodehydroascorbate reductases (MDHARs) in the cytoplasm or NADH-dependent Cytb_5 reductase. Chemical structures were drawn using Chemical Sketch Tool (https://www.rcsb.org/chemical-sketch).

Besides *VTC2* and *VTC4* (Mora-Macías et al., 2017; Figure 4C), the present transcriptome analysis revealed that the monodehydroascorbate reductase-encoding gene *MDHAR3* gene was also highly up-regulated in response to P deficiency (Figure 4C). Similar to *HYP1*, *MDHAR3* expression was progressively induced as cultivation on low-P medium was prolonged (Figure 38). By stably co-expressing the translational fusion HYP1:GFP and MDHAR3:BFP it was possible to demonstrate that MDHAR3 and HYP1 proteins accumulate in P-deficient roots and co-localize especially in the root cap cells of root tips (Figure 39).

Expression of *MDHARs* in response to several conditions of abiotic stress (*e.g.*, high light intensity, cadmium toxicity, drought, heat, and salt treatments) has been already reported in many plant species, including Arabidopsis (Kubo et al., 1999; Leterrier et al., 2005), wild tomato (*Solanum pennellii;* Mittova et al., 2003), tobacco (Gechev et al., 2003), *Oryza sativa* (Oidaira et al., 2000), and *Pinus sylvestris* (Tao et al., 1998). Furthermore, increase in MDHAR activity and in total ascorbate content in response to various oxidative stresses has also been extensively reported in many plant species, such as in conifer needles (Mehlhorn et al., 1986), leaves of wheat (Mishra et al., 1993) and spinach (Schöner and Krause, 1990), and submerged rice seedlings (Ushimaru et al., 1992). However, the involvement of MDHARs in root adaptation to low P or their crosstalk with CYBDOM proteins has not been studied before.

Since the increased activity of HYP1 oxidizes the cytosolic ascorbate pools (Figure 42C), and *MDHAR3* is induced under low P (Figure 4D and Figure 38A and C), it was hypothesized that HYP1 and MDHAR3 might function as an integrated electron transfer mechanism for modulating primary root growth in response to low-P conditions. After assessing primary roots of the *hyp1 mdhar3* double mutant grown on low P, results indicated that *HYP1* and *MDHAR3* are epistatic (Figure 40). Moreover, by assessing gene expression of single and double mutants for *HYP1* and *MDHAR3*, it was shown that MDHARs may present functional redundancy among them; for instance, when *MDHAR3* is disrupted, *MDHAR1*/*2* are upregulated at least under control conditions (Figure 40C) The present results suggest further that the activity of HYP1 is determinant for the overall growth of primary roots under P-scarce conditions. Since the results using oocytes showed that high concentrations of reduced ascorbate in the cytosol induce high Fe(III) reduction outside the cells (Figure 19), it was hypothesized that fast ascorbate recycling is necessary to maintain high HYP1 activity. However, overexpression of *MDHAR3* in wild-type background did not improve root growth under low P (Figure 41). Previous studies involving the ectopic expression of *MDHARs* reported increased tolerance to freezing stress in *Brassica rapa* plants (Shin et al., 2013), while silencing *MDHAR* genes in So*lanum lycopersicum* led to decreased plant growth and yield (Truffault et al., 2016). Because *HYP1*-overexpressing P-deficient roots were shown to favor the conversion of reduced pools of cytosolic ascorbate to oxidized ascorbate (Figure 42C), one should expect that a higher activity of MDHAR3-dependent cytosolic ascorbate recycling would improve primary root growth of plants with high HYP1 activity. Following this idea, future studies should assess the cytosolic concentrations of reduced and oxidized ascorbate in root tips of the *mdhar3* mutant and *MDHAR3*-overexpressing plants. Nonetheless, the P-dependent regulation and the partial co-localization of MDHAR3 and HYP1 in several cells in the meristem suggest that both proteins act in concert, with MDHAR3 maintaining sufficient cytosolic pools of reduced ascorbate for undisturbed HYP1 function (Figure 43).

6.3 HYP1 counteracts malate-induced Fe accumulation in P-deprived roots

The accumulation of soluble Fe(III)-malate complexes in the apoplast of root tips has been proposed as a key determinant to the inhibition of primary root growth under low-P conditions (Balzergue et al., 2017; Mora-Macías et al., 2017). Once mobilized, Fe is more prone to engage in redox cycling reactions, producing ROS and triggering aberrant callose deposition (Müller et al., 2015). The ability of cells in the root apical meristem to store Fe in the apoplast in a less reactive form likely becomes more limited as apoplastic Pi pools get depleted (Müller et al., 2015). Based on these findings, it was hypothesized that HYP1-mediated Fe(III) reduction prevents excessive accumulation of malate-mobilized Fe in the apoplast. Indeed, while roots of *hyp1* mutant plants exhibited strong accumulation of Fe in the apoplast under low P, almost no stainable apoplastic Fe was detected in the primary root meristem of plants overexpressing *HYP1* (Figure 8 and Figure 29). Another evidence that supports this idea is presented in Figure 33, which shows that HYP1 activity was critical only when ALMT1 and LPRs were active in root tips. Thus, these results indicated that HYP1 activity was required to counteract the malate-induced Fe accumulation in P-deprived roots and, therefore, to maintain growth and integrity of roots exposed to a low-P medium containing Fe (Figure 33). Moreover, the cell type-specific complementation of *hyp1* mutant indicated that HYP1 activity is especially critical around the stem cell niche and in early cortical and endodermal cells in the proximal root apical meristem, where HYP1 is indispensable to maintain meristem integrity and root growth (Figure 35A-E). It is within this zone that *HYP1* expression and protein accumulation is most strongly induced in response to low P and where increased callose deposition is detected in the root apical meristem of *hyp1* plants (Figure 4B-C and Figure 28B-C). Thus, in the context of P deficiency, the function of HYP1 appears to be less critical to support whole-plant Fe nutrition but rather to maintain Fe homeostasis in root tips. These findings suggested that the reductase activity of HYP1 effectively controls apoplastic Fe pools, thereby protecting the sensitive root meristem from malate-induced Fe stress under low P availability.

Like HYP1, also CRR was shown to be critical for root growth under low P. This CYBDOM was identified within a set of differentially abundant proteins from a proteomic analysis of a double mutant for the ER chaperones CALNEXIN1 and 2. Here, the characterization of a generated *hyp1 crr* double mutant revealed that disruption of both CYBDOMs resulted in even higher sensitivity to low P (Figure 6 and Figure 7). Although these results may indicate the existence of functional redundancy between HYP1 and CRR, it is also possible that the two proteins play partially non-overlapping functions. In fact, while disruption of *CRR* also leads to increased Fe accumulation in the root meristem, it only negatively affects

meristem length and not mature cell length (Clúa et al., 2024). However, neither Clúa et al. (2024) nor the present study (Figure 18) was able to detect clear *CRR* promoter activity in the primary root tip. Nonetheless, considering the large number of CYBDOMs and the partially overlapping tissue-specific expression domains, high functional redundancy among CYBDOMs is expected.

Interestingly, the main strategy-I mechanism of Fe uptake formed by FRO2 and IRT1 is not present in the root meristem and elongation zone (Vert et al., 2002; Connolly et al., 2003). Although future studies with Fe tracers will be required to quantify the Fe uptake capacity of cells within these two zones, it was hypothesized that an enzyme-mediated ferric reduction, independent of HYP1, would be enough to maintain root growth under low P. To test this hypothesis, one initial attempt was made to complement *hyp1* by expressing *FRO2* in the primary root meristem. As shown in Annex Figure 8, *proHYP1*-driven expression of *FRO2* in the *hyp1* mutant did not complement the short-root phenotype of *hyp1* plants under low P (Annex Figure 8). However, it remains to be determined whether FRO2 was indeed accumulating in meristematic cells and, if so, correctly targeted to the plasma membrane in these cells. Thus, other approaches were used to investigate the proposed link between ferric reduction and low P tolerance, such as the cultivation of plants with an Fe(II) source. Since it was possible to rescue the short-root phenotype of *hyp1* plants by supplying $FeCl_2$ to the low-P medium, ferric reduction appears indeed to be critical for primary root growth maintenance under low P (Figure 37A-C). Another approach that supports that HYP1-mediated apoplastic Fe reduction is necessary in the root response to low P availability is shown in Figure 36E-F, where higher levels of Fe(II) were detected in P-deficient root tips with increased HYP1 activity compared to those which HYP1 is absent.

Ferric reduction at the plasma-membrane surface could provide ferrous ions for uptake via a yet uncharacterized Fe uptake mechanism active in the root meristem. The HYP1-dependent disappearance of apoplastic Fe in root tips of P-deficient roots (Figure 28), provides initial evidence for the existence of such mechanism. Furthermore, the expression of *VACUOLAR IRON TRANSPORTER 1* (*VIT1*) was significantly up-regulated in roots of *35S::HYP1* plants (Figure 31C). VIT1 is a tonoplast-located Fe transporter involved with Fe import into the vacuoles (Kim et al., 2006; Gollhofer et al., 2014). The upregulation of *VIT1* in roots of *35S::HYP1* plants, which exhibit less stainable Fe in the apoplast (Figure 28), might indicate that storage of Fe in the vacuoles is stimulated. Another independent evidence for possible Fe internalization in P-deprived root tips was presented in Figure 37D-E. After treating plants shortly with a low P-medium containing a promptly available source of Fe (in the form of $FeCl_2$), followed by Perls/DAB staining of Fe, stainable Fe was concentrated in internal dot-like structures (Figure 37D-E). Whether these structures refer to Fe being stored in vacuoles

or ferritins remains to be confirmed. Nevertheless, these results further support the existence of a root tip-active mechanism of Fe uptake or detoxification in P-deficient roots as a protective mechanism against the excessive accumulation of malate-mobilized Fe in the apoplast.

The upregulation of *HYP1* in P-deficient roots indicates that this proposed root tip-active Fe acquisition mechanism is under a different regulation than FRO2 and IRT1 in the root hair zone. One possibility to explain this difference is that cells in the root apex are more sensitive to Fe-triggered radical formation in the apoplast (Müller et al., 2015; Liu et al., 2022a; Liu et al., 2022b; Naumann et al., 2022). Such Fe-dependent modulation of root growth may attenuate growth of roots in contact with low P-containing soil patches and increase exploration of P in the topsoil. In the root apex, *LPR1* and *ALMT1* are expressed in the stem cell niche and early cortical and endodermal cells (Müller et al., 2015; Mora-Macías et al., 2017; Naumann et al., 2022), thus partially overlapping with *HYP1* under low-P conditions. Since the activity of the multicopper oxidase LPR1 maintains higher Fe levels in the apoplast and the malate secreted by ALMT1 facilitates Fe(III) mobilization (Müller et al., 2015; Mora-Macías et al., 2017), this potentially increases the risk that apoplastic Fe engages in redox cycling and ROS formation. In this context, HYP1-mediated Fe(III) reductase activity may either supply or, if the formed Fe(II) is immediately taken up, remove the substrate for LPR1. The first scenario can be supported by the fact that wild-type and *HYP1*-overexpressing plants exposed to low P presented increased accumulation of Fe(II) in the root tips compared to *hyp1* mutant (Figure 36E and F). Alternatively, accumulating Fe(II) may potentially be used by LPR1 to generate Fe(III), thereby closing the Fe-dependent redox cycle in the apoplast. However, since lower Fe pools were detected in P-deficient root tips of wild-type plants compared to *hyp1* mutant (Figure 36A and B), it seems that the second scenario is more likely to occur. In this case, these results suggest that Fe(III) reduction by HYP1 could help plants to fine tune root growth in low-P soils while simultaneously protecting root apical meristem integrity against P deficiency-induced Fe toxicity.

Recent discoveries have linked certain plant CYBDOMs with auxin-regulated peroxidases, laccases, and GDSL-motif-containing lipases expressed in root endodermal cells, suggesting potential coregulation pathways (Ursache et al., 2021). Investigating whether plant CYBDOMs can influence cell wall composition or properties, alongside their ability to reduce various apoplastic electron acceptors, poses intriguing questions. Furthermore, CYBDOMs may also function in ascorbate recycling in the apoplast. In fact, it has been recently shown that the cytochrome *b*561 protein *CYB561A* mediates electron transport from vacuolar ascorbate to cytosolic monodehydroascorbate (Gradogna et al., 2023). Disruption of *CYB561A* almost completely abolished trans-tonoplast electron currents elicited by ascorbate and FeCN in isolated vacuoles and significantly increased leaf anthocyanin accumulation under

excessive illumination. Another recent study has reported the role of OsCYBDOMG1 in the regulation of salt tolerance, plant growth, and grain yield in rice (*Oryza sativa* L. ssp. *japonica*) by positively affecting ascorbate biosynthesis and redox state (Deng et al., 2023). Furthermore, investigations into the cooperation between proton pumps and plasma membrane redox systems have unveiled potential energy dissipation pathways, such as the proposed involvement of a plasma membrane isoform of CYB561 in excess light energy dissipation in wild watermelon (*Citrullus lanatus*) (Nanasato et al., 2005). Regardless of the specific physiological electron acceptors involved, CYBDOMs are emerging as critical components of a membrane-bound redox system in plants.

Taken together, by examining the phenotypic alterations resulting from modified *HYP1* expression at the organismal level, this study illuminates the physiological roles of the so far poorly characterized CYBDOM proteins. More specifically, the present thesis elucidated the role of a novel ascorbate-dependent mechanism constituted by a plasma membrane-bound metalloreductase and a cytosolic ascorbate recycling enzyme, suggesting a model in which MDAHR3 and, especially, HYP1 modulate Fe accumulation and Fe-dependent growth of roots exposed to external medium with limited P availability (Figure 43). The present evidence indicates that the uncovered ascorbate-dependent mechanism protects the root apical meristem against deleterious effects of the malate-driven Fe accumulation induced in root tips in response to P deficiency.

7 References

Abel, S. (2011). Phosphate sensing in root development. *Curr Opin Plant Biol* **14**:303–309.

Ai, P., Sun, S., Zhao, J., Fan, X., Xin, W., Guo, Q., Yu, L., Shen, Q., Wu, P., Miller, A. J., *et al.* (2009). Two rice phosphate transporters, OsPht1; 2 and OsPht1; 6, have different functions and kinetic properties in uptake and translocation. *The Plant Journal* **57**:798–809.

Alewell, C., Ringeval, B., Ballabio, C., Robinson, D. A., Panagos, P., and Borrelli, P. (2020). Global phosphorus shortage will be aggravated by soil erosion. *Nat Commun* **11**:4546.

Arai, Y., and Sparks, D. L. (2007). Phosphate reaction dynamics in soils and soil components: A multiscale approach. *Advances in agronomy* **94**:135–179.

Aravind, L. (2001). DOMON: an ancient extracellular domain in dopamine β-monooxygenase and other proteins. *Trends Biochem Sci* **26**:524–526.

Arnaud, C., Bonnot, C., Desnos, T., and Nussaume, L. (2010). The root cap at the forefront. *C R Biol* **333**:335–343.

Asard, H., Terol-Alcayde, J., Preger, V., Del Favero, J., Verelst, W., Sparla, F., Pérez-Alonso, M., and Trost, P. (2000). *Arabidopsis thaliana* sequence analysis confirms the presenceof cyt *b*-561 in plants: Evidence for a novel protein family. *Plant Physiology and Biochemistry* **38**:905–912.

Asard, H., Barbaro, R., Trost, P., and Bérczi, A. (2013). Cytochromes *b* 561: ascorbate-mediated trans-membrane electron transport. *Antioxid Redox Signal* **19**:1026–1035.

Aung, K., Lin, S.-I., Wu, C.-C., Huang, Y.-T., Su, C., and Chiou, T.-J. (2006). *pho2*, a phosphate overaccumulator, is caused by a nonsense mutation in a *microRNA399* target gene. *Plant Physiol* **141**:1000–1011.

Austin, S., and Mayer, A. (2020). Phosphate homeostasis- a vital metabolic equilibrium maintained through the INPHORS signaling pathway. *Front Microbiol* **11**:539723.

Bajželj, B., Richards, K. S., Allwood, J. M., Smith, P., Dennis, J. S., Curmi, E., and Gilligan, C. A. (2014). Importance of food-demand management for climate mitigation. *Nat Clim Chang* **4**:924–929.

Balzergue, C., Dartevelle, T., Godon, C., Laugier, E., Meisrimler, C., Teulon, J.-M., Creff, A., Bissler, M., Brouchoud, C., Hagege, A., *et al.* (2017). Low phosphate activates STOP1-ALMT1 to rapidly inhibit root cell elongation. *Nat Commun* **8**:15300.

Bari, R., Datt Pant, B., Stitt, M., and Scheible, W.-R. (2006). PHO2, microRNA399, and PHR1 define a phosphate-signaling pathway in plants. *Plant Physiol* **141**:988–999.

Bashtovyy, D., Bérczi, A., Asard, H., and Páli, T. (2003). Structure prediction for the di-heme cytochrome *b* 561 protein family. *Protoplasma* **221**:31–40.

Bérczi, A., Su, D., and Asard, H. (2007). An Arabidopsis cytochrome *b*561 with trans-membrane ferrireductase capability. *FEBS Lett* **581**:1505–1508.

Bernal, M., Casero, D., Singh, V., Wilson, G. T., Grande, A., Yang, H., Dodani, S. C., Pellegrini, M., Huijser, P., Connolly, E. L., *et al.* (2012). Transcriptome sequencing identifies SPL7-regulated copper acquisition genes FRO4/FRO5 and the copper dependence of iron homeostasis in Arabidopsis. *Plant Cell* **24**:738–761.

Bhosale, R., Giri, J., Pandey, B. K., Giehl, R. F. H., Hartmann, A., Traini, R., Truskina, J., Leftley, N., Hanlon, M., Swarup, K., *et al.* (2018). A mechanistic framework for auxin dependent Arabidopsis root hair elongation to low external phosphate. *Nat Commun* **9**:1409.

Bieleski, R. L., and Ferguson, I. B. (1983). Physiology and metabolism of phosphate and its compounds. In *Inorganic plant nutrition*, pp. 422–449. Springer.

Biniek, C., Heyno, E., Kruk, J., Sparla, F., Trost, P., and Krieger-Liszkay, A. (2017). Role of the NAD (P) H quinone oxidoreductase NQR and the cytochrome b AIR12 in controlling superoxide generation at the plasma membrane. *Planta* **245**:807–817.

Birnbaum, K., Shasha, D. E., Wang, J. Y., Jung, J. W., Lambert, G. M., Galbraith, D. W., and Benfey, P. N. (2003). A gene expression map of the Arabidopsis root. *Science (1979)* **302**:1956–1960.

Blilou, I., Xu, J., Wildwater, M., Willemsen, V., Paponov, I., Friml, J., Heidstra, R., Aida, M., Palme, K., and Scheres, B. (2005). The PIN auxin efflux facilitator network controls growth and patterning in Arabidopsis roots. *Nature* **433**:39–44.

Borrelli, P., Robinson, D. A., Panagos, P., Lugato, E., Yang, J. E., Alewell, C., Wuepper, D., Montanarella, L., and Ballabio, C. (2020). Land use and climate change impacts on global soil erosion by water (2015-2070). *Proceedings of the National Academy of Sciences* **117**:21994–22001.

Bowman, R. A., and Cole, C. V (1978). Transformations of organic phosphorus substrates in soils as evaluated by $NaHCO_3$ extraction. *Soil Sci* **125**:49–54.

Broadley, M., Brown, P., Cakmak, I., Rengel, Z., and Zhao, F. (2012). Function of nutrients: micronutrients. In *Marschner's mineral nutrition of higher plants*, pp. 191–248. Elsevier.

Burkhead, J. L., Gogolin Reynolds, K. A., Abdel-Ghany, S. E., Cohu, C. M., and Pilon, M. (2009). Copper homeostasis. *New Phytologist* **182**:799–816.

Bustos, R., Castrillo, G., Linhares, F., Puga, M. I., Rubio, V., Pérez-Pérez, J., Solano, R., Leyva, A., and Paz-Ares, J. (2010). A central regulatory system largely controls transcriptional activation and repression responses to phosphate starvation in Arabidopsis. *PLoS Genet* **6**:e1001102.

Carpenter, S. R., and Bennett, E. M. (2011). Reconsideration of the planetary boundary for phosphorus. *Environmental Research Letters* **6**:14009.

Catarecha, P., Segura, M. D., Franco-Zorrilla, J. M., García-Ponce, B., Lanza, M., Solano, R., Paz-Ares, J., and Leyva, A. (2007). A mutant of the Arabidopsis phosphate transporter PHT1; 1 displays enhanced arsenic accumulation. *Plant Cell* **19**:1123–1133.

Chacón-López, A., Ibarra-Laclette, E., Sánchez-Calderón, L., Gutiérrez-Alanís, D., and Herrera-Estrella, L. (2011). Global expression pattern comparison between low phosphorus insensitive 4 and WT Arabidopsis reveals an important role of reactive oxygen species and jasmonic acid in the root tip response to phosphate starvation. *Plant Signal Behav* **6**:382–392.

Chaney, R. L., Brown, J. C., and Tiffin, L. O. (1972). Obligatory reduction of ferric chelates in iron uptake by soybeans. *Plant Physiol* **50**:208–213.

Chen, D. L., Delatorre, C. A., Bakker, A., and Abel, S. (2000). Conditional identification of phosphate-starvation-response mutants in *Arabidopsis thaliana*. *Planta* **211**:13–22.

Cheng, H. Y., Sanusi, S., and Bin Othman, S. (2020). Effect of Christmas Island rock phosphate and rice straw compost application on soil phosphorus availability and maize (Zea mays L.) growth in a tropical acid soil of Kelantan, Malaysia. *Open Agric* **5**:150–158.

Clough, S. J., and Bent, A. F. (1998). Floral dip: a simplified method for Agrobacterium-mediated transformation of *Arabidopsis thaliana*. *The Plant Journal* **16**:735–743.

Clúa, J., Montpetit, J., Jimenez-Sandoval, P., Naumann, C., Santiago, J., and Poirier, Y. (2024). A CYBDOM protein impacts iron homeostasis and primary root growth under phosphate deficiency in Arabidopsis. *Nat Commun* **15**:423.

Colangelo, E. P., and Guerinot, M. Lou (2004). The essential basic helix-loop-helix protein FIT1 is required for the iron deficiency response. *Plant Cell* **16**:3400–3412.

Connolly, E. L., Campbell, N. H., Grotz, N., Prichard, C. L., and Guerinot, M. Lou (2003). Overexpression of the FRO2 ferric chelate reductase confers tolerance to growth on low iron and uncovers posttranscriptional control. *Plant Physiol* **133**:1102–1110.

Cordell, D., Rosemarin, A., Schröder, J. J., and Smit, A. L. (2011). Towards global phosphorus security: A systems framework for phosphorus recovery and reuse options. *Chemosphere* **84**:747–758.

Costa, A., Barbaro, M. R., Sicilia, F., Preger, V., Krieger-Liszkay, A., Sparla, F., De Lorenzo, G., and Trost, P. (2015). AIR12, a *b*-type cytochrome of the plasma membrane of *Arabidopsis thaliana* is a negative regulator of resistance against Botrytis cinerea. *Plant Science* **233**:32–43.

Daram, P., Brunner, S., Rausch, C., Steiner, C., Amrhein, N., and Bucher, M. (1999). Pht2; 1 encodes a low-affinity phosphate transporter from Arabidopsis. *Plant Cell* **11**:2153–2166.

Delhaize, E., and Randall, P. J. (1995). Characterization of a phosphate-accumulator mutant of *Arabidopsis thaliana*. *Plant Physiol* **107**:207–213.

Deng, P., Cao, C., Shi, X., Jiang, Q., Ge, J., Shen, L., Guo, C., Jiang, L., Jing, W., and Zhang, W. (2023). OsCYBDOMG1, a cytochrome b 561 domain-containing protein, regulates salt tolerance and grain yield in rice. *Theoretical and Applied Genetics* **136**:76.

Dong, B., Rengel, Z., and Delhaize, E. (1998). Uptake and translocation of phosphate by *pho2* mutant and wild-type seedlings of *Arabidopsis thaliana*. *Planta* **205**:251–256.

Dong, J., Piñeros, M. A., Li, X., Yang, H., Liu, Y., Murphy, A. S., Kochian, L. V, and Liu, D. (2017). An Arabidopsis ABC transporter mediates phosphate deficiency-induced remodeling of root architecture by modulating iron homeostasis in roots. *Mol Plant* **10**:244–259.

Drew, M. C. (1975). Comparison of the effects of a localised supply of phosphate, nitrate, ammonium and potassium on the growth of the seminal root system, and the shoot, in barley. *New phytologist* **75**:479–490.

Duan, K., Yi, K., Dang, L., Huang, H., Wu, W., and Wu, P. (2008). Characterization of a sub-family of Arabidopsis genes with the SPX domain reveals their diverse functions in plant tolerance to phosphorus starvation. *The Plant Journal* **54**:965–975.

Epstein, E., and Bloom, A. J. (2004). *Mineral nutrition of plants: principles and perspectives*. Sinauer.

Fang, Z., Shao, C., Meng, Y., Wu, P., and Chen, M. (2009). Phosphate signaling in Arabidopsis and *Oryza sativa*. *Plant Science* **176**:170–180.

Ferreira, P. C., Hemerly, A. S., Engler, J. D., Van Montagu, M., Engler, G., and Inzé, D. (1994). Developmental expression of the arabidopsis cyclin gene *cyc1At*. *Plant Cell* **6**:1763–1774.

Fitter, A. H., and Hay, R. K. M. (2012). *Environmental physiology of plants*. Academic press.

Flatmark, T., and Terland, O. (1971). Cytochrome *b*561 of the bovine adrenal chromaffin granules. A high potential *b*-type cytochrome. *Biochimica et Biophysica Acta (BBA)-Bioenergetics* **253**:487–491.

Foyer, C. H., Kyndt, T., and Hancock, R. D. (2020). Vitamin C in plants: novel concepts, new perspectives, and outstanding issues. *Antioxid Redox Signal* **32**:463–485.

Franco-Zorrilla, J. M., Martín, A. C., Leyva, A., and Paz-Ares, J. (2005). Interaction between phosphate-starvation, sugar, and cytokinin signaling in Arabidopsis and the roles of cytokinin receptors CRE1/AHK4 and AHK3. *Plant Physiol* **138**:847–857.

Franco-Zorrilla, J. M., Valli, A., Todesco, M., Mateos, I., Puga, M. I., Rubio-Somoza, I., Leyva, A., Weigel, D., García, J. A., and Paz-Ares, J. (2007). Target mimicry provides a new mechanism for regulation of microRNA activity. *Nat Genet* **39**:1033–1037.

Ganasen, M., Togashi, H., Takeda, H., Asakura, H., Tosha, T., Yamashita, K., Hirata, K., Nariai, Y., Urano, T., Yuan, X., *et al.* (2018). Structural basis for promotion of duodenal iron absorption by enteric ferric reductase with ascorbate. *Commun Biol* **1**:120.

Gechev, T., Willekens, H., Van Montagu, M., Inzé, D., Van Camp, W., Toneva, V., and Minkov, I. (2003). Different responses of tobacco antioxidant enzymes to light and chilling stress. *J Plant Physiol* **160**:509–515.

Gerasimaite, R., Pavlovic, I., Capolicchio, S., Hofer, A., Schmidt, A., Jessen, H. J., and Mayer, A. (2017). Inositol pyrophosphate specificity of the SPX-dependent polyphosphate polymerase VTC. *ACS Chem Biol* **12**:648–653.

Gho, Y.-S., and Jung, K.-H. (2019). Comparative expression analyses of rice and Arabidopsis phosphate transporter families revealed their conserved roles for the phosphate starvation response. *Plant Breed Biotechnol* **7**:42–49.

Gibson, S. W., and Todd, C. D. (2015). Arabidopsis AIR12 influences root development. *Physiology and molecular biology of plants* **21**:479–489.

Giehl, R. F. H., Flis, P., Fuchs, J., Gao, Y., Salt, D. E., and Von Wirén, N. (2023). Cell type-specific mapping of ion distribution in *Arabidopsis thaliana* roots. *Nat Commun* **14**:3351.

Gilbert, N. (2014). Environment: The disappearing nutrient. Nature News 461, 716–718. Published in. *Resour Conserv Recycl* **93**:178–187.

Gollhofer, J., Timofeev, R., Lan, P., Schmidt, W., and Buckhout, T. J. (2014). Vacuolar-iron-transporter1-like proteins mediate iron homeostasis in Arabidopsis. *PLoS One* **9**:e110468.

Gonzalez, E., Solano, R., Rubio, V., Leyva, A., and Paz-Ares, J. (2005). PHOSPHATE TRANSPORTER TRAFFIC FACILITATOR1 is a plant-specific SEC12-related protein that enables the endoplasmic reticulum exit of a high-affinity phosphate transporter in Arabidopsis. *Plant Cell* **17**:3500–3512.

Gradogna, A., Lagostena, L., Beltrami, S., Tosato, E., Picco, C., Scholz-Starke, J., Sparla, F., Trost, P., and Carpaneto, A. (2023). Tonoplast cytochrome *b* 561 is a transmembrane ascorbate-dependent monodehydroascorbate reductase: functional characterization of electron currents in plant vacuoles. *New Phytologist* **238**:1957–1971.

Grillet, L., and Schmidt, W. (2017). The multiple facets of root iron reduction. *J Exp Bot* **68**:5021–5027.

Grillet, L., Ouerdane, L., Flis, P., Hoang, M. T. T., Isaure, M.-P., Lobinski, R., Curie, C., and Mari, S. (2014). Ascorbate efflux as a new strategy for iron reduction and transport in plants. *Journal of Biological Chemistry* **289**:2515–2525.

Grizzetti, B., Billen, G., Davidson, E. A., Winiwarter, W., de Vries, W., Fowler, D., Howard, C. M., Bleeker, A., Sutton, M. A., Lassaletta, L., *et al.* (2020). Global nitrogen and phosphorus pollution. *Just Enough Nitrogen: Perspectives on how to get there for regions with too much and too little nitrogen* Advance Access published 2020.

Gruber, B. D., Giehl, R. F. H., Friedel, S., and von Wirén, N. (2013). Plasticity of the Arabidopsis root system under nutrient deficiencies. *Plant Physiol* **163**:161–179.

Gu, Z. (2022). Complex heatmap visualization. *Imeta* **1**:e43.

Guo, B., Jin, Y., Wussler, C., Blancaflor, E. B., Motes, C. M., and Versaw, W. K. (2008). Functional analysis of the Arabidopsis PHT4 family of intracellular phosphate transporters. *New Phytologist* **177**:889–898.

Gutiérrez-Alanís, D., Yong-Villalobos, L., Jiménez-Sandoval, P., Alatorre-Cobos, F., Oropeza-Aburto, A., Mora-Macías, J., Sánchez-Rodríguez, F., Cruz-Ramírez, A., and Herrera-Estrella, L. (2017). Phosphate starvation-dependent iron mobilization induces CLE14 expression to trigger root meristem differentiation through CLV2/PEPR2 signaling. *Dev Cell* **41**:555–570.

Gutiérrez-Alanís, D., Ojeda-Rivera, J. O., Yong-Villalobos, L., Cárdenas-Torres, L., and Herrera-Estrella, L. (2018). Adaptation to phosphate scarcity: tips from Arabidopsis roots. *Trends Plant Sci* **23**:721–730.

Hallberg, B. M., Bergfors, T., Bäckbro, K., Pettersson, G., Henriksson, G., and Divne, C. (2000). A new scaffold for binding haem in the cytochrome domain of the extracellular flavocytochrome cellobiose dehydrogenase. *Structure* **8**:79–88.

Hamburger, D., Rezzonico, E., MacDonald-Comber Petétot, J., Somerville, C., and Poirier, Y. (2002). Identification and characterization of the Arabidopsis *PHO1* gene involved in phosphate loading to the xylem. *Plant Cell* **14**:889–902.

Hammond, J. P., and White, P. J. (2008). Sucrose transport in the phloem: integrating root responses to phosphorus starvation. *J Exp Bot* **59**:93–109.

Hansen, J. C., Cade-Menun, B. J., and Strawn, D. G. (2004). Phosphorus speciation in manure-amended alkaline soils. *J Environ Qual* **33**:1521–1527.

Harrison, A. F. (1982). Labile organic phosphorus mineralization in relationship to soil properties. *Soil Biol Biochem* **14**:343–351.

Harrison, A. F. (1987). Mineralisation of organic phosphorus in relation to soil factors, determined using isotopic 32P labelling.p. NERC/ITE.

Heazlewood, J. L., Tonti-Filippini, J. S., Gout, A. M., Day, D. A., Whelan, J., and Millar, A. H. (2004). Experimental analysis of the Arabidopsis mitochondrial proteome highlights signaling and regulatory components, provides assessment of targeting prediction programs, and indicates plant-specific mitochondrial proteins. *Plant Cell* **16**:241–256.

Herrera-Estrella, L., and López-Arredondo, D. (2016). Phosphorus: the underrated element for feeding the world. *Trends Plant Sci* **21**:461–463.

Hindt, M. N., and Guerinot, M. Lou (2012). Getting a sense for signals: regulation of the plant iron deficiency response. *Biochimica et Biophysica Acta (BBA)-Molecular Cell Research* **1823**:1521–1530.

Hinsinger, P. (2001). Bioavailability of soil inorganic P in the rhizosphere as affected by root-induced chemical changes: a review. *Plant Soil* **237**:173–195.

Hirayama, T., Okuda, K., and Nagasawa, H. (2013). A highly selective turn-on fluorescent probe for iron (II) to visualize labile iron in living cells. *Chem Sci* **4**:1250–1256.

Hoang, M. T. T., Almeida, D., Chay, S., Alcon, C., Corratge-Faillie, C., Curie, C., and Mari, S. (2021). AtDTX25, a member of the multidrug and toxic compound extrusion family, is a vacuolar ascorbate transporter that controls intracellular iron cycling in Arabidopsis. *New Phytologist* **231**:1956–1967.

Hoehenwarter, W., Mönchgesang, S., Neumann, S., Majovsky, P., Abel, S., and Müller, J. (2016). Comparative expression profiling reveals a role of the root apoplast in local phosphate response. *BMC Plant Biol* **16**:1–21.

Hossain, M. A., and Asada, K. (1985). Monodehydroascorbate reductase from cucumber is a flavin adenine dinucleotide enzyme. *Journal of Biological Chemistry* **260**:12920–12926.

Huang, C.-F., Yamaji, N., and Ma, J. F. (2010). Knockout of a bacterial-type ATP-binding cassette transporter gene, *AtSTAR1*, results in increased aluminum sensitivity in Arabidopsis. *Plant Physiol* **153**:1669–1677.

Huang, T.-K., Han, C.-L., Lin, S.-I., Chen, Y.-J., Tsai, Y.-C., Chen, Y.-R., Chen, J.-W., Lin, W.-Y., Chen, P.-M., Liu, T.-Y., *et al.* (2013). Identification of downstream components of ubiquitin-conjugating enzyme PHOSPHATE2 by quantitative membrane proteomics in Arabidopsis roots. *Plant Cell* **25**:4044–4060.

Iyer, L. M., Anantharaman, V., and Aravind, L. (2007). The DOMON domains are involved in heme and sugar recognition. *Bioinformatics* **23**:2660–2664.

Jain, A., Wilson, G. T., and Connolly, E. L. (2014). The diverse roles of FRO family metalloreductases in iron and copper homeostasis. *Front Plant Sci* **5**:100.

Jakoby, M., Wang, H.-Y., Reidt, W., Weisshaar, B., and Bauer, P. (2004). FRU (BHLH029) is required for induction of iron mobilization genes in *Arabidopsis thaliana*. *FEBS Lett* **577**:528–534.

Jasinski, S. M. (2024). *Mineral Commodity Summaries 2024*. Washington DC, United States.

Jeong, J., and Guerinot, M. Lou (2009). Homing in on iron homeostasis in plants. *Trends Plant Sci* **14**:280–285.

Jiang, M., Sun, L., Isupov, M. N., Littlechild, J. A., Wu, X., Wang, Q., Wang, Q., Yang, W., and Wu, Y. (2019). Structural basis for the Target DNA recognition and binding by the MYB domain of phosphate starvation response 1. *FEBS J* **286**:2809–2821.

Jobbagy, E. G., and Jackson, R. B. (2001). The distribution of soil nutrients with depth: global patterns and the imprint of plants. *Biogeochemistry* **53**:51–77.

Jumper, J., Evans, R., Pritzel, A., Green, T., Figurnov, M., Ronneberger, O., Tunyasuvunakool, K., Bates, R., Žíidek, A., Potapenko, A., *et al.* (2021). Highly accurate protein structure prediction with AlphaFold. *Nature* **596**:583–589.

Jung, H., Gayomba, S. R., Rutzke, M. A., Craft, E., Kochian, L. V, and Vatamaniuk, O. K. (2012). COPT6 is a plasma membrane transporter that functions in copper homeostasis in Arabidopsis and is a novel target of SQUAMOSA promoter-binding protein-like 7. *Journal of Biological Chemistry* **287**:33252–33267.

Kampfenkel, K., Kushnir, S., Babiychuk, E., Inzé, D., and Van Montagu, M. (1995). Molecular characterization of a putative *Arabidopsis thaliana* copper transporter and its yeast homologue. *Journal of Biological Chemistry* **270**:28479–28486.

Kanno, S., Arrighi, J.-F., Chiarenza, S., Bayle, V., Berthome, R., Peret, B., Javot, H., Delannoy, E., Marin, E., Nakanishi, T. M., *et al.* (2016). A novel role for the root cap in phosphate uptake and homeostasis. *Elife* **5**:e14577.

Karthikeyan, A. S., Varadarajan, D. K., Mukatira, U. T., D'Urzo, M. P., Damsz, B., and Raghothama, K. G. (2002). Regulated expression of Arabidopsis phosphate transporters. *Plant Physiol* **130**:221–233.

Katoh, K., and Standley, D. M. (2013). MAFFT multiple sequence alignment software version 7: improvements in performance and usability. *Mol Biol Evol* **30**:772–780.

Kavanaugh, M. P., Miller, D. G., Zhang, W., Law, W., Kozak, S. L., Kabat, D., and Miller, A. D. (1994). Cell-surface receptors for gibbon ape leukemia virus and amphotropic murine retrovirus are inducible sodium-dependent phosphate symporters. *Proceedings of the National Academy of Sciences* **91**:7071–7075.

Kiiskinen, M., Korhonen, M., and Kangasjärvi, J. (1997). Isolation and characterization of cDNA for a plant mitochondrial phosphate translocator (*Mpt1*): ozone stress induces *Mpt1* mRNA accumulation in birch (Betula pendula Roth). *Plant Mol Biol* **35**:271–279.

Kim, S. A., Punshon, T., Lanzirotti, A., Li, L., Alonso, J. M., Ecker, J. R., Kaplan, J., and Guerinot, M. Lou (2006). Localization of iron in Arabidopsis seed requires the vacuolar membrane transporter VIT1. *Science (1979)* **314**:1295–1298.

Kim, D., Paggi, J. M., Park, C., Bennett, C., and Salzberg, S. L. (2019). Graph-based genome alignment and genotyping with HISAT2 and HISAT-genotype. *Nat Biotechnol* **37**:907–915.

Kloer, D. P., Hagel, C., Heider, J., and Schulz, G. E. (2006). Crystal structure of ethylbenzene dehydrogenase from Aromatoleum aromaticum. *Structure* **14**:1377–1388.

Krämer, U. (2024). Metal Homeostasis in Land Plants: A Perpetual Balancing Act Beyond the Fulfilment of Metalloproteome Cofactor Demands. *Annual Review of Plant Biology* **75**:27–65.

Krüger, M., Teste, F. P., Laliberté, E., Lambers, H., Coghlan, M., Zemunik, G., and Bunce, M. (2015). The rise and fall of arbuscular mycorrhizal fungal diversity during ecosystem retrogression. *Mol Ecol* **24**:4912–4930.

Kruse, J., Abraham, M., Amelung, W., Baum, C., Bol, R., Kühn, O., Lewandowski, H., Niederberger,J., Oelmann, Y., Rüger, C., Santner, J., Siebers, M., Spohn, M., Vestergren, J., Siebers, N., Vogts, A., Leinweber, P. (2015). Innovative methods in soil phosphorus research: A review. *Journal of Plant Nutrition and Soil Science* **178**:43–88.

Kubo, A., Aono, M., Nakajima, N., Saji, H., Tanaka, K., and Kondo, N. (1999). Differential responses in activity of antioxidant enzymes to different environmental stresses in *Arabidopsis thaliana*. *J Plant Res* **112**:279–290.

Laha, D., Parvin, N., Hofer, A., Giehl, R. F. H., Fernandez-Rebollo, N., von Wirén, N., Saiardi, A., Jessen, H. J., and Schaaf, G. (2019). Arabidopsis ITPK1 and ITPK2 have an evolutionarily conserved phytic acid kinase activity. *ACS Chem Biol* **14**:2127–2133.

Lambers, H., Shane, M. W., Cramer, M. D., Pearse, S. J., and Veneklaas, E. J. (2006). Root structure and functioning for efficient acquisition of phosphorus: matching morphological and physiological traits. *Ann Bot* **98**:693–713.

Lambers, H., Martinoia, E., and Renton, M. (2015). Plant adaptations to severely phosphorus-impoverished soils. *Curr Opin Plant Biol* **25**:23–31.

Lambers, H., de Britto Costa, P., Cawthray, G. R., Denton, M. D., Finnegan, P. M., Hayes, P. E., Oliveira, R. S., Power, S. C., Ranathunge, K., Shen, Q., *et al.* (2022). Strategies to acquire and use phosphorus in phosphorus-impoverished and fire-prone environments. *Plant Soil* **476**:133–160.

Lampropoulos, A., Sutikovic, Z., Wenzl, C., Maegele, I., Lohmann, J. U., and Forner, J. (2013). GreenGate-a novel, versatile, and efficient cloning system for plant transgenesis. *PLoS One* **8**:e83043.

Larsen, S. (1967). Soil phosphorus. *Advances in agronomy* **19**:151–210.

Larsen, P. B., Geisler, M. J. B., Jones, C. A., Williams, K. M., and Cancel, J. D. (2005). *ALS3* encodes a phloem-localized ABC transporter-like protein that is required for aluminum tolerance in Arabidopsis. *The Plant Journal* **41**:353–363.

LeBlanc, M. S., McKinney, E. C., Meagher, R. B., and Smith, A. P. (2013). Hijacking membrane transporters for arsenic phytoextraction. *J Biotechnol* **163**:1–9.

Lee, J., Peña, M. M. O., Nose, Y., and Thiele, D. J. (2002). Biochemical characterization of the human copper transporter Ctr1. *Journal of Biological Chemistry* **277**:4380–4387.

Leman, J. K., Weitzner, B. D., Lewis, S. M., Adolf-Bryfogle, J., Alam, N., Alford, R. F., Aprahamian, M., Baker, D., Barlow, K. A., Barth, P., *et al.* (2020). Macromolecular modeling and design in Rosetta: recent methods and frameworks. *Nat Methods* **17**:665–680.

Lequeux, H., Hermans, C., Lutts, S., and Verbruggen, N. (2010). Response to copper excess in *Arabidopsis thaliana*: impact on the root system architecture, hormone distribution, lignin accumulation and mineral profile. *Plant Physiology and Biochemistry* **48**:673–682.

Leterrier, M., Corpas, F. J., Barroso, J. B., Sandalio, L. M., and del Río, L. A. (2005). Peroxisomal monodehydroascorbate reductase. Genomic clone characterization and functional analysis under environmental stress conditions. *Plant Physiol* **138**:2111–2123.

Levin, E. Y., Levenberg, B., and Kaufman, S. (1960). The enzymatic conversion of 3, 4-dihydroxyphenylethylamine to norepinephrine. *Journal of Biological Chemistry* **235**:2080–2086.

Lex, A., Gehlenborg, N., Strobelt, H., Vuillemot, R., and Pfister, H. (2014). UpSet: visualization of intersecting sets. *IEEE Trans Vis Comput Graph* **20**:1983–1992.

Li, W., and Lan, P. (2015). Genome-wide analysis of overlapping genes regulated by iron deficiency and phosphate starvation reveals new interactions in Arabidopsis roots. *BMC Res Notes* **8**:1–16.

Li, L., Cheng, X., and Ling, H.-Q. (2004). Isolation and characterization of Fe (III)-chelate reductase gene LeFRO1 in tomato. *Plant Mol Biol* **54**:125–136.

Liao, H., Rubio, G., Yan, X., Cao, A., Brown, K. M., and Lynch, J. P. (2001). Effect of phosphorus availability on basal root shallowness in common bean. *Plant Soil* **232**:69–79.

Liao, Y., Smyth, G. K., and Shi, W. (2014). featureCounts: an efficient general purpose program for assigning sequence reads to genomic features. *Bioinformatics* **30**:923–930.

Lin, S.-I., Chiang, S.-F., Lin, W.-Y., Chen, J.-W., Tseng, C.-Y., Wu, P.-C., and Chiou, T.-J. (2008). Regulatory network of *microRNA399* and *PHO2* by systemic signaling. *Plant Physiol* **147**:732–746.

Linkohr, B. I., Williamson, L. C., Fitter, A. H., and Leyser, H. M. O. (2002). Nitrate and phosphate availability and distribution have different effects on root system architecture of Arabidopsis. *The Plant Journal* **29**:751–760.

Liu, T.-Y., Huang, T.-K., Tseng, C.-Y., Lai, Y.-S., Lin, S.-I., Lin, W.-Y., Chen, J.-W., and Chiou, T.-J. (2012). PHO2-dependent degradation of PHO1 modulates phosphate homeostasis in Arabidopsis. *Plant Cell* **24**:2168–2183.

Liu, F., Xu, Y., Jiang, H., Jiang, C., Du, Y., Gong, C., Wang, W., Zhu, S., Han, G., and Cheng, B. (2016). Systematic identification, evolution and expression analysis of the *Zea mays* PHT1 gene family reveals several new members involved in root colonization by arbuscular mycorrhizal fungi. *Int J Mol Sci* **17**:930.

Liu, Y., Maniero, R. A., Giehl, R. F. H., Melzer, M., Steensma, P., Krouk, G., Fitzpatrick, T. B., and von Wirén, N. (2022a). PDX1. 1-dependent biosynthesis of vitamin B6 protects roots from ammonium-induced oxidative stress. *Mol Plant* **15**:820–839.

Liu, X. X., Zhang, H. H., Zhu, Q. Y., Ye, J. Y., Zhu, Y. X., Jing, X. T., Du, W. X., Zhou, M., Lin, X. Y., Zheng, S. J., *et al.* (2022b). Phloem iron remodels root development in response to ammonium as the major nitrogen source. *Nat Commun* **13**:561.

López-Bucio, J., Hernández-Abreu, E., Sánchez-Calderón, L., Nieto-Jacobo, M. F., Simpson, J., and Herrera-Estrella, L. (2002). Phosphate availability alters architecture and causes changes in hormone sensitivity in the Arabidopsis root system. *Plant Physiol* **129**:244–256.

Lopez-Hernandez, D., Flores, D., Siegert, G., and Rodriguez, J. V (1979). The effect of some organic anions on phosphate removal from acid and calcareous soils. *Soil Sci* **128**:312–326.

Lu, P., Ma, D., Yan, C., Gong, X., Du, M., and Shi, Y. (2014). Structure and mechanism of a eukaryotic transmembrane ascorbate-dependent oxidoreductase. *Proceedings of the National Academy of Sciences* **111**:1813–1818.

Ludwiczek, S., Rosell, F. I., Ludwiczek, M. L., and Mauk, A. G. (2008). Recombinant expression and initial characterization of the putative human enteric ferric reductase Dcyt*b*. *Biochemistry* **47**:753–761.

Luengo, C., Brigante, M., Antelo, J., and Avena, M. (2006). Kinetics of phosphate adsorption on goethite: comparing batch adsorption and ATR-IR measurements. *J Colloid Interface Sci* **300**:511–518.

Lynch, J. P., and Brown, K. M. (2001). Topsoil foraging–an architectural adaptation of plants to low phosphorus availability. *Plant Soil* **237**:225–237.

Makavitskaya, M., Svistunenko, D., Navaselsky, I., Hryvusevich, P., Mackievic, V., Rabadanova, C., Tyutereva, E., Samokhina, V., Straltsova, D., Sokolik, A., *et al.* (2018). Novel roles of ascorbate in plants: induction of cytosolic Ca^{2+} signals and efflux from cells via anion channels. *J Exp Bot* **69**:3477–3489.

Martín, A. C., Del Pozo, J. C., Iglesias, J., Rubio, V., Solano, R., De La Peña, A., Leyva, A., and Paz-Ares, J. (2000). Influence of cytokinins on the expression of phosphate starvation responsive genes in Arabidopsis. *The Plant Journal* **24**:559–567.

Martinez, P., and Persson, B. L. (1998). Identification, cloning and characterization of a derepressible Na^+-coupled phosphate transporter in *Saccharomyces cerevisiae*. *Mol Gen Genet* **258**:628–638.

McKie, A. T., Barrow, D., Latunde-Dada, G. O., Rolfs, A., Sager, G., Mudaly, E., Mudaly, M., Richardson, C., Barlow, D., Bomford, A., *et al.* (2001). An iron-regulated ferric reductase associated with the absorption of dietary iron. *Science (1979)* **291**:1755–1759.

Mehlhorn, H., Seufert, G., Schmidt, A., and Kunert, K. J. (1986). Effect of SO_2 and O_3 on production of antioxidants in conifers. *Plant Physiol* **82**:336–338.

Meyer, S., De Angeli, A., Fernie, A. R., and Martinoia, E. (2010). Intra-and extra-cellular excretion of carboxylates. *Trends Plant Sci* **15**:40–47.

Mimura, T. (1999). Regulation of phosphate transport and homeostasis in plant cells. In *International review of cytology*, pp. 149–200. Elsevier.

Mimura, T., Sakano, K., and Shimmen, T. (1996). Studies on the distribution, re-translocation and homeostasis of inorganic phosphate in barley leaves. *Plant Cell Environ* **19**:311–320.

Mishra, N. P., Mishra, R. K., and Singhal, G. S. (1993). Changes in the activities of anti-oxidant enzymes during exposure of intact wheat leaves to strong visible light at different temperatures in the presence of protein synthesis inhibitors. *Plant Physiol* **102**:903–910.

Misson, J., Thibaud, M.-C., Bechtold, N., Raghothama, K., and Nussaume, L. (2004). Transcriptional regulation and functional properties of Arabidopsis Pht1; 4, a high affinity transporter contributing greatly to phosphate uptake in phosphate deprived plants. *Plant Mol Biol* **55**:727–741.

Misson, J., Raghothama, K. G., Jain, A., Jouhet, J., Block, M. A., Bligny, R., Ortet, P., Creff, A., Somerville, S., Rolland, N., *et al.* (2005). A genome-wide transcriptional analysis using *Arabidopsis thaliana* Affymetrix gene chips determined plant responses to phosphate deprivation. *Proceedings of the National Academy of Sciences* **102**:11934–11939.

Mittova, V., Tal, M., Volokita, M., and Guy, M. (2003). Up-regulation of the leaf mitochondrial and peroxisomal antioxidative systems in response to salt-induced oxidative stress in the wild salt-tolerant tomato species Lycopersicon pennellii. *Plant Cell Environ* **26**:845–856.

Młodzińska, E., and Zboińska, M. (2016). Phosphate uptake and allocation–a closer look at *Arabidopsis thaliana* L. and *Oryza sativa* L. *Front Plant Sci* **7**:210483.

Mora-Macías, J., Ojeda-Rivera, J. O., Gutiérrez-Alan\'\is, D., Yong-Villalobos, L., Oropeza-Aburto, A., Raya-González, J., Jiménez-Dom\'\inguez, G., Chávez-Calvillo, G., Rellán-Álvarez, R., and Herrera-Estrella, L. (2017). Malate-dependent Fe accumulation is a critical

checkpoint in the root developmental response to low phosphate. *Proceedings of the National Academy of Sciences* **114**:E3563–E3572.

Mudge, S. R., Rae, A. L., Diatloff, E., and Smith, F. W. (2002). Expression analysis suggests novel roles for members of the Pht1 family of phosphate transporters in Arabidopsis. *The Plant Journal* **31**:341–353.

Mukherjee, I., Campbell, N. H., Ash, J. S., and Connolly, E. L. (2006). Expression profiling of the Arabidopsis ferric chelate reductase (FRO) gene family reveals differential regulation by iron and copper. *Planta* **223**:1178–1190.

Müller, J., Toev, T., Heisters, M., Teller, J., Moore, K. L., Hause, G., Dinesh, D. C., Bürstenbinder, K., and Abel, S. (2015). Iron-dependent callose deposition adjusts root meristem maintenance to phosphate availability. *Dev Cell* **33**:216–230.

Nanasato, Y., Akashi, K., and Yokota, A. (2005). Co-expression of cytochrome *b* 561 and ascorbate oxidase in leaves of wild watermelon under drought and high light conditions. *Plant Cell Physiol* **46**:1515–1524.

Naumann, C., Heisters, M., Brandt, W., Janitza, P., Alfs, C., Tang, N., Nienguesso, A. T., Ziegler, J., Imre, R., Mechtler, K., *et al.* (2022). Bacterial-type ferroxidase tunes iron-dependent phosphate sensing during Arabidopsis root development. *Current Biology* **32**:2189–2205.

Njus, D. (1983). The chromaffin vesicle and the energetics of storage organelles. *J Auton Nerv Syst* **7**:35–40.

Njus, D., and Radda, G. K. (1978). Bioenergetic processes in chromaffin granules a new perspective on some old problems. *Biochimica et Biophysica Acta (BBA)-Reviews on Bioenergetics* **463**:219–244.

Nussaume, L., Kanno, S., Javot, H., Marin, E., Pochon, N., Ayadi, A., Nakanishi, T. M., and Thibaud, M.-C. (2011). Phosphate import in plants: focus on the PHT1 transporters. *Front Plant Sci* **2**:83.

Oakhill, J. S., Marritt, S. J., Gareta, E. G., Cammack, R., and McKie, A. T. (2008). Functional characterization of human duodenal cytochrome *b* (Cybrd1): Redox properties in relation to iron and ascorbate metabolism. *Biochimica et Biophysica Acta (BBA)-Bioenergetics* **1777**:260–268.

Ockenden, M. C., Hollaway, M. J., Beven, K. J., Collins, A. L., Evans, R., Falloon, P. D., Forber, K. J., Hiscock, K. M., Kahana, R., Macleod, C. J. A., *et al.* (2017). Major agricultural changes required to mitigate phosphorus losses under climate change. *Nat Commun* **8**:161.

Oelkers, E. H., and Valsami-Jones, E. (2008). Phosphate mineral reactivity and global sustainability. *Elements* **4**:83–87.

Oidaira, H., Sano, S., Koshiba, T., and Ushimaru, T. (2000). Enhancement of antioxidative enzyme activities in chilled rice seedlings. *J Plant Physiol* **156**:811–813.

Ojeda-Rivera, J. O., Oropeza-Aburto, A., and Herrera-Estrella, L. (2020). Dissection of root transcriptional responses to low pH, aluminum toxicity and iron excess under Pi-limiting conditions in Arabidopsis wild-type and stop1 seedlings. *Front Plant Sci* **11**:543941.

Okuyama, E., Yamamoto, R., Ichikawa, Y., and Tsubaki, M. (1998). Structural basis for the electron transfer across the chromaffin vesicle membranes catalyzed by cytochrome b561:

analyses of cDNA nucleotide sequences and visible absorption spectra. *Biochimica et Biophysica Acta (BBA)-Protein Structure and Molecular Enzymology* **1383**:269–278.

Paffrath, V., Tandron Moya, Y. A., Weber, G., von Wirén, N., and Giehl, R. F. H. (2024). A major role of coumarin-dependent ferric iron reduction in strategy I-type iron acquisition in Arabidopsis. *Plant Cell* **36**:642–664.

Pant, B. D., Buhtz, A., Kehr, J., and Scheible, W.-R. (2008). MicroRNA399 is a long-distance signal for the regulation of plant phosphate homeostasis. *The Plant Journal* **53**:731–738.

Park, A. K., Kim, I.-S., Do, H., Jeon, B. W., Lee, C. W., Roh, S. J., Shin, S. C., Park, H., Kim, Y.-S., Kim, Y.-H., *et al.* (2016). Structure and catalytic mechanism of monodehydroascorbate reductase, MDHAR, from *Oryza sativa* L. japonica. *Sci Rep* **6**:33903.

Péret, B., Clément, M., Nussaume, L., and Desnos, T. (2011). Root developmental adaptation to phosphate starvation: better safe than sorry. *Trends Plant Sci* **16**:442–450.

Péret, B., Desnos, T., Jost, R., Kanno, S., Berkowitz, O., and Nussaume, L. (2014). Root architecture responses: in search of phosphate. *Plant Physiol* **166**:1713–1723.

Pérez-Torres, C.-A., Lopez-Bucio, J., Cruz-Ramírez, A., Ibarra-Laclette, E., Dharmasiri, S., Estelle, M., and Herrera-Estrella, L. (2008). Phosphate availability alters lateral root development in Arabidopsis by modulating auxin sensitivity via a mechanism involving the TIR1 auxin receptor. *Plant Cell* **20**:3258–3272.

Picco, C., Scholz-Starke, J., Festa, M., Costa, A., Sparla, F., Trost, P., and Carpaneto, A. (2015). Direct recording of trans-plasma membrane electron currents mediated by a member of the cytochrome *b* 561 family of soybean. *Plant Physiol* **169**:986–995.

Pierzynski, G. M., McDowell, R. W., and Thomas Sims, J. (2005). Chemistry, cycling, and potential movement of inorganic phosphorus in soils. *Phosphorus: Agriculture and the environment* **46**:51–86.

Platre, M. P., Satbhai, S. B., Brent, L., Gleason, M. F., Cao, M., Grison, M., Glavier, M., Zhang, L., Gaillochet, C., Goeschl, C., *et al.* (2022). The receptor kinase SRF3 coordinates iron-level and flagellin dependent defense and growth responses in plants. *Nat Commun* **13**:4445.

Poirier, Y., and Bucher, M. (2002). Phosphate transport and homeostasis in Arabidopsis. *The Arabidopsis book/American Society of Plant Biologists* **1**.

Ponting, C. P. (2001). Domain homologues of dopamine β-hydroxylase and ferric reductase: roles for iron metabolism in neurodegenerative disorders? *Hum Mol Genet* **10**:1853–1858.

Porra, R. J., Thompson, W. A. A., and Kriedemann, P. E. (1989). Determination of accurate extinction coefficients and simultaneous equations for assaying chlorophylls a and b extracted with four different solvents: verification of the concentration of chlorophyll standards by atomic absorption spectroscopy. *Biochimica et Biophysica Acta (BBA)-Bioenergetics* **975**:384–394.

Preger, V., Tango, N., Marchand, C., Lemaire, S. D., Carbonera, D., Di Valentin, M., Costa, A., Pupillo, P., and Trost, P. (2009). Auxin-responsive genes AIR12 code for a new family of plasma membrane *b*-type cytochromes specific to flowering plants. *Plant Physiol* **150**:606–620.

Puga, M. I., Mateos, I., Charukesi, R., Wang, Z., Franco-Zorrilla, J. M., de Lorenzo, L., Irigoyen, M. L., Masiero, S., Bustos, R., Rodríguez, J., *et al.* (2014). SPX1 is a phosphate-dependent inhibitor of Phosphate Starvation Response 1 in Arabidopsis. *Proceedings of the National Academy of Sciences* **111**:14947–14952.

Qi, W., Manfield, I. W., Muench, S. P., and Baker, A. (2017). AtSPX1 affects the AtPHR1–DNA-binding equilibrium by binding monomeric AtPHR1 in solution. *Biochemical Journal* **474**:3675–3687.

Raghothama, K. G. (1999). Phosphate acquisition. *Annu Rev Plant Biol* **50**:665–693.

Rajniak, J., Giehl, R. F. H., Chang, E., Murgia, I., von Wirén, N., and Sattely, E. S. (2018). Biosynthesis of redox-active metabolites in response to iron deficiency in plants. *Nat Chem Biol* **14**:442–450.

Ravet, K., and Pilon, M. (2013). Copper and iron homeostasis in plants: the challenges of oxidative stress. *Antioxid Redox Signal* **19**:919–932.

Remy, E., Cabrito, T. R., Batista, R. A., Teixeira, M. C., Sá-Correia, I., and Duque, P. (2012). The Pht1; 9 and Pht1; 8 transporters mediate inorganic phosphate acquisition by the *Arabidopsis thaliana* root during phosphorus starvation. *New Phytologist* **195**:356–371.

Reymond, M., Svistoonoff, S., Loudet, O., Nussaume, L., and Desnos, T. (2006). Identification of QTL controlling root growth response to phosphate starvation in *Arabidopsis thaliana*. *Plant Cell Environ* **29**:115–125.

Reyt, G., Boudouf, S., Boucherez, J., Gaymard, F., and Briat, J.-F. (2015). Iron-and ferritin-dependent reactive oxygen species distribution: impact on Arabidopsis root system architecture. *Mol Plant* **8**:439–453.

Richards, S. L., Wilkins, K. A., Swarbreck, S. M., Anderson, A. A., Habib, N., Smith, A. G., McAinsh, M., and Davies, J. M. (2015). The hydroxyl radical in plants: from seed to seed. *J Exp Bot* **66**:37–46.

Richardson, A. E., Hocking, P. J., Simpson, R. J., and George, T. S. (2009). Plant mechanisms to optimise access to soil phosphorus. *Crop Pasture Sci* **60**:124–143.

Ried, M. K., Wild, R., Zhu, J., Pipercevic, J., Sturm, K., Broger, L., Harmel, R. K., Abriata, L. A., Hothorn, L. A., Fiedler, D., *et al.* (2021). Inositol pyrophosphates promote the interaction of SPX domains with the coiled-coil motif of PHR transcription factors to regulate plant phosphate homeostasis. *Nat Commun* **12**:384.

Riemer, E., Qiu, D., Laha, D., Harmel, R. K., Gaugler, P., Gaugler, V., Frei, M., Hajirezaei, M.-R., Laha, N. P., Krusenbaum, L., *et al.* (2021). ITPK1 is an $InsP_6$/ADP phosphotransferase that controls phosphate signaling in Arabidopsis. *Mol Plant* **14**:1864–1880.

Ritchie, M. E., Phipson, B., Wu, D. I., Hu, Y., Law, C. W., Shi, W., and Smyth, G. K. (2015). limma powers differential expression analyses for RNA-sequencing and microarray studies. *Nucleic Acids Res* **43**:e47–e47.

Robinson, N. J., Procter, C. M., Connolly, E. L., and Guerinot, M. Lou (1999). A ferric-chelate reductase for iron uptake from soils. *Nature* **397**:694–697.

Römheld, V. (1987). Different strategies for iron acquisition in higher plants. *Physiol Plant* **70**.

Roschzttardtz, H., Conéjéro, G., Curie, C., and Mari, S. (2009). Identification of the endodermal vacuole as the iron storage compartment in the Arabidopsis embryo. *Plant Physiol* **151**:1329–1338.

Rubio, V., Linhares, F., Solano, R., Martín, A. C., Iglesias, J., Leyva, A., and Paz-Ares, J. (2001). A conserved MYB transcription factor involved in phosphate starvation signaling both in vascular plants and in unicellular algae. *Genes Dev* **15**:2122–2133.

Ryan, P. R., Delhaize, E., and Jones, D. L. (2001). Function and mechanism of organic anion exudation from plant roots. *Annu Rev Plant Biol* **52**:527–560.

Sancenón, V., Puig, S., Mira, H., Thiele, D. J., and Peñarrubia, L. (2003). Identification of a copper transporter family in *Arabidopsis thaliana*. *Plant Mol Biol* **51**:577–587.

Sancenón, V., Puig, S., Mateu-Andrés, I., Dorcey, E., Thiele, D. J., and Peñarrubia, L. (2004). The Arabidopsis copper transporter COPT1 functions in root elongation and pollen development. *Journal of Biological Chemistry* **279**:15348–15355.

Sánchez-Calderón, L., López-Bucio, J., Chacón-López, A., Gutiérrez-Ortega, A., Hernández-Abreu, E., and Herrera-Estrella, L. (2006). Characterization of low phosphorus insensitive mutants reveals a crosstalk between low phosphorus-induced determinate root development and the activation of genes involved in the adaptation of Arabidopsis to phosphorus deficiency. *Plant Physiol* **140**:879–889.

Sattari, S. Z., Bouwman, A. F., Martinez Rodríguez, R., Beusen, A. H. W., and Van Ittersum, M. K. (2016). Negative global phosphorus budgets challenge sustainable intensification of grasslands. *Nat Commun* **7**:10696.

Schachtman, D. P., Reid, R. J., and Ayling, S. M. (1998). Phosphorus uptake by plants: from soil to cell. *Plant Physiol* **116**:447–453.

Schagerlöf, U., Wilson, G., Hebert, H., Al-Karadaghi, S., and Hägerhäll, C. (2006). Transmembrane topology of FRO2, a ferric chelate reductase from *Arabidopsis thaliana*. *Plant Mol Biol* **62**:215–221.

Schmidt, H., Günther, C., Weber, M., Spörlein, C., Loscher, S., Böttcher, C., Schobert, R., and Clemens, S. (2014). Metabolome analysis of *Arabidopsis thaliana* roots identifies a key metabolic pathway for iron acquisition. *PLoS One* **9**:e102444.

Schöner, S., and Krause, G. H. (1990). Protective systems against active oxygen species in spinach: response to cold acclimation in excess light. *Planta* **180**:383–389.

Secco, D., Baumann, A., and Poirier, Y. (2010). Characterization of the rice PHO1 gene family reveals a key role for OsPHO1; 2 in phosphate homeostasis and the evolution of a distinct clade in dicotyledons. *Plant Physiol* **152**:1693–1704.

Shen, J., Yuan, L., Zhang, J., Li, H., Bai, Z., Chen, X., Zhang, W., and Zhang, F. (2011). Phosphorus dynamics: from soil to plant. *Plant Physiol* **156**:997–1005.

Shin, H., Shin, H.-S., Dewbre, G. R., and Harrison, M. J. (2004). Phosphate transport in Arabidopsis: Pht1; 1 and Pht1; 4 play a major role in phosphate acquisition from both low-and high-phosphate environments. *The Plant Journal* **39**:629–642.

Shin, S.-Y., Kim, I.-S., Kim, Y.-S., Lee, H., and Yoon, H.-S. (2013). Ectopic expression of *Brassica rapa* L. MDHAR increased tolerance to freezing stress by enhancing antioxidant systems of host plants. *South African journal of botany* **88**:388–400.

Smyth, G. K. (2004). Linear models and empirical bayes methods for assessing differential expression in microarray experiments. *Stat Appl Genet Mol Biol* **3**.

Srivastava, S., Upadhyay, M. K., Srivastava, A. K., Abdelrahman, M., Suprasanna, P., and Tran, L.-S. P. (2018). Cellular and subcellular phosphate transport machinery in plants. *Int J Mol Sci* **19**:1914.

Stefanovic, A., Arpat, A. B., Bligny, R., Gout, E., Vidoudez, C., Bensimon, M., and Poirier, Y. (2011). Over-expression of PHO1 in Arabidopsis leaves reveals its role in mediating phosphate efflux. *The Plant Journal* **66**:689–699.

Svistoonoff, S., Creff, A., Reymond, M., Sigoillot-Claude, C., Ricaud, L., Blanchet, A., Nussaume, L., and Desnos, T. (2007). Root tip contact with low-phosphate media reprograms plant root architecture. *Nat Genet* **39**:792–796.

Tamura, K., Stecher, G., and Kumar, S. (2021). MEGA11: molecular evolutionary genetics analysis version 11. *Mol Biol Evol* **38**:3022–3027.

Tao, D.-L., Öquist, G., and Wingsle, G. (1998). Active oxygen scavengers during cold acclimation of Scots pine seedlings in relation to freezing tolerance. *Cryobiology* **37**:38–45.

Teng, W., Zhao, Y.-Y., Zhao, X.-Q., Chen, X.-P., and Tong, Y.-P. (2017). Genome-wide identification, characterization, and expression analysis of PHT1 phosphate transporters in wheat. *Front Plant Sci* **8**:260127.

Thibaud, M.-C., Arrighi, J.-F., Bayle, V., Chiarenza, S., Creff, A., Bustos, R., Paz-Ares, J., Poirier, Y., and Nussaume, L. (2010). Dissection of local and systemic transcriptional responses to phosphate starvation in Arabidopsis. *The Plant Journal* **64**:775–789.

Ticconi, C. A., and Abel, S. (2004). Short on phosphate: plant surveillance and countermeasures. *Trends Plant Sci* **9**:548–555.

Ticconi, C. A., Lucero, R. D., Sakhonwasee, S., Adamson, A. W., Creff, A., Nussaume, L., Desnos, T., and Abel, S. (2009). ER-resident proteins PDR2 and LPR1 mediate the developmental response of root meristems to phosphate availability. *Proceedings of the National Academy of Sciences* **106**:14174–14179.

Truffault, V., Gest, N., Garchery, C., Florian, A., Fernie, A. R., Gautier, H., and Stevens, R. G. (2016). Reduction of MDHAR activity in cherry tomato suppresses growth and yield and MDHAR activity is correlated with sugar levels under high light. *Plant Cell Environ* **39**:1279–1292.

Tsubaki, M., Takeuchi, F., and Nakanishi, N. (2005). Cytochrome *b*561 protein family: expanding roles and versatile transmembrane electron transfer abilities as predicted by a new classification system and protein sequence motif analyses. *Biochimica et Biophysica Acta (BBA)-Proteins and Proteomics* **1753**:174–190.

Turner, B. L. (2007). Inositol phosphates in soil: amounts, forms and significance of the phosphorylated inositol stereoisomers. *Inositol phosphates: linking agriculture and the environment* Advance Access published 2007.

Turner, B. L., Newman, S., Cheesman, A. W., and Reddy, K. R. (2007). Sample pretreatment and phosphorus speciation in wetland soils. *Soil Science Society of America Journal* **71**:1538–1546.

Tyburski, J., Dunajska-Ordak, K., Skorupa, M., and Tretyn, A. (2012). Role of ascorbate in the regulation of the *Arabidopsis thaliana* root growth by phosphate availability. *J Bot* **2012**.

Ursache, R., De Jesus Vieira Teixeira, C., Dénervaud Tendon, V., Gully, K., De Bellis, D., Schmid-Siegert, E., Grube Andersen, T., Shekhar, V., Calderon, S., Pradervand, S., *et al.* (2021). GDSL-domain proteins have key roles in suberin polymerization and degradation. *Nat Plants* **7**:353–364.

Ushimaru, T., Shibasaka, M., and Tsuji, H. (1992). Development of the O_2^- - Detoxification System during Adaptation to Air of Submerged Rice Seedlings. *Plant Cell Physiol* **33**:1065–1071.

Van Kauwenbergh, S. J. (2010). *World phosphate rock reserves and resources*. Ifdc Muscle Shoals.

Vance, C. P., Uhde-Stone, C., and Allan, D. L. (2003). Phosphorus acquisition and use: critical adaptations by plants for securing a nonrenewable resource. *New Phytologist* **157**:423–447.

Versaw, W. K., and Harrison, M. J. (2002). A chloroplast phosphate transporter, PHT2; 1, influences allocation of phosphate within the plant and phosphate-starvation responses. *Plant Cell* **14**:1751–1766.

Vert, G., Grotz, N., Dédaldéchamp, F., Gaymard, F., Guerinot, M. Lou, Briat, J.-F., and Curie, C. (2002). IRT1, an Arabidopsis transporter essential for iron uptake from the soil and for plant growth. *Plant Cell* **14**:1223–1233.

Wan, Y., Wang, Z., Xia, J., Shen, S., Guan, M., Zhu, M., Qiao, C., Sun, F., Liang, Y., Li, J., *et al.* (2020). Genome-wide analysis of phosphorus transporter genes in Brassica and their roles in heavy metal stress tolerance. *Int J Mol Sci* **21**:2209.

Wang, L., and Nancollas, G. H. (2008). Calcium orthophosphates: crystallization and dissolution. *Chem Rev* **108**:4628–4669.

Wang, Y., Ribot, C., Rezzonico, E., and Poirier, Y. (2004). Structure and expression profile of the Arabidopsis PHO1 gene family indicates a broad role in inorganic phosphate homeostasis. *Plant Physiol* **135**:400–411.

Wang, G.-F., Li, W.-Q., Li, W.-Y., Wu, G.-L., Zhou, C.-Y., and Chen, K.-M. (2013). Characterization of rice NADPH oxidase genes and their expression under various environmental conditions. *Int J Mol Sci* **14**:9440–9458.

Wang, Q., Shi, H., Huang, R., Ye, R., Luo, Y., Guo, Z., and Lu, S. (2021). AIR12 confers cold tolerance through regulation of the CBF cold response pathway and ascorbate homeostasis. *Plant Cell Environ* **44**:1522–1533.

Ward, J. T., Lahner, B., Yakubova, E., Salt, D. E., and Raghothama, K. G. (2008). The effect of iron on the primary root elongation of Arabidopsis during phosphate deficiency. *Plant Physiol* **147**:1181–1191.

Waters, B. M., Blevins, D. G., and Eide, D. J. (2002). Characterization of FRO1, a pea ferric-chelate reductase involved in root iron acquisition. *Plant Physiol* **129**:85–94.

Whitfield, H., White, G., Sprigg, C., Riley, A. M., Potter, B. V. L., Hemmings, A. M., and Brearley, C. A. (2020). An ATP-responsive metabolic cassette comprised of inositol tris/tetrakisphosphate kinase 1 (ITPK1) and inositol pentakisphosphate 2-kinase (IPK1) buffers diphosphosphoinositol phosphate levels. *Biochemical Journal* **477**:2621–2638.

Wild, R., Gerasimaite, R., Jung, J.-Y., Truffault, V., Pavlovic, I., Schmidt, A., Saiardi, A., Jessen, H. J., Poirier, Y., Hothorn, M., *et al.* (2016). Control of eukaryotic phosphate homeostasis by inositol polyphosphate sensor domains. *Science (1979)* **352**:986–990.

Wu, H., Li, L., Du, J., Yuan, Y., Cheng, X., and Ling, H.-Q. (2005). Molecular and biochemical characterization of the Fe (III) chelate reductase gene family in *Arabidopsis thaliana*. *Plant Cell Physiol* **46**:1505–1514.

Wu, T., Hu, E., Xu, S., Chen, M., Guo, P., Dai, Z., Feng, T., Zhou, L., Tang, W., Zhan, L. I., *et al.* (2021). clusterProfiler 4.0: A universal enrichment tool for interpreting omics data. *The innovation* **2**.

Yi, Y., and Guerinot, M. Lou (1996). Genetic evidence that induction of root Fe (III) chelate reductase activity is necessary for iron uptake under iron deficiency. *The Plant Journal* **10**:835–844.

Yu, G. (2021). Enrichplot: visualization of functional enrichment result. *R package version* **1**.

Yuan, Y. X., Zhang, J., Wang, D. W., and Ling, H. Q. (2005). AtbHLH29 of *Arabidopsis thaliana* is a functional ortholog of tomato FER involved in controlling iron acquisition in strategy I plants. *Cell Res* **15**:613–621.

Zechmann, B. (2018). Compartment-specific importance of ascorbate during environmental stress in plants. *Antioxid Redox Signal* **29**:1488–1501.

Zhang, Y., and Zhang, Y. (2013). Biological role of ascorbate in plants. *Ascorbic acid in plants: biosynthesis, regulation and enhancement* Advance Access published 2013.

Zhang, D., Su, D., Bérczi, A., Vargas, A., and Asard, H. (2006). An ascorbate-reducible cytochrome *b*561 is localized in macrophage lysosomes. *Biochimica et Biophysica Acta (BBA)-General Subjects* **1760**:1903–1913.

Zheng, L., Baumann, U., and Reymond, J.-L. (2004). An efficient one-step site-directed and site-saturation mutagenesis protocol. *Nucleic Acids Res* **32**:e115–e115.

Zheng, Z., Wang, Z., Wang, X., and Liu, D. (2019). Blue light-triggered chemical reactions underlie phosphate deficiency-induced inhibition of root elongation of Arabidopsis seedlings grown in Petri dishes. *Mol Plant* **12**:1515–1523.

Zhu, W., Miao, Q., Sun, D., Yang, G., Wu, C., Huang, J., and Zheng, C. (2012). The mitochondrial phosphate transporters modulate plant responses to salt stress via affecting ATP and gibberellin metabolism in *Arabidopsis thaliana*. *journals.plos.org* Advance Access published 2012.

Zhu, J., Lau, K., Puschmann, R., Harmel, R. K., Zhang, Y., Pries, V., Gaugler, P., Broger, L., Dutta, A. K., Jessen, H. J., *et al.* (2019). Two bifunctional inositol pyrophosphate kinases/phosphatases control plant phosphate homeostasis. *Elife* **8**:e43582.

Ziegler, J., Schmidt, S., Chutia, R., Müller, J., Böttcher, C., Strehmel, N., Scheel, D., and Abel, S. (2016). Non-targeted profiling of semi-polar metabolites in Arabidopsis root exudates uncovers a role for coumarin secretion and lignification during the local response to phosphate limitation. *J Exp Bot* **67**:1421–1432.

8 Appendix

Annex Table 1. Calculated amount of Fe provided by 100 µM Fe(III)-EDTA (~13% Fe) and 150 µM $FeCl_3$ and determined soluble fraction. The amount of soluble Fe in freshly prepared half-strength MS medium (without agar) containing either 100 µM Fe(III)-EDTA (~13% Fe) or 150 µM $FeCl_3$ were determined by ICP-MS in filtrates recovered after passing the nutrient medium through a 0.45-µm filter. Shown are means ± s.d. (*n* = 4 independent measurements).

Fe source	Fe amount supplied (ng mL^{-1})	
	Calculated	Soluble
100 µM Fe(III)-EDTA	4771.65	3171.09 ± 142.83
150 µM $FeCl_3 \cdot 6H_2O$	8376.59	1.78 ± 0.64

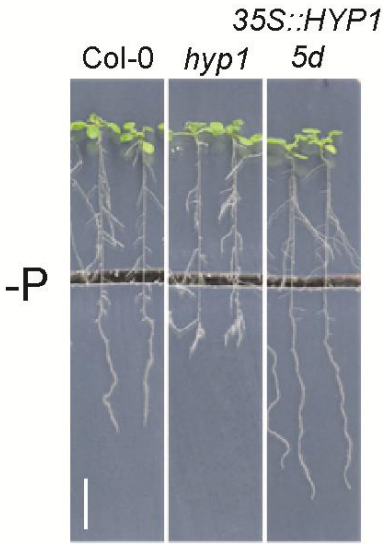

Annex Figure 1. In a light-protected plate, the short-root phenotype of *hyp1* plants was detected also when potential diffusion of Fe(II) from the light-exposed upper part of the agar was prevented by spatially separating the upper and lower part of the agar at the beginning of the experiment.

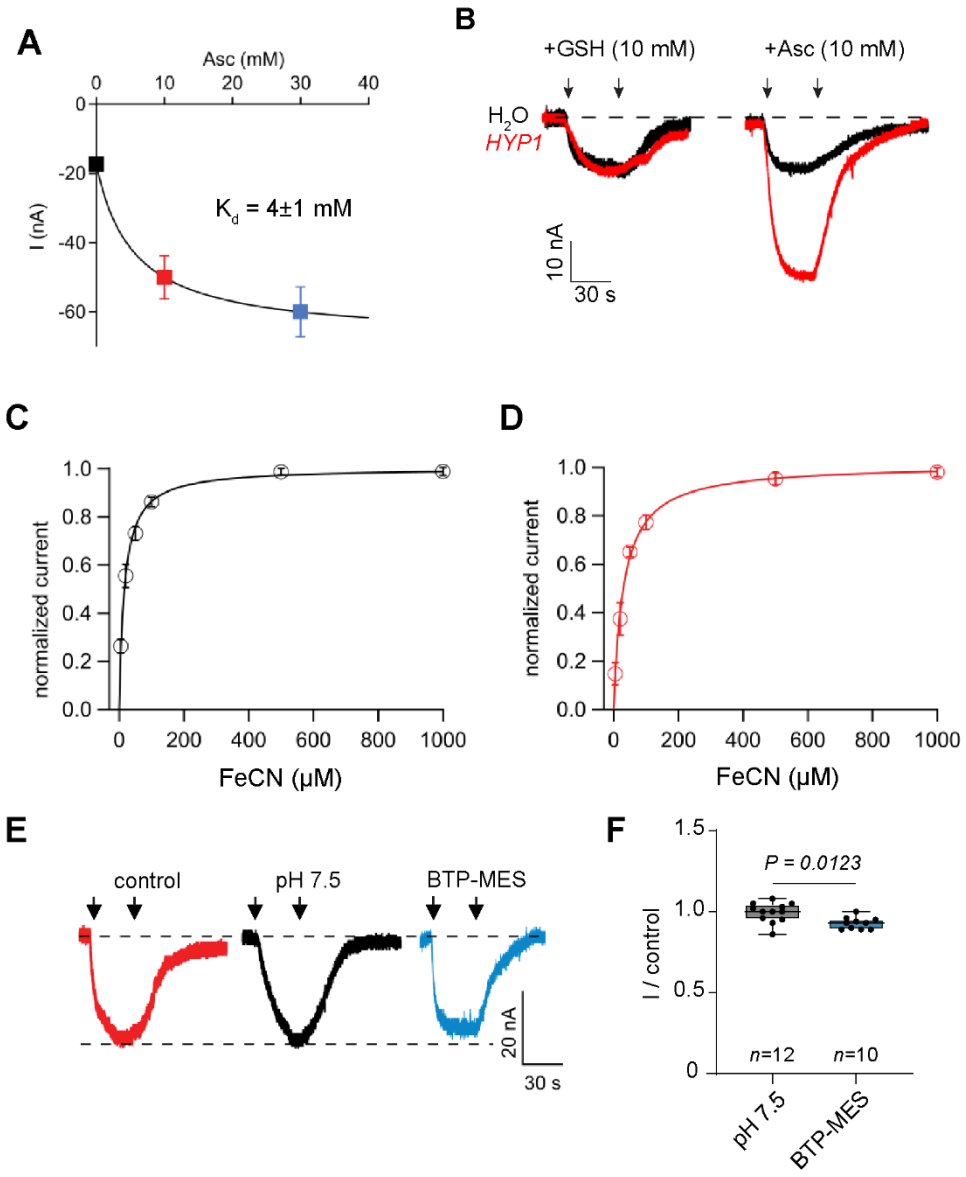

Annex Figure 2. HYP1-mediated electron currents in *X. laevis* oocytes are ascorbate- and Fe(III)-dependent, but independent of ion fluxes.

(**A**) Dependence of HYP1-elicited currents on the ascorbate concentration resulting from ascorbate injection (Asc_{inj}). Data points were subjected to a fit with the Michaelis-Menten function $I=I_{max}/(1+K_D/(Asc_{cyt} + Asc_{inj})$ (continuous lines) giving I_{max} = 68 ± 8 nA, K_D=4 ± 1 mM, Asc_{cyt} = 1.5 ± 0.2 mM. Values are the mean ± s.d. (*n* = 6 independent oocytes). (**B**) HYP1-mediated currents elicited in *X. laevis* oocytes by 1 mM $[Fe(CN)_6]^{3-}$ (ferricyanide) before (black traces) and after (red traces) injection with the indicated concentrations of glutathione (+GSH) and ascorbate (+Asc). (**C** and **D**) Dependence of HYP1-elicited currents on external $[Fe(CN)_6]^{3-}$ (ferricyanide; FeCN) before and after ascorbate injection (+ 10 mM Asc). Data points were normalized to the value at 1 mM FeCN/Asc_{cyt} and fitted with a Michaelis-Menten function (continuous lines) giving the following parameters: $K_F(Asc_{cyt})$ = 18 ± 2 µM, $K_F(As_{ccyt}$ + 10 mM) = 30 ± 2 µM. Symbols represent means ± s.d. (Asc_{cyt}, *n* = 10 independent oocytes and Asc_{cyt} + 10 mM Asc, *n* = 6 independent oocytes). Membrane current recordings (**E**) and normalized currents to control (**F**) in oocytes injected with *HYP1* cRNA upon exposure to 1 mM $[Fe(CN)_6]^{3-}$ (ferricyanide; FeCN) in control solution (red trace) or in modified solutions with pH set to 7.5 (black trace) and with with NaCl, KCl, $CaCl_2$ and $MgCl_2$ replaced with BTP-MES (blue trace). Holding voltage at -20 mV. The left and right arrows indicate the addition and removal of ferricyanide, respectively. Mean values of normalized current to control ± s.d. (pH 7.5, *n* = 10 independent oocytes and BTP-MES, *n* = 6 independent oocytes). P value according to two-tailed, Student's *t*-test. Experiments were performed and data obtained in collaboration with the research group of Prof. Dr. Armando Carpaneto (NRC/University of Genoa, Italy).

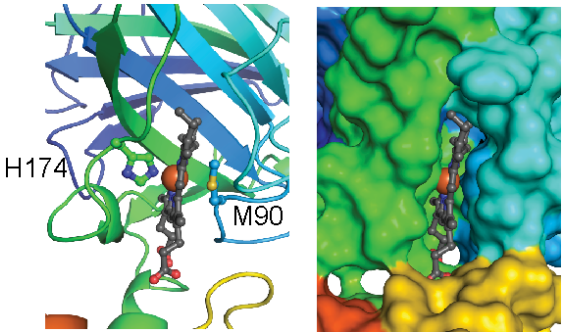

Annex Figure 3. Prediction of *b*-heme coordination site at the DOMON domain.

Computational docking of a *b*-heme molecule by a conserved methionine and histidine pair in the DOMON domain, and surface presentation showing a predicted solvent-exposed side. Red spheres indicate the atom Fe at the center of a *b*-heme. Prediction was done by Dr. Georg Künze (University of Leipzig, Germany) using AlphaFold (Jumper et al., 2021).

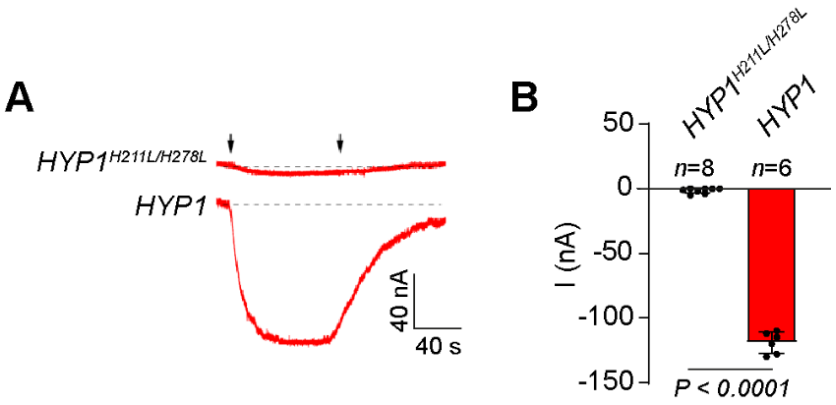

Annex Figure 4. Trans-plasma membrane current recordings in *X. laevis* oocytes injected *HYP1* cRNA or with a mutated *HYP1* variant carrying substitutions in the *b*-heme coordination sites in the apical part of the cytochrome *b*561 core (HYP1$^{H211L/H278L}$).

Current traces (**A**) and mean current amplitudes (**B**) recorded with $[Fe(CN)_6]^{3-}$ (ferricyanide) after injection of 10 mM ascorbate in standard bath solution (pH 5.5) at a holding potential of -20 mV. The left and right arrows indicate the addition and removal of ferricyanide, respectively. Values represent means ± s.d. (*HYP1*, *n* = 6 independent oocytes and *HYP1*$^{H211L/H278L}$, *n* = 8 independent oocytes). *P* value according to two-tailed Student's *t*-test. Experiments were performed and data obtained in collaboration with the research group of Prof. Dr. Armando Carpaneto (NRC/University of Genoa, Italy).

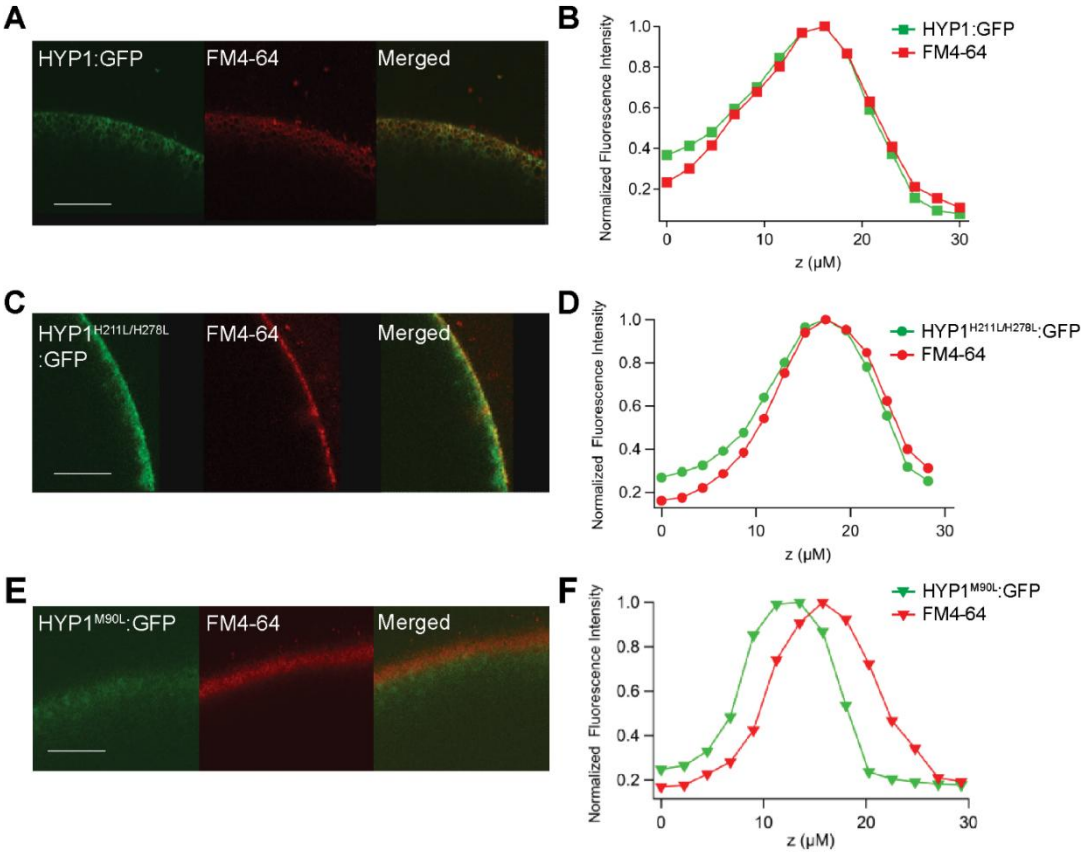

Annex Figure 5. Plasma membrane localization of wild-type and mutated HYP1 variants in *X. laevis* oocytes.

Laser scanning confocal images showing the border of an oocyte expressing wild-type HYP1:GFP (**A**), and HYP1$^{H211L/H278L}$:GFP (**B**) and HYP1^{M90L}:GFP (**C**) mutated variants of HYP1. The plasma membrane was stained with FM4-64. The fluorescence intensity profiles of GFP (green) and FM4-64 signals (red) were calculated along the z axis of the oocyte border at the bottom for wild-type HYP1:GFP (**B**), and HYP1$^{H211L/H278L}$:GFP (**D**) and HYP1^{M90L}:GFP (**F**) mutated variants of HYP1. The fluorescence was normalized at the maximal value for each signal. Similar results were obtained in *n* = 6 independent oocytes. Scale bars, 30 µm. Experiments were performed and data obtained in collaboration with the research group of Prof. Dr. Armando Carpaneto (NRC/University of Genoa, Italy).

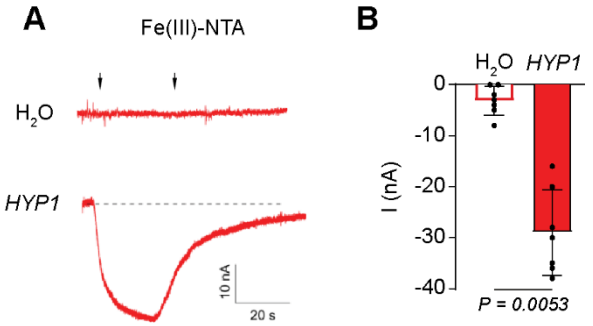

Annex Figure 6. *HYP1* cRNA-injected oocytes are able to reduce extra-cytosolic Fe(III)-NTA.

Trans-plasma membrane currents (**A**) and mean amplitudes (**B**) elicited by 1 mM Fe(III)-NTA in *X. laevis* oocytes injected with water (H_2O) or cRNA of *HYP1* (*HYP1*). Oocytes were pre-injected with 10 mM ascorbate and traces recorded at a holding potential of -120 mV. The left and right arrows indicate the addition and removal of Fe(III)-NTA. Bars represent means ± s.d. (H_2O -injected, *n* = 6-7 and *HYP1*-injected, *n* = 4-7 independent oocytes). *P* value according to two-tailed Student's *t*-test. Experiments were performed and data obtained in collaboration with the research group of Prof. Dr. Armando Carpaneto (NRC/University of Genoa, Italy).

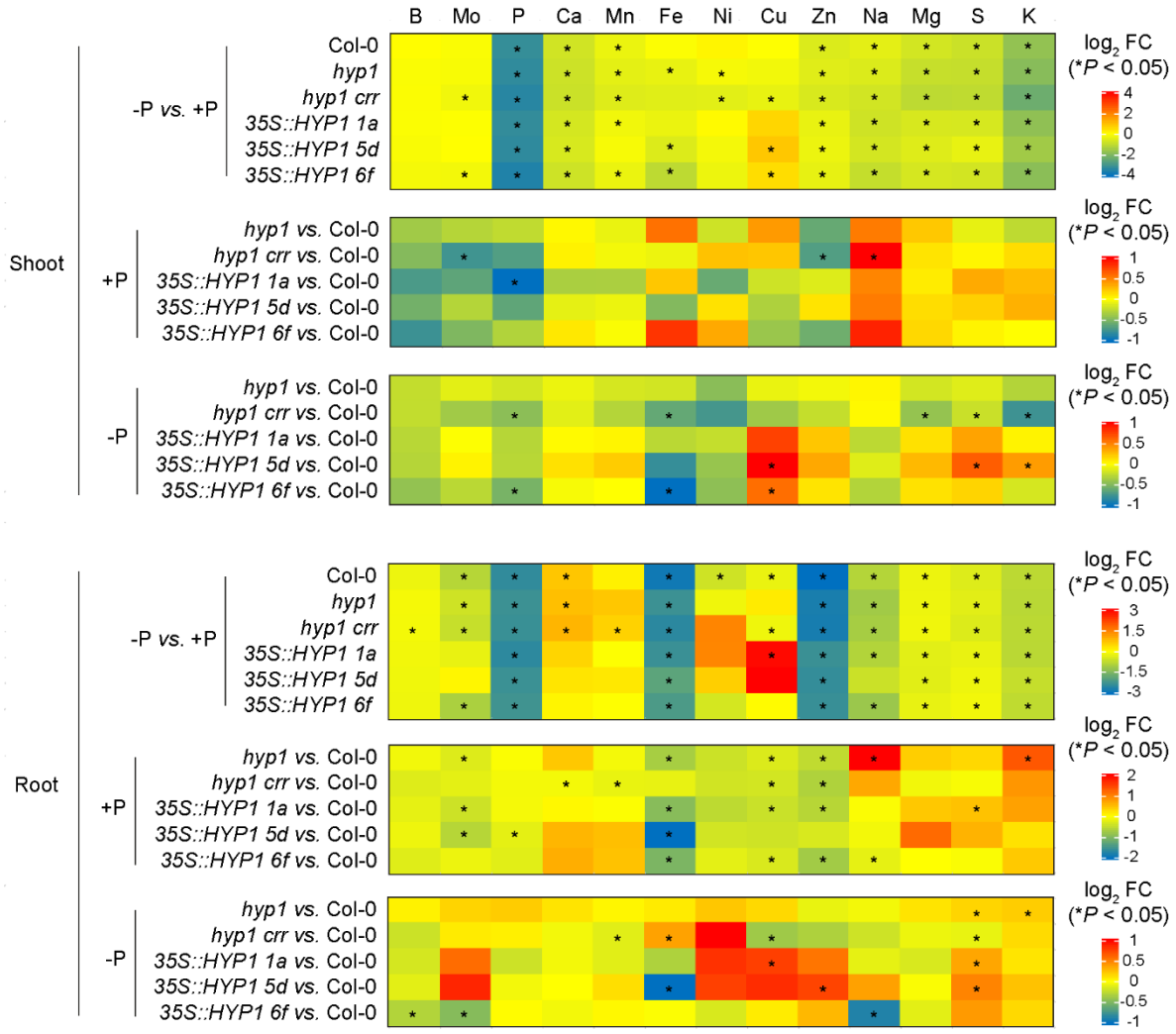

Annex Figure 7. Ionome of plants grown under sufficient- and low-P conditions.

Heatmap showing ionome in $\log_2$-fold change (FC) of shoot and roots of wild type (Col-0), hyp1, hyp1 crr, and three independent transgenic lines overexpressing HYP1, grown on sufficient- and low-P (+P and -P, respectively). Ten-day-old seedlings were transferred to a fresh medium containing 625 µM P (+P) or 5 µM P (-P) and analyzed after 20 days. Bars represent means ± s.d. ($n = 4$ replicates containing 4 plants each). Asterisks indicate significant differences according to one-sided Student *t*-test ($P < 0.05$).

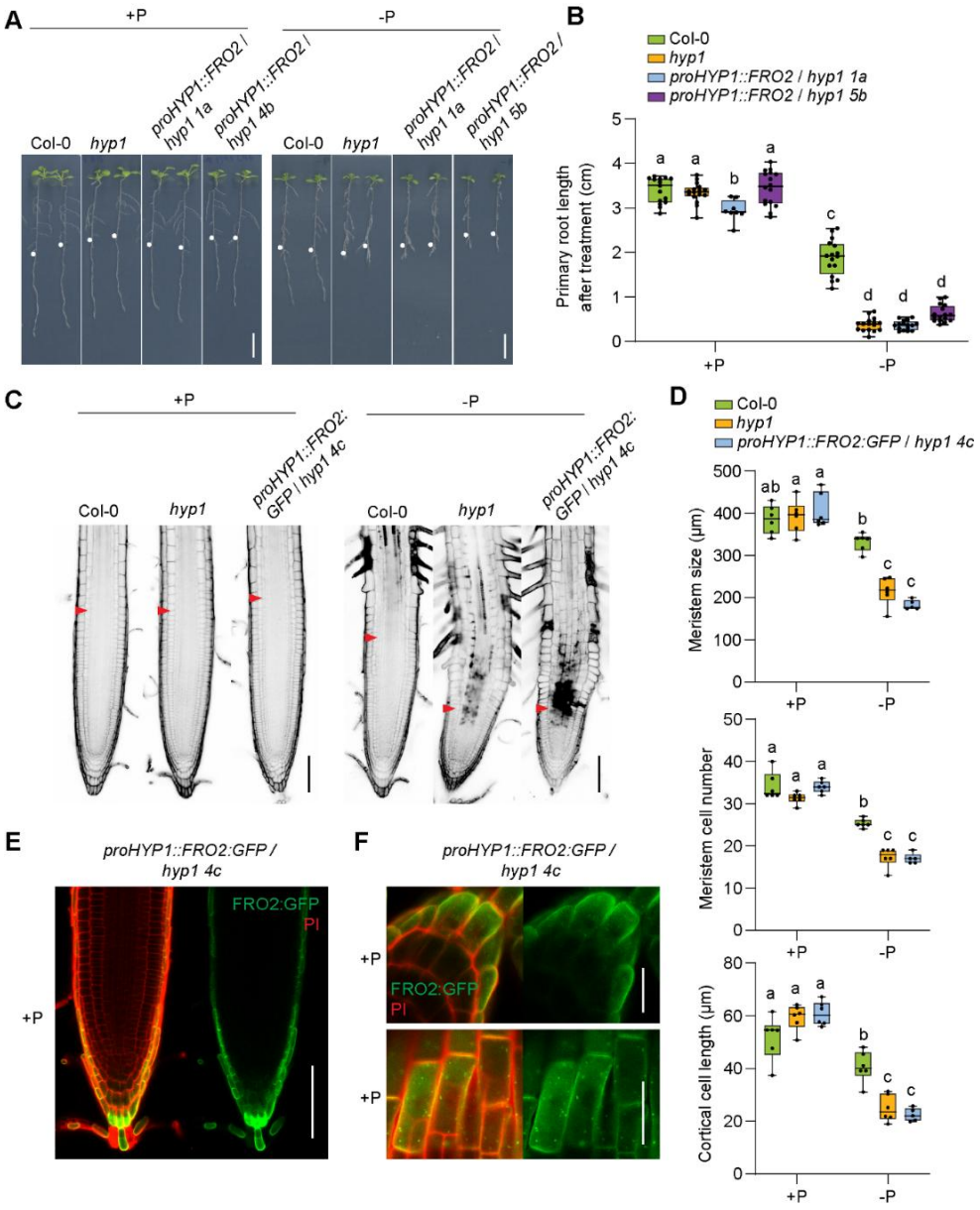

Annex Figure 8. Ongoing attempts to complement *hyp1* with *FRO2*.

Appearance (**B**) and primary root length (**B**) of wild-type (Col-0), *hyp1* mutant, and two *hyp1* independent transgenic lines expressing *FRO2* under the control of the *HYP1* promoter grown for 6 days on sufficient or low P conditions (+P or -P, respectively). Ten-day-old seedlings were transferred to a fresh medium containing 625 µM P (+P) or 5 µM P (-P) with 150 µM $FeCl_3$ and analyzed after 6 days. White dots indicate the position of the primary roots at the day of transfer. (**C**) Confocal images of propidium iodide-stained root tips of wild-type (Col-0), *hyp1* mutant, and one *hyp1* independent transgenic line expressing *FRO2:GFP* under the control of the *HYP1* promoter after transferring ten-day-old seedlings to a fresh medium containing 625 µM P (+P) or 5 µM P (-P) with 150 µM $FeCl_3$. Measurements were taken after 2 days after subjecting plants to the indicated treatments. Red arrowheads indicate the boundary between meristem zone. (**D**) Quantification of meristem cell length (upper panel), meristem cell number (middle panel), and mature cortical cell length (bottom panel). Data are presented as boxplots with each dot representing the datapoint of one biological replicate. For the boxplots, central horizontal lines, median; edges of boxes, 25th (bottom) and 75th (top) percentiles; whiskers, minimum and maximum. The letters indicate significant differences (one-way ANOVA followed by post-hoc Tukey's test, $P < 0.05$; n = 16 (**B**), n = 5-6 independent plants (**D**)). Confocal imaging of primary root meristem (**E**) and root cap cells (**F**) of one *hyp1* transgenic line expressing *FRO2:GFP* driven by *HYP1* promoter, counterstained with propidium iodide (PI). Ten-day-old seedlings were transferred to a fresh medium containing 5 µM P (-P) with 150 µM $FeCl_3$ and analyzed after 2 days. Scale bars, 1 cm (**A**), 100 µm (**C** and **E**), 20 µm (**F**).

9 List of abbreviations

%	percentage
~	approximately
°	degree
°C	degree Celsius
µg	microgram
µM	micromolar
½ MS	half-strength MS
A	amper
Å	angstrom (equal to a length of 10^{-10} m)
Al	aluminum
arb. unit	arbitrary unit
AIR12	*AUXIN-INDUCED IN ROOT CULTURES 12*
ALMT1	*ALUMINUM-ACTIVATED MALATE TRANSPORTER 1*
ANOVA	analysis of variance
AO	ascorbate oxidase
APX	ascorbate peroxidase
ASC	ascorbate (reduced form)
Asc_{cyt}	cytosolic ascorbate
BCDS	bathocuproine disulfonic acid
BFP	blue fluorescent protein
BRN1	*BEARSKIN 1*
BTP	1,3-bis[tris(hydroxymethyl)methylamino]propane
CaMV 35S	Cauliflower Mosaic Virus 35S promoter
cDNA	complementary DNA
cm	centimeter
CN	cyanide
Cq	quantification cycle
cRNA	complementary RNA
Cu	copper
CYBASC	diheme *b*-containing cytochrome *b*561 protein
CYBDOM	Cyt*b*561 transmembrane protein containing DOMON domain
CYCB1;1	CYCLIN-DEPENDENT PROTEIN KINASE 1;1
Cyt*b*561	Cytochrome *b*561
Cα	alpha-carbon
d	day
DAB	3,3′-Diaminobenzidine
Dcyt*b*	duodenal cytochrome *b*
DEG	differentially expressed gene
DHA	dehydroascorbate (fully oxidized form of ascorbate)
DHAR	dehydroascorbate reductase
DNA	deoxyribonucleic acid
DOMON	β-monooxygenase N-terminal
DW	dry weight
EDTA	2,2',2'',2'''-(Ethane-1,2-diyldinitrilo)tetraacetic acid
FC	fold-change
FCR	ferric-chelate reductase

FDR	false discovery rate
Fe	iron
Fe(II); Fe^{2+}	ferrous iron
Fe(III); Fe^{3+}	ferric iron
For	forward
FRO2	FERRIC CHELATE REDUCTASE OXIDASE 2
FW	fresh weight
gDNA	genomic DNA
GFP	green fluorescent protein
GO	gene ontology
GPI	glycosylphosphatidylinositol
GSH	glutathione
GUS	β-glucuronidase
kV	kilovolt
h	hour
HCL	hierarchical clustering
HEPES	2-[4-(2-hydroxyethyl)piperazin-1-yl]ethanesulfonic acid
His	histidine
HYP1	HYPERSENSITIVE TO LOW P1
Hz	Hertz
I	current
ICP-MS	inductively coupled plasma mass spectrometry
IRT1	*IRON-REGULATED TRANSPORTER1*
kb	kilobase
log2 FC	log_2 fold-change
LPR1	*LOW PHOSPHATE ROOT 1*
LPR2	*LOW PHOSPHATE ROOT 2*
M	molar
MDHA	monodehydroascorbate (oxidized form of ascorbate)
MDHAR	monodehydroascorbate reductase
MES	2-(N-morpholino)ethanesulfonic acid
mg	milligram
min	minute
mL	milliliter
mM	millimolar
mm	millimeter
mm Hg	millimeter of mercury
mM^{-1} cm^{-1}	molar extinction coefficient
MS	Murashige and Skoog medium
mV	millivolt
MΩ	megaohm
n	number of independent replicates
№	number
nA	nanoamper
NADH	nicotinamide adenine dinucleotide hydrogen
NADPH	nicotinamide adenine dinucleotide phosphate
ng	nanogram
nL	nanoliter

nm	nanometer
NTA	nitrilotriacetate
ORF	open reading frame
P	phosphorus
PCR	polimerase chain reaction
PDB	Protein Data Bank
Pi	phosphate
PI	propidium iodide
PLT2	*PLETORA 2*
PM	plasma membrane
pro	promoter
QC	quiescent center
qPCR	quantitative PCR
RAM	root apical meristem
Rev	reverse
RMSDs	root-mean-square deviation of atomic positions
RNA	ribonucleic acid
rpm	rotation per minute
RT	room temperature
s	second
SALK	Salk Institute Genomic Analysis Laboratory
s.d.	standard deviation
SGN1	*SCHENGEN 1*
SHR	*SHORT ROOT*
T-DNA	transfer DNA
UBQ2	*UBIQUITIN2*
UTR	untranslated region
v/v	volume per volume
VTC1	*VITAMINC1*
W	watt
w/v	weight per volume
WOX5	*WUSCHEL-RELATED HOMEOBOX 5*
wt%	weight by percentage
z	distance
µm	micrometer
µmol m^{-2} s^{-1}	photon flux

10 Acknowledgement

I would like to express my sincere gratitude to Prof. Dr. Nicolaus von Wirén, for graciously accepting me into his working group, providing constant motivation, and offering key scientific input that significantly contributed to the success of this project.

My deepest thanks to Dr. Ricardo F. H. Giehl, whose insightful discussions, steady support, and expert supervision were of great importance throughout the entire duration of this research. I am sure I will always benefit from the invaluable experiences and insights I have gained from him, both professionally and personally.

I also would like to extend my gratitude to all the members of the dissertation committee, whose constructive criticism and valuable advice have greatly enhanced the quality of this work.

Many thanks also to my collaborators Dr. Georg Künze (University of Leipzig, Germany) and Prof. Dr. Armando Carpaneto (University of Genoa, Italy) and their team, whose collaboration and joint efforts have enriched the scope and impact of this research, and to the German Research Foundation (Deutsche Forschungsgemeinschaft, DFG) agency for their generous financial support, without which this project would not have been possible.

I would like to thank also the dedicated technical support team at IPK, whose hard work and expertise have been indispensable in overcoming technical challenges encountered during the course of this study. My deepest thanks go to the technicians Annett Bieber, Elis Fraust, Jacqueline Fuge, and Dr. Yudelsy T. Moya, and also to Mr. Geyer and his team in the greenhouse.

My heartfelt appreciation to all my friends at IPK and in Brazil who have provided the best company and support, both directly and indirectly, during the highs and lows of this academic journey.

I am deeply grateful to my family for their great support and encouragement throughout my life as a PhD student. Their belief in my potential, despite the challenges of time and distance, has been invaluable in helping me stay motivated and balanced during this intense period.

Finally, I thank to all those whose names may not be explicitly mentioned here but who have been valuable contributors, thank you for your role in making this achievement possible. Your support has been instrumental, and I am truly grateful for the collective effort that has brought this thesis to fruition.

11 Curriculum Vitae

Name:	Rodolfo Augusto Maniero
ORCID:	https://orcid.org/0000-0002-1074-8034
Email:	maniero@ipk-gatersleben.de

Education:

05/2020-ongoing	PhD Student at the Leibniz-Institute of Plant Genetics and Crop Plants Research (IPK), Department of Physiology and Cell Biology (PZB), Gatersleben, Germany
	Research Group: Molecular Plant Nutrition
	Supervisor: Prof. Dr. Nicolaus von Wirén
	Enrolled at the Martin-Luther University Halle/Wittenberg, Germany, Institute for Biology
	Dissertation title: Identification and characterization of genes involved with iron-dependent root growth under limiting phosphorus
01/2017-06/2019	Center for Nuclear Energy in Agriculture, University of São Paulo, Brazil
	Master study course: Biology in Agriculture and Environment
	Master thesis on the subject: Functional characterization of gene encoding ammonium transporter ScAMT3;3 from sugarcane (*Saccharum* spp.)
02/2011-01/2017	ESALQ, University of São Paulo, Brazil
	Bachelor study course: Agricultural Engineering
	Bachelor thesis at the Center for Nuclear Energy in Agriculture in University of São Paulo (Brazil) on the subject: Molecular characterization and hormonal regulation of a male sterile mutant in tomato (*Solanum lycopersicum* L. cv Micro-Tom) involving the transformation of stamens into pistils and petals into sepals
01/2014-12/2014	University of Illinois at Urbana-Champaign, USA
	Training, 2 semesters of “graduation-sandwich”,
	Bachelor Plant Production
	Brazilian Scientific Mobility Program Scholarship

Conferences and scientific training during the PhD study:

Conferences - oral presentations:

08.07-12.07.2024	21st International Symposium on Iron Nutrition and Interactions in Plants (ISINIP), Düsseldorf, Germany. “Exploring the role of an electron transport mechanism in Fe-dependent root growth under low P”. 2024 (flash talk)
15.05-18.05.2023	10th International Symposium on Root Development, Ghent, Belgium. “A novel class of metalloreductases critical for root growth maintenance under low phosphorus availability”. 2023
24.05-28.05.2021	ISRR11 and ROOTING2021: Root Biology Never Sleeps (online). “A novel ascorbate-dependent mechanism of meristem protection under low phosphorus driven by HYP1”. 2021. (flash talk)

Conferences - poster presentations:

08.07-12.07.2024	21st International Symposium on Iron Nutrition and Interactions in Plants (ISINIP), Düsseldorf, Germany. “Exploring the role of an electron transport mechanism in Fe-dependent root growth under low P”. 2024 (Best Poster Award)
04.09-06.09.2023	Institute Day 2023, IPK, Gatersleben. “Identification of a novel type of iron reductases required under P deficiency”. 2023
03.07-04.07.2023	Plant Science Student Conference 2023 (PSSC), IPK Gatersleben. “A novel class of metalloreductases critical for root growth maintenance under low phosphorus availability”. 2023
30.06-13.07.2022	Mistral Montpellier, France. “A novel electron transporter putatively involved with iron reduction in plants”. 2022
15.06-18.06.2021	Plant Science Student Conference 2021 (PSSC), IPK Gatersleben. “A novel ascorbate-dependent mechanism of meristem protection under low phosphorus driven by HYP1”. 2021
24.05-28.05.2021	ISRR11 and ROOTING2021: Root Biology Never Sleeps (online). “A novel ascorbate-dependent mechanism of meristem protection under low phosphorus driven by HYP1”. 2021
22.09-24.09.2021	Bilateral Conference of the German Society of Plant Nutrition (DGP), Kiel, Germany. “Identification of novel genes regulating plant responses to phosphorus availability”. 2021

Practical scientific training:

18.09-22.09.2023	Protein Structure Workshop, IPK, Gatersleben
13.03-17.03.2023	de.NBI Data Management Course, IPK, Gatersleben
30.06-13.07.2022	MISTRAL international summer school on ion and water transport in plants, Montpellier, France
10.08.2021-21.04.2022	Goethe-Institut e.V, Germany, Intensive German course level A2
28.10.2020	“How to generate a scientific paper”, IPK, Gatersleben

Further activities:

09.02.2022-present	Organizing committee of IPK Club
03.07-04.07.2023	Member of the core organization committee for the 2023 Plant Science Student Conference; IPK Gatersleben
27.10.2021-23.02.2023	Member of the IPK PhD Student Board
15.06-18.06.2021	Member of the core organization committee for the 2021 Plant Science Student Conference; IPK Gatersleben

Supervision activity:

11/2023-12/2023	Supervision of an PhD candidate for research in molecular plant nutrition on “the effects of chitosan on root phenotype of *Arabidopsis thaliana*” - Katharina Eickelpasch (University of Münster, Germany)
06/2023-08/2023	Supervision of an undergraduate student for research in molecular plant nutrition on the “characterization of a novel class of plant metalloreductases” - Seydin Erhan Gönül (Bilkent University, Turkey)
08/2020-09/2020	Supervision of an undergraduate student for research in molecular plant nutrition - Franziska Lindecke

Publications:

Maniero, R. A., Picco, C., Hartmann, A., Engelberger, F., Gradogna, A., Scholz-Starke, J., Melzer, M., Künze, G., Carpaneto, A., von Wirén, N., Giehl, R. F. H. (2024). Ferric reduction by a CYBDOM protein counteracts increased iron availability in root meristems induced by phosphorus deficiency. Nature Communications, 15, 422.

Maniero, R. A., Koltun, A., Vitti, M., Factor, B. G., de Setta, N., Camara, A.S., Lima, J. E., and Figueira, A. (2023). Identification and functional characterization of the sugarcane (*Saccharum* spp.) AMT2-type ammonium transporter ScAMT3;3 revealed a presumed role in shoot ammonium remobilization. Frontiers in Plant Science, 14, 1299025.

Koltun, A., **Maniero, R. A.**, Vitti, M., de Setta, N., Giehl, R. F., Lima, J. E., and Figueira, A. (2022). Functional characterization of the sugarcane (*Saccharum* spp.) ammonium transporter AMT2;1 suggests a role in ammonium root-to-shoot translocation. Frontiers in Plant Science, 13, 1039041.

Liu, Y., **Maniero, R. A.**, Giehl, R. F., Melzer, M., Steensma, P., Krouk, G., Fitzpatrick, T. B., and von Wirén, N. (2022). PDX1.1-dependent biosynthesis of vitamin B6 protects roots from ammonium-induced oxidative stress. Molecular Plant, 15(5), 820-839.

12 Eidesstattliche Erklärung/Declaration on oath

Hiermit versichere, dass ich die vorliegende Arbeit selbstständig verfasst habe, dass ich keine anderen Quellen und Hilfsmittel als die angegebenen benutzt habe und dass ich die Stellen der Arbeit, dich ich anderen Werken – auch elektronischen Medien – dem Wortlaut oder Sinn nach entnommen habe, in jedem Fall unter Angabe der Quelle als Entlehnung kenntlich gemacht habe. Die Arbeit wurde bisher in gleicher oder ähnlicher Form keiner anderen Institution oder Prüfungsbehörde vorgelegt.

I hereby declare that I have written the submitted thesis independently and without illicit assistance of third parties. I have not used any other reference and sources than those listed in the thesis or engaged any plagiarism. All references and sources used in the presented work are properly cited and acknowledged. Further, I declare that the presented work has not been previously submitted for the purpose of academic examination, either in its original or similar form, anywhere else.

_____ _____

Ort/Place, Datum/Date Unterschrifft/Signature

13 Erklärung über bestehende Vorstrafen und anhängige Ermittlungsverfahren/Declaration concerning Criminal Record and Pending Investigations

Hiermit erkläre ich, dass ich weder vorbestraft bin noch dass gegen mich Ermittlungsverfahren anhängig sind.

I hereby declare that I have no criminal record and that no preliminary investigations are pending against me.

_____ _____

Ort/Place, Datum/Date Unterschrifft/Signature